INVESTIGATIONS ON MECHANISTIC MODELS FOR ANNULAR FLOW DRYOUT AND POST DRYOUT HEAT TRANSFER PHENOMENA

By

Arnab Dasgupta

ENGG01200804005

Bhabha Atomic Research Centre, Mumbai

A thesis submitted to the

Board of Studies in Engineering Sciences

In partial fulfillment of requirements for the Degree of

DOCTOR OF PHILOSOPHY

of

HOMI BHABHA NATIONAL INSTITUTE

March, 2017

Homi Bhabha National Institute[1]

Recommendations of the Viva Voce Committee

As members of the Viva Voce Committee, we certify that we have read the dissertation prepared by Arnab Dasgupta entitled "Investigations on mechanistic models for annular flow dryout and post dryout heat transfer phenomena" and recommend that it may be accepted as fulfilling the thesis requirement for the award of Degree of Doctor of Philosophy.

Chairman – Prof. G.K. Dey (for).	6/2/17 Asso. Dean HBNI	Date: 06/02/17
Guide / Convener – Prof. P.K. Vijayan		Date: 6/2/17
Examiner – Prof. Sreenivas Jayanti, IIT Madras, Chennai		Date: 6/2/17
Member 1- Prof. A.P. Tiwari	06/2/17	Date:
Member 2- Prof. S.S. Taliyan		Date:
Member 3- Prof. M.K. Samal		Date: 06.02.2017

Final approval and acceptance of this thesis is contingent upon the candidate's submission of the final copies of the thesis to HBNI.

I/We hereby certify that I/we have read this thesis prepared under my/our direction and recommend that it may be accepted as fulfilling the thesis requirement.

Date: 6/2/17

Place: Anushakti Nagar

<Prof. P.K. Vijayan>

Guide

[1] This page is to be included only for final submission after successful completion of viva voce.

Version approved during the meeting of Standing Committee of Deans held during 29-30 Nov 2013

* I could not attend the meeting as I was out of station but I knew the research work of the candidate and found the work satisfactory.

STATEMENT BY AUTHOR

This dissertation has been submitted in partial fulfillment of requirements for an advanced degree at Homi Bhabha National Institute (HBNI) and is deposited in the Library to be made available to borrowers under rules of the HBNI.

Brief quotations from this dissertation are allowable without special permission, provided that accurate acknowledgement of source is made. Requests for permission for extended quotation from or reproduction of this manuscript in whole or in part may be granted by the Competent Authority of HBNI when in his or her judgment the proposed use of the material is in the interests of scholarship. In all other instances, however, permission must be obtained from the author.

Arnab Dasgupta

DECLARATION

I, hereby declare that the investigation presented in the thesis has been carried out by me. The work is original and has not been submitted earlier as a whole or in part for a degree / diploma at this or any other Institution / University.

Arnab Dasgupta

List of Publications arising from the thesis

Journal

1. Arnab Dasgupta, D.K Chandraker, K. Suhasith, B. Raghavendra Reddy, R. Rajalakshmi, A.K. Nayak, S.P. Walker, P.K. Vijayan, G.F. Hewitt, "Experimental investigation on dominant waves in upward air-water two-phase flow in churn and annular regime", Experimental Thermal and Fluid Science, Vol. 81, 2017, pages 147-163.

2. Arnab Dasgupta, D.K. Chandraker, P.K. Vijayan, S.P. Walker, "An assessment of the correlations for entrainment and deposition rates in annular flow for dryout prediction", Multiphase Science and Technology, Vol. 28 (2), 2016, pages 99-133.

3. Arnab Dasgupta, D.K. Chandraker, P.K. Vijayan, "SCADOP: Phenomenological Modeling of Dryout in Nuclear Fuel Rod Bundles", Nuclear Engineering and Design, Vol. 293, November 2015, pages 127-137.

4. Arnab Dasgupta, D.K. Chandraker, A.K. Nayak, P.K. Vijayan, "Prediction of vapor film thickness below a Leidenfrost drop", ASME Journal of Heat Transfer, Vol. 137(12), December 2015, pages 124501-1-5.

5. A. Dasgupta, D.K. Chandraker, A.K. Vishnoi, P.K. Vijayan, "A new methodology for estimation of initial entrainment fraction in annular flow for improved dryout prediction", Annals of Nuclear Energy, Volume 75, January 2015, Pages 323-330.

International conferences:

1. Arnab Dasgupta, D K Chandraker, A.K. Nayak, P.K. Vijayan, A. Rama Rao, S.P. Walker, "Development and validation of a model for predicting direct heat transfer

from the fuel to droplets in the post dryout regime", ANS Embedded Topical meeting on Advances in Thermal Hydraulics 2016, New Orleans, LA, June 11-16, 2016

2. Arnab Dasgupta, D K Chandraker, A K Nayak, P K Vijayan, S Kshirasagar, B R Reddy, S P Walker, "Visualization of large waves in churn and annular two-phase flow", 23rd National and 1st ISHMT-ASTFE HMTC, Thiruvananthapuram, Dec 17-20, 2015.
3. A. Dasgupta, D.K. Chandraker, A.K. Nayak, P.K. Vijayan, "Prediction Of Vapor Film Thickness Below A Leidenfrost Drop", 22th National and 11th ISHMT-ASME HMTC, Kharagpur, Dec 28-31, 2013.
4. Arnab Dasgupta, D.K. Chandraker, P.K. Vijayan, "A Phenomenological Model for Prediction of Dryout in Nuclear Fuel Rod Bundles", Paper No. N9P0135, NUTHOS-9, Kaohsiung, Taiwan, 2012.
5. Arnab Dasgupta, D.K. Chandraker, P.K. Vijayan and D. Saha, "A Mechanistic Model Based on Film Depletion for Prediction of Dryout Power in Tubular Geometry", paper no. N13P1112 NURETH-13, 2009.
6. A. Dasgupta, D. K. Chandraker and P. K. Vijayan, "SCADOP: A Computer Code for Steady State Subchannel Analysis of Nuclear Fuel Bundles", 19th National and 8th ISHMT-ASME, HMTC, Hyderabad, 2008.

Arnab Dasgupta

DEDICATIONS

To Maa Saraswati, the giver of all knowledge

To my parents, who gave me the life to pursue knowledge

To the research community, with the hope that my work increments world knowledge

ACKNOWLEDGEMENTS

At the outset I should thank my guide Prof. P.K. Vijayan for being a source of inspiration for my doctoral work. It was in fact he who had encouraged me to pursue the doctoral program. He had ensured substantial freedom and flexibility in my work while at the same time giving direction to it.

I would also like to thank members of my doctoral committee, who have been supportive all through the work and provided critical comments and suggestions.

I must also thank Dr. D.K. Chandraker and Mr. Alok Vishnoi with whom I have worked since the beginning of my career. The fact that they work in the same field has helped me a lot. The in depth discussions which I had with them were instrumental in shaping the final form of my work. Thanks are also due to Dr. A.K. Nayak from whom I learnt the importance of questioning. Truly, it is questions which lead to answers.

I also consider it my good fortune to get the opportunity (through a separate official assignment) to discuss the subject with Prof. G.F. Hewitt – the man without whom the present understanding of annular two-phase flow, worldwide, would have been in a much poorer state. His knowledge and zeal both have imbibed a lasting impression on me. I sincerely hope an iota of it has percolated into this thesis as well. I must also thank Prof. S.P. Walker (Imperial College London) for insightful discussions and providing new perspectives on my work.

For the present work, I have been helped by many of my colleagues and seniors; Mrs. R. Rajalakshmi, Mr. G.J. Gorade, Dr. P.P. Kulkarni, Mr. S. Kshirsagar, Mr. B.R. Reddy, my office (101) room-mates – Yogesh, Arun, Mainak, Pradeep, Mahesh, Purnendra, Saikat and Abhishek all deserve a special mention. There are numerous other people who I would like to acknowledge, but the list is too long to be accommodated in a couple of pages. I thank all of them.

I am also grateful to examiners of my thesis – Prof. Sreenivas Jayanti and Dr. Jean-Marie Le Corre for their critical comments and in-depth review. Going through their reviews has led me to looking at the things from an altogether different perspective. This has reflected in the thesis as well at appropriate junctures.

My family has been a supporting pillar for me, not just for this doctoral endeavor but in all other walks of life as well. My uncle S.P. Sengupta would always ask me and encourage me to do my doctoral work with full dedication. My parents and sister have inspired me in every walk of life including this.

I must mention the immense patience and understanding nature of my wife, Seemita, lovely daughter, Divyani and son Anagh. During my doctoral work, there have been times when I have not been able to devote time to them but they have been generous enough to excuse that.

Finally I would like to thank Bhabha Atomic Research Centre (BARC) for the excellent facilities for research work without which none of this work would have been possible.

CONTENTS

LIST OF FIGURES

LIST OF TABLES

NOMENCLATURE

a	Constant in CISE correlation, eqn. (2.1) (dimensionless)
A	Subchannel area (m^2)
b	Constant in CISE correlation, eqn. (2.1) (dimensionless)
B	Vaporization rate (kg/m^2s)
c	Conduction coefficient in subchannel eqn. (W/mK)
C	Droplet concentration (kg/m^3)
C_{boil}	Constant
d	Diameter (m)
d_{eq}	Equivalent diameter of a channel. In case of flow in a circular tube this is the inside diameter (m)
D	Deposition rate (kg/m^2s)
e	Thickness of vapor layer (m)
E	Entrainment rate mostly used for that caused due to shear (kg/m^2s)
E_{boil}	Boiling induced entrainment (kg/m^2s)
Eo	Eotvos number (dimensionless), defined in eqn. (3.11)
f_i	Interfacial friction factor (dimensionless)
f	Wave frequency (Hz)
F_g	Gravity Force (N)
F_m	Momentum force (N)
F_p	Pressure force (N)
Fr	Froude number (dimensionless), defined in eqn. (3.13)

g Acceleration due to gravity (m/s^2)

G Mass flux referenced to channel cross-section (kg/m^{2}s)

h Specific Enthalpy (kJ/kg), also heat transfer coefficient (W/m^{2}K) in chapter 2 and 7

h_{fg} Specific enthalpy for vaporization (kJ/kg)

i Index used variously to denote the spatial or time increment etc.

j Superficial velocity (m/s)

k Deposition coefficient (m/s)

k_e Entrainment constant in eqn.

k_v Thermal conductivity of vapor phase (W/mK)

K_{kum} Constant in Kumar correlation (dimensionless)

K_{pr} Constant in Pearce correlation (dimensionless)

$K1$ Constant in equation (2.5)

$K2$ Constant in equation (2.5)

l Mixing length for turbulent cross-flow between adjacent subchannels (m)

L_b Boiling Length (m)

m Mass flow rate (kg/s)

n Constant in Adamsson and Anglart entrainment rate equation (2.19) (dimensionless)

Nu Nusselt number, hl/k (dimensionless) where h is heat transfer coefficient, l is a characteristic length and k is the fluid thermal conductivity

N_μ Viscosity number, $\mu_l \Big/ \sqrt{\rho_l \sigma \sqrt{\sigma / g\left(\rho_l - \rho_g\right)}}$ (dimensionless)

p Pressure (Pa)

Pr Prandtl number (dimensionless), ratio of momentum to thermal diffusivity.

q' Heat input per unit length to a subchannel (kW/m)

q'' Heat flux (kW/m^2)

r Distance along radial direction (m)

r_{bot} Bottom radius of Leidenfrost drop (m)

Re Reynolds number (dimensionless), ratio of inertial to viscous forces

s Width of gap between two subchannels (m)

Sc Schmidt number (dimensionless), ratio of momentum to mass diffusivity

Sr Strouhal number (dimensionless), non-dimensional frequency defined in eqn. (3.8)

T Temperature (^{o}C)

u Fluid velocity (m/s)

u_* Friction velocity (m/s)

v_w Wave velocity (m/s)

V_{dep+} Non dimensional deposition velocity (dimensionless), defined in eqn. (2.4).

We_l Liquid phase Weber number (dimensionless), $G_l^2 d_{eq} \big/ \rho_l \sigma$

We_k Weber number for deposition (dimensionless), defined in eqn. (2.14).

We_m Modified Weber number(dimensionless), defined in eqn. (3.1).

x, X Thermodynamic quality (dimensionless)

y^+ Non-dimensional distance from wall. (dimensionless)

z Distance along channel axis in reference to pipe flow. Otherwise distance along Vertical direction. (m)

Greek symbols

α Void fraction (dimensionless). Also used to represent thermal diffusivity (m^2/s) in chapter 7.

α_{lf} Fraction of cross-sectional area occupied by liquid film in annular flow (dimensionless).

δ Thickness of liquid film in annular flow (m).

Δ_i Interaction time of non-contacting droplets and heated wall (s)

Γ Mass diffusivity of drops in annular flow (m^2/s).

τ_i Interfacial shear stress (N/m^2).

τ_{p+} Dimensionless particle relaxation time(dimensionless), defined in eqn. (2.3).

τ_w Wall shear stress (N/m^2).

σ Surface tension (N/m).

σ_B Stefan-Boltzmann constant (W/m^2K^4).

ρ Density (kg/m^3).

μ Dynamic viscosity (Pa-s).

π_e Entrainment parameter (dimensionless) defined in eq. (2.22)..

λ Wavelength (m).

φ_G Gray body factor (dimensionless).

φ_l^2 Two-phase frictional multiplier.

$\forall$ Volume of liquid entrained from the tip of a single wave (m^3).

ψ Inclination angle measured from vertical (degrees).

ζ_h Heated perimeter (m).

ζ_w Wetted perimeter (m).

Subscripts

g	Gas/vapor.
l	Liquid.
p	Particle.
r	Rod.

ABSTRACT

Boiling heat transfer is one of the most efficient means of energy transport. In Boiling Water Reactors (BWRs), it is the mode of heat transfer under normal operating conditions. The maximum power that can be extracted for a given core flow in a BWR is limited by a phenomenon called dryout. The occurrence of dryout is marked by a sudden deterioration in heat transfer coefficient and sharp rise in surface temperature. For a nuclear reactor, depending on the extent of surface temperature excursion and its duration, this may translate into clad failure and release of radioactivity. Dryout and the ensuing clad temperatures thus present a serious safety concern. Though the occurrence of dryout in itself would not imply clad failure, it is a very important margin used to limit the operating power of a reactor. Essentially, the nuclear fuel is safe from a thermal-hydraulic point of view prior to dryout. After dryout, failure may occur depending on the extent of clad surface temperature excursion, which again is a function of local flow and power. In view of the uncertainties associated with local flow and power during a transient, the reactor power is limited during normal operation so that dryout is not encountered even during the worst operational transients. At the same time, from the perspective of a designer, it is desirable to maximize the power that can be derived for a given core configuration. The ability to predict dryout and post dryout temperature rise reliably is thus of interest to reactor designers, operators and regulators. While a good estimate of dryout leads to more realistic operating safety margins, proper estimation of post-dryout heat transfer allows better estimate of temperature excursion and its duration, which are important in assessing the possible damage to fuel and decision making for post accident strategies viz., ECC inventory, flow rates, time of injection etc.

The importance of dryout has been recognized since the advent of BWRs. Design of BWRs was solely reliant on correlations developed from experiments on full scale clusters. The correlations developed are dependent on geometry of the fuel bundle. Even changes in local peaking factors, axial heat flux profile or spacer geometry would affect the applicability of a correlation. Changes in afore-mentioned parameters thus require re-experimentation for regulatory approval. Bundle experimentations are extremely expensive and it is desired that such experiments are substantiated by pre-test analysis. This has led to a lot of work wherein tubular (and simulated subchannel) dryout data (and correlations) are applied to bundles with certain empirical correction factors. The empirical approach towards prediction of dryout has hence led to proliferation of correlations. However, there is often some case for which it might not be possible to get an applicable correlation or there may be cases where there exists the choice of multiple correlations for a situation giving widely differing values.

These shortcomings of the purely empirical approach led to the development of phenomenological (or mechanistic) models which are discussed in the present work. These models rely on numerically tracking the liquid film in annular steam-water flow. Such a model brings down the level of empiricism by correlating more basic quantities (deposition and entrainment rate) and is expected to be independent of rod bundle geometry and heat flux profile.

The models are however only as good as the constitutive correlations for entrainment and deposition and there are of course uncertainties associated with the application of generic deposition and entrainment correlations (which have been derived from tube experiments) for rod bundles. Part of the reason for this is the fact that these correlations are empirically derived and there are no guidelines for choice of the appropriate correlation. Secondly, the errors introduced by their application to non-circular geometries (as in rod bundles) are not well known. Further there are always unknowns in the model which are often treated in an essentially ad-hoc fashion. One such unknown is the entrained fraction at the onset of annular flow, commonly known as Initial Entrainment Fraction (IEF) for which no experimental data exist and models are scanty. Additional modeling complexity is introduced due to spacers which are used in nuclear fuel bundles for maintaining inter-rod spacing. Modeling the effect of spacers requires at-least one additional empirical correlation which is dependent on spacer geometry.

Due to foregoing reasons, mechanistic models are not considered sufficient for licensing. While it would be too ambitious to expect that the regulatory philosophy is going to change in near future, it is beyond doubt that the use of mechanistic models can aid immensely during the design of rod bundles and can cut down the number of experiments required for regulatory clearances. Improvements in the mechanistic models are thus of use for the nuclear community. The present efforts are directed towards reducing the empiricism in this model. In this direction, the following is done:

1. Experiments have been done on characteristics of waves in churn and annular flow. This is important in view of the importance of waves on deposition and entrainment process. The experimental data can be used in future for simulation of the deposition phenomena in particular.
2. An assessment of deposition and entrainment rates has been carried out. The assessment procedure is different from the previous assessments available in literature in that the performance of deposition-entrainment correlations is assessed

in tandem. The correlation sets are assessed against various annular flow experimental data and theoretical considerations. The better set is finally identified.

3. A new methodology is presented for estimation of IEF. Improvement in annular flow predictions is observed upon application of this methodology.

Finally a more self contained mechanistic model is proposed by using the new IEF methodology along with the better entrainment-deposition correlation set. This model is applied to rod bundles using the subchannel methodology and a computational tool SCADOP is developed.

The other problem of interest to reactor safety closely related to dryout is called post-dryout heat transfer. In a nuclear reactor, dryout (and thus post-dryout) is not anticipated under normal operating conditions as the coolant flow and operating power are fixed so as to not result into dryout. Since post dryout is associated with surface temperatures in excess of rewetting temperatures, the study and modeling of post dryout phenomena for reactor safety is relevant when the power levels are much lower than operating power. Such conditions may occur after a Loss of Coolant Accident (LOCA), where even though reactor trip ensures low power, the loss of coolant coupled with stored heat and decay heat leads to dryout. During the reflood phase following a LOCA, annular flow conditions may be encountered at low reflooding rate. The tip of the annular film marks the wetting front, downstream of which is the post dryout region. The droplets entrained from this film are carried downstream and aid in precursory cooling. The prediction of post dryout heat transfer is complicated, in particular, due to the thermal non-equilibrium of vapour and the difficulties in predicting heat transfer from the wall to droplets. There are two modes in which the wall-to-drop heat transfer takes place – when the drops are contacting the wall

(i.e., below rewetting temperature) and when the drops are non-wetting (beyond rewetting temperature). The heat transfer to non-wetting droplets is modeled in the present work. The model is validated against indirect data on thickness of the vapor layer underneath the drop. The model is further applied (with some assumptions) to conditions of relevance to nuclear reactor. A reasonable agreement was observed.

1 INTRODUCTION

Nuclear energy, when it was first harnessed for peaceful purposes in the 1950s, showed promise as a source of clean energy which could power mankind for many centuries. In 1954, Obninsk nuclear power plant (5 MWe) in Russia (erstwhile USSR) became the first nuclear power plant to be connected to the grid. This was followed by Calder Hall (1956) in United Kingdom and Shippingport (1958) power plant in United States. The Calder Hall and Shippingport reactors produced a substantially greater power of 60 MWe each.

Nuclear reactors have evolved since these early reactors, with presently operating and proposed reactors having much greater power output and many enhanced safety features. Nuclear energy now provides for slightly over 11% of the world's total energy needs. In terms of installed capacity, it translates to 381365 MWe. The growth in the share of nuclear energy in the last 60 years, especially in Europe and America, is indeed remarkable and does underline the economic feasibility of nuclear power. The major growth in nuclear power took place during 1970s to late 1990s. This growth was scarred by two major accidents at Three Mile Island and Chernobyl reactors. More recently the Fukushima nuclear disaster which was caused by a rare natural calamity has severely decelerated the growth of nuclear power. In fact, Germany where about 20% of the electricity is nuclear took a decision to phase out nuclear power by 2022. The issue of nuclear safety unless addressed properly can create a serious roadblock for nuclear energy. Safety issues had been taken in all seriousness by the nuclear community, even prior to Fukushima accident, leading to development of innovative and evolutionary safety concepts and new reactors. However, after Fukushima, it has been realized as a harsh reality that most of the reactors under operation are the older 1970s and 1980s reactors when such advanced concepts were still in infancy. The ability to analyze, ascertain and enhance the safety of the operational reactors is thus still a matter of concern for the nuclear community. Since 426 of the 443 reactors currently operating worldwide as well as many of the proposed future generation reactors are water cooled reactors, more reliable thermal-hydraulic models for water cooled reactors are desirable not just for the evolutionary reactor concepts but also for ensuring safety in existing plants.

Water may not be the best available coolant in terms of operating temperature and pressure but it definitely has been the most natural choice for obvious reasons. The good heat transfer properties of water are further enhanced after boiling initiates. The advantages of using boiling water over single phase water as a coolant are summarized below:

1. Boiling leads to more efficient heat transfer.
2. It is easier to maintain pressure in a boiling water system due to the presence of steam, which being compressible doesn't allow sudden increase or decrease in system pressure.
3. In the conception stage of BWRs, natural circulation instead of forced circulation was envisaged as the mode for heat transfer [1]. Boiling systems provide a greater natural circulation driving head leading to the selection of boiling water as coolant.
4. In vessel type BWRs, boiling causes voiding, leading to reduced moderation and negative reactivity insertion. This fact helped the reactor designs to ensure that chain reaction is arrested well before the reactor became runaway.

As a rule of nature, advantages come bundled with disadvantages, allowing boiling in a system is no exception. The phenomenon of boiling transition variedly known as Critical Heat Flux (CHF), dryout etc. is a serious safety concern. Breaching this limit could lead to fuel failure. CHF thus limits the maximum allowable operating heat flux. A proper knowledge of this condition allows extracting the maximum possible power from the reactor without compromising on safety. Its accurate prediction is thus important for designers, operators and regulators alike. Saturated flow boiling occurs in the heat transport system of BWRs. The water enters the core as single phase coolant and moves up the core extracting heat from the nuclear fuel. In this process, it undergoes phase change. In a conventional BWR, bubbly, slug, churn and annular two-phase flow regimes are encountered. The possible mechanism for boiling transition in annular flow regime, described in §2.1, is the physical drying out of the liquid film adjacent to the wall. This phenomenon (known as dryout), if it occurs, would lead to excursion of clad surface temperature and possible clad failure resulting in radioactivity release. Thus it is avoided by design in nuclear reactors under operational states and Anticipated Operational Occurrences (AOOs).

Under postulated accidents like Loss of Coolant Accident (LOCA) dryout might occur (in both BWRs and PWRs) and clad surface temperature could exceed the rewetting temperature. Under such conditions, safety of the fuel pins is ensured through Emergency Core Cooling System (ECCS). The emergency coolant is initially unable to wet fuel pins (as they are above the rewetting temperature). As heat transfer proceeds in this liquid deficient regime, the pins cool down till the temperature drops to a value such that the emergency water is able to wet the clad and ensure fast cooling. Predictions of heat transfer in this regime, known as the post-dryout regime, are also important for accident analysis.

1.1 Problem statement

In the foregoing, two typical problems of importance to nuclear safety – dryout and post-dryout heat transfer have been highlighted.

Conventionally dryout has been predicted through empirical correlations based on operating parameters like mass-flux, pressure, quality, cluster geometry, boiling length etc. This approach though workable does not allow a single correlation to describe the complete range of operating parameters. The multitude of combinations of the different operating parameters and the desire to have a single framework describing CHF has culminated into development of the CHF look-up table [2]. Mechanistic models of CHF are a valuable alternative to such empirical treatment and have been developed in parallel for a few decades now.

The mechanistic approach relies on modeling the basic phenomena leading to occurrence of CHF. Further, they allow better treatment of effects of heat flux distribution and complex geometry. Mechanistic modeling of annular flow dryout, the subject of this thesis, comprises of computing the depletion of the liquid film due to entrainment and vaporization. This depletion is partly offset by deposition of drops into the film. The model relies upon the models and correlations for entrainment and deposition rates. Further it also requires the amount of entrained fraction at onset of annular flow (or Initial Entrainment fraction, IEF). Many correlations are available in the literature for entrainment and deposition rates. One of the objectives of the present work is to identify the better set of entrainment and deposition rate correlations. Since entrainment and deposition are significantly influenced by the disturbance waves on the annular film, their study follows as a natural course. With regards to the closure for IEF, there is scarcity of both experiments and models. Typically, no experiments are available which provide values of IEF in diabatic scenario. An attempt has been made in the present work to provide a methodology for IEF prediction.

The post-dryout heat transfer mechanisms are (very much like dryout) dependent on the flow regime encountered. For low qualities, Inverted Annular Film Boiling (IAFB) is observed [3]. This regime is characterized by a core of liquid (as continuous liquid stream or slugs) flow separated from the heated wall by a layer of vapor. The heat transfer takes place across this vapor layer. At high qualities, mist flow regime is observed. This regime is also known as dispersed flow since the droplets are dispersed in a flow of vapor. In this regime, the droplets are unable to wet the wall. Thus the associated boiling regime is known as Dispersed Flow Film Boiling (DFFB). DFFB follows as a natural consequence of dryout. In terms of modeling this regime, some parallel can be drawn from the annular film flow model. Of course modifications like no entrainment (as there is no film), modified vaporization (as now the surface heat flux also goes into superheating the vapor) are required. Also, the surface heat flux is now controlled by the surface temperature. Nevertheless, the mechanistic model does present a viable option for analysis of post dryout phenomena as outlined by Hewitt and Govan [4]. Unlike the pre-dryout regime where surface heat flux goes into solely vaporizing the liquid film, in this regime the surface heat is extracted by both vapor flow and droplets which deposit towards it. Chatzikyriakou [5] has shown that the wall-to-droplet mode of heat transfer can contribute as much as 10% of total heat transfer. Models available in literature differ on the inclusion of this term. However, it may be said with certainty that this mechanism must be taken into account to improve the predictions of best estimate codes. Currently available models for

DFFB heat transfer which incorporate the wall–drop heat transfer use either of the following methodologies

a. Semi-empirical heat transfer coefficients (Forslund and Rohsenow[6], Moose and Ganic[7])
b. Reliance on full scale CFD simulations (Chatzikyriakou [5]) or
c. Mechanistic models like those used by Andreani and Yadigaroglu [8] and Guo and Mishima [9].

Considering the ease of application and greater physical basis of the mechanistic model, a similar model has been developed in the present work. Further the model has been validated against experimental data available in literature [10]. The present validation complements the work done by previous workers, in whose case the complete DFFB heat transfer package was validated. The present validation of a single DFFB mechanism; wall–drop heat transfer bolsters the mechanistic prediction scheme.

1.2 Objectives of the work

The major objective of this work is to improve the mechanistic models available for annular flow dryout and post dryout heat transfer by attempting to resolve the unknowns in the model. The gap areas are first identified in the mechanistic models. In particular, for annular flow modeling,

1. There are no guidelines for choice of deposition and entrainment rate correlation.
2. There is a scarcity of models/correlations to evaluate the entrained fraction at onset of annular flow.
3. Most of the correlations for deposition and entrainment are purely empirical. Possibly a lot can be gained by detailed studies on wave structures in annular flow.

In the present work, the first two gap areas have been addressed. The third is a big subject and in this work, only experiments determining wave characteristics have been performed. It is expected that the data thus generated can be of use for more mechanistic models of deposition and entrainment processes.

In case of post-dryout heat transfer, it is identified that the wall-to-drop heat transfer in the film boiling regime is important for post dryout heat transfer. In spite of many studies, few models are applicable for heat transfer to impinging droplets. The objective of the present work in this regard is to develop a model for Leidenfrost drops and evaluate its effectiveness in predicting scenarios of interest to post dryout heat transfer in nuclear reactors.

1.3 Outline of the thesis

A survey of the literature related to mechanistic modeling and post dryout heat transfer to drops is given in chapter 2. The chapter also identifies the possible scope for improvement in the models. Chapter 3 presents the experiments conducted as a part of the present work to determine the characteristics of waves in churn and annular flow. These waves have an important bearing on the entrainment and deposition of droplets. Some results from this study are used to construct a model (described in chapter 4) for estimation of the entrained fraction at the onset of annular flow. This is an essential and important boundary condition for the mechanistic modeling annular flow. This methodology coupled with the better deposition and entrainment rate correlation derived from an assessment of correlations in chapter 5 results in an improved dryout prediction model. This model and its validation against data available in literature is also the subject of chapter 5. The application of the model to rod bundle geometry is presented in Chapter 6. Computations of dryout power are also presented in this chapter. Chapter 7 presents the model for wall-to-drop heat transfer in post dryout regime. Finally conclusions and suggestions for future work are presented in chapter 8.

2 LITERATURE REVIEW

The discovery of the phenomenon of Critical Heat Flux (CHF) in 1934 by Nukiyama was driven by the desire to produce maximum possible steam flow rate and thus power from a fired boiler. This was a seminal discovery and the original Japanese paper was translated to English and published in 1965 [11]. By definition, for a heat-flux controlled surface, CHF corresponds to the condition at which a small increase in heat flux would lead to an inordinate rise in surface temperature. The idea of CHF as being the maximum possible heat flux revolutionized the design of boilers. More than 80 years after Nukiyama's discovery, CHF is still a subject of active research. It is in fact one of the major criterion which determines the maximum power that can be extracted from nuclear fuel clusters.

2.1 Phenomenology of CHF in flow boiling

The exact details of the flow and heat transfer configuration in a nuclear reactor are different from the pool boiling experimental configuration of Nukiyama. In a saturated pool, at a given pressure, the wall superheat is sufficient to quantify the surface heat flux. In flow boiling however, other parameters like mass flux and quality become significantly important. Due to the dependence on greater number of parameters, flow boiling is generally not amenable to be represented on simple plots like the pool boiling curve (Figure 2-1). Nevertheless, there have been efforts to represent the flow boiling phenomena in a graphical form. One such representation is the forced convection boiling surface (Figure 2-2) given by Collier and Thome [12].

For a particular quality, the forced convection boiling curve is similar to the pool boiling curve. It may be noticed however that the term CHF has not been used. Instead, 'Departure from Nucleate Boiling (DNB)' and 'Dryout' are used depending on quality. Further, Post-DNB the surface temperature rise is generally much higher than post-dryout. This is because dryout heat fluxes are much lower than DNB heat fluxes. The observed differences and thus the distinction between DNB and dryout lies in the different two-phase flow patterns and mechanisms causing the sudden drop in heat transfer beyond the maximum heat flux.

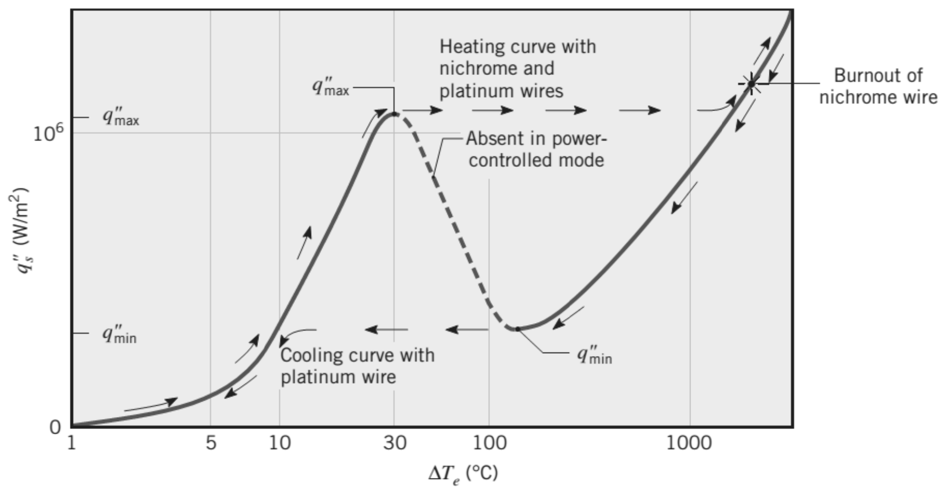

Figure 2-1: Nukiyama Pool Boiling curve reproduced from Incropera and Dewitt [13]

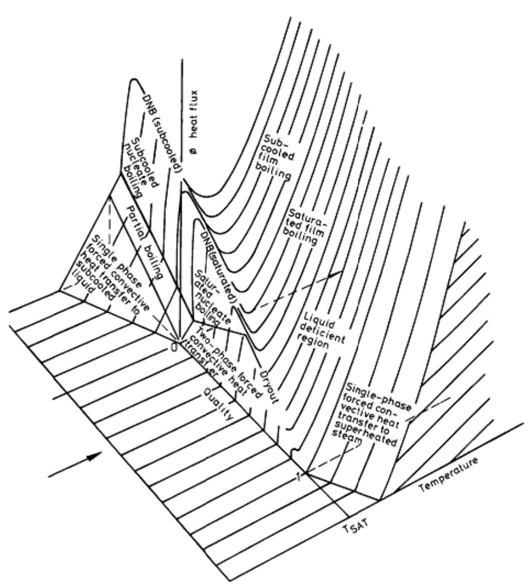

Figure 2-2: The boiling surface, from Collier and Thome [12]

2.1.1 Departure from Nucleate Boiling

DNB is typical of subcooled and low quality flows. The mechanisms leading to deterioration of heat transfer under such conditions have been described by Hewitt [14] and are represented in Figure 2-3. In cases where subcooling is high, the bubbles are generally located near to the wall (Figure 2-3a). Under such circumstances, locally high nucleation may lead to formation of a vapor clot leading to poor heat transfer at that location and temperature shoot up. At somewhat higher qualities (Figure 2-3b), a bubble boundary layer is formed which prevents the ingress of liquid towards the surface. Finally, a vapor layer forms on the surface leading to DNB. In the slug flow regime (Figure 2-3c), the liquid film around a slug bubble may dry out before being replenished by incoming liquid. Le Corre et al. [15] have shown through dimensional analysis that for any particular pressure these three mechanisms of DNB can be adequately demarcated using liquid Weber number, We_l and thermodynamic quality. They have also concluded through literature survey that DNB does not necessarily require the formation of a dry patch and can occur even in the presence of a very thin liquid layer under a vapor clot. This might be due to the high surface heat flux which prevails in DNB conditions (Figure 2-2)

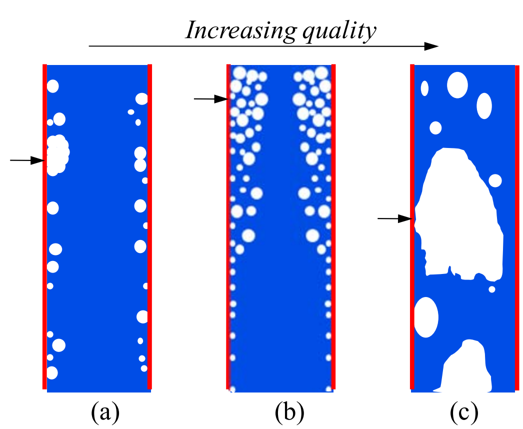

Figure 2-3: Mechanisms of DNB in upward flow: (a) Vapor clot, (b) Bubble crowding, (c) Local dry patch. Location of DNB is indicated by arrow.

2.1.2 Dryout

Dryout is generally observed at intermediate to high qualities in the annular flow regime and as the name implies occurs due to drying out (Figure 2-4) of the thin annular film [16].

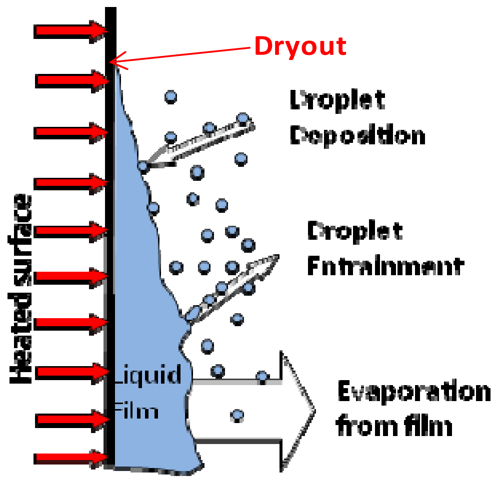

Figure 2-4: Phenomenology of dryout

The phenomenology of vapor clot type DNB is similar to that occurring in pool boiling. The behavior is hence very local in nature with little influence of upstream conditions. It has been observed by De Bortoli et al. [17] that the effect of upstream history increases upon increasing quality and is particularly dominant for annular flow dryout. In their experiments, they compared the burnout (DNB or dryout) heat flux for a tube uniformly heated with a heat flux $q_3^{"}$ against another tube which had uniform heating ($q_1^{"}$) for ~99% of the length and a heat flux spike ($q_2^{"} = 1.98q_1^{"}$) towards the end of length. It was seen (Figure 2-5) that for highly subcooled conditions burnout occurred when $q_3^{"} = q_2^{"}$. For very high qualities, critical condition corresponded to $q_3^{"} = q_1^{"}$.

Since in nuclear reactors, the heat flux varies along the length and as upstream heat flux also has a bearing on the boiling transition (DNB or dryout) phenomena no particular heat flux can be identified as being ‘critical’. Thus the concept of Critical power rather than Critical Heat Flux (CHF) is more meaningful for Boiling Water Reactors (BWRs) [18].

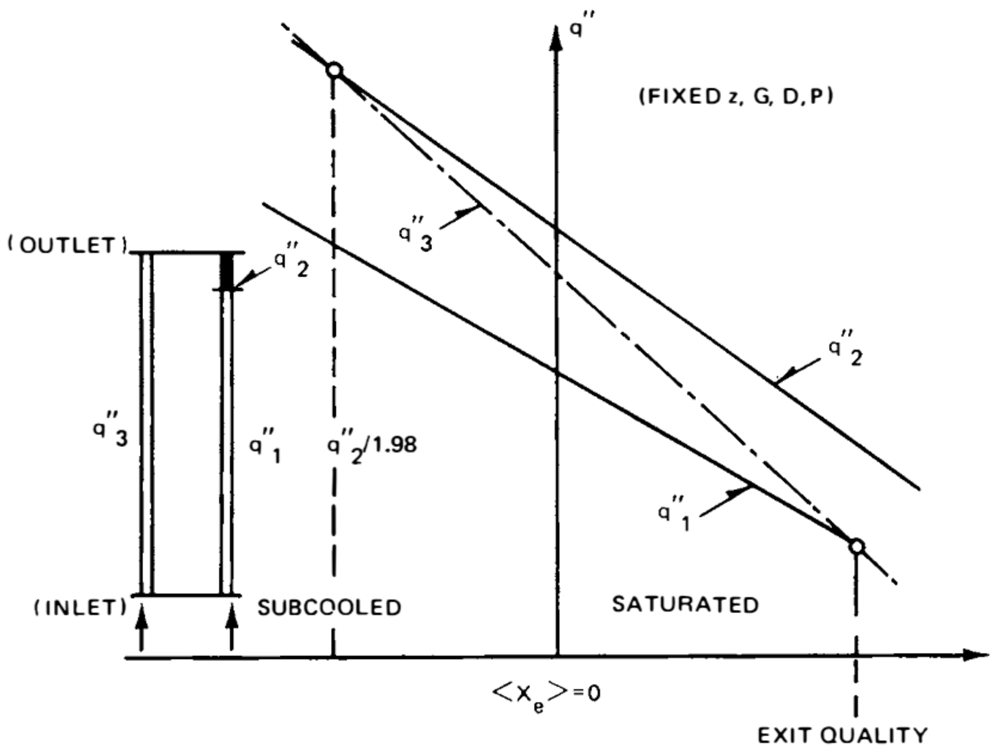

Figure 2-5: De Bortoli et al. [17] **hot patch experiment**

The present work concentrates on improving predictions of dryout. Thus very limited references will be made to DNB in the following sections and chapters.

The phenomenology of CHF also has a lot of bearing on the relevance of post-CHF heat transfer studies. It may be made out from Figure 2-2 that post-DNB temperatures for water based systems are generally in excess of melting temperatures of most engineering materials. Post-dryout, the temperatures are moderate (though a safety concern) in the sense that melting is often precluded. Talking of post-dryout (and not post-DNB) heat transfer studies is thus relevant as there is a good chance that the heater material (the fuel clad in nuclear reactors) has not melted away. Indeed, even in postulated Loss of Coolant

Accident (LOCA) in Pressurized Water Reactors, temperature excursion following the loss of coolant is due to the dryout mechanism as the shutdown system brings the reactor power to decay power levels. Nevertheless, there is a need to estimate the extent of post-dryout temperature rise and its duration as, under those cases, accelerated corrosion (rather than fuel melting) may lead to clad failure.

The cooling of the core through Emergency Core Cooling System (ECCS) may, depending upon the re-flood rate, follow the dryout events in reverse order i.e., a wet front moving (as against movement of a dry patch during dryout). In such cases, the rate processes involved in dryout are used in modeling precursory cooling by drops. However, there is some contention in literature regarding the importance of this cooling.

While sections 2.2 and 2.3 are devoted to the literature survey on dryout modeling, section 2.4 presents efforts to extend the model to post-dryout scenario and the gray areas.

2.2 Prediction of dryout: Failure of operating parameter correlations

Presently there exist numerous correlations for prediction of dryout in flow boiling. The major reason for such a multitude of correlations is that flow boiling CHF depends on many operating parameters as outlined in the previous section. Majority of these correlations are derived from data on uniformly heated channels. However as shown in previous section there is a significant effect of axial heat flux distribution. Thus the predictions of these correlations have to be corrected for heat flux profile. These corrections are again empirical. Empiricism piled upon empiricism leads to conditions where these correlations are applicable only in the range of experiments from which they are derived.

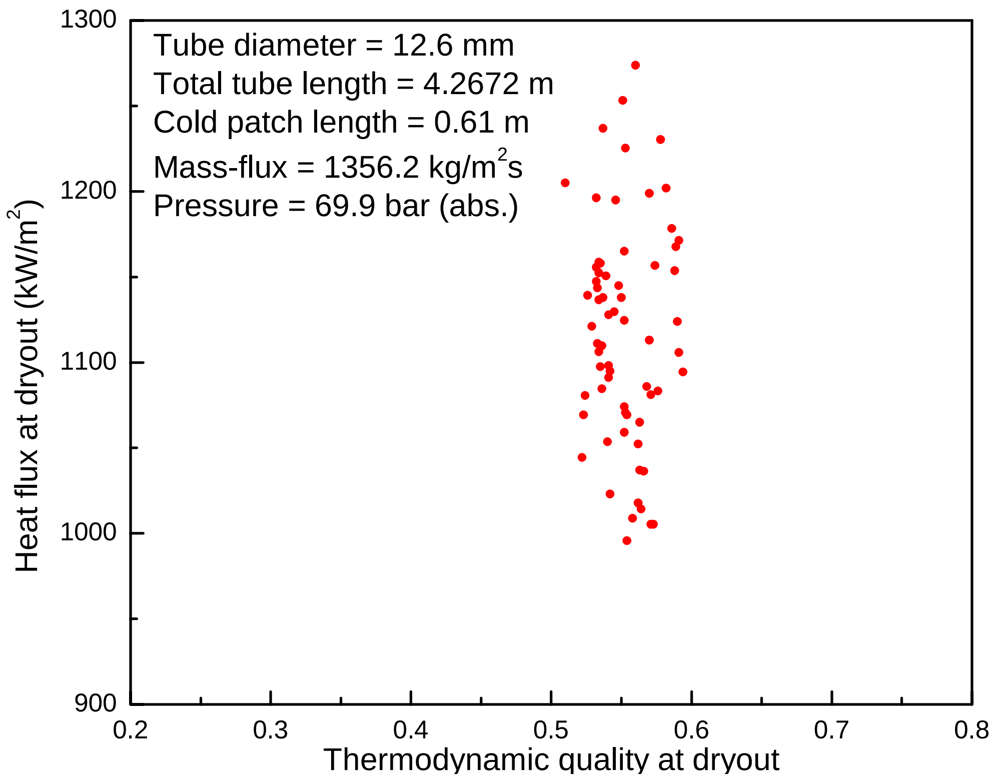

Figure 2-6: Data of Bennett et al. [19] **plotted on a flux-quality plot**

For tubular geometries, one of the widely accepted correlations is the CHF look-up table [2]. The table is derived from a database of over 33000 experimental data on tubes of various lengths and diameters. Strictly speaking, the look-up table is not a correlation as it does not provide any functional relation. But it does correlate and present in tabular form, the data from different sources as applicable to a hypothetical 8 mm inside diameter tube.

The range of applicability of the table is wide (Pressure = 0.1–21 MPa; Mass-flux = 0–8000 kg/m^{2}s; Quality = -0.5 – 1.0). The Look-up table philosophy is based on the *local conditions approach*, i.e., for a given tube diameter, pressure and mass-flux the dryout heat flux is dependent only on the local quality. This approach is also known as the flux-quality $\left(q'' - X_c\right)$ approach. However as discussed in the previous section (Figure 2-5), this assumption is incorrect especially for dryout. The cold patch experiments of Bennett et al.

[19] highlight this fallacy from another point of view. In the experiments, they observed that for the same pressure, mass-flux, inlet conditions and exit quality, the local heat flux at dryout changes upon changing the location of the cold patch (Figure 2-6). Hence the local heat flux is not a unique function of local quality at dryout.

The failure of the local conditions approach is also evident from the Shiralkar [20] experiments (Figure 2-7a) using Freon-114 with non-uniform heating. Multiple critical heat fluxes are obtained for the same local quality upon changing axial heat flux profile. Thus, it may be said with certainty that the correlations based on local conditions approach, even though used widely, are inadequate to describe dryout phenomena; in particular for cases where heat flux is non-uniform.

Due to this shortcoming, another family of correlations based on the so called *integral approach* was developed. These correlations aimed at incorporating by some means the upstream history effect. Tong F-factor and critical quality-boiling length (X_c–L_b) are the two widely used approaches. While the Tong-F factor approach is based on a modification of flux-quality approach, the (X_c–L_b) approach specifies that the critical quality is a function of the boiling length. Lahey and Moody [18] have shown that though these approaches have different functional form, they are equivalent. Tong F-factor based approach is mostly used to correct the results of DNB correlations as they are based on the flux-quality approach. The (X_c–L_b) correlations are mostly used for dryout predictions. Well known correlations of this type are the proprietary GEXL correlation [21] and CISE-4 correlation (eqn. (2.1)).

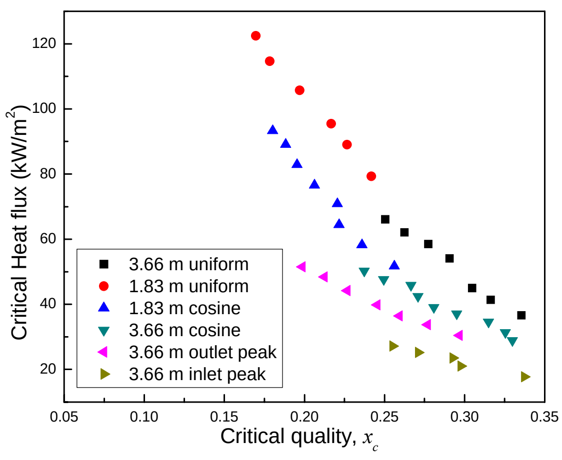

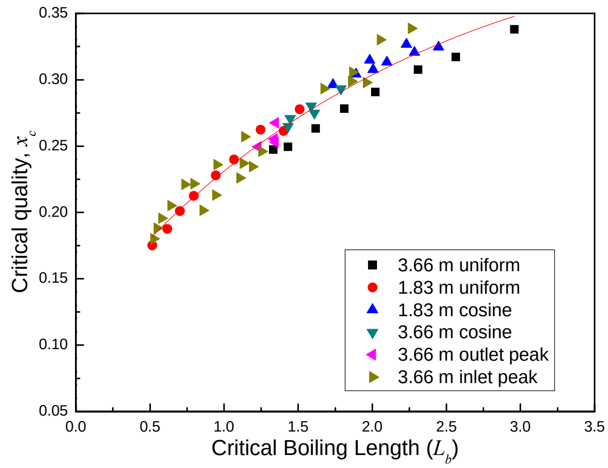

Figure 2-7: Dryout conditions with non-uniform heating plotted on (a) flux-quality plot and (b) critical quality-boiling length plot. Annulus test section (ID=14.3mm; OD=22.3mm), pressure = 8.66 bar (abs.), mass-flux = 732.4 kg/m^{2}s, Test fluid=Freon-114 (data from Shiralkar [20]**)**

$$x_c = \frac{aL_b}{L_b + b} \tag{2.1}$$

a and *b* are constants and functions of pressure and mass flux and hydraulic diameter.

The effectiveness of the integral approach is evident from Figure 2-7(b), where the same data as in Figure 2-7(a) is plotted on a critical quality-boiling length plot. It is seen that the data for different heat flux profiles fall around one best-fit line. It may thus be said that the integral approach provides a better correlation of dryout phenomena. It indicates that the critical quality should be a function of the boiling length. In other words, if the boiling length is not changed, the critical quality should remain the same. In their experiments, Bennett et al. [19] introduced a 0.61 m long cold patch in a 4.27 m long tube which was otherwise uniformly heated, and evaluated the dryout power. Now, keeping all other parameters the same, a change in the location of the cold patch should not alter the boiling length and quality corresponding to dryout conditions. However, it is seen that altering the position of the cold patch alters the dryout power and thus critical quality and boiling length. Hence a unique relation between critical quality and boiling length does not exist.

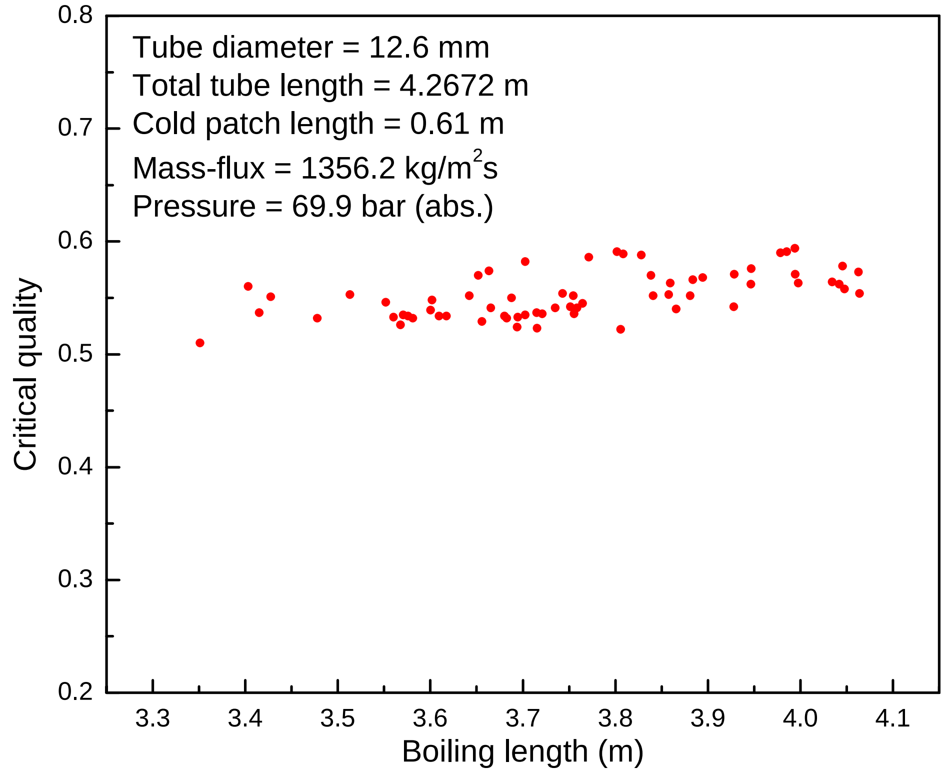

Figure 2-8: Data of Bennett et al. [19] **plotted on critical quality-boiling length plot**

This is also indicated if Bennett et al. [19] data are plotted on a (X_c–L_b) plot (Figure 2-8). A change in boiling length apparently has no influence on the critical quality.

At this point it is worthwhile to mention that the issues highlighted are specific to non-uniform heating. Since non-uniform heat flux profiles are the norm rather than exception in nuclear reactors, it may be concluded that the empirical correlations, though derived from extensive experimental data, are inadequate to describe and predict the dryout phenomena. Essentially, for a correlation derived out of purely uniform or some non-uniform heat flux data, the problem becomes that of extrapolation where the uncertainties are larger (as compared to interpolation). This effect of non-uniform heat flux is broadly given the name 'history effect'. In essence it signifies the fact that at any particular point, the distribution of liquid phase between film and droplets would depend on upstream conditions (or upstream history).

A physical picture of annular flow would explain the history effect and inherent flaw in the local conditions approach. The figure shows two heated tubes of same inside diameter and having the same total mass flux. It is seen that the equivalence of thermodynamic quality and pressure at any point does not signify the amount of liquid flowing in the film. Thus tube 1, having a greater film flow rate (at dashed location) has a greater margin over dryout than tube 2, even though the quality and pressure are the same.

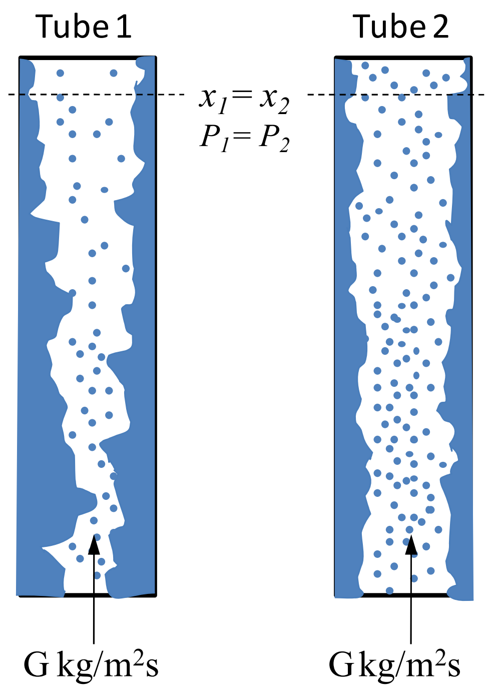

Figure 2-9:Physical reasoning for the failure of Local conditions approach – same gross local conditions but different film-drop split

The difference in the entrainment among the tubes arises due to the upstream history (different initial entrainment, different heat flux profile presence of spacer like obstructions etc.).

A corollary to this would be the probable occurrence of dryout at different qualities but same boiling length leading to in principle failure of the critical quality – boiling length approach. Further, as boiling length depends only on inlet conditions and total heat input regardless of axial flux profile, (X_c–L_b) approach is also, in principle unable to cater to the history effect.

It is reiterated that the inherent handicap with the correlation based approach is related to the large number of factors on which dryout depends. These factors are basically dependent on the configuration of the flow – flow regime, local bubble generation, entrainment and deposition etc. Correlating dryout based on operating parameters is thus a very difficult exercise of trying to correlate the effect of all these local parameters with operating pressure, mass-flux, diameter, quality etc. Most of the correlations are hence applicable to a limited operating parameter band. In rod bundles, geometry is an additional parameter which apparently cannot be correlated. Dryout or Critical Power correlations are bundle specific and determined through expensive experimental program. Changes in bundle geometry (often done with the objective of improving thermal-hydraulic performance) would in general require re-experimentation. Further, it is not feasible to test all possible heat-flux shapes which might exist during reactor operation.

2.3 Prediction of dryout: The mechanistic solution

The mechanistic model for dryout aims to overcome the deficiencies of the correlation approach by understanding and modeling the basic processes which influence the evolution of the liquid film in annular flow. Notable references of such mechanistic film dryout models are Whalley et al. [22], Wurtz [23], Hewitt and Govan [4] and Okawa et al. [24] who have applied the model to tubular geometries. Others like Tomiyama et al. [25], Sugawara et al. [26], Naitoh et al. [27], Adamsson and LeCorre [28] and Talebi and Kazeminejad [29] have applied the approach to rod bundle situations.

The understanding of the importance of liquid film on dryout in annular flow is largely due to the work carried out by Hewitt and co-workers and is amply discussed in their book [30]. In a series of experiments [16,31] they have shown that the dryout actually occurs due to the breakdown of the liquid film in annular flow.

Dryout is preceded by the thinning of the liquid film and appearance of a small intermittent dry patch. On increasing power, this patch grows and new patches start appearing around it. These patches have a continuous existence however, their boundaries are oscillating. The liquid film, instead of covering the entire circumference, now flows in narrow streams between the dry patches. Thus some cooling continues even if the liquid film has broken down. It was experimentally [16] seen that physical burnout characterized by sharp temperature rise, occurs at a power slightly higher than that for film breakdown.

The most important observation (Figure 2-10) from the point of view of mechanistic modeling is that the curves for film flow rate extrapolate to zero at close to burnout power. Further, the depletion of the film is rather smooth. These experiments provided the basis for the conjecture that dryout corresponds to the complete disappearance of film flow rate from the heater surface. Mechanistic models thus aim to model this depletion of film flow rate. The major processes which influence the evolution of the film are best represented in the form of the ordinary differential equation (2.2).

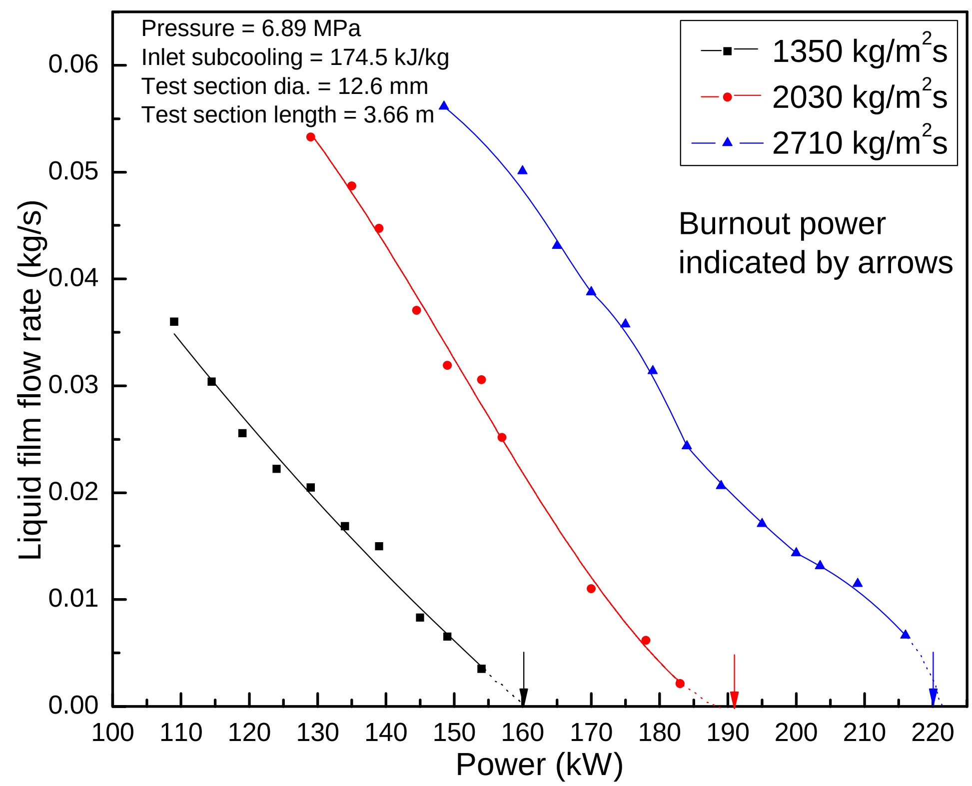

Figure 2-10: Effect of increasing power on film flow rate at end of heated section. (data of Bennett et al. [31]**)**

$$\frac{dG_{lf}}{dz} = \frac{4}{d_{eq}}\left(D - E - B\right) \tag{2.2}$$

In general, the gas core in annular flow contains entrained droplets. The motion of these droplets is governed by velocity field in the gas core. Due to the wavy interface and high turbulence in the gas core, droplets deposit from the core to the film. Deposition, represented by deposition flux, D, adds to the total film flow rate. The shear due to the gas core also causes entrainment of droplets from the wavy film. This process is quantified as the entrainment flux, E. Entrainment represents a decrement in the film flow rate. The vaporization flux, B is a function of the wall heat flux and can be determined from heat balance as the film is saturated. These processes are conventionally called rate processes. The models (or correlations) of entrainment and deposition rates are the heart of mechanistic film dryout model and are primarily what distinguish one model from another. Herein lays the inherent advantage of mechanistic modeling. Since these models bring down the level of empiricism from correlating operating parameters (like power, pressure, mass-flux and quality) to correlating/modeling more basic quantities (entrainment and deposition), the use of a mechanistic model verified in tubes may be more readily justified for use in bundles. Also, a mechanistic model that has been verified against experimental data in bundles can be used for further predictions in case of changes in bundle geometry/power profile under similar operating conditions. Indeed, the ability of phenomenological models inherently to predict the effect of non-uniform power profiles [32] is one of its greatest advantages.

The available models and correlations for entrainment and deposition rate processes are discussed in §2.3.1 and §2.3.2. It is not attempted in these sections to enumerate all available correlations and models but a flavor of the various types and underlying principles is provided.

One concept particularly important from the point of view of understanding and modeling the rate processes is that of equilibrium annular flow. When adiabatic annular flow occurs in long channels, beyond a certain length, there is no appreciable change in the entrained fraction (though some change would essentially occur due to pressure drop along the length). Such conditions are known as equilibrium annular flow and represent the dynamic equilibrium between deposition and entrainment rates. If the entrained fraction is less than the equilibrium value, then net mass transfer will occur from the film to droplet field through entrainment and vice-versa.

2.3.1 Deposition rate

The process of droplet deposition in annular two-phase flows has often been likened to particle laden pipe flows [30] for obvious reasons. There are some differences though. Firstly the droplet laden core in annular flow is bounded by a dynamic wavy film instead of a smooth pipe. Secondly, the droplets deform, disintegrate and coalesce unlike particles. Further, most of the studies with particles consider a uniform particle size; drops in annular flow have a variation of sizes (and shapes). In spite of these differences, valuable insights about the droplet deposition process can be obtained from particle deposition studies.

Particle deposition is seen to be strongly influenced by its size. One of the parameters which represents particle size is the particle relaxation time, τ_{p+}.

$$\tau_{p+} = \frac{\rho_p d_p^2 u_*^2}{18\mu_g^2} \tag{2.3}$$

Young and Leeming [33] have categorized the particle deposition process into three different regimes – diffusional deposition, diffusion impaction and inertia moderated, based on τ_{p+}. They have reasoned that the particle movement towards the wall is primarily driven by the gradient of turbulent kinetic energy which manifests as a force. They refer to this as the turbophoretic force. In pipe flows, the turbulent kinetic energy is zero at the walls and increases to a maximum approximately at y^+~50. It then reduces much gradually attaining a somewhat lower value at the pipe centerline. Since the gradient of turbulent kinetic energy is much larger near the wall, deposition takes place. Of course particle motion does not completely follow gas phase turbulence and particle inertia and turbulence history shape the particle motion.

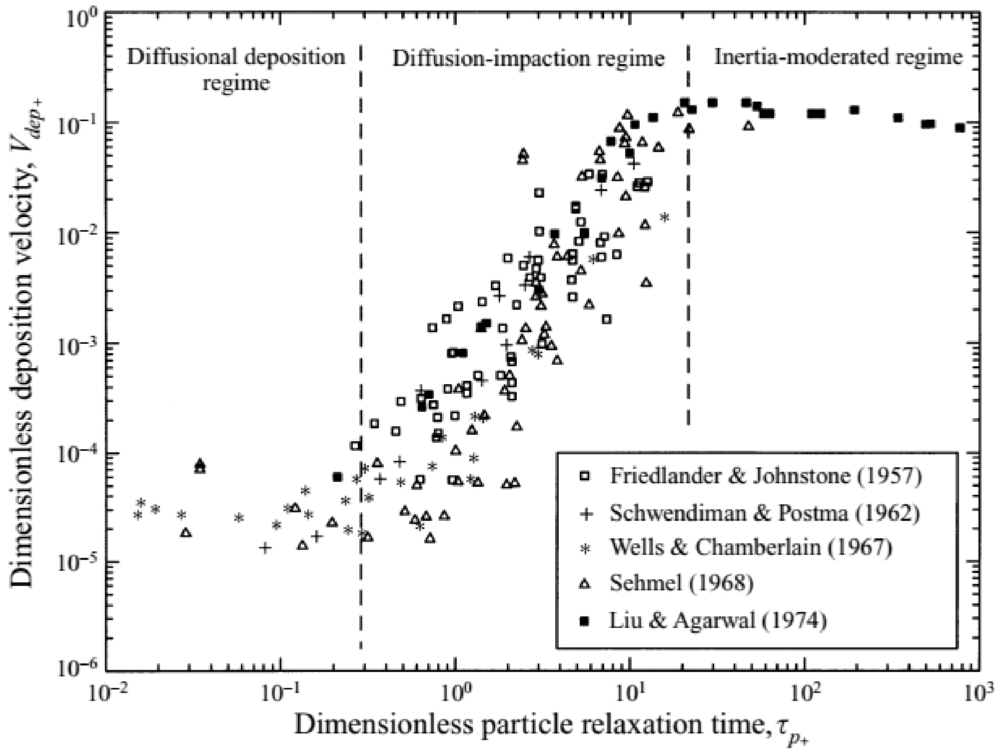

Figure 2-11: Particle deposition in fully turbulent pipe flow. Compilation of various data available in literature (from Young and Leeming [33]**)**

The non-dimensional deposition flux, V_{dep+}, defined in eqn. (2.4) is seen (Figure 2-11) to reduce with τ_{p+} in the diffusional deposition regime (τ_{p+} < 0.3), where particle diameters are very small and Brownian diffusion governs. In the diffusion-impaction regime (0.3 < τ_{p+} < 20), as the particle diameter increases, the particles become more responsive to turbulent eddies in the gas core. The deposition rate thus increases dramatically. In the inertia-moderated regime (τ_{p+} > 20), the particles become so large (and heavy) that after acquiring sufficient momentum from large eddies in the turbulent core reach the wall in near free flight. As the particle sizes increase, they respond more sluggishly to turbulence and thus the deposition flux reduces monotonically in this regime.

$$V_{dep+} = \frac{D}{Cu_*} \tag{2.4}$$

Caraghiaur and Anglart [34] have mentioned that the droplet sizes in annular flow cause them to fall in the inertia-moderated regime. Thus, in a strict sense, gradient diffusion hypothesis should not apply to droplet deposition process. Further, it is experimentally observed that 90% of the droplet mass flux is carried by only 10% of droplets [35] indicating that the majority of deposition mass flux is contributed through large drops. However, a fit of the inertia moderated regime in Figure 2-11 gives the following relation.

$$D = \left\{ u_* \left(\frac{K1}{\tau_{P+}} \right)^{K2} \right\} C \tag{2.5}$$

Here $K1$ and $K2$ are constants with best fit values of 6.792 x 10^{-5} and 0.14621 respectively. This may be interpreted as a form of the widely used deposition rate equation which is based on the diffusion mass-transfer hypothesis:

$$D = kC \tag{2.6}$$

This equation draws from the experimental observation [36] that in equilibrium annular flows, droplet concentration is nearly constant along the tube diameter and falls sharply near the film-gas interface. Assuming a zero concentration at interface and concentration C in the core gives eqn. (2.6), with k, the mass transfer coefficient known as the deposition coefficient. It can be seen that k has the units of velocity. Physically it represents a radial velocity which drives the particle to the wall. Of course, since the mechanism is diffusion, the velocity in question also has to be bi-directional. The friction velocity u_* is the most appropriate representation of such a radial fluctuating component of velocity in pipe flows. The coefficient of droplet concentration, C in eqn. (2.5) (the term in curly brackets) is analogous to k and the influence of u_* is evident. The term appearing apart from u_* is related to particle inertia and indicative that particle motion does not exactly follow the motion of the gas field.

As mentioned earlier, there is a range of droplet sizes in annular flow. The idea of representation of *k* in terms of a representative drop inertia (as in eqn. (2.5)) is thus not very practical. The deposition rate is derived experimentally through either double extraction method [37,38] or tracer technique [39,40].

The double extraction method, as the name suggests incorporates two porous extraction devices. One placed downstream of the other. The film is first completely extracted at the upstream device. Whatever is deposited beyond this point is then extracted at the downstream porous device. The devices are spaced such that the film (after extraction at first point) does not grow thick enough to allow entrainment from its surface.

The tracer technique involves continuously injecting a known concentration of tracer into the annular film and measuring the concentration of tracer at different distances downstream from the injection location. The deposition (and entrainment) rates can be derived from a balance of the mass and concentration.

Apart from these techniques, the concept of deposition controlled dryout (slow dryout where prior to dryout there is some length where the film becomes thin enough for entrainment to cease) is also used to evaluate deposition rate in diabatic flows [30]. In such cases, the deposition rate is equal to the vaporization rate and can thus be obtained from a heat balance.

The deposition rate, *k* is correlated from such measurements of deposition rate. One of the earliest such correlations (eqn. (2.7)) is due to Paleev and Filipovich [41] who conducted experiments in a rectangular channel. They had observed the deposition coefficient to reduce with concentration. They had non-dimensionalized the deposition coefficient by considering its ratio with the gas core velocity. This results in the computed k to depend upon gas flow rate.

$$\frac{k}{j_g} = 0.022\,\mathrm{Re}_g^{-0.25}\left(\frac{C}{\rho_g}\right)^{-0.26} \tag{2.7}$$

Due to the diffusion like behavior of deposition, the deposition coefficient has also been correlated as Sherwood number [30] analogous to Nusselt number in heat transfer in a turbulent pipe flow.

$$\frac{kd_{eq}}{\Gamma} = 0.023\,\mathrm{Re}_g^{0.8}\,Sc^{1/3} \tag{2.8}$$

Here Γ is the mass diffusivity. Upon expanding the gas phase Reynolds number and Schmidt number and rearranging, we obtain equation (2.9) where the deposition constant is non-dimensionalised by taking its ratio with gas phase velocity

$$\frac{k}{u_g} = 0.023\,\mathrm{Re}_g^{-0.2}\,Sc^{-2/3} \tag{2.9}$$

The drop deposition process is however a turbulent (not molecular) process and the turbulent mass diffusivity of droplets, Γ is not readily available. The Schmidt number is thus often taken equal to the Prandtl number [42]. In this correlation, the dependence on droplet concentration is not accounted for. But allowance for it can be made as has been done by Sugawara [42]. His correlation is applicable for pressures ranging from atmospheric to 7 MPa and $0.04 \le \left(C/\rho_g\right) \le 10$.

$$\frac{k}{u_g} = 9 \times 10^{-3}\left(\frac{C}{\rho_g}\right)^{-0.5}\mathrm{Re}_g^{-0.2}\,Sc^{-2/3} \tag{2.10}$$

These correlations however lack in non inclusion of the surface tension term. The influence of surface tension on deposition coefficient was seen from the work of Whalley et al. [22]. Based on the dominating influence of surface tension, Katto [43] correlated the deposition coefficient as a function of surface tension alone. His correlation (eqn.(2.11)), though dimensional is valid over a wide range of pressures (0.2-18 MPa).

$$k = \begin{cases} 0.405\sigma^{0.915} & \sigma \le 0.0383 \text{ N/m} \\ 9.48 \text{ x } 10^{4}\sigma^{4.70} & \sigma > 0.0383 \text{ N/m} \end{cases} \qquad (2.11)$$

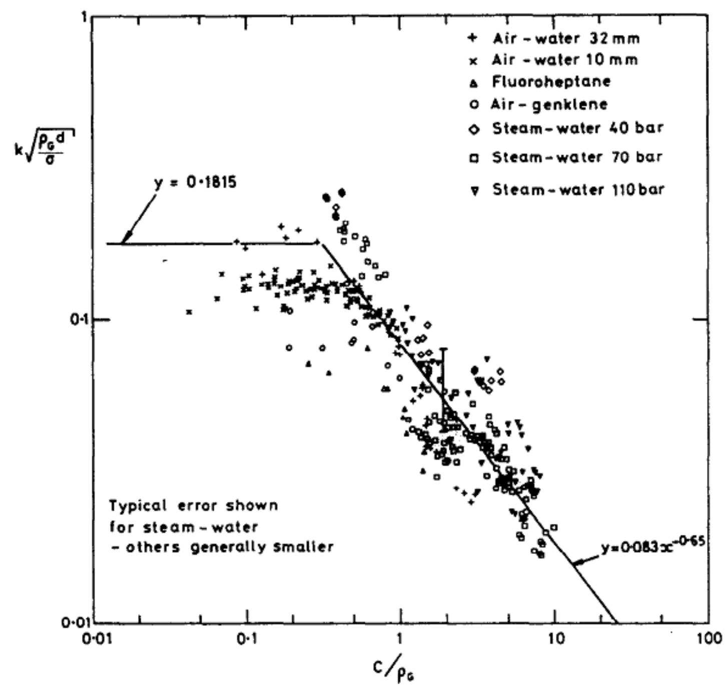

Figure 2-12:Hewitt and Govan correlation for deposition coefficient (from Hewitt and Govan [4]**)**

Another correlation, incorporating the effect of surface tension is that due to Hewitt and Govan [4]. This correlation (eqn.(2.12)) which is a best fit for a wide range of data for different fluids (Figure 2-12) is non-dimensional and includes most of the parameters except gas phase velocity.

$$k\sqrt{\frac{\rho_g d_{eq}}{\sigma}} = 0.18 \qquad ;\left(\frac{C}{\rho_g}\right) \leq 0.3$$
$$= 0.083\left(\frac{C}{\rho_g}\right)^{-0.65} \qquad ;\left(\frac{C}{\rho_g}\right) > 0.3 \tag{2.12}$$

Here the deposition coefficient is made non-dimensional upon dividing it by the term $\sqrt{\sigma/\rho_g d_{eq}}$. Eqn. (2.12) can be re-written as:

$$\frac{k}{j_g}\sqrt{We_k} = 0.18 \qquad ;\left(\frac{C}{\rho_g}\right) \leq 0.3$$
$$= 0.083\left(\frac{C}{\rho_g}\right)^{-0.65} \qquad ;\left(\frac{C}{\rho_g}\right) > 0.3 \tag{2.13}$$

Where, the Weber number We_k is given by,

$$We_k = \frac{\rho_g j_g^2 d_{eq}}{\sigma} \tag{2.14}$$

Eqn. (2.13) explains the significance of using term $\sqrt{\sigma/\rho_g d_{eq}}$ in eqn (2.12). Since the Weber number is indicative of the droplet size in annular flow, the term actually attempts to incorporate the droplet size and is thus possibly functionally more suitable than using simply the gas velocity (or superficial gas velocity). More recent work by Okawa and Kataoka [44] also prescribe using the same term. Okawa et al. correlation [24], derived from the same data as that of Hewitt and Govan [4] is given by:

$$k\sqrt{\frac{\rho_g d_{eq}}{\sigma}} = 0.0632\left(\frac{C}{\rho_g}\right)^{-0.5} \tag{2.15}$$

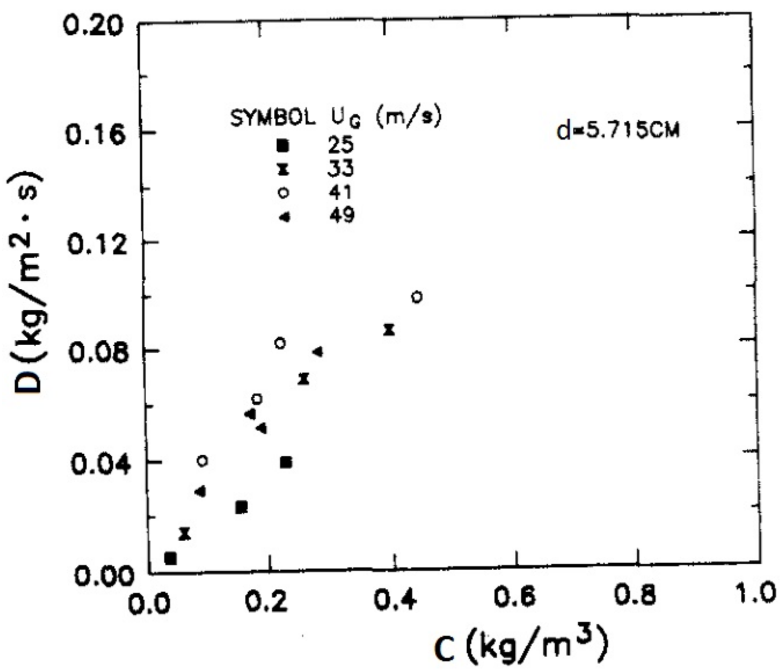

Figure 2-13: Deposition rate in a 5.715 cm tube; the effect of gas velocity (from Schadel et al. [40])

The dependence on gas superficial velocity in eqn. (2.13) is however artificial. That the gas velocity does not have any significant effect on the deposition rate has also been observed by Schadel et al.[40] in their experiments (Figure 2-13) using the tracer technique.

It is definitely intriguing that gas velocity which is the driving force for deposition should not have an effect. The studies on particle laden flows in pipes [34] also point towards the fact that the deposition rate should directly depend on the friction velocity which is a function of gas velocity.

Apart from the empirical deposition rate correlations discussed above, attempts have been made to simulate the deposition process through first principles [34,45]. These works use a Lagrangian approach to simulate the droplet motion in a smooth pipe. Actually the droplet laden core sees a dynamic wavy interface. Thus such simulations, though a better approach than correlations, are not truly representative of the deposition process in annular flow.

2.3.2 Entrainment rate

The correlations of entrainment rate available in literature are derived from experimental data on entrained fraction. When entrainment rate is evaluated from entrained fraction data in developing annular flows, a deposition rate correlation is also required (eqn. (2.16)).

$$E = \frac{d_{eq}}{4}\left(\frac{dG_d}{dz}\right) + D \tag{2.16}$$

Such correlations even while correlating the equilibrium entrainment are inherently dependent on the correlation for deposition rate [46]. These type of correlations, though able to capture the non-equilibrium effects are dependent on the correlation for deposition coefficient. Using them with any correlation other than the one from which they are derived would invalidate the analysis and not lead to experimentally observed equilibrium entrainment values. One such non-equilibrium correlation given by Kataoka et al. [46] is given in eqn. (2.17).

$$E = \left(\begin{array}{c} 1.2 \text{ x } 10^3 \, \mathrm{Re}_l^{-0.5} \, \mathrm{Re}_{lf\infty}^{-0.25} \, We_m^{-1.5} \left(\mathrm{Re}_{lf} - \mathrm{Re}_{lf\infty}\right) * \Phi\left(\mathrm{Re}_{lf} - \mathrm{Re}_{lf\infty}\right) \\ + 6.6 \text{x } 10^{-7} \, \mathrm{Re}_l^{0.74} \, \mathrm{Re}_{lf\infty}^{0.185} \, We_m^{0.925} \left(\frac{\mu_g}{\mu_l}\right)^{0.26} \end{array} \right) \frac{\mu_l}{d_{eq}} \tag{2.17}$$

The alternate method of deriving entrainment rate is based on the concept of equilibrium annular flow. Here there are two techniques; one is similar to that already described i.e., the entrainment rate is assumed to be equal to the equilibrium value.

$$E = kC_{eq} \tag{2.18}$$

C_{eq} is the droplet concentration corresponding to equilibrium annular flow. This relation (eqn.(2.18)) forces simulations of annular flow to achieve experimental equilibrium concentration. This is indeed a very important criterion which needs to be satisfied. However, the length required for achievement of equilibrium annular flow does not figure in the relation and different correlations of this type may give different lengths to equilibrium. Further, the entrainment rate is still dependent on the correlation for deposition rate. Correlations of the type eqn. (2.18) require a relation for equilibrium concentration. One such relation is the fit given by Tomiyama et al. [25]:

$$C_{eq} = \begin{cases} 186.349(\tau_i\delta/\sigma)^2 + 0.185919(\tau_i\delta/\sigma) - 0.0171915 & (\tau_i\delta/\sigma) \le 0.047 \\ 92.6903(\tau_i\delta/\sigma)^2 + 10.5584(\tau_i\delta/\sigma) - 0.309705 & 0.047 < (\tau_i\delta/\sigma) \le 0.1 \\ 51.6429(\tau_i\delta/\sigma)^2 + 27.1302(\tau_i\delta/\sigma) - 1.65863 & 0.1 < (\tau_i\delta/\sigma) \le 0.3 \\ 145.8329(\tau_i\delta/\sigma)^{2.13707} & (\tau_i\delta/\sigma) > 0.3 \end{cases} \tag{2.19}$$

The usage of the parameter $(\tau_i\delta/\sigma)$ was first proposed by Hutchinson and Whalley [47]. The dependence of C_{eq} on $(\tau_i\delta/\sigma)$ is shown in Figure 2-14. Eqn. (2.19) is in fact the best fit to the curve obtained by them. The choice of $(\tau_i\delta/\sigma)$ as a parameter is very appropriate as the interfacial shear stress τ_i signifies the tendency to disrupt the film, whilst the quantity σ/δ (surface tension over film thickness) is a measure of the resistance of the film against disruption.

Ishii and Mishima [48] observing higher scatter in the region with low $(\tau_i\delta/\sigma)$ suggested that a single non-dimensional parameter is insufficient to properly describe equilibrium entrainment. They have advocated the use of a modified Weber number and liquid Reynolds number. Their correlation is given by eqn. (2.20). Variations and improvements of this form are available in the more recent correlations [46,49,50].

$$C_{eq} = \rho_g \tanh(7.25\text{x}10^{-7} We_m^{1.25}\,\mathrm{Re}_l^{0.25}) \, G_l \big/ G_g \text{, where,}$$
$$We_m = \frac{\rho_g j_g^2 d_{eq}}{\sigma}\left(\frac{\rho_l - \rho_g}{\rho_g}\right)^{1/3} \qquad \mathrm{Re}_l = \frac{\rho_l j_l d_{eq}}{\mu_l} \tag{2.20}$$

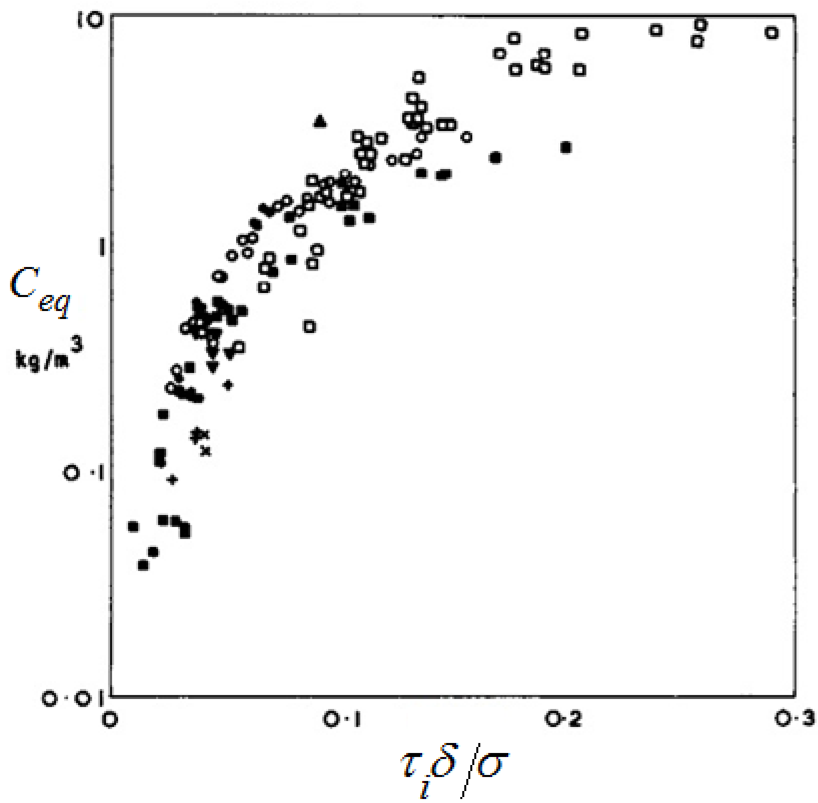

Figure 2-14: Experimentally observed equilibrium concentration, apparently dependent on the dimensionless group $(\tau_i \delta / \sigma)$ (from Hutchinson and Whalley [47]**)**

Nevertheless, the non-dimensional group $(\tau_i \delta / \sigma)$ is still used widely. Relatively recently Okawa et al. [51] have also used essentially the same parameter to correlate entrainment rate. Their correlation is broadly represented as:

$$E = k_e \rho_l \pi_e^n \tag{2.21}$$

Where,

$$\pi_e = \frac{f_i \rho_g j_g^2}{\sigma / \delta} \tag{2.22}$$

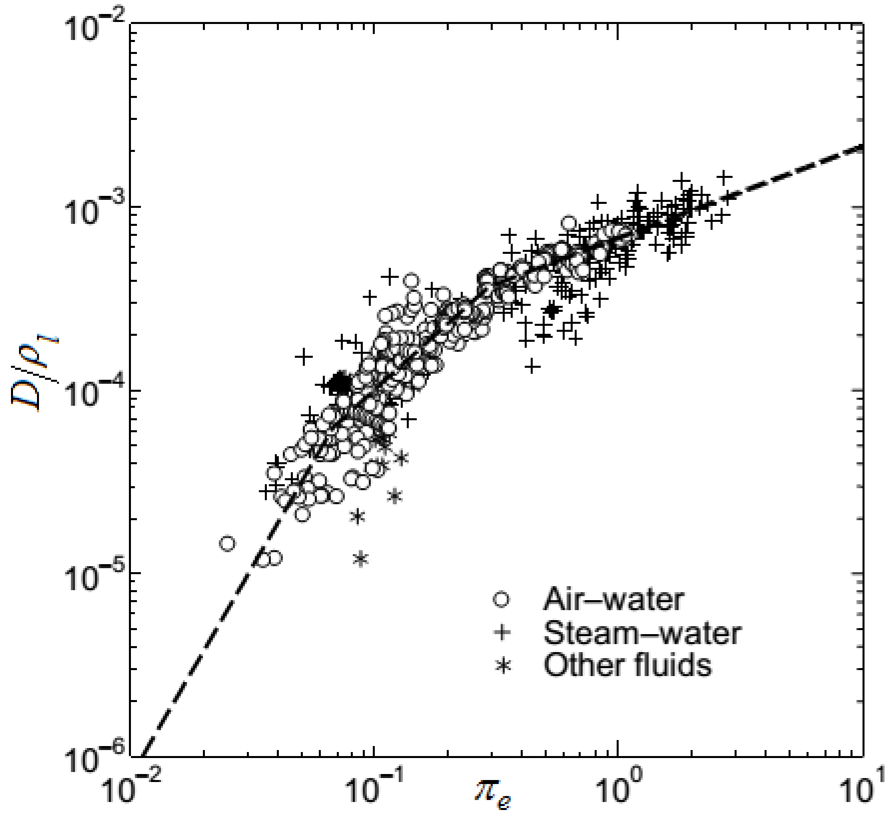

Figure 2-15: Okawa entrainment correlation and experimental data (from Okawa et al. [51]**)**

This form has also been advocated by other researchers [32]. The numerator of parameter π_e is the interfacial shear stress computed using the gas phase inertia. k_e and n are constants derived from experimental fit obtained upon equating entrainment and deposition, stating explicitly,

$$\frac{E}{\rho_l} = k_e \pi_e^n = \frac{D}{\rho_l} \tag{2.23}$$

Thus, the volumetric entrainment rate (which is equal to the deposition rate at equilibrium) can be plotted (Figure 2-15) as a function of π_e and the constants k_e and n evaluated.

This form of entrainment rate correlation is not dependent on the deposition rate correlation and is also able to predict the equilibrium concentration properly. This correlation has been independently found to yield good match with experimental data [52] on entrainment rate.

A particularly encouraging characteristic of entrainment-deposition correlations which is observed from Figure 2-15 and Figure 2-12 is the ability to correlate, through proper choice of correlating parameters, irrespective of the fluid used.

One particular phenomenon which is not incorporated into equation (2.21) is the cessation of entrainment below a threshold value of film flow rate. In the context of Figure 2-14 and Figure 2-15 this region would be classified as the *thin film region* and would fall towards the left in abscissa. Though the predicted equilibrium entrainment (or entrainment rate) is 2-3 orders of magnitude smaller, cessation of entrainment is not predicted. In literature the criterion being referred to in this paragraph is known as the *criterion for onset of entrainment*. Hewitt and Govan [4] have included this criterion in their entrainment rate correlation (eqn. (2.24)).

$$
\begin{aligned}
E &= 5.75 \text{ x } 10^{-5} G_g \left[\left(G_{lf} - G_{lfc} \right)^2 \frac{\rho_l d_{eq}}{\rho_g^2 \sigma} \right]^{0.316} \qquad ; G_{lf} > G_{lfc} \\
&= 0 \qquad ; G_{lf} \le G_{lfc}
\end{aligned}
\tag{2.24}
$$

This correlation again is independent of the deposition rate correlation. The critical liquid film flow rate, G_{lfc} below which entrainment is not possible is obtained as:

$$
\frac{G_{lfc} d_{eq}}{\mu_l} = \text{Re}_{lfc} = \exp\left(5.8504 + 0.4249 \frac{\mu_g}{\mu_l} \sqrt{\frac{\rho_l}{\rho_g}} \right) \tag{2.25}
$$

The choice of non-dimensional correlating parameter in this correlation is not as obvious as it was with the previous entrainment correlations discussed. However, Adamsson [53] through a very clever rearrangement of terms has shown that the bracketed term in eqn.

(2.24) can be reduced to a combination of Weber number (based on film flow rate) and density ratio.

In a more recent work, Okawa and Kataoka [44] have also chosen to improve on the earlier model [51] and use a modified non dimensional parameter π_{e1} which incorporates the concept of onset of entrainment.

$$\pi_{e1} = \frac{f_i \rho_g \left(j_g^2 - j_{gc}^2 \right)}{\sigma / \delta} \tag{2.26}$$

Here j_{gc} is the critical superficial gas velocity required for onset of entrainment obtained from Ishii and Grolmes [54] correlation. There is an apparent distinction in the parameter influencing the onset of entrainment between equations (2.24) and (2.26). While the former uses film flow as the governing parameter, the latter uses gas flow. Instinctively it seems that both should have an influence. The physical reasoning for criteria for onset of entrainment have been discussed in detail by Ishii and Grolmes [54]. An understanding of these criteria is intimately linked to the mechanisms for entrainment.

In boiling flows, initial entrainment of liquid into the vapor core occurs during the transition from slug flow to annular flow. As the vapor velocity increases due to increase in total vapor content (due to boiling), the vapor disrupts the liquid slugs to form a continuous vapor core. The disruption of the slugs results in the entrainment of the liquid contained in the slugs (type 5 in Figure 2-16). Hence the initial entrained fraction is quite high in boiling flows. Once the annular flow regime is attained, entrainment is seen to be caused by the following mechanisms [54]:

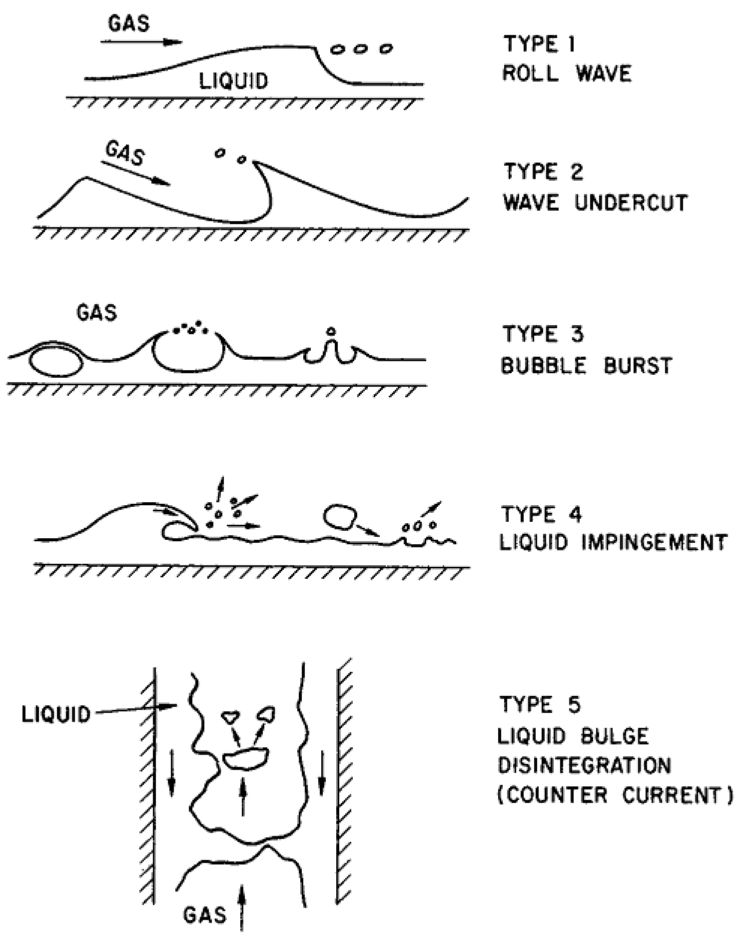

Figure 2-16: Various mechanisms of entrainment (from Ishii and Grolmes [54]**)**

- Shear induced entrainment: Break up of disturbance waves in annular film due to rolling (occurs at high film Reynolds number) or under-cutting (occurs at low film Reynolds number). These are shown as types 1 and 2 in Figure 2-16.
- Bubble induced entrainment: Release of vapor bubbles from the film cause entrainment as they leave the surface of the film. This is shown as type 3 in Figure 2-16.
- Entrainment due to deposition: Some entrainment takes place from the surface when a liquid droplet impacts on the liquid film (type 4 in Figure 2-16). This effect is however difficult to quantify and mostly taken care of in deposition correlations.

Type 3 and 4 fall in a group which may loosely be termed entrainment due to secondary phenomena and from the point of view of the onset of entrainment, type 1 and type 2 mechanisms only are important. Ishii and Grolmes through an analysis of data available in literature demarcate the film flow into three regimes with different mechanisms governing the onset of entrainment (Figure 2-17).

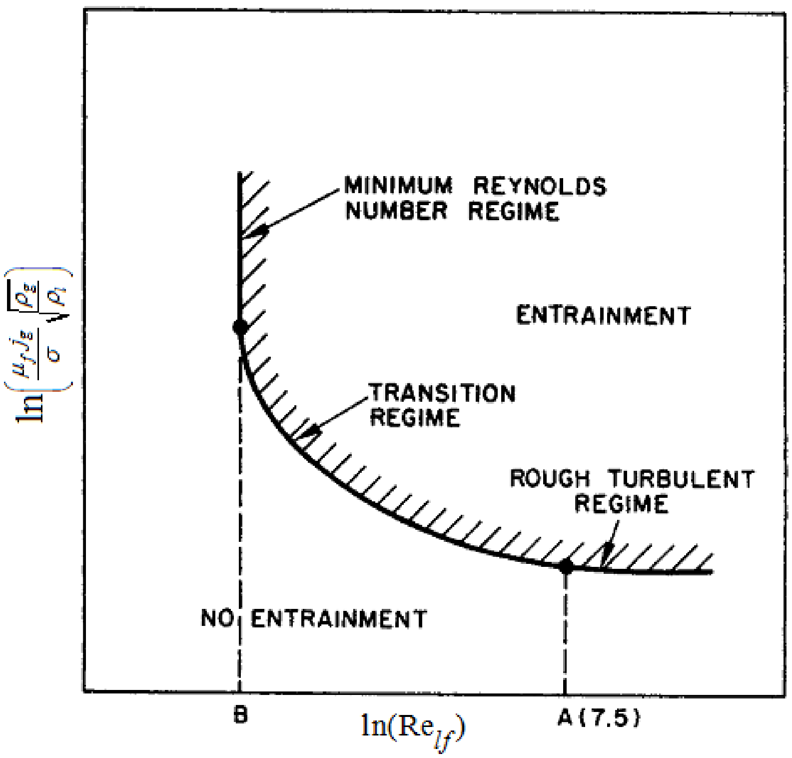

Figure 2-17: Typical boundary for onset of entrainment in annular flow. (from Ishii and Grolmes [54]**)**

In the transition regime (between A and B in Figure 2-17) the critical gas velocity for entrainment becomes a function of film flow Reynolds number. In this regime, at higher film Reynolds number (> ~160) the mechanism of entrainment is through shearing off of roll wave crests. A semi mechanistic approach has led to development of the following criteria in this regime. These criteria (eqn.(2.27)) are a best fit for data in the range $160 < \mathrm{Re}_{lf} < 1635$.

$$\frac{\mu_l j_g}{\sigma}\sqrt{\frac{\rho_g}{\rho_l}} \geq 11.78 N_\mu^{0.8}\,\mathrm{Re}_{lf}^{-1/3}; \quad \text{for} \quad N_\mu \leq 1/15$$
$$\geq 1.35\,\mathrm{Re}_{lf}^{-1/3}; \qquad \text{for} \quad N_\mu > 1/15 \tag{2.27}$$

N_μ is the viscosity number and dependent only on fluid properties. In the rough turbulent regime (around and beyond A), i.e., where the film Reynolds number exceeds 1500 to 1750, the roll wave shearing mechanism is still dominant. However, the thicker film makes interfacial friction (and thus shear) less dependent of film Reynolds number. The critical gas velocity for entrainment is correlated in this regime as:

$$\frac{\mu_l j_g}{\sigma}\sqrt{\frac{\rho_g}{\rho_l}} \geq N_\mu^{0.8}; \quad \text{for} \quad N_\mu \leq 1/15, \quad \mathrm{Re}_{lf} > 1635$$
$$\geq 0.1146; \text{for} \quad N_\mu > 1/15, \quad \mathrm{Re}_{lf} > 1635 \tag{2.28}$$

Towards the lower film Reynolds number (less than 160 for up flows) the entrainment mechanism is seen to shift to wave undercut leading to a much sharper increase in the critical gas velocity. In this regime the best fit gives:

$$\frac{\mu_l j_g}{\sigma}\sqrt{\frac{\rho_g}{\rho_l}} \geq 1.5\,\mathrm{Re}_{lf}^{-1/2}; \quad \mathrm{Re}_{lf} < 160 \tag{2.29}$$

Ishii and Grolmes have further argued that there exists a minimum film Reynolds number below which no entrainment is theoretically possible. This value would correspond to the film thickness falling within the viscous sublayer of the gas flow. Under such conditions, disturbance waves would be suppressed. Their [54] expression for this minimum film Reynolds number is:

$$\mathrm{Re}_{lfc} = \left(\frac{y^+}{0.347}\right)^{3/2}\left(\frac{\rho_l}{\rho_g}\right)^{3/4}\left(\frac{\mu_l}{\mu_g}\right)^{3/2} \tag{2.30}$$

With reasonable values of y^+, the critical film Reynolds number is seen to be much smaller than that observed experimentally [55] by other workers. Nevertheless, eqn. (2.30) does provide a lower limit for the critical film Reynolds number. Further, it may be concluded that the existence of disturbance waves is necessary but not sufficient for onset of entrainment. It is shown (later) in the present work that the onset of entrainment from waves in annular flow is not sufficient to guarantee sustained entrainment in the core.

The understanding of shear mechanism of entrainment has also led to development of some models for entrainment rate based on assumed wave shape. Such work has been done by Holowach et al. [56].

$$E = 0.0311 \mathrm{Re}_{lf} \left(\frac{\rho_l}{\rho_g} \right) N_\mu \frac{\forall \rho_l u_{gc} - u_l}{\lambda^3 \left(1 - \alpha_{lf}\right)^{0.5}} \tag{2.31}$$

Their correlation (eqn.(2.31)), though physically appealing requires values and approximations for quantities such as volume of liquid entrained from a single wave, $\forall$ and wavelength, λ (spacing between successive disturbance waves) which are not readily available. Moreover sinusoidal approximation for the wave which is chaotic and dynamic is questionable. Thus correlations of this kind are rarely used. More so when empirical correlations of the type described earlier are plenty. It must however be stated that mechanistic correlations such as eqn. (2.31) are a progressive way forward towards better modeling of annular flow dryout.

In the sections 2.3.1 and 2.3.2 an attempt has been made to give a general flavor of the deposition and entrainment rate correlations and their broad forms. There are of course numerous such correlations and it is not in the scope of this thesis to enlist and describe all of them. But the point which is intended to be underlined is that a designer or analyst, attempting to predict dryout mechanistically, has a choice of a large number of correlations and it is often difficult to ascertain which would be the best.

Also, the influence of the disturbance waves in the entrainment process is significant and has been widely reported in literature. However, that these waves may also have an influence on deposition rate is postulated in this work. Indeed better models of deposition and entrainment can be obtained only after thorough studies on disturbance waves. This is discussed in a later chapter where some important characteristics of disturbance waves are studied.

2.3.3 Evaluation of other closures

Though not explicitly stated above, the correlations for entrainment and deposition rates, depending on their exact functional form require certain other relationships; important among them are those for film thickness and interfacial friction factor (or interfacial shear stress).

A simple model for prediction of annular flow pressure drop was given by Wallis [57]. He assumed that annular flow pressure drop can be evaluated by considering the flow of the droplet entrained gas core to be equivalent to flow in a rough pipe, with the roughness being measured as a function of liquid film thickness. The effect of droplets is accounted for by assuming a homogenous gas core density, ρ_{vc} and superficial velocity, j_{vc}.

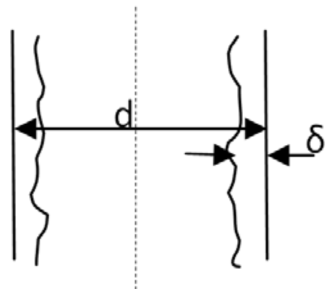

Figure 2-18: Geometric description of annular film

From Figure 2-18, the void fraction α and film thickness δ can be related as:

$$\left(1-\alpha\right)=\frac{4\delta}{d}\left(1-\frac{\delta}{d}\right) \tag{2.32}$$

The interface between the gas and liquid is usually wavy, and much of the interfacial shear stress is due to form drag on these waves. If we assume $u_g >> u_l$ then, we can treat the situation as a gas (or gas with entrained liquid) stream flowing through a rough pipe of diameter $\left(d-2\delta\right)$. Wallis showed that the interfacial friction factor in terms of gas core superficial velocity is:

$$f_{vci}=\frac{\tau_i}{\frac{1}{2}\rho_{vc}j_{vc}^2}=f_{vc}\left[1+90\left(1-\alpha\right)\right]\approx f_{vc}\left[1+360\frac{\delta}{d}\right] \tag{2.33}$$

Where the vapor core friction factor is approximated from Blasius relationship,

$$f_{vc}=0.079\left(\mathrm{Re}_{vc}\right)^{-0.25} \tag{2.34}$$

From these two equations (2.33) and (2.34), we may write for the pressure drop (or in other words the interfacial friction)

$$\left(\frac{dp}{dz}\right)=\frac{4\tau_i}{d}=\frac{4}{d}0.079\,\mathrm{Re}_{vc}^{-0.25}\left(1+360\frac{\delta}{d}\right)\left(\frac{1}{2}\rho_{vc}j_{vc}^2\right) \tag{2.35}$$

From equation (2.35) it is clear that the interfacial shear stress and film thickness are intimately linked and another equation is required for the evaluation of these quantities.

In annular flows, there exists a unique relation between the film flow rate, film thickness and total pressure drop. This is better explained by considering a force balance within a circumferential slice of the liquid film. The flow of vapor core over the wavy film interface causes a shear stress, τ_i to be imposed at the interface. This tends to push the film upwards. This upwards motion is resisted by the gravitational force and no slip condition at the wall. The no slip condition manifests itself as a radially varying shear stress in the film resisting film motion. This opposing shear, τ is equal to interfacial shear stress, τ_i at the interface and wall shear stress, τ_w at the wall. These stresses are indicated in Figure 2-19. From a force balance, the following equation can be written:

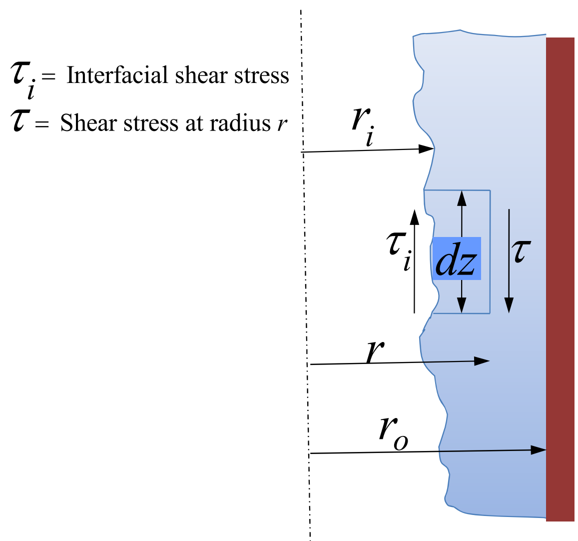

Figure 2-19: Force balance within the liquid film

$$\tau = \tau_i \left(\frac{r_i}{r} \right) + \frac{1}{2} \left(\rho_l g + \frac{dp}{dz} \right) \left(\frac{r_i^2 - r^2}{r} \right) \tag{2.36}$$

Now, considering $\tau = -\mu \dfrac{du}{dr}$, we obtain velocity distribution within the liquid film as,

$$u = f(r, \tau_i, \frac{dp}{dz}) \tag{2.37}$$

Equation (2.37) can be used to evaluate the total film flow rate, m_{lf}.

$$m_{lf} = \int_{r_i}^{r_o} 2\pi r u.dr \tag{2.38}$$

Upon integration, m_{lf} is obtained as a function of average film thickness ($\delta = r_o - r_i$), interfacial shear stress (τ_i) and total pressure drop (dp/dz).

$$m_{lf} = f(\delta, \tau_i, \frac{dp}{dz}) \tag{2.39}$$

The interfacial shear stress can be obtained independently from considerations of the pressure drop in vapor core (eqn.(2.33)). Thus, the film flow rate becomes a function of only film thickness and total pressure drop.

$$m_{lf} = f(\delta, \frac{dp}{dz}) \tag{2.40}$$

The relation expressed by equation (2.40) is the triangular relationship. Knowledge of any two quantities is required to get the third unknown quantity from the triangular relationship. In most of the cases, knowledge of two quantities is not available. Assumptions thus have to be made. Generally, assumption is made about the liquid film flow rate. Film thickness, δ can thus be calculated from triangular relationship once pressure gradient is obtained from gas core momentum equation. A simplification of the triangular relationship is described in what follows.

A qualitative description of annular two phase flow may be made by assuming the following [30]

1. Film thickness is very small in comparison to tube diameter.
2. Shear stress in the film is constant and equal to wall shear stress.
3. All the liquid flowing in the pipe flows in the film.

4. Gravitational and acceleration effects can be ignored in both phases.

A simple force balance on the liquid film then gives:

$$-\left(\frac{dp}{dz}\right) = \frac{4\tau_w}{d} = \frac{2\rho_l u_{lf}^2}{d}\left(\frac{\tau_w}{\frac{1}{2}\rho_l u_{lf}^2}\right) \tag{2.41}$$

The pressure gradient for the liquid film flowing alone in the tube is given as:

$$-\left(\frac{dp}{dz}\right)_l = \frac{2f_l\rho_l j_l^2}{d}\text{; where } f_l = \frac{\tau_w}{\frac{1}{2}\rho_l j_l^2} \tag{2.42}$$

Hence,

$$\phi_l^2 = \frac{(dp/dz)}{(dp/dz)_l} = \left(\frac{\tau_w / \frac{1}{2}\rho_l u_{lf}^2}{f_l}\right)\left(\frac{u_{lf}^2}{j_l^2}\right) \tag{2.43}$$

Since we have assumed all liquid to flow in the film, $u_{lf} = j_l/(1-\alpha)$, therefore,

$$\phi_l^2 = \frac{(dp/dz)}{(dp/dz)_l} = \left(\frac{\tau_w / \frac{1}{2}\rho_l u_{lf}^2}{f_l}\right)\frac{1}{(1-\alpha)^2} \tag{2.44}$$

$\tau_w / \frac{1}{2}\rho_l u_{lf}^2$ can be considered as a friction factor for the liquid film. It can be shown that the Reynolds number for the liquid film based on equivalent diameter concept is the same as that when the liquid phase alone is flowing in the pipe. Thus it may be argued that the friction factors are the same. Hence eqn. (2.44) can be written as:

$$\phi_l^2 = \frac{(dp/dz)}{(dp/dz)_l} = \frac{1}{(1-\alpha)^2} \tag{2.45}$$

Empirical correlations relating pressure drop and void fraction point towards similar relationship. Turner and Wallis [58] have suggested the following relation to take into account entrainment, thus allowing its application to annular flows with entrainment which is essential for dryout modeling as near to dryout, major portion of liquid flows as entrained droplets.

$$\phi_{lf}^2 = \frac{(dp/dz)}{(dp/dz)_{lf}} = \frac{1}{(1-\alpha)_{lf}^2} \tag{2.46}$$

In this modification, the single-phase pressure drop for the total liquid flow is replaced by single-phase pressure drop for that part of the liquid flow which is in the film. Using eqn. (2.32) and assuming $\delta/d << 1$, this equation can be also written as:

$$\left(\frac{dp}{dz}\right)_{lf} = \left(\frac{4\delta}{d}\right)^2 \left(\frac{dp}{dz}\right) \tag{2.47}$$

Equation (2.47) is a simplification of the triangular relationship. The film flow rate is assumed to be known from knowledge of entrainment and flow quality. $(dp/dz)_{lf}$ is calculated using film friction factor based on film Reynolds number ($\mathrm{Re}_{lf} = 4\delta\rho_l u_{lf}/\mu_l$). Generally usage of laminar friction factor is suggested [24,25]. The triangular relationship is also the basis for other correlations of film thickness like that by Okawa et al. [24]

$$\delta = \frac{1}{4}\sqrt{\frac{f_l \rho_l}{f_i \rho_g}} \frac{j_l}{j_g} d \tag{2.48}$$

2.3.4 Effect of heat flux on rate processes

The effect of surface heat flux on either deposition and/or entrainment rates has not been incorporated in any of the correlations mentioned above. However, whether or not it will have an effect is a question which has led to some contradictory answers. Before the experimental evidence from literature is discussed, the mechanism by which heat flux might affect the rate processes in annular flow are highlighted:

2.3.4.1 Possible mechanisms for effect on deposition rate

The radial velocities in the vapour core lead to the deposition of droplets. Increase in heat flux would lead to increase in the velocity of the vapour ejecting normal to the film surface. This causes an impediment to droplet movement towards the film. In particular, the fluctuating radial velocities at the vapour liquid interface are modified due to heat flux. The droplet size however plays a very important role. It is only the small droplets which are really affected by near interface turbulence. The larger ones are simply shot (inertial deposition) through to the film. Considering that most of the droplets existing in steam water annular flow have sizes which make them fall in the inertial deposition regime [34,35] it is these larger drops which would be the greatest contributors to deposition. Thus the effect of heat flux would be to reduce deposition, but most probably only slightly. Peng [59], through an order of magnitude analysis of the fluctuating velocities and using the Prandtl mixing length hypothesis obtained a relation for deposition coefficient (eqn. (2.49)) which bears resemblance with the Sugawara correlation (eqn. (2.10)).

$$\frac{k}{u_g} = 5 \text{ x } 10^{-3} \left(\frac{C}{\rho_g}\right)^{-0.5} \mathrm{Re}_g^{-0.2}\, \mathrm{Pr}_g^{-2/3} \left(\frac{\rho_l}{\rho_g}\right)^{0.2} \qquad (2.49)$$

2.3.4.2 Possible mechanisms for effect on entrainment rate

The most obvious way in which heat flux can affect entrainment is through nucleation within the film which would lead to bubbles growing and bursting on film surface (type 3 in Figure 2-16). This would of course lead to an increase in entrainment over and above that occurring due to shear. Celata et al. [60] and Okawa et al. [51] include this effect in their work. In both these works the correlation given by Ueda et al. [61], eqn. (2.50) was used.

$$E_{boil} = c_{boil}\left(\frac{q^{"}}{h_{fg}}\right)^{2.5}\left(\frac{\delta_{vk}}{\sigma\rho_g}\right)^{0.75} \qquad (2.50)$$

Another possible mechanism affecting the entrainment rate (suggested by Peng [59]) is due to the vapour velocity normal to the film surface. This would cause cushioning effect for the flow of vapor core and reduction in the interfacial stress leading to lesser entrainment than in adiabatic conditions.

Though generally it is believed that bubble nucleation is suppressed in annular flow, experimental evidence to the contrary has been provided by Barbosa et al. [62]. They have also qualitatively observed an enhanced entrainment. There are however no direct experimental evidences showing significance of lateral vapor velocity (i.e., normal to the film) on deposition and entrainment rates.

2.3.4.3 Experimental evidence for the effect of heat flux

Experimental evaluation of the effect of heat flux on entrainment and deposition rates is tricky. Probably there are only two types of experiments in which the effect of heat flux has been examined.

The first type of experiment are those by Hewitt and co-workers [63,64] at AERE, Harwell. In principle the method involves experimental evaluation of the entrained flow rate in the annular flow regime in a tube having a heated and unheated section. When this entrained flow rate is plotted as a function of length along the tube, a change in slope of the curve at juncture of heated and unheated sections would indicate an effect of heat flux. Mathematically, the principle may be explained from equation (2.51) governing the mass balance of entrained flow rate.

$$\frac{dG_d}{dz} = \frac{4}{d_{eq}}\left(E - D\right) \tag{2.51}$$

The left hand side of this equation represents the slope of the entrained flow vs. length curve. In diabatic flow, this slope changes with the quality (which changes with length). The cessation of heat flux beyond a certain point ensures that just before and just after that point all conditions except for heat flux are the same. Thus the slope of curve (dG_d/dz) would change at that point if and only if heat flux has an effect on $\left(E - D\right)$. In experiments at low pressure [63] as well as high pressure [64] conditions, no effect of heat flux was found.

The other type of experiment has been conducted by Russian workers (Milashenko et al. [65]). In their experiments, steam-water mixture in equilibrium annular flow was heated in a short section. Two major assumptions were made in this work; droplet deposition was assumed to be zero for the operating conditions (based on experimental work of Doroschuk and Levitan [66]). Further, the change in quality in the small heated section is assumed to be negligible. By varying heat flux in the heated section, the change in entrainment was observed and quantified as the effect of heat flux on entrainment rate. They had obtained a significant effect of heat flux. Functionally they correlated the entrainment rate to vary as heat flux raised to the power 1.3. The correlation is dimensional and apparently indicates that entrainment rate would vanish when heat flux falls to zero. This is an unphysical scenario. Nevertheless, they did observe an effect of heat flux.

One of the major differences in the Harwell and Russian experiments is the magnitude of heat flux used in the experiments. While in the former, they were of the order of 1 MW/m^2 (which are typical of BWR), in the latter substantially higher heat flux upto 4 MW/m^2 have been considered. Since the Harwell data are more relevant to BWR applications it may be said that neglect of boiling induced entrainment will not lead to major errors. This has also been observed by Adamsson and Anglart [67] who found better results upon neglecting boiling induced entrainment.

2.3.5 Initial Entrainment Fraction (IEF)

IEF refers to the fraction of liquid entrained at the onset of annular flow. To better explain the problem of IEF, reference has to be made to the film mass balance equation (2.2). This equation has to be solved from the onset of annular flow. Thus a boundary value of film flow rate is required. Generally the available correlations for transition to annular flow [68–70] would provide the transition quality, x^{trns}. From this, the total liquid flow rate at transition can be deduced. Mathematically the problem reduces to the determination of IEF which is the fraction of liquid entrained at onset of annular flow.

$$G_{lf}^{trns} = G\left(1 - x^{trns}\right)\left(1 - \mathrm{IEF}\right) \tag{2.52}$$

$$G_{d}^{trns} = G\left(1 - x^{trns}\right)\mathrm{IEF} \tag{2.53}$$

In literature scanty work has been reported for measurement and prediction of entrained fraction at the onset of annular flow. Most of the efforts in mechanistic modeling have been confined towards development of models and correlations for rate processes. It is only recently (the earliest paper dealing with this matter in seriousness is that of Barbosa et al. [71] in 2002) that work in this field has been taken up. In some of the earlier works [25,27] it is seen that the dryout predictions are not very sensitive to IEF. This however, as seen in Figure 2-20, from a comparison of prediction from various available correlations, is not generally true.

Some other workers [42] recognising the influence of IEF have in fact used it as a parameter to tune their predictions to experimental data. In view of this, a reliable prediction scheme is required for IEF. Otherwise the credibility of mechanistic dryout predictions is always questionable.

One of the assumptions commonly used for prediction of IEF is that the entrained fraction at the onset of annular flow corresponds to that for hydrodynamic equilibrium [4,24]. The IEF is determined by equalizing the expressions for entrainment rate and deposition rate at the transition location. There is however no strong basis for making this assumption. It has been shown by Barbosa et al. [71] that the IEF predicted using this assumption is not in good agreement with experiments.

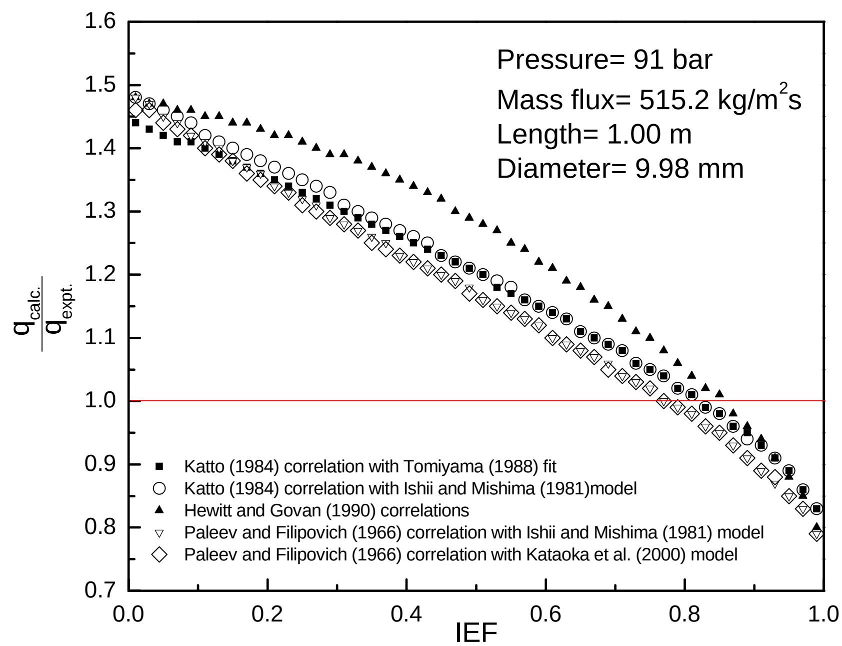

Figure 2-20: Effect of IEF on prediction of dryout power for different entrainment-deposition correlation sets. The predictions are for a single experimental data point. (Experimental data of Becker et al. [72]**)**

Barbosa et al. [71] carried out experimental investigations on the entrained fraction in air-water churn and annular flow regimes. These experiments were carried out at low pressure

(1.7 to 5 bara) and relatively low liquid mass flux (up to 350 kg/m^2s). In these experiments, water was injected through a porous sinter mounted on the pipe wall. One of the major findings of this study was that the entrained liquid fraction reaches minima at the onset of annular flow. Their experiments have yielded entrained fraction at the onset of annular flow as low as 0.1 to 0.2. However, these results cannot be directly applied to the case of diabatic single component annular flow. The reason for this is firstly that the conditions of the experiment do not simulate the actual conditions existing in high pressure steam-water flows relevant to boiling water reactors. Secondly and more importantly, these experiments were carried out in equilibrium flows, i.e., the flow rates of air and water were adjusted so as to obtain a particular flow regime and sufficient development length was provided for the flow to develop before the entrained fraction was measured. In boiling flows, such equilibrium is never achieved, and the high entrainment during the slug-churn transition due to the vapour bursting the liquid slug (type 5 in Figure 2-16) plays a substantial role in determining the entrained fraction at the onset of annular flow. It is due to this reason that the IEF predicted using the correlation of Barbosa et al. [71] gives much lesser values than those required for proper dryout prediction (Ahmad et al. [73]). The importance of history effect is also demonstrated in experiments by Gill and Hewitt [36] where they have shown that the amount of liquid flowing as entrained droplets is strongly dependent on the method of liquid injection. They observed that the entrained fraction in the case of peripheral injection through a porous sinter (zero IEF) is much smaller than that in case of centre jet injection (100% IEF) even after a considerable pipe length.

For the prediction of entrained fraction at the onset of annular flow, Ahmad et al. [73] and Wang et al. [74] have used deposition-entrainment model from the beginning of churn flow, thus the entrained fraction at the onset of annular flow, i.e., IEF is obtained during the calculations. It may be expected that since the integration of the phenomenological equations begins from a point which is further upstream, the effect of the boundary conditions on dryout is reduced. This method however requires the value of entrained fraction at the onset of churn flow. Thus the problem of IEF prediction is not solved but only replaced by prediction of another boundary value. Further, the entrainment and deposition rate models validated for annular flow are used in churn flow regime, which needs to be verified. Studies on churn flow regime might actually hold the key to better understanding and modeling of the initial entrainment. Such studies are referred to in greater detail in chapter 3.

Recently, Oh et al. [75] have developed a correlation for IEF by considering adiabatic and diabatic experimental data [23] near to computed transition point. Their correlation is given as following:

$$IEF = 1 - \max\left(0.2, \min\left(0.8, e^{\left(0.5\mathrm{Re}/10^5\right)}\right)\right) \tag{2.54}$$

Re is the Reynolds number defined using the total flow rate and liquid viscosity. The correlation is dimensionless, simple to use and is derived from data which span a wide range (pressure: 30 – 90 bar, Re: 38000 – 426000, Hydraulic dia.: 9 – 20 mm). The correlation is however purely experimental and derived from little experimental data (46 data points).

In view of the foregoing, there is a need to address the IEF problem. While with the deposition and entrainment correlations, the analyst faces the *problem of plenty*, with Initial Entrainment fraction (IEF), it is a *problem of scarcity*.

2.4 Post-dryout heat transfer

The occurrence of dryout is precluded during normal operation of nuclear reactors. However under certain accident conditions, dryout might occur. The most important such accident is the Loss of Coolant Accident (LOCA). The loss of coolant from the core with associated fall in pressure results in reduction in flow and increased voiding. With a properly functioning reactor protection system, the reactor would shut down under such cases. The prevailing heat flux after LOCA (which is the decay heat) is about two orders of magnitude lower than operating heat flux. Under those conditions, generally annular flow is observed. With reduction in flow due to loss of coolant, the liquid film starts to vanish from the fuel pins leading to temperature excursion (in excess of rewetting temperature). This is known as the *blowdown* phase of LOCA. Depending upon reactor design, emergency coolant is introduced into the core at a certain point after blowdown. In PWRs the injection takes place through the inlet plenum, located at the bottom of the core. The emergency coolant then rewets and cools the surface. The exact mechanism of cooling however depends upon the rate of injection of emergency coolant, also known as *reflooding*. This has been depicted nicely by Andreani and Yadigaroglu [76].

At high reflood rates (schematic on right in Figure 2-21), Inverted Annular Film Boiling (IAFB) is observed with a non-wetting liquid jet in core. This water jet is separated from the heated fuel pins by a layer of vapor. The present work focuses on the other case of low reflood rate (schematic on left in Figure 2-21). At low reflood rates, annular flow regime is observed.

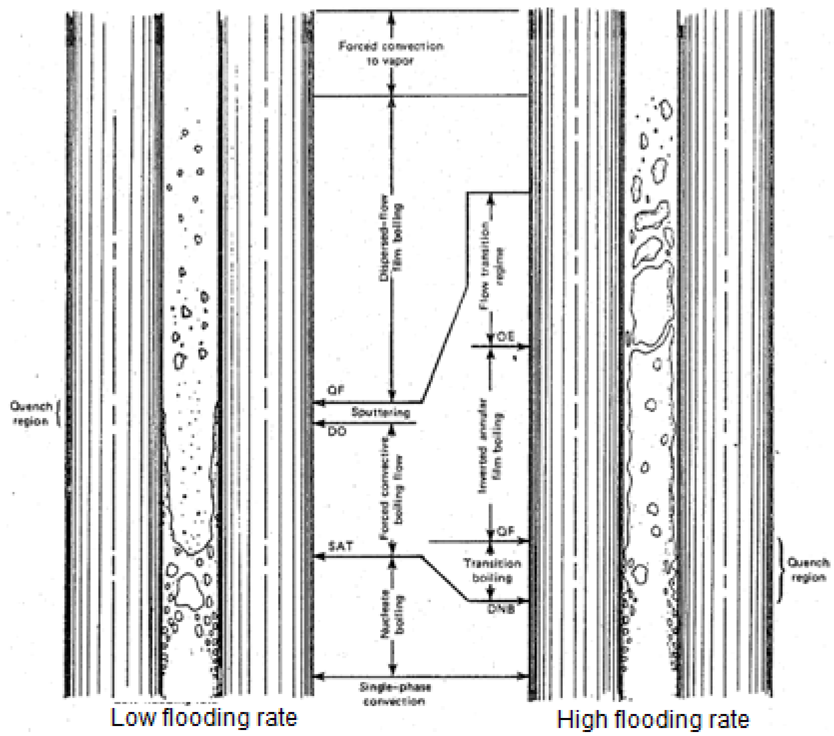

Figure 2-21: Reflood Mechanism for different flooding rates; schematic (from Andreani and Yadigaroglu [76]**)**

The chronology of events in this case is opposite to what would occur in dryout. The ECC water (dispersed as droplets in vapor flow) is initially unable to wet the (dry) fuel clad surface which is above the rewetting temperature. This regime is thus known as the Dispersed Flow Film Boiling (DFFB) or Mist Flow Film Boiling (MFFB)[77]. The heat transfer in this regime leads to lowering of surface temperature till finally liquid-surface contact can be achieved. This re-wetting front is known as the *Quench front* (QF in Figure 2-21). Somewhere upstream the dryout (DO in Figure 2-21) condition is met. The phenomena occurring in zone between QF and DO is given the name *sputtering*. From the point of view of boiling regime, this falls in *transition boiling*. Annular flow is also observed if ECC water is sprayed from the top (as in BWRs). The exact physics is however somewhat different due to countercurrent flow of vapor generated (moving upwards) and water (moving downwards as the film and drops). The quench front is still characterized by sputtering; upstream of which dryout condition is observed. The reduction in surface temperature after re-wetting is very fast (~200^{o}C/s). Thus literally, the rewetting-front is considered equivalent to the quench front.

2.4.1 Modeling approaches for Post-dryout phenomena

From the point of view of thermal-hydraulic safety after LOCA, the occurrence of rewetting is considered sufficient to ensure cooling of the pins. Conventionally, the time required for rewetting (and thus cooling of fuel pins) is quantified using a *rewetting velocity* or *quench front velocity*. Expressions for the rewetting velocity have been derived through the conduction controlled model [18] of rewetting phenomena. These models which are probably the most basic ones for analysis of reflood phase require an estimate of heat transfer ahead of the wet front (i.e., in the DFFB regime). In parlance of post-dryout heat transfer, this heat transfer is known as *pre-cursory cooling*. One of the most obvious assumptions [78] is to assume no heat transfer to coolant in the DFFB region (as generally the heat transfer in this region is much poorer than that in the wetted region) and use a typical boiling heat transfer coefficient for the wetted region. This would lead to an overly conservative (under-)estimate of the rewetting velocity. More recent models [79] have advocated the use of an exponentially decaying heat transfer coefficient downstream of the rewetting front. The reasoning behind such variation of heat transfer coefficient is cited to be the slowly reducing heat transfer due to vaporization of drops. This approach though effective, does not provide much insight into the DFFB mechanisms.

The other extremity in detailing of post-dryout modeling is exemplified by Andreani and Yadigaroglu [8,80] who simulate the DFFB regime through a hybrid Eulerian-Lagrangian model. The vapor flow field is derived from Eulerian model and droplet motion is then computed through Lagrangian mechanics. Appropriate closures are provided for droplet hydrodynamics and heat transfer. The model allows simulating range of droplet sizes instead of one particular droplet size. One of the issues with such models is the huge computational resources required for reactor scale simulations. Even more detailed CFD simulations have also been done by Chatzikyriakou [5].

The middle path of one-dimensional mechanistic modeling has been pioneered by Hewitt and Govan [4] who attempted to arrive at the rewetting velocity mechanistically by solving the transient film evolution equation (2.55).

$$\frac{\partial\left(\rho_l \alpha_{lf}\right)}{\partial t}+\frac{\partial G_{lf}}{\partial z}=\frac{4}{d_{eq}}\left(D-E-B\right) \tag{2.55}$$

In the transient simulations, they [4] increase the inlet mass flux in a tube which has already undergone dryout. With time the dryout point moves downstream. However as noted by them [4], the model is too simplistic as it ignores the important fact that droplets would not be able to wet the surface under all circumstances. Hence the deposition flux predicted by their deposition model (eqn. (2.12)) might not be able to actually wet the wall. Further, the mechanistic model also needs rewetting temperature to be specified explicitly. They had shown that predictions are more physically valid by using correlation for heat transfer in the non-wetted region. Best estimate codes like COBRA-TF [81] employed in reactor safety analysis use a similar methodology with models and correlations for DFFB heat transfer.

2.4.2 State of the art in modeling DFFB heat transfer

Keeping in view the foregoing, it may be said that the heat transfer in the DFFB region needs to be modeled to arrive at better mechanistic predictions of rewetting phenomena. A great body of work, spanning more than 2 decades, in this field has emanated from Rohsenow and his co-workers [6,82–88] at MIT laboratories. From experimental studies it is seen that the DFFB regime is in thermal non-equilibrium. Some early studies [6] have observed thermodynamic quality of 3 with droplets present in the core. An estimation of the degree of non-equilibrium is one of the challenges of DFFB modeling. From the point of view of heat transfer mechanisms, there are three paths through which the wall heat flux is carried away by the two-phase mixture flowing in the mist flow regime [9]:

1. Heat transfer from wall to vapor (convection and radiation)
2. Heat transfer from vapor to liquid drops (convection and radiation)
3. Heat transfer from wall to liquid drops (near wall and radiation)

The radiation component of heat transfer is represented by the radiation heat flux, q''_{rad}, which can be obtained from the generic equation:

$$q''_{rad,12} = \varphi_G \sigma_B \left(T_1^4 - T_2^4\right) \tag{2.56}$$

Here φ_G and σ_B are the gray body factor and Stefan-Boltzmann constant. T_1 and T_2 are the temperatures of the media among which the radiative heat transfer takes place.

The convective heat transfer from wall to vapor is usually handled by some modification of the single phase forced convection heat transfer correlation; Forslund and Rohsenow [6] used modified Dittus-Boelter equation, Groeneveld and Delorme [89] used Hadaller correlation [90], Varone and Rohsenow [88] proposed multiplicative correction factors to single phase heat transfer coefficient to include the effect of dispersed phase, Guo and

Mishima [9] used the Reynolds analogy etc. The heat transfer can be represented by an appropriate heat flux as in equation (2.57)

$$q''_{c,wv} = h_{wv}\left(T_w - T_v\right) \tag{2.57}$$

It must be mentioned at this stage that CFD models like those of Andreani and Yadigaroglu [8] model this component of heat transfer and correlations for wall to vapor heat transfer coeficient, h_{wv} are not required. The second component of heat transfer from the superheated vapor to liquid drops is represented by equation (2.58) which is similar in form to eqn. (2.57).

$$q''_{c,vd} = h_{vd}\left(T_v - T_d\right) \tag{2.58}$$

The heat transfer coefficient is derived from correlations which have the basic form of Ranz-Marshall correlation [91], eqn. (2.59).

$$Nu_{vd} = \frac{h_{vd} d_d}{k_v} = 2.0 + 0.6\,\mathrm{Re}^{1/2}\,\mathrm{Pr}^{1/3} \tag{2.59}$$

From a study of the literature, it may be said that at least philosophically there is an agreement between the present models with regards to the approach for modeling of the convective heat transfer from wall to vapor and from vapor to droplets.

The same cannot however be said about the third mechanism i.e., heat transfer to droplets near the wall. There are some models [82,89] which do not consider this to be a significant contributor and thus neglect it. While many others [6–9,85–88] do consider the effect. Moose and Ganic [7] and later Chatzikyriakou [5] have found that this mechanism can contribute up to 10% of the total heat extracted from the wall. Chatzikyriakou [5] carried out detailed CFD simulations on impinging droplets to evaluate the heat transferred to a single droplet. They also performed experiments to validate the simulations. Such detailed

CFD calculation is however not viable for simulating actual scenarios. A more practical solution is to develop models for wall-to-drop heat transfer which can act as closure models either for generalized CFD codes or one-dimensional codes. The former is exemplified by the use of Kendall and Rohsenow [92] model by Andreani and Yadigaroglu [8] and the latter by models such as Guo and Mishima [9]. The wall–drop heat transfer closure in these models, are based on computing the heat transfer to a single drop. The total heat transfer is then evaluated by taking into consideration the flux of droplets depositing on the wall. These models however do not independently validate each mechanism (i.e., wall–drop, wall–vapor, vapor–drop). Rather the performance of the model as a whole is compared against experimental data. One of the reasons for this is the unavailability of such data during the development of these models. Lately however, experiments [5,10] have been carried out in which the wall–drop heat transfer has been directly or indirectly quantified. These experiments provide an opportunity to revisit the mechanistic models for wall–drop heat transfer and evaluate their performance.

In view of the complexities involved in modeling of post-dryout heat transfer, another approach – Film boiling Look up table [3] has also been developed based on experimental determination of heat transfer coefficients in the post dryout regime.

2.5 Effect of spacers on dryout and post dryout heat transfer

Spacers are an important and indispensable part of a nuclear fuel bundle. There are many reasons why they are essential, primary among them being maintaining inter-rod spacing, preventing hotspots, arresting flow induced vibrations. Spacers also lead to enhanced mixing and their proper design leads to improvement in thermal-hydraulic aspects of the bundle. From the point of view of present work, spacers have an overarching influence on all the phenomena listed earlier in this chapter. The modeling of how spacers would influence the different parameters important for dryout and post-dryout modeling is a challenging task in itself and is not the aim of the present work. However, for the sake of providing the complete picture and its probable influence on the outcomes of the present work, the effect of spacers is discussed.

2.5.1 Spacer effect on dryout

Dryout, as has been detailed earlier is governed by the processes of deposition, entrainment and vaporization. It is quite obvious that spacers will not influence the vaporization, but they definitely influence the deposition and entrainment rates in their vicinity. This effectively leads to modification in the evolution of the liquid film. Janssen [93] has reported change in dryout power based on the position of spacer. To obtain a greater understanding of the spacer effect, studies were performed by Shiralkar and Lahey [94]. They studied the effect of relatively simple (simpler than the nuclear fuel spacers) geometrical obstacles on the film flow rate over a flat plate. For a given air flow rate, the liquid flow rate was reduced till dry patch was observed. Two types of dry patches were observed by them (Figure 2-22). Type 1 dry patch occurred upstream of the obstacle and was attributed to the stagnation of the vapor stream on the upstream face of the obstacle and formation of horse shoe vortices leading to scrubbing out of the liquid film around that region. Type 2 dry patch was observed downstream of some obstacles and occurs due to stagnation of the wake flow behind the obstacles. Type 2 however was not obtained in all cases and was preceded by type 1 dry patch. The severity of the thinning of liquid film and eventual drying out was also a function of the obstacle shape.

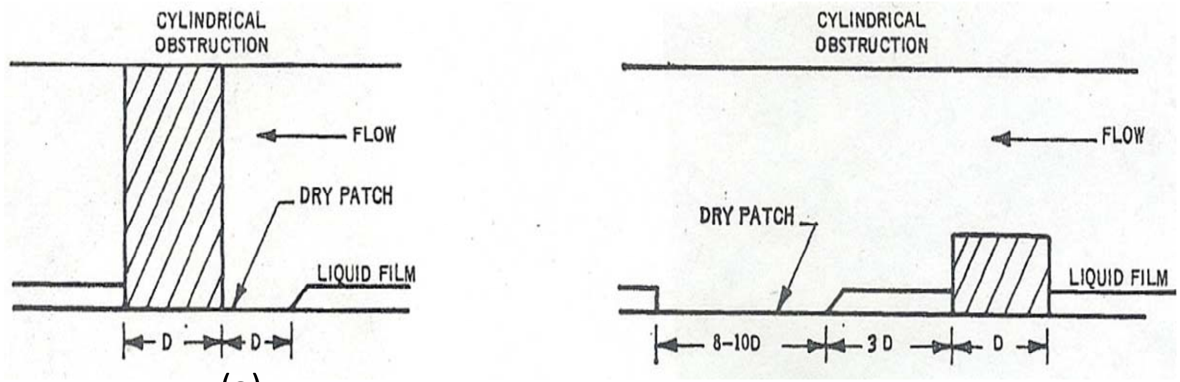

(a) (b)

Figure 2-22: Dry patches observed by Shiralkar and Lahey [94] **(a) Type 1 and (b) Type 2 (from Shiralkar and Lahey** [94]**)**

Shiralkar and Lahey [94] experiments thus indicate two important things; firstly, there is a propensity for dry patch to form upstream of spacers and secondly, the shape of spacer is important in determining the extent of its effect. Further, their experiments would apparently indicate a reduction in the dryout power upon introduction of spacers, due to thinning of the film. However, the situation inside rod bundles is somewhat more complicated due to the tight pitch and existence of entrained droplets. Spacers lead to enhanced entrainment and deposition rates by causing churning of the vapor flow field and disturbance in the liquid film. Literature is thus not very conclusive about whether spacers lead to enhancement or reduction of dryout power. Janssen [93] has reported both increase and decrease in dryout power based on spacer location, mass flux and prevailing steam quality.

To understand and model the effect of spacers in rod bundles, experiments have been performed by many researchers. Here only a few salient ones are mentioned. Tomiyama and Yokomizo [95] performed film thickness measurements in air-water annular flow in a 3 x 3 simulated BWR fuel cluster. They found that film thickness reduced upstream of the spacer and recovered after that. This was postulated to be due to blockage caused by the spacer. The extent of recovery downstream of the spacer was lesser for higher liquid flow rates indicating some portion of the film which got entrained due to spacer did not redeposit. They however have not given details of the spacer geometry which would have an important effect. Studies with two different spacers designs have been reported by Nishida et al. [96] who conducted experiments in mock-up bundles with 4 x4 and 9 x 9 elements. They found, in contrast to Tomiyama and Yokomizo [95], that changes in the spacer shape could also lead to increase in film thickness downstream of spacer. They concluded that spacers influence the film flow in the downstream region by two means viz., modifying the gas flow field and interacting with the liquid film. Both of these in turn lead to changes in deposition and entrainment rates. Kawahara et al. [97] have reported that introduction of mixing vanes leads to significant increase in droplet deposition due to swirling action. This leads to increased film thickness downstream of the spacer.

Mori and Fukano [98] have conducted low pressure (slightly above atmospheric) dryout experiments in annulus geometry to ascertain the effect of spacer. Apart from temperature measurements, their setup allowed visualization of dryout phenomena. They observed dryout occurred consistently upstream of the spacer. A schematic of their test section and results are shown in Figure 2-23. It is seen that upstream of the spacer, dry patch develops and then spans the complete circumference Figure 2-23b. Downstream of the spacer, intermittent dry patches are observed, but they don’t sustain and thus do not lead to dryout.

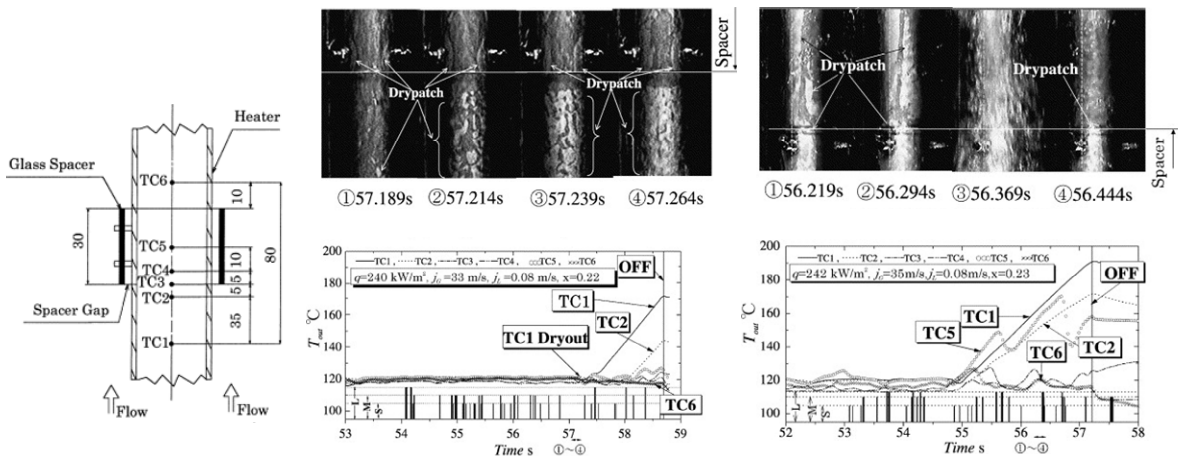

(a) (b) (c)

Figure 2-23: The effect of spacer on film flow and dryout. (a) test section schematic, (b) Visualization and temperature traces upstream of spacer, (c) Visualization and temperature traces upstream of spacer (from Mori and Fukano [98]**)**

Mori and Fukano [98] have concluded that dry patches downstream of the spacer are cooled by the following disturbance wave. Dryout was not seen to occur directly beneath the spacer. Quite interestingly, for their conditions, they did not observe any appreciable effect of presence (or absence) of spacer on dryout power. They further conclude that spacers have a stronger effect on the downstream side. On the upstream, the spacer effect was negligible.

With regards to modeling, the generally adopted philosophy is that since spacers enhance the turbulence in their vicinity, the effect is reflected as a local increase in the deposition coefficient (refer eq.(2.6)) downstream of the spacer. Since the deposition coefficient by its nature incorporates the lateral fluctuating component of velocity, this is a satisfactory approach. There are different ways in which the quantum of deposition coefficient enhancement is computed. Some use ratio of the fluctuating velocities [95], others use turbulent kinetic energy enhancement [99]. In models which explicitly use the equilibrium entrainment concept for evaluation of entrainment rates, the enhancement in deposition coefficient will increase entrainment rates as well [95,96]. However, there are models which account for an increase only in the deposition rates [99,100].

A mechanistic model for grid type spacers (without vanes) has been developed by Yano et al. [101–103]. They observe that turbulence enhancement alone is insufficient to explain the increase in deposition over a short length after the spacer. They have attributed the integral effect of spacers as a result of three separate phenomena:

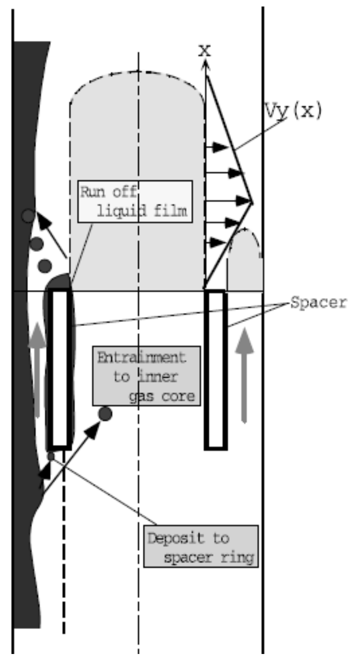

Figure 2-24: Schematic depiction of the three component effect of ring type spacer (from Yano et al. [103]**)**

1. Drift flow effect: This is caused due in the recovery of the gas flow splits due to spacer. The thin region sandwiched between the spacer and fuel pins has low velocity. Downstream of the spacer, there is a lateral wall directed flow which drives the entrained drops to the wall. The end effect is an increased deposition downstream of the spacer.
2. Narrow channel effect: It is postulated that the narrow gap existing between the spacer and the fuel pin, does not allow the complete film to pass through; some gets

entrained while some gas flows in the ‘narrow channel’. This leads to an enhanced entrainment upstream of the spacer.

3. Run-off effect: This refers to the literal running off of the liquid film flowing over the spacer from the downstream edge of the spacer. Towards the downstream edge, the liquid breaks into drops. Further, deposition is enhanced due to drift flow effect.

Narrow channel effect was not observed in the very recent visualization experiments of Pham and Kunugi [104]. They conducted experiments in a 3 x 3 rod cluster with spacers, typical to those used in BWRs. They however did observe the run-off effect. The importance of run-off on deposition enhancement is due to the fact that spacers, through run off provide an additional source of droplet generation and entrainment. As against this, in a bare geometry (without spacers), disturbance waves are the only source of entrainment.

Due to the complex geometrical features of nuclear rod bundle spacers and the complexities inherent to entrainment process, the use of CFD has been restricted to evaluation of deposition and its enhancement [27,105–107]. These works have employed Lagrangian particle tracking methods for droplets in annular flow to evaluate the enhancement in deposition. Yamamoto et al. [106] have shown that there exists a close correspondence between predicted deposition enhancement and dryout power enhancement.

From the point of view of the work presented in this thesis, probably the most important effect of spacers is the fact that they locally disturb the liquid film, modify the rate processes and tend to discretize the location of dryout occurrence; dryout tends to occur near upstream of spacers. Further, the entrained fraction gets modified downstream of a spacer. Nevertheless, the equations of the mechanistic model can be used with local modifications (to account for spacers) to predict the behavior.

2.5.2 Spacer effect in post-dryout

As opposed to importance of hydrodynamics of the liquid film for prediction of dryout, the post dryout phenomena are underlined by heat transfer. The absence of the liquid film makes it easier to speculate the effect of the spacer. It may be said that spacer causes enhanced droplet deposition in its downstream, leading to improved heat transfer and lowering of temperatures. Further, the turbulence enhancement due to spacer leads to improved heat transfer to vapor phase. Indeed such enhancement has been observed experimentally by Anghel and Anglart [108]. In some cases they [108] also observed quenching downstream of the spacer. The vapor superheat is also found to reduce downstream of the spacer. Yoder [109] in his exhaustive review has mentioned that the effect of reduction in vapor superheat is felt as reduction in wall superheat at locations farther than where the hydrodynamic effects of the spacer grid exist. Like in annular flows, the extent of heat transfer improvement is linked to the spacer shapes. Spacers are also seen to have a pronounced effect on the drop sizes with the average drop size reducing downstream of the spacer [110]. This leads to increase in interfacial area and heat transfer. Generally, It has also been possible to predict the improvement in heat transfer using CFD models [107]. However the droplet dynamics are particularly difficult to predict.

2.6 Concluding remarks

From a study of the literature relevant to modeling of annular two-phase flows, it is seen that the mechanistic model presents a viable approach for prediction of dryout and have the potential to succeed where conventional approaches fail. The reliability and robustness of the mechanistic model depends on the models and correlations used for the various closures.

The distinguishing feature among the different mechanistic models available in literature is the choice of entrainment and deposition rate correlations. Indeed a model is only as good as the correlations it uses. With time many correlations have evolved for the prediction of these rate processes. A researcher in this field has to choose the better set of correlations and most often no guidelines are available to make that choice. Some assessment of correlations is required to assist in this.

The majority of deposition and entrainment rate correlations are essentially empirical in nature. One of the reasons for this might be that the present understanding of disturbance waves and the effect they have on entrainment and deposition processes is insufficient for modeling these rate processes. A detailed study of the disturbance waves is thus essential towards developing a more robust mechanistic annular flow model. This would nevertheless be a challenging task considering the complex wave structures and their tight coupling with the gas flow field.

Another important closure is that of Initial Entrainment Fraction (IEF). In literature there is scanty work on this subject. However as has been shown in the foregoing, IEF has an important bearing on dryout predictions. It is also worth mentioning that the initial entrainment in annular flow (in diabatic situation as in a reactor) takes place at the transition from churn to annular flow. The churning effect due to counter current motion of falling liquid film and upwards moving vapor leads to formation of large waves from which huge entrainment takes place. The study of waves in the churn flow regime is thus of interest to generate a new closure model for IEF.

Literature shows that the annular flow mechanistic model can also be extended to post-dryout scenario. The modeling of wall-to-drop heat transfer presents a challenging prospect as not many standard treatments (like the single phase heat transfer coefficient applicable to vapor flows etc.) are available in literature. Mechanistic description of the wall–drop heat transfer is a promising option which has been used in literature. However the performance of such a model has not been verified independent of other processes. Such comparison would provide more confidence in the model.

3 EXPERIMENTAL STUDIES IN CHURN AND ANNULAR FLOWS

The annular flow regime, as already described, is characterized by the presence of a thin wall-adhering liquid film and a central gas core. Depending on the gas and liquid velocities, the gas core may or may not entrain liquid droplets. The liquid film is wavy and consists of intermittent large waves known as disturbance waves. Prediction of the liquid entrainment fraction and the rates of entrainment and deposition are important for mass transfer and phase change studies, as are widely undertaken (inter alia) to predict dryout in BWR flow channels.

The behavior of such waves is one of the most important characteristics in annular flow (and in churn flow, an associated flow regime prior to transition to annular) in determining entrainment, and possibly deposition, rates. Traditionally, most of the efforts towards prediction of entrainment and deposition are purely empirical in nature (§2.3.1 and §2.3.2), but the thrust of much current work is for these empirical approaches to become more mechanistic [56,111], informed by an (at least) qualitative understanding of the flow.

Such phenomenological modeling depends on good experimental data; on measurements of quantities such as entrainment rates and deposition rates, and on observations of 'intermediate' quantities such as the frequencies and form of disturbance waves.

There is a wide parameter space of interest, ranging from the high pressures and flows associated with normal operation in a BWR, to the low pressures and low flows important in studying various fault conditions.

A major motivation of the work reported in this chapter was to augment the rather sparse availability of experimental data for nuclear-relevant small tubes, in particular by extending it into the low liquid and gas flow region, of particular interest for fault studies. This had combined objectives:-

The first was to allow the validity of existing correlations, largely based on measurements outside this region, or for which the experimental range cannot be ascertained, to be investigated for this region. Demonstration that correlations used in safety analyses are truly valid for the parameter space in which they are applied is naturally necessary to satisfy regulators.

Secondly, by measuring the fullest possible set of parameters, in particular wavelength, frequency, wave speed, film thickness and flow rates, it is hoped to provide additional insights into the flow characteristics that would aid those attempting to build semi-empirical phenomenological models of the dryout process. Disturbance waves, being large amplitude waves, have been identified as the major source of entrainment [37,54]. This fact is also highlighted by Sawant et al. [49] who have indicated the importance of disturbance wave studies for the evaluation of entrained fraction. In the literature are reports of attempts to model the rate of entrainment through simplified representations of the wave [56]. Such models require various wave characteristics such as wavelength and speed, which can only be determined experimentally.

The role of disturbance waves in influencing deposition has been less considered. Since disturbance waves change markedly the flow area available to the high-speed vapor core (e.g. Han et al. [112]), especially in small diameter channels, the core velocity will be modified by the waves, and one might expect that the rate of deposition might consequently be modified. Part of this second motivation was to provide data for future investigation into a possible particular mechanism whereby these waves could influence deposition. In Figure 3-1 is shown a typical disturbance wave, and an idealized sketch, with postulated vapour streamlines.

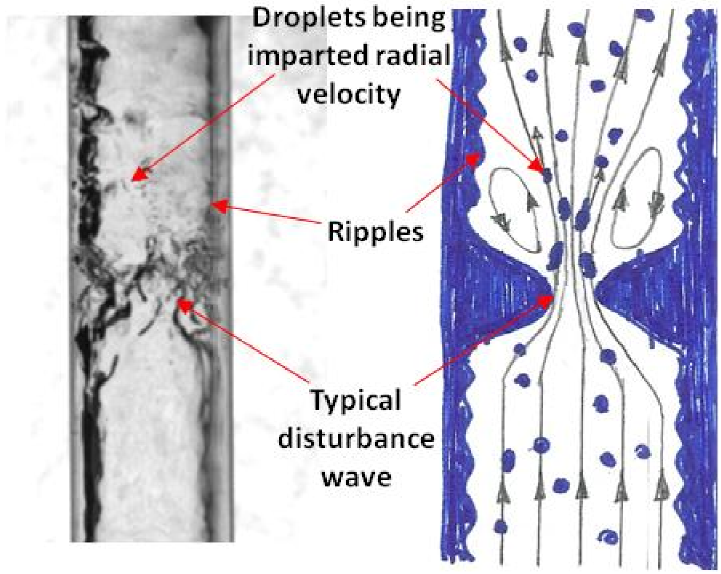

Figure 3-1: Typical disturbance wave and its simplified representation, and postulated flow field

Droplets already entrained upstream of the wave, especially inertial droplets, might be deposited directly into the upstream face of the wave [113], if they are unable to follow the rapid radially-inwards acceleration of the vapour. The rapid radial expansion of the gas flow, and possible recirculation, downstream of the wave might similarly increase deposition rates. Since the waves themselves are believed to be a major entrainment source, it could indeed be that a large fraction of drops are born directly into this high-deposition environment. This effect of the waves on deposition rate does not feature explicitly in any of the deposition rate correlations. This might be due to the fact that normally experimental determination of deposition rate involves measuring deposition after completely removing the film [38] and thus no waves exist when the deposition rate is measured. By ‘construction’, the models and correlations for deposition rate do not admit any influence of waves. The velocity of the disturbance waves relative to the gas, as well as their size and other characteristics, all seem likely to affect the radial velocities generated. Thus disturbance wave velocity, amplitude, wavelength and time period, along with the vapor flow rate, are all important quantities that are required to be known to investigate this further. Determining these was part of second motivation; though wave amplitudes have not been evaluated in this work.

Thirdly, these experiments provide additional entrainment data for validation of the mechanistic model developed during the course of this work. Since the experiments are done with air and water, validation against this data adds greater confidence in the applicability of the mechanistic model.

The objective behind study of waves in churn flow stems from their influence on the Initial Entrainment Fraction (IEF) in diabatic flows. Lately the mechanistic model has also been extended into churn flow regime [73,74] to compute (or rather obviate) IEF required for annular flow calculations. It is expected that the study of waves in churn flow regime would aid in better modeling of this regime. This topic is further discussed in chapter 4 where some of the observations from the present experiments are used to develop an IEF prediction methodology.

In §3.1 some background literature with respect to waves in annular and churn flow regimes is described setting the stage for the present measurements on wave characteristics. A discussion on the measurements and correlations for entrainment and rate processes has been given in chapter 2 and thus not repeated here. In §3.2 the experimental arrangements are described, discussing the experimental techniques and some qualitative observations which shape the data interpretation. In §3.3 measured characteristics of waves in churn and annular flow regimes are reported. These are compared with correlations and data reported in literature in §3.4. The measurements of film flow rate and film thickness are reported in §3.5. A note on the experimental uncertainties is given in §3.7 and conclusions are drawn in §3.8.

3.1 State of knowledge about waves, as evident from literature

Based on the mechanism of formation, in literature large waves in annular flow are called *disturbance waves* and those in churn flow regime are called *flooding waves*. There have been many measurements reported for disturbance waves, and only what are possibly the most relevant ones for the present work are summarized here. Most of these measurements have been carried out in air-water experiments primarily because of the ease of experimentation.

In the literature, pioneering and very informative work on study of disturbance wave characteristics has been done by Nedderman and Shearer [114] and Hall-Taylor et al. [115] who used cine films to determine wave characteristics in annular flow. Hall-Taylor et al. [115] used in addition conductance probes to measure the liquid film thickness, but they found that such probes tend to give spurious signals for large ripples. They found the wave velocity to be a function of both air and liquid flow rates, although the dependence on air flow rate was dominant. In both these works, wave frequency was found to be a function of both air and water flow rates. However at higher water flow rates, dependence on water flow rate was not observed [114]. The tube diameter used in these experiments was 31.8 mm, which is much larger than the hydraulic diameters (~10mm) in nuclear reactor bundles. Nevertheless, these experiments gave a good insight into the characteristics of disturbance waves.

Azzopardi [116] and Thwaites et al. [117] conducted similar studies on the same 31.8mm diameter pipe, and their observations were mostly in line with previous works. Thwaites et al. [117] found that below a particular gas flow rate the wave frequency was independent of gas flow rate, whilst above this value there was approximately linear increase with gas flow rate.

The generation of waves is related to the interplay of surface tension forces with the varying pressures induced by the vapor core flowing over a perturbed surface. One might speculate that the perturbation of the vapor flow for a given surface deformation, and the consequent tendency to induce waves, might be greater for small diameter tubes or when the surface tension is lesser. Tomida and Okazaki [118] conducted experiments in a 10 mm diameter tube. They observed that the wave frequency and wave velocity remain constant at very low gas flows but increase linearly with gas flow for a given liquid flow rate. Han et al. [112], through reconstruction of wave structures, observed that in a 9.5 mm diameter tube the area occupied by the wave was up to 20% of the total flow area. The general trends in disturbance wave characteristics reported by them were in agreement with reports for large diameter pipes. Sawant et al. [119] determined the characteristics of disturbance waves at a range of pressures above atmospheric in a 9.4 mm diameter pipe. They concluded that only two non-dimensional numbers, a modified Weber number and the liquid-phase Reynolds number were needed to predict the dependence of disturbance wave velocity and amplitude on pressure, gas phase flow rate and liquid phase flow rate. (The Weber number is in essence a measure of the relative size of surface tension and momentum forces.)

Recently Pham et al. [120,121] have conducted visual studies on disturbance waves in air-water annular flow in a 3 x 3 rod bundle with spacer. Among the wave characteristics, they report measurements only of the wave velocity which they found to have a similar variation with superficial gas velocity as in tubular experiments.

Compared to annular flow, experiments on flooding waves in churn flow regime are relatively few. Vijayan et al. [122] have studied the flooding mechanism in transparent tubes of different diameters. They report that large circumferentially coherent waves do not exist in large diameter tubes. However, in smaller tubes, relevant to the hydraulic diameters encountered in nuclear fuel clusters, flooding is associated with large, circumferentially coherent waves, increased entrainment and larger pressure drop. With regards to studies on flooding wave characteristics, the visualization experiments of Govan et al. [123] and Barbosa et al. [124] in 31.8 mm bore tube and Wang et al. [125] in 19 and 34 mm bore tubes are notable. Since film thickness is large in churn flow regime, wall mounted conductance probes are prone to errors, thus visualization is preferred over conductance probe signal for determination of wave characteristics. Nevertheless, pin type conductance probes have been used by some researchers [126] for determining mean film thickness in post-flooding conditions. However, they have not used the data for reconstruction of transient wave shape. These previous experiments were conducted with air-water at atmospheric conditions. Visualization was done by having a transparent porous pipe section through which water was injected while air flowed in the core. Greater clarity on construction of the injection section can be obtained in §3.2 as a similar injection section (mixing chamber) has been used in the present work. They [123–125] had observed the flooding waves to appear more frequently with increase in gas flow rate. It is appropriate to mention at this point that in the present visualization experiments, attention was not concentrated at the injection section but ~ 2 m downstream of the mixing chamber. This is unlike previous experiments [123–125] in which the growth and movement of flooding waves was observed at the injection section. Another difference between the previous and present experiments is the absence of liquid downflow at the mixing chamber in the present experiments. However it has been shown [127] that the zone downstream of the mixing chamber is effectively decoupled from the upstream i.e., the characteristics of flooding waves is not dependent on existence (or non existence) of liquid flowing downwards at the injection.

Table 3-1: Different techniques and measurements by researchers on waves

REFERENCES	I.D mm	MEASUREMENTS REPORTED					TECHNIQUE USED
		λ *m*	*f* *Hz.*	v_w m/s	G_g kg/m^{2}s	G_l kg/m^{2}s	
Nedderman and Shearer [114]	31.8	N	Y	Y	18-103	11-231	Cine films
Hall Taylor et. al. [115]	31.8	N	Y	Y	23-58	10-33	Cine films
Tomida and Okazaki [118]	10	N	Y	Y	3-100	128-910	Film thickness measurement
Azzopardi B.J [116]	31.8	N	Y	Y	32-80	16-160	Cine films & film thickness measurement
Thwaites et al. [117]	31.8	N	Y	Y	11-41	50-379	Film thickness measurement
Wolf et. al. [128]	31.8	N	Y	Y	71-154	10-120	Film thickness measurement
Han et. al. [112]	9.5	N	Y	Y	100 - 200	18-47	Film thickness measurement
Sawant et. al. [119]	9.4	Y	Y	Y	8-656	70-700	Film thickness measurement
Barbosa et al. [124]	31.8	Y	Y	Y	3-7	4-11	Cine films
Wang et al. [125]	19 & 34	N	Y	N	5-12	53-280	Cine films
Present data	*11*	*Y*	*Y*	*Y*	*8-83*	*21-79*	Cine films

Table 3-1 summarizes some of the main relevant literature on measurement of wave properties, and the techniques used therein. These experiments were carried out with air and water. Except for Sawant et al., who have conducted experiments at different pressures viz., 1.2, 4.0 and 5.8 bar, all other experiments listed in Table 3-1 are at near atmospheric pressure (up to 1.5bar). For the sake of completeness, the conditions of the present experiments are also shown in the table. The present experiments were also conducted at near atmospheric pressures.

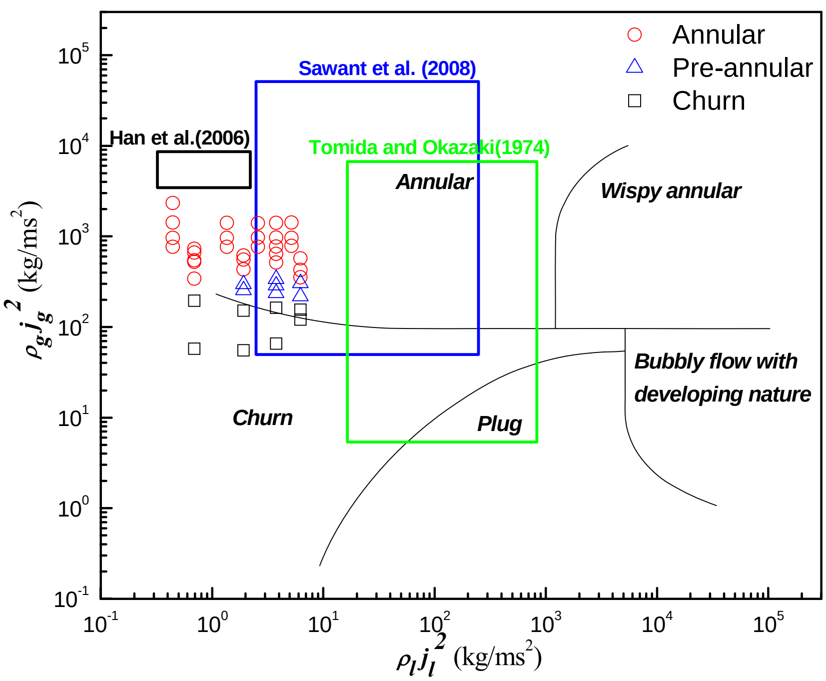

Figure 3-2: The parameter space covered by the present measurements (discrete symbols), and the ranges covered previous small-tube experiments [112,118,119] **for wave characteristics, plotted on Hewitt and Roberts** [129] **flow pattern map**

The parameter space in which the present data (marked discrete symbols) falls is shown on the Hewitt and Roberts [129] flow pattern map (Figure 3-2). Also shown on the map are the parameter ranges of previous experiments [112,118,119] for determining wave characteristics in small diameter (8-12 mm) tubes. In our observations, red circles were of annular flow, black squares of churn, and blue triangles of the regime that we have denoted 'pre-annular'. These observations match very closely with the boundaries delineated in the map. It may be seen that Tomida and Okazaki [118] report experiments well into the churn and slug flow regimes but they have not discussed churn flow explicitly in their work. The present experiments aim to widen the range of measurements available in nuclear-relevant small diameter (8-12 mm) pipes, providing better coverage in particular in the low liquid and gas flow region.

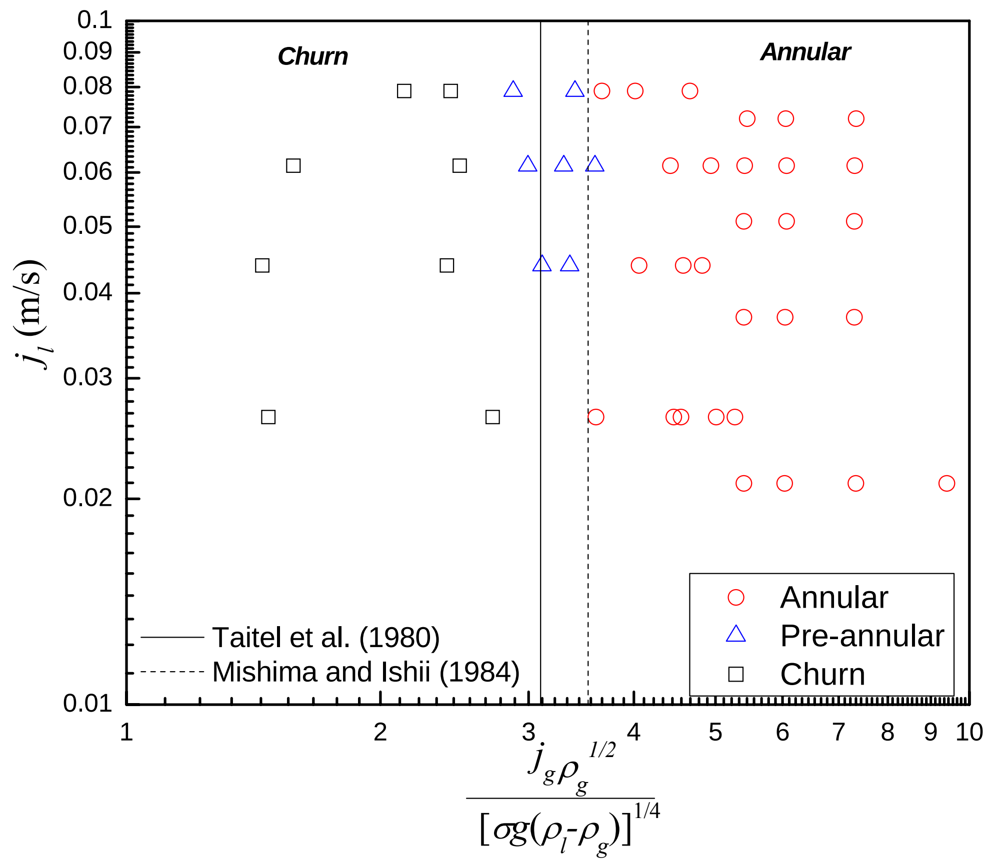

Figure 3-3:Present data plotted on Taitel et al. [69] **and Mishima and Ishii** [70] **flow pattern maps**

The Hewitt and Roberts flow pattern map is totally experimental in nature. As against this, flow pattern transition criteria have been developed based on transition mechanism. Examples of such flow pattern maps are those by Taitel et al. [69] and Mishima and Ishii [70]. It is informative to gauge these flow pattern maps against the present data. This is done in Figure 3-3. The churn-annular transition relevant to the present work is exclusively shown in the flow pattern map (Figure 3-3).

It is seen that the transition criteria given by Taitel et al. [69] and Mishima and Ishii [70] are able to identify the observed transition nicely. It must be mentioned however that towards the right of dotted line Mishima and Ishii [70] predict annular flow with entrainment. The present annular flow data (red circles) are seen to lie on the right of this dotted line. But entrainment was not observed (described in detail in §3.5) in all the cases. Taitel et al. [69] criterion does not make any such distinction between annular flow with and without entrainment.

In these flow pattern maps also, the pre-annular flow is seen to delineate churn and annular flow regimes.

3.2 Experimental facility

The core of the facility is a vertical test section formed from a 2.5 m long acrylic tube, of 11 mm internal diameter (Figure 3-4). Chosen flow rates of air and water are introduced into the base of this test section. The air and water are metered through orifice meter, R1 and rotameter R2 respectively to flow in the mixing chamber (Figure 3-5).

Water enters into the outer annulus of the mixing chamber and seeps in from sides of the inner pipe (having the same diameter as the test section) through perforations of 1.5 mm diameter. The perforated inner pipe was 30 mm long. The air flowing in the inner pipe carries the water along with it in the form of film at the periphery and some entrained droplets (not always!). A continuous water film was observed at the end of the mixing chamber. Due to stagnant tap water in the mixing chamber, brown colored scaling is observed in Figure 3-5

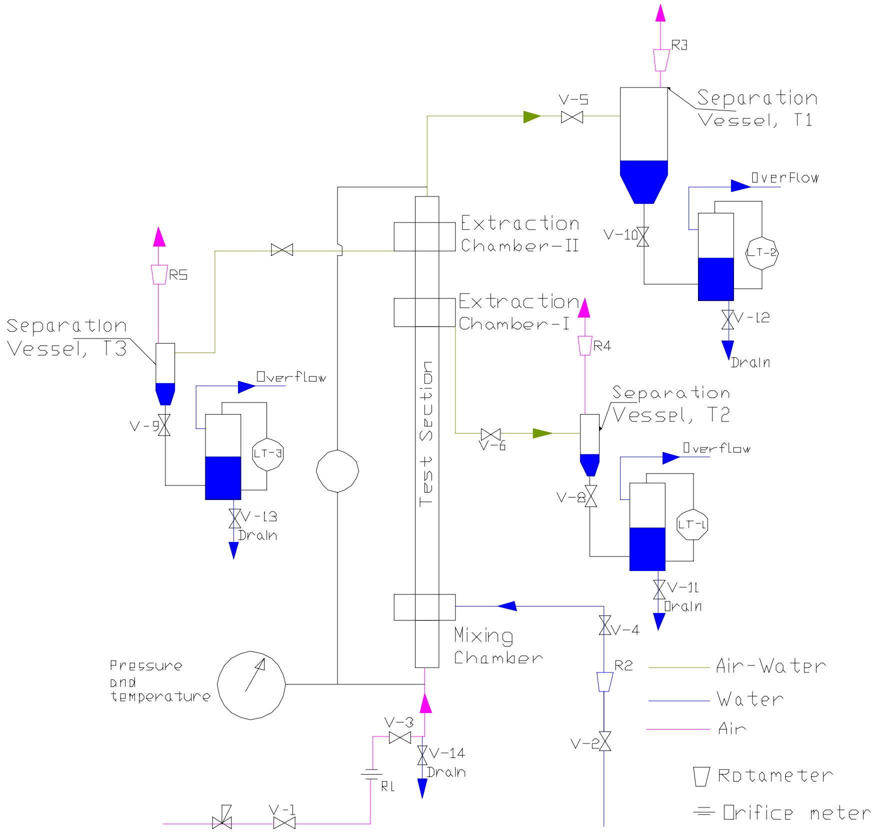

Figure 3-4: Schematic of the experimental facility

At the end of test section, film thickness is measured using circumferential conductance probes. A short distance (30 mm) downstream of these measurements, the film is extracted across a porous device housed in the extraction chamber-I by operating valve V-6. The pressure differential needed to extract the film can be enhanced by manipulating valve V-5. The extracted air-water mixture is passed to a separation vessel (typically a vortex chamber kind of arrangement), T2. Here the extracted air and water are separated and individual rates of extraction determined. Another extraction chamber and associated separation vessel (T3) is present 200 mm downstream of the first chamber. A photograph of the extraction chambers along with the location of conductance probes and separation vessels is shown in Figure 3-6. The extraction chamber assembly housing the porous device and consisting of the conductance probe is shown in Figure 3-7.

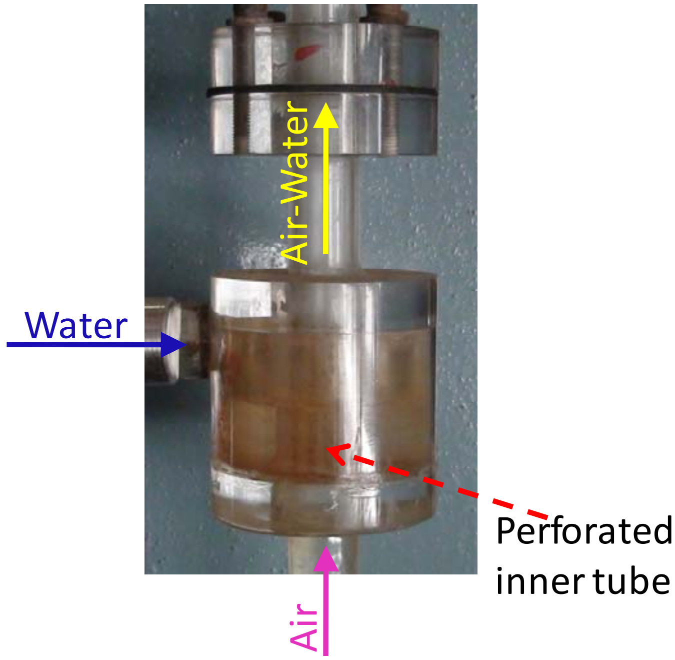

Figure 3-5: Mixing chamber showing entry points for air and water

The portion of the flow (air + droplets) which is not extracted continues to flow to the separation vessel T1. In T1, the air and water are separated. The air flows through the rotameter, R3 and the water is metered in a collection vessel.

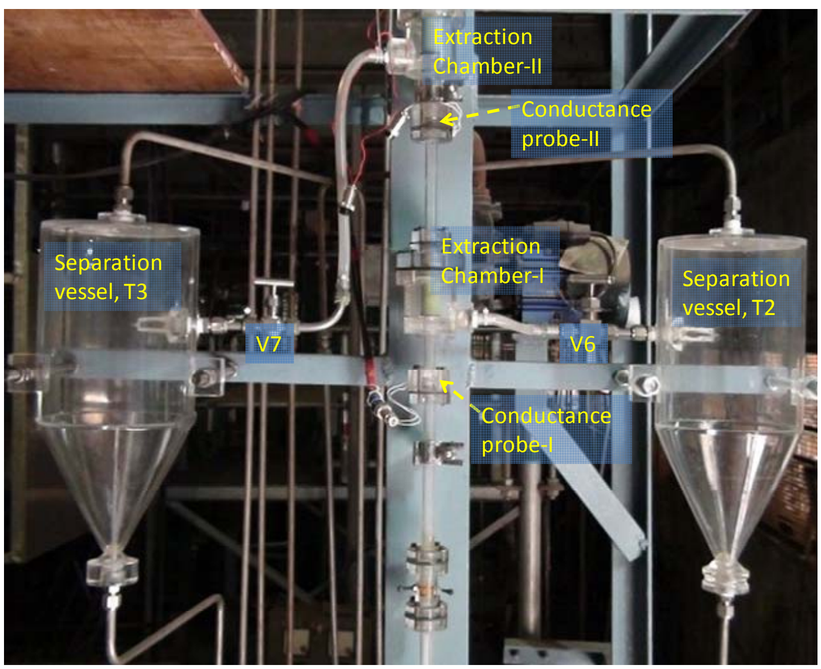

Figure 3-6: Arrangement of extraction chambers and separation vessels

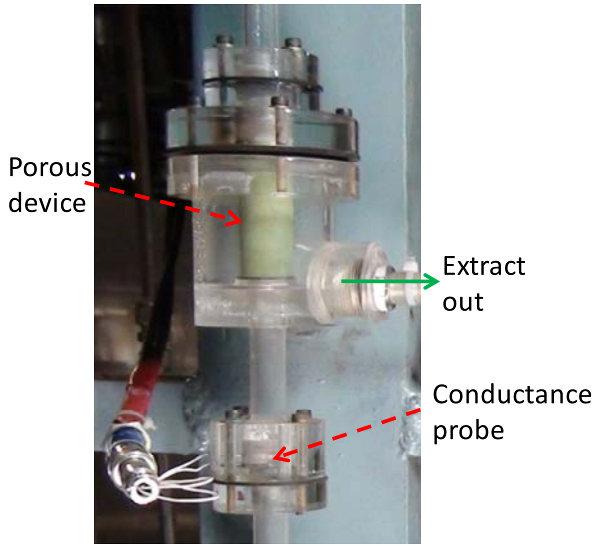

Figure 3-7: Extraction chamber along with circumferential conductance probe

3.2.1 Instruments, techniques and measurements

The inlet water and air flow rates are measured using a calibrated variable area flow meter (0.1 to 1 LPM) and orifice meter (60-300 LPM) respectively. Measurement of pressure and temperature are available in the inlet air line. Each separation vessel has a variable area flow meter (1-10 LPM) connected to it for measurement of extraction flow rate. The extracted water flow rate is measured by computing the rate of level rise in graduated cylindrical collection vessels.

Apart from these conventional instruments, certain advanced instruments have been used. These and other techniques used for measurement (or deduction) of desired quantities are described in the following.

3.2.1.1 Photographic image capture for obtaining wave details

In this work, high speed photography is used to observe and determine the characteristics of disturbance waves. Being a transparent acrylic facility, photography can be performed at any location. Wolf et al. [128] have found that a length of ~100 diameters is sufficient for the development of disturbance waves. In the present setup, photography has been done approximately 2m (182 diameters) downstream of the mixing chamber.

A Motion Blitz camera (resolution 1 Mega pixel, adjustable x-y distribution, with a frame rate of 1000 frames per second) was used to photograph the flow in the tube. Lighting was arranged to be from behind a white screen; see Figure 3-8. This provided diffuse illumination, ensuring no reflections, and allowing us to gain clear images of the structures in annular flow.

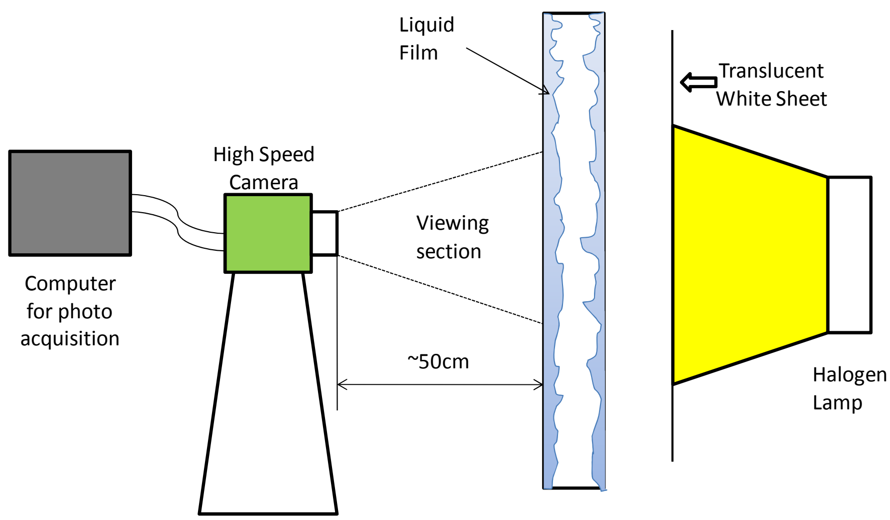

Figure 3-8: Photographic arrangement

3.2.1.2 Image processing for evaluation of wave characteristics

The natural technique to determine the wave velocity is to manually follow a wave in a high speed sequence of photographs, and measure the distance travelled in a particular time. This technique is however cumbersome for large numbers of waves, and is difficult to repeat and check. It is much easier to find wave velocities if wave streaks are available on a distance versus time plot.

Distance versus time (d-t) plots were generated by Hall Taylor et. al. [115], by arduously tracking each and every disturbance wave from cine films.

Following Alekseenko et al. [130], in this work d-t plots were generated by processing of obtained images. In essence the technique involves extracting a single pixel-wide portion of an image, giving a view of the entire tube length photographed, but of only 1 pixel's width of the tube perimeter. The image from the same pixels in the subsequent photograph, (here) 1ms later, is then extracted, and placed "to the right" of the first strip, and so on and on. This generates a composite image. This is as "tall" as the length of tube surveyed, and is one pixel wide for (here) each millisecond of the period captured in the image. Any feature of the flow (for example, a wave crest) moving up the tube, thus appears as a sloping line moving from lower left to upper right in this composite image.

Examples of such images are shown in Figure 3-9. The more chaotic the flow, the darker it appears. Many interesting observations can be made from these plots: first of them being the ability to distinguish flooding waves and disturbance waves from ripples and secondly, the ability to quantitatively classify churn and annular flow from the motion of ripples. While in annular flow, ripples are always seen to move upwards, in churn flow intermittently falling film leads to downward motion of ripples also. A distinct flow regime having momentarily stagnant ripples was also observed in the experiments. This regime is referred to as pre-annular in this work. That this regime demarcates churn and annular flow is also seen in Figure 3-2 where the pre-annular region is sandwiched by the churn and annular flow regimes. Other interesting observations are the ones like coalescence of waves; considering image in Figure 3-9 (b), about a dozen disturbance waves enter the photographed region during the 1,000 ms covered by the composite image. Their speeds are similar, but an occasional faster one is seen to 'overtake' and coalesce with the one in front of it.

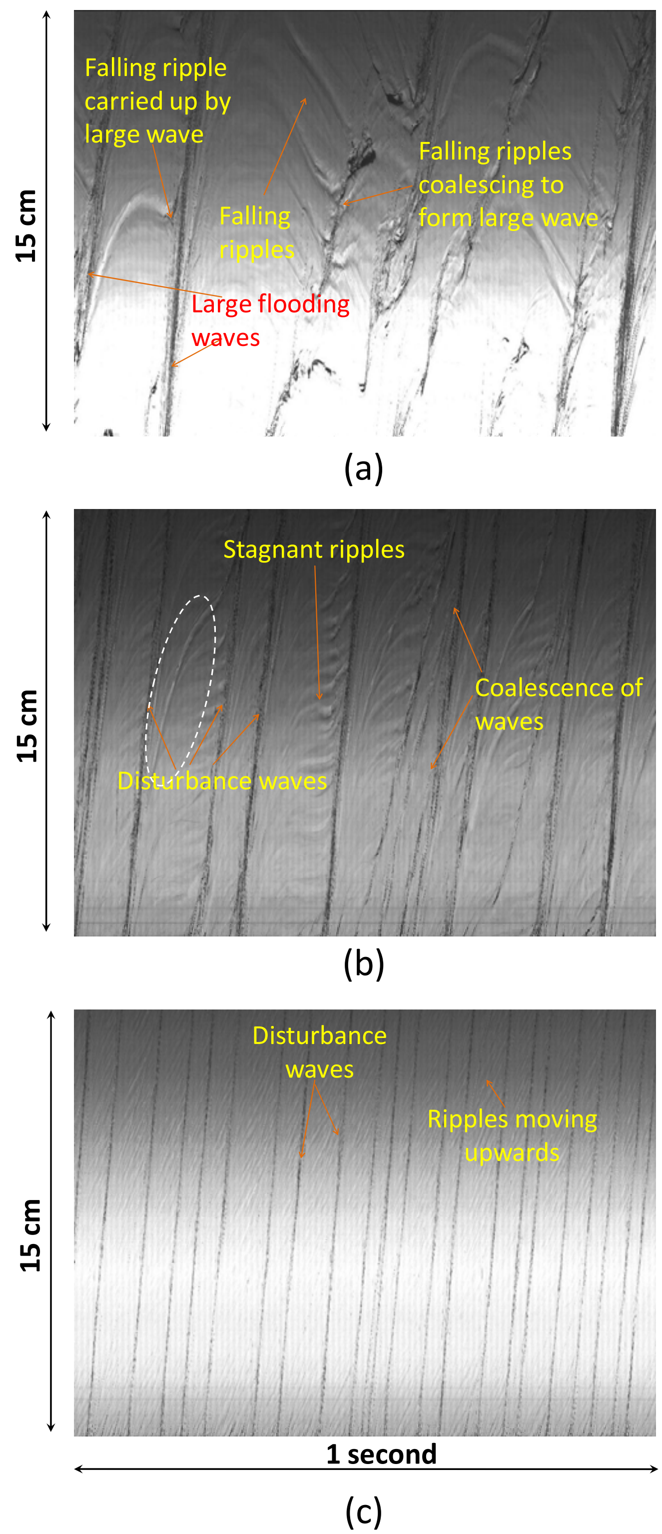

Figure 3-9: Distance versus Time (d-t) plots and demarcation of different flow regimes from the plots. (a) churn flow; j_g = 6.3 m/s Re_l = 542 **(b) Pre-annular flow;** j_g = 10.9 m/s Re_l = 976 **(c) Annular flow;** j_g = 22.9 m/s Re_l = 629

Smaller, less chaotic ripples are also visible in these photographs. In Figure 3-9(a), for example, we see a ripple left behind by 'wave 1', slowing down and eventually beginning to fall back, only to be engulfed by 'wave 2'. Such qualitative characteristics of the flow which can be deduced from the d-t plots are described in greater detail in §3.3.

Distance-time plots present a straightforward way to obtain the *wave velocity*, v_w essentially by extracting the gradient of the line associated with the wave.

The time period, T, between successive waves was obtained from the d-t plots by measuring the distance between intersections of the wave streaks and a horizontal line on the plot. It may be seen from Figure 3-9 that there is a variation in the period between waves. The maximum, minimum and average period was recorded by observing at least ten waves for each result reported. Given then the velocities of the waves, and their period, the distance between successive waves, λ, was calculated. (Note that in the literature, and here, the term 'wavelength' is invariably used for this. In this usage it refers simply to the distance between waves).

It may be seen from the d-t plot for churn flow (Figure 3-9a) that the wave streaks are not as well ordered as in annular and pre-annular flows. Some flooding waves apparently do not carry all the way along the channel. This is better visualized in raw image sequences.

Two sequences, A and B are shown in Figure 3-10. The former shows the coalescence of flooding waves and the latter shows disappearance of a flooding wave. The photos in a sequence are spaced apart by 10 ms unless indicated. In sequence A, necking is observed due to a large, circumferentially asymmetric ripple (lower end of the pictures) which is moving downwards. In the 4th picture of sequence A, flooded conditions lead to bag break-up type entrainment. The impetus due to this causes the flooding wave to move upwards albeit with a much reduced amplitude (5th photograph in sequence A). Meanwhile another downstream ripple seems to be nearly stationary. 30 ms later, a large flooding wave comes and sweeps away both these smaller flooding disturbances.

Sequence B shows a contrasting scenario, a different large flooding wave comes from below; but is seen to lose its integrity after some distance and finally disappear.

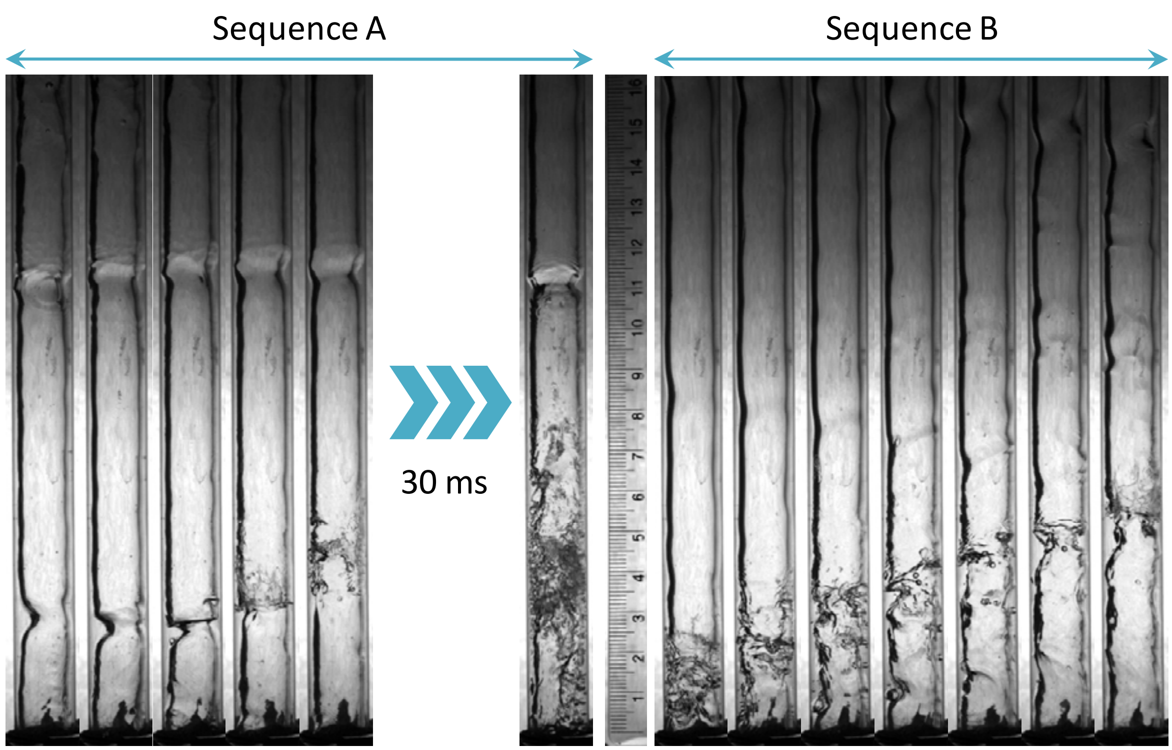

Figure 3-10: Two sequences showing short lived large waves in churn flow; j_g = 6.3 m/s Re_l = 542

In the present work, the characteristics of only sustained large waves are observed. These waves are distinguishable by the bold dark lines in d-t plot which sustain whole distance along the frame. As against this, the previous experiments [123–125] concentrate over a smaller axial length and do not distinguish between sustained and short lived waves (like those in sequence A and B). This might lead to previous studies interpreting more frequent flooding waves for a given gas and liquid flow. Though short lived waves qualify to be called flooding waves, it is expected that the sustained waves would be more important in ensuring upflow of liquid than the short lived ones. Thus, the present large wave identification and characterization seems more relevant than previous works.

3.2.1.3 Film extraction technique for measurement of film flow rate

The film flow rate is measured using the film extraction technique. The process of film extraction relies on the porous device contained in the extraction chamber. The porous device has an inside diameter which matches with that of the test section. When the extraction valve (V6 or V7) is opened, the air-water mixture flows out into the separation vessel. The flow rate of this mixture depends on:

1. Air and water flow rates,
2. Pressure differential between test section and separation vessel,
3. Porous sinter characteristics (porosity and pore size), and
4. Extraction valve opening.

Increasing the opening of V6 leads to extraction of air-water mixture at a greater rate. The flow rate of extracted liquid (also referred to as Liquid Take-off, LTO) is determined by passing it into a graduated collection tank while maintaining a constant level in the separation vessel (using valve V-8, see Figure 3-4). LTO is ascertained by the rate of level rise in the collection tank. Each separation vessel has connected to it a separate collection tank.

The rate at which air is extracted (Gas Take-off, GTO) is determined through rotameter mounted on separation vessel.

For obtaining the value of film flow rate, an extraction curve is plotted between LTO and GTO with each point on the curve corresponding to a specific valve opening. The inference of the film flow rate is explained through a typical schematic in Figure 3-11.

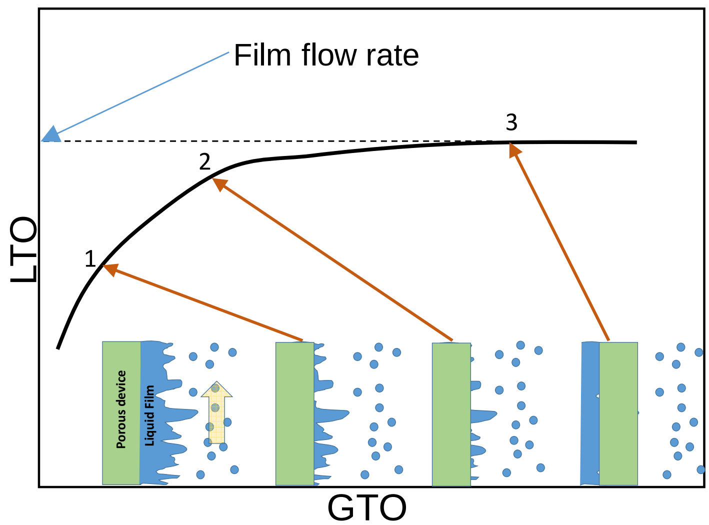

Figure 3-11: Typical extraction curve [131]

Due to the wavy nature of the film, some air invariably gets sucked out across the porous device (point 1). With increase in valve opening, a major portion of the film gets sucked out (point 2). However, the incremental increase in LTO with GTO reduces as the amount of film remaining to be extracted reduces. At point 3, when LTO becomes equal to film flow rate, further increase in GTO will not lead to increase in LTO as there is no liquid left on the walls. Although there are still droplets left in the core, they are moving at a much faster velocity and sucking them out is not easy due to large flow resistance offered by the porous device, which in this case was a sintered NiO_2-YSZ sleeve.

If, on the other hand, instead of a porous device, perforated tube is used which offers smaller resistance, droplets may also be extracted. This leads to the type of extraction curve shown in Figure 3-12. Such curves have been obtained by Wurtz [23] who used perforated tube instead of porous sinters. Due to the greater difficulty in extracting droplets (due to their higher axial velocity), this region of the curve has a lower slope. It is surprising then that Singh et al. [132] had obtained curves similar to Figure 3-12 even though sinters had been used.

In the present experiments, curves of type of Figure 3-12 were obtained initially while using sinters. However visualization of the extraction process (enabled due to the transparent extraction chamber) led to the finding that in those cases, extraction was taking place mostly through either top or bottom of the sinter where it butts against the chamber. When the sealing at the ends of the sinter was properly ensured, extraction curve of the type of Figure 3-11 were consistently obtained.

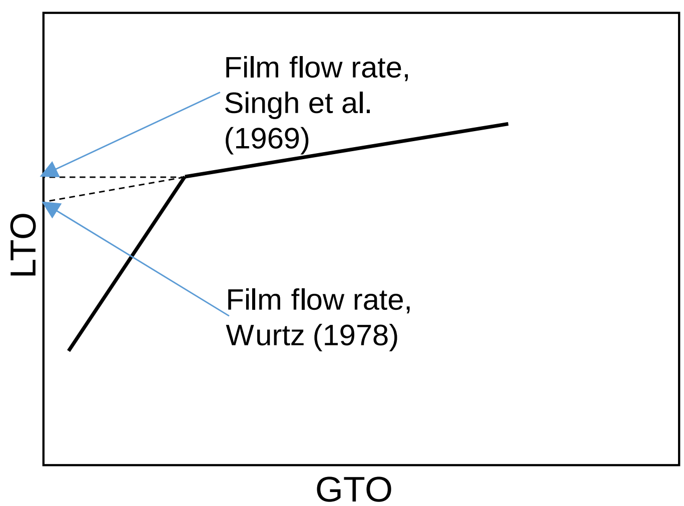

Figure 3-12: Alternate extraction curve observed in literature [23,132]

In the present experiments LTO and GTO refer to the volumetric flow rates of extracted water and air respectively. The maximum gas extraction never exceeded 15% of the mainstream gas flow.

Apart from the extraction curve, the complete removal of the film could also be ascertained in the transparent length between the two extraction chambers. This transparent section can be seen in Figure 3-6.

3.2.1.4 Circumferential conductance probe for measurement of film thickness

Conductance probes have been widely used [100,118,119,133] for measurement of film thickness in annular flow. In this work a circumferential conductance probe developed at BARC (Rajalakshmi et al. [134]) has been used. A similar probe was used by Chandraker et al. [100]. The sensor works on the principle of difference in conductivity between the liquid phase (higher conductivity) and gaseous phase (lower conductivity). Tap water has been used in the experiments as de-mineralized water is not conducting enough for the probe to respond. The variations which might exist in conductivity of tap water were compensated by normalizing the sensor output with full water output to obtain only the relative change in conductance value. The normalization was carried out before and after every experiment.

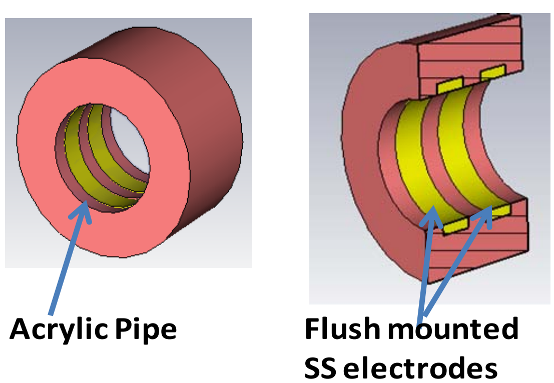

Figure 3-13: Schematic of circumferential conductance probe used in the experiments

The probe consists of two ring type stainless steel electrodes flush mounted on the inner surface of the acrylic pipe. The sensor is excited with a 10 μA, 1 kHz current source, voltage output of which varies with film thickness. The sensor was calibrated up to 2mm, but sensitivity was observed to diminish for film thickness in excess of ~0.25 mm. This works fine for films in annular flow as they are often much thinner. The sensor was connected to a data acquisition system with a sampling frequency of 5 Hz.

3.3 Experimental results on waves in churn and annular flow regimes

Since visual measurements of waves have been carried out, it is possible to give both qualitative and quantitative descriptions of wave motion. The qualitative descriptions (§3.3.1) are given first followed by quantification of wave characteristics (§3.3.2). The experimental results for the different cases are tabulated in Appendix-1.

3.3.1 General observations on waves in different flow regimes

A typical set of 'raw' images is shown in Figure 3-14. The wave structures in churn and annular flow were seen to be very different from each other. In churn flow the film is thicker, waves are larger and so is the axial expanse of the disturbed region. The disturbed region is characterized by large upwards moving waves and entrainment in the core. This is to be expected due to the intermittent counter-current motion of the liquid film and the air. This counter-current motion coincides with the wave generation and entrainment from these waves. In annular flow the disturbed region occupies a much smaller length (Figure 3-14) and there is co-current motion of air and water. The entrainment is also thus much less than in churn flow. Based on visual observations, the extent (in terms of pipe diameters) of the disturbance region has been plotted as a function of gas momentum flux in Figure 3-15. The axial expanse of a disturbance region is defined to be from the location where increased entrainment or greater disturbance is seen on the liquid film to the point after which no such disturbances are visible. Since such a definition of axial expanse is subjective, especially in churn flow where as seen in Figure 3-10 the extent of disturbed region varies as the flooding wave moves along. Thus the inferred axial expanse is averaged over at least 10 waves for each values plotted in Figure 3-15. For each wave in the churn flow regime, the maximum disturbed length observed was taken to be the disturbance length.

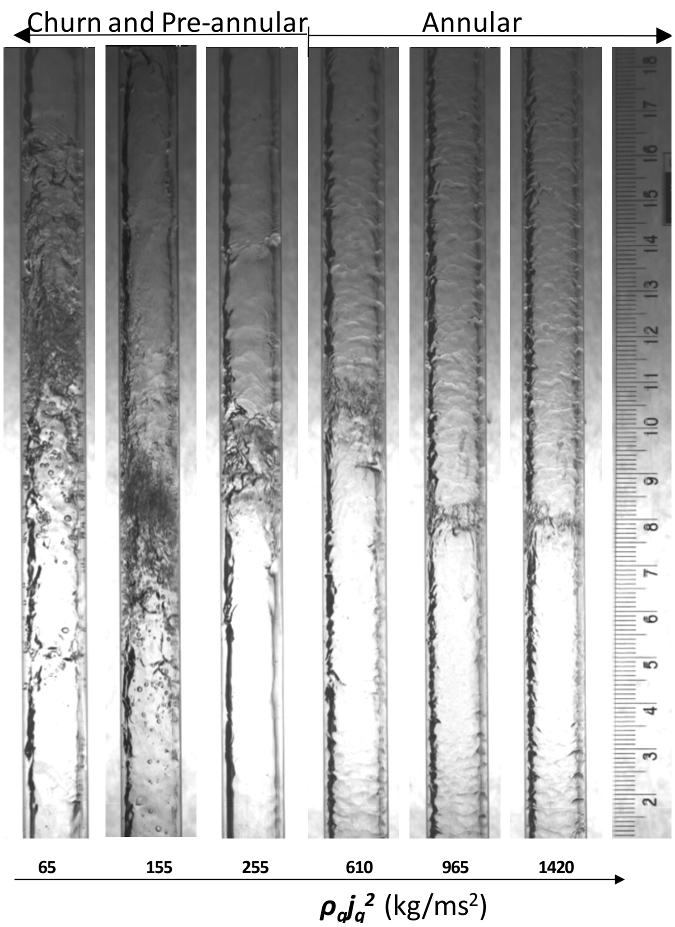

Figure 3-14: Churn to annular flow regime transition as seen in terms of axial expanse of the disturbed region. Successive pictures show the increasing gas momentum flux

The quantification of the length of the disturbed region might be important in quantifying the effect of churn flow on Initial Entrainment Fraction (IEF) (as described in greater detail in §4.1.2). In fact there have recently been some other attempts [73,74] to make semi-quantitative models involving this churn flow region (which is obtained upstream of annular flow in heated tubes). This has been motivated by the fact that having at least an approximate 'non-arbitrary' means to predict the IEF is a desirable improvement to the phenomenological modelling of annular flow dryout. In turn, these efforts stand to gain from improved observational data in this region, which is the motivation for our attempts here in this regard.

The utility of distance-time plots in quantifying the existence of the different flow regimes – churn, annular and pre-annular has been mentioned in §3.2.1.2. There are other inferences which can be drawn from these processed images in conjunction with the raw images and videos. The waves in churn and annular flow are distinctly different from each other.

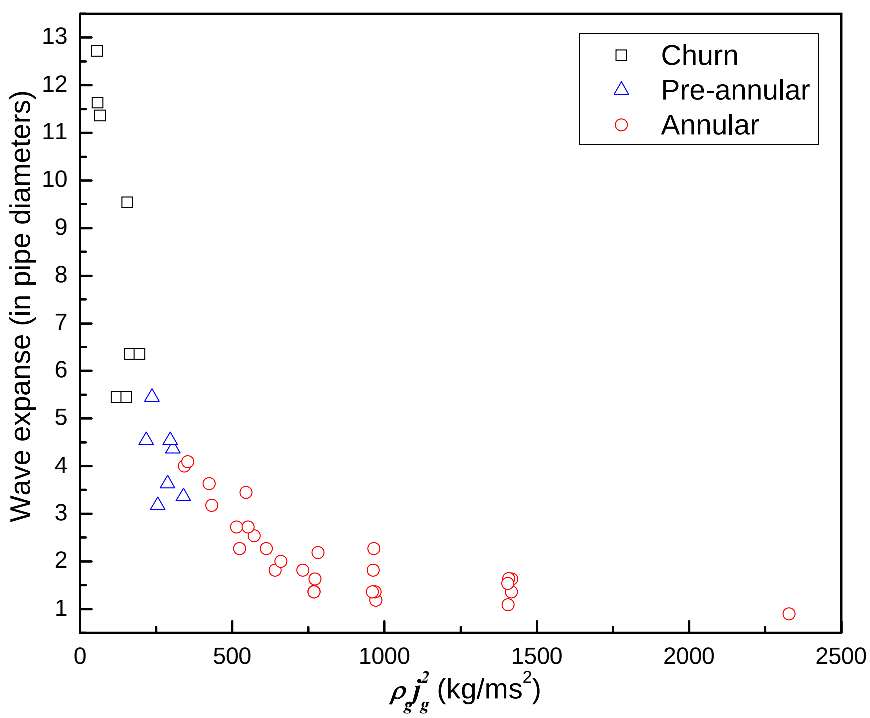

Figure 3-15: Quantification of disturbance length in terms of pipe diameter

Churn flow: In this regime the liquid film tends to fall intermittently (as is seen in Figure 3-9(a)) under the action of gravity. The downward motion of the film is decelerated when ripples are formed on the film, and these ripples are acted upon by the high speed upflow of gas. As more ripples are generated, they coalesce, forming an increasing constriction to the gas flow, till the time at which the local gas velocity at the constriction is sufficiently high to carry the falling film upwards. This gives rise to a flooding wave. At certain times the flooding waves are distinct and are carried all along the tube length. At other times, flooding waves form by ripple coalescence but do not persist all along the length. Such is evident from the case where coalescing falling ripples are shown in Figure 3-9(a). Large (flooding) waves in churn flow are lesser in number than in pre-annular or annular flows. In this regime, it is the flooding waves which lead to a net upwards movement of liquid.

Annular flow: In this regime, both large-amplitude 'disturbance' waves and smaller 'ripples' are observed. As evidenced by the steeper slope on the d-t plot (Figure 3-9c), the disturbance waves move faster than the ripples. It seems these waves provide much of the impetus for the film to move upwards, generally being observed to move faster than both the 'film itself' and the smaller ripples.

The relation between disturbance waves and ripples has been studied by Alekseenko et al. [135]. They have presented the following picture of the interaction of disturbance waves and ripples – The arrival of a disturbance wave accelerates the ripples downstream. These downstream ripples then disappear into the disturbance wave. New ripples are generated on the back slopes of the disturbance wave. These newly formed ripples initially have a velocity close to the disturbance wave but they slow down (while still having upwards motion) only to be accelerated and annihilated again by a subsequent disturbance wave.

The disturbance waves pass 'through', and accelerate the ripples. The ripples then slow down (but still have upwards motion) only to be accelerated again by a subsequent disturbance wave.

The origin of disturbance waves itself is a subject of active research. Zhao et al. [133] have stressed upon the circumferential coherence as one of the important characteristics of disturbance waves. They have observed development of such coherence over a length of 25-50 diameters. Relatively recently, Alekseenko et al. [136] have concluded from spacio-temporal analysis of the wave streaks in downward annular flow that disturbance waves result from coalescence of ripples very near to the inlet (or beginning of annular flow) region. This is unlike churn flow regime where large waves keep getting generated by the coalescing of falling ripples far away from entry region.

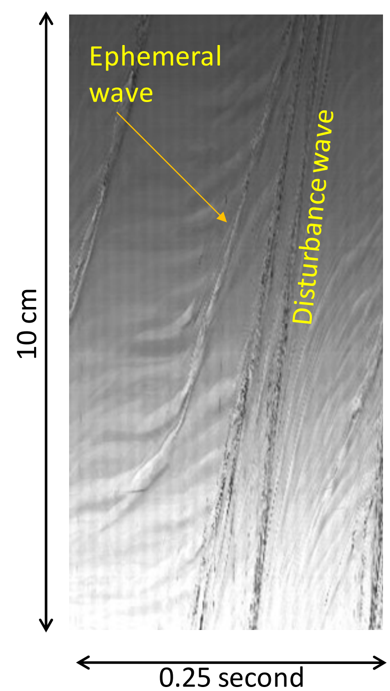

Figure 3-16: Formation of ephemeral wave as seen on x-t plot corresponding to pre-annular flow regime (Re$_l$ = 759, j_g = 11.8 m/s)

Pre-annular flow: In this work it has been possible to identify and characterize a distinct intermediate region between the churn and annular flow regimes. In this regime momentarily stagnant ripples are observed (Figure 3-9b). This regime is here classified as *pre-annular* flow. It is also seen upon plotting on the flow pattern maps (Figure 3-2 and

Figure 3-3) that this flow regime lies at the interface of churn and annular flow regimes. The behavior of large waves and ripples in this regime is also intermediate between the two regimes. For instance, like churn flow, an occasional large wave (which is smaller than the usual disturbance waves) is seen to form, evidently by coalescence of ripples (Figure 3-16). Such short lived low amplitude (can be inferred from the lighter streak in x-t plot, Figure 3-16) waves have been identified in literature as ephemeral waves [136–138]. The ephemeral wave is seen to be engulfed by the next disturbance wave coming from below. The existence of stationary ripples also indicates possible existence of flow reversal mechanism characteristic of churn flow. The usage of the term ‘disturbance wave’ (and not flooding wave) to describe the large waves in pre-annular flow follows from the fact that their parametric behavior is similar to disturbance waves in annular flow (as seen in next section).

Wolf et al. [128] had seen that in annular flows, fully developed wave structures are formed after about 100 diameters; wave coalescence was not observed beyond this length. In pre-annular regime, as in present case, coalescence is observed (Figure 3-9b) even after 180 diameters downstream of inlet. It is further seen that ripples are generated not only on back slopes of disturbance waves but also on back slopes of relatively faster ripples. One such example is shown encircled in Figure 3-9(b).

In view of the foregoing, it may be said that pre-annular regime identifies operating parameters in which short lived ephemeral waves are encountered along the length of the channel. Also, the wave structure is not fully developed and disturbance wave coalescence takes place at long distances from the entry.

Though pre-annular regime does not have any special significance in that it cannot be considered as a separate flow pattern and definitely is a subset of annular flow, it is expected that further study of waves in this regime would lead to better understanding of the churn-to-annular transition and whether and what exactly differentiates disturbance waves from flooding waves.

Since pre-annular regime is observed at the juncture of churn and annular flows, it will be encountered only in upwards co-current gas-liquid flow. Thus this regime is possibly of no consequence in the other flow orientations.

A general observation from Figure 3-9 is the increase in the spatio-temporal uniformity of the ripples as we proceed from churn to annular flow regime. Alekseenko et al. [130] have found that the spatial frequency of ripple generation by disturbance waves in annular flow is effectively independent of gas or liquid flow rates. It may thus be inferred that a disturbance wave releases as many slow ripples as it engulfs. This, combined with our earlier inference on the absence of ripples immediately downstream of the short lived flooding wave as the reason for their short life leads us to hypothesize that the presence of ripples is necessary for sustained large wave motion. A possible picture of fully developed wave structures in annular flow is hence proposed where larger, faster disturbance waves move on a substrate of smaller, slower ripples. The disturbance wave propagates by progressively accumulating the downstream ripples and releasing ripples into its upstream from its back end. In the process it also accelerates the ripples.

3.3.2 Quantification of wave characteristics

The variation of wave velocity, frequency and wavelength computed as described in §3.2.1.2 have been plotted as a function of superficial gas velocity, j_g. Further, as has been suggested by Sawant et al. [119], the results are shown in terms of the modified Weber number, We_m.

$$We_m = \frac{\rho_g j_g^2 d_{eq}}{\sigma}\left(\frac{\rho_l - \rho_g}{\rho_g}\right)^{\frac{1}{3}} \tag{3.1}$$

And for each point the liquid Reynolds number, Re_l is also noted:

$$\mathrm{Re}_l = \frac{\rho_l j_l d_{eq}}{\mu_l} \tag{3.2}$$

3.3.2.1 Wave velocity

The wave velocities are shown in Figure 3-17(a) and (b) as a function of superficial gas velocity and in Figure 3-17(c) and (d) as functions of the modified Weber number, We_m. The results are presented separately for churn and pre-annular flow (indicated by hollow symbols), and annular flow. In the annular flow regime the wave velocity is seen to increase with increase in j_g and We_m. For a particular superficial gas velocity or Weber number, the velocity is seen to increase with increase in Re_l. This is in line with earlier reported experiments on annular flow. Similar dependence on Re_l is also observed in churn and pre-annular region.

In churn flow, however, the wave velocity reduces with an increase in gas velocity. This is in contradiction to the general perception of increasing wave velocity with gas flow. After all, it is the gas flow which drives the film and the waves on it. The following interpretation is suggested:

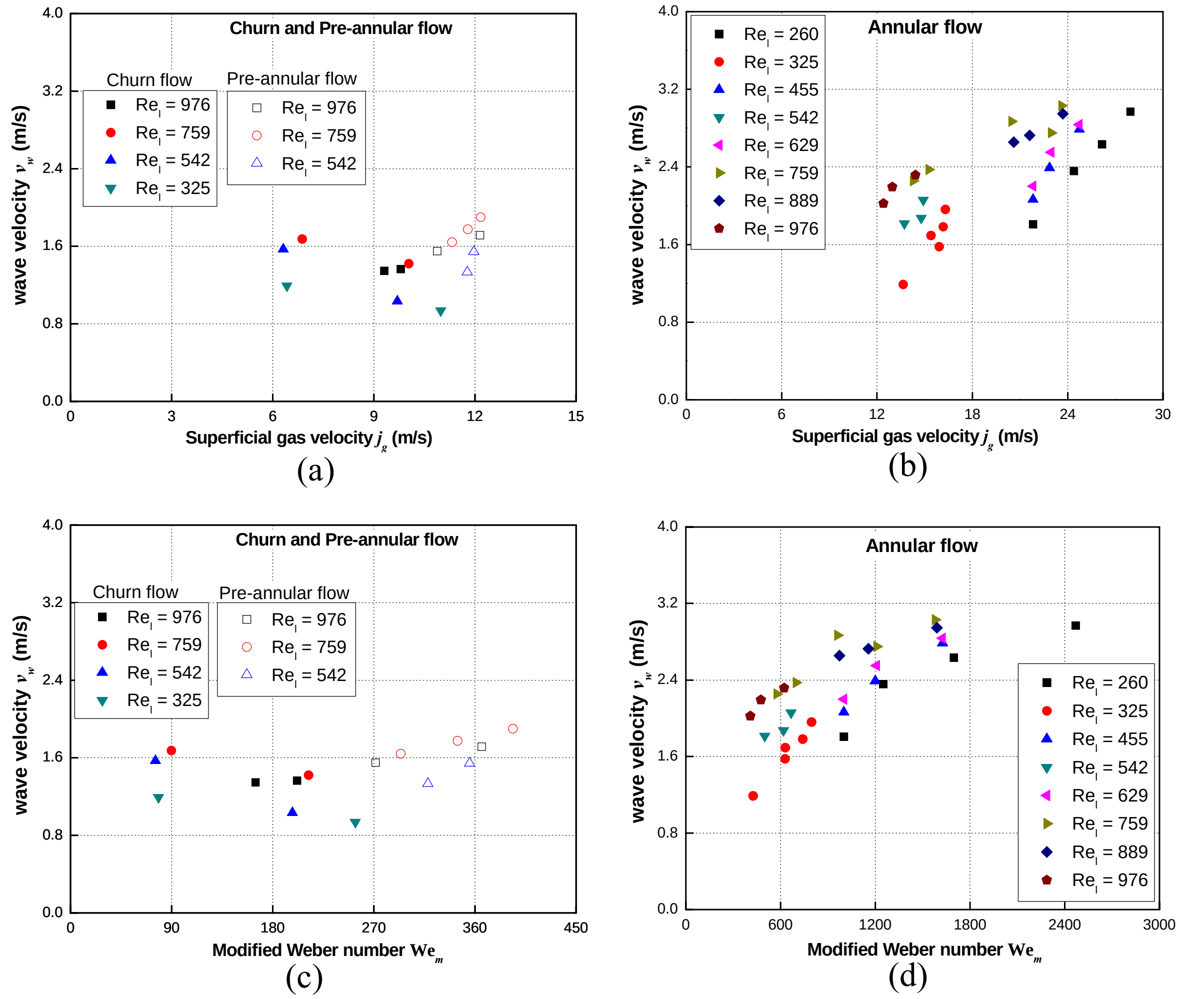

Figure 3-17: Measured wave velocity versus superficial gas velocity for (a) churn, pre-annular and (b) annular flows, and versus Weber number for (c) the churn and pre-annular and (d) the annular regimes. The liquid Reynolds number for each set is indicated

In churn flow, the mechanism for upwards flow of liquid is flooding waves generated by coalescence of falling ripples. When ripples coalesce, there is initially a series of closely spaced constrictions (see for example Figure 3-1, where a similar constriction is shown, albeit for annular flows), each corresponding to a falling ripple. Finally when these constrictions come close together, locally the gas velocity becomes large and the cluster of ripples is pushed up. At lower gas velocities greater numbers of ripples coalesce (as the force pushing upwards is lower). This leads to a greater constriction in flow area and a higher gas velocity at that location. The higher gas velocity would lead to greater wave velocity. Another complementary line of reasoning would be that for a given liquid flow rate (Re_l), mass balance has to ensure that the liquid throughput is maintained. If greater number of ripples coalesce (as is the case at low gas flow), the flooding wave, which maintains the positive up-flow, has to move at higher velocity.

3.3.2.2 Gas - wave relative velocities

The velocity of the gas relative to the wave is one of the quantities that, as indicated in the introductory note of this chapter, is expected to be important for simulations of droplet deposition phenomena. Specifically such data (along with information on wave shape) are useful while applying Lagangian mechanics to investigate the influence of disturbance waves on deposition. In literature, though Lagrangian studies have been undertaken, the presence of waves has not been acknowledged [34,45]. Measurements of this relative velocity are one of our major motivations.

The relative velocity, $\left(j_g - v_w\right)$ is plotted in Figure 3-18 for the different cases. In view of the fact that the film occupies only a very small cross sectional area (the measurements of film thickness in §3.6 indicate the average film thickness to be of the order of 0.1 mm while test section inside diameter is 11 mm), $\left(j_g - v_w\right)$ can be considered to be a good approximation of the velocity of gas relative to the wave.

The relative velocity increases with j_g in all the flow regimes. Though the wave velocity was seen to depend on Re_l, the relative velocity shows no observable dependence. This might be because relative velocity is much higher than wave velocity.

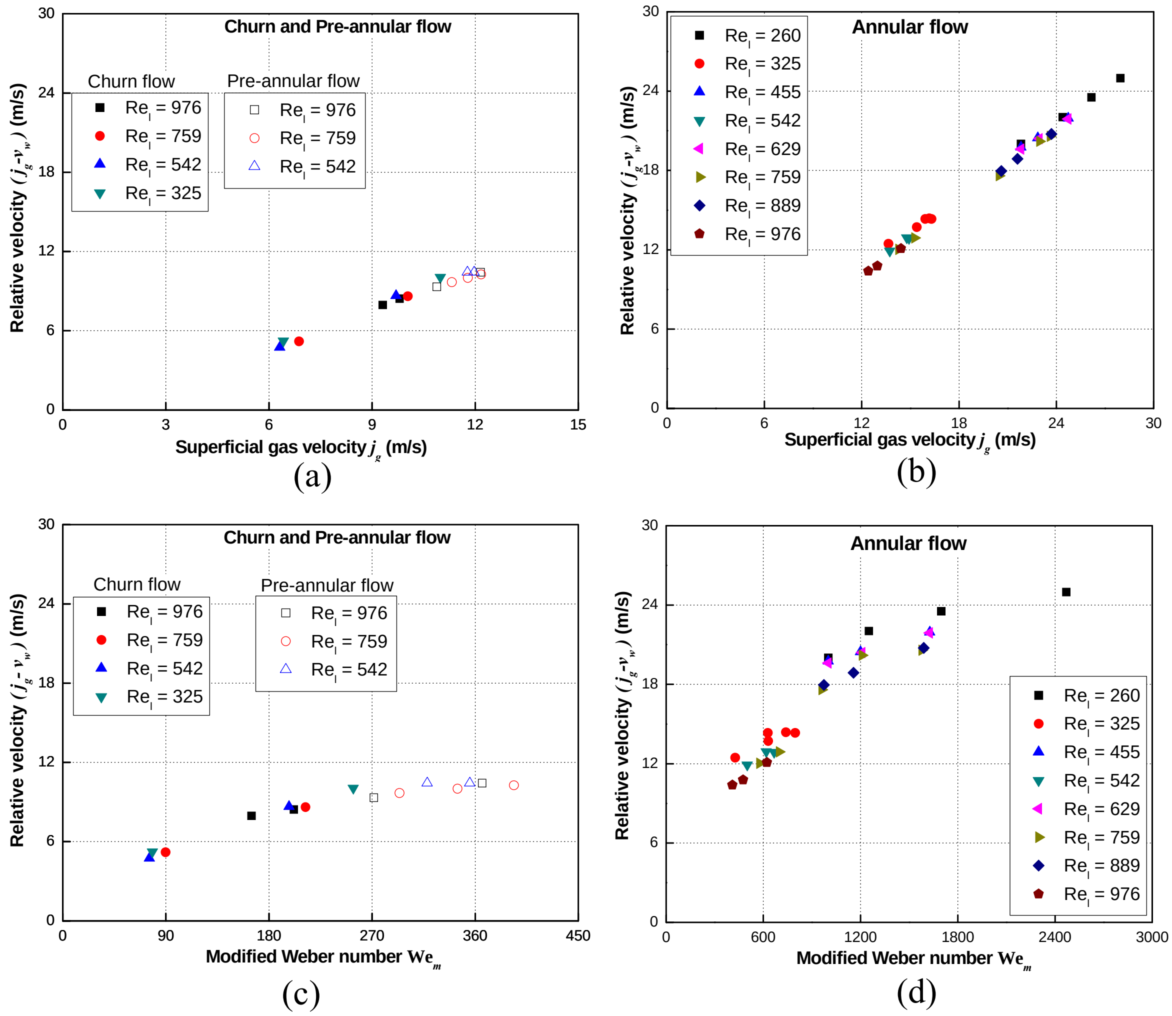

Figure 3-18: Measured relative velocity versus superficial gas velocity for (a) churn, pre-annular and (b) annular regions, and versus Weber number for (c) churn, pre-annular and (d) annular regions

3.3.2.3 Wave frequency

The wave frequency (inverse of time period between successive waves) obtained in the present experiments is plotted in Figure 3-19. As mentioned earlier (§3.2.1.2) and observable in distance-time plots (Figure 3-9), there is a band of frequencies. Further, the maximum and minimum frequencies are not distributed evenly about the average value. The bars shown in Figure 3-19 represent the natural variation in wave frequency (and not the errors in the measurement). In the present study the average frequency is seen to increase both with increase in gas flow rate (and Weber number) as well as liquid flow rate in the annular flow regime. This is in line with the observations of Han et al. [139] and Nedderman and Shearer [114].

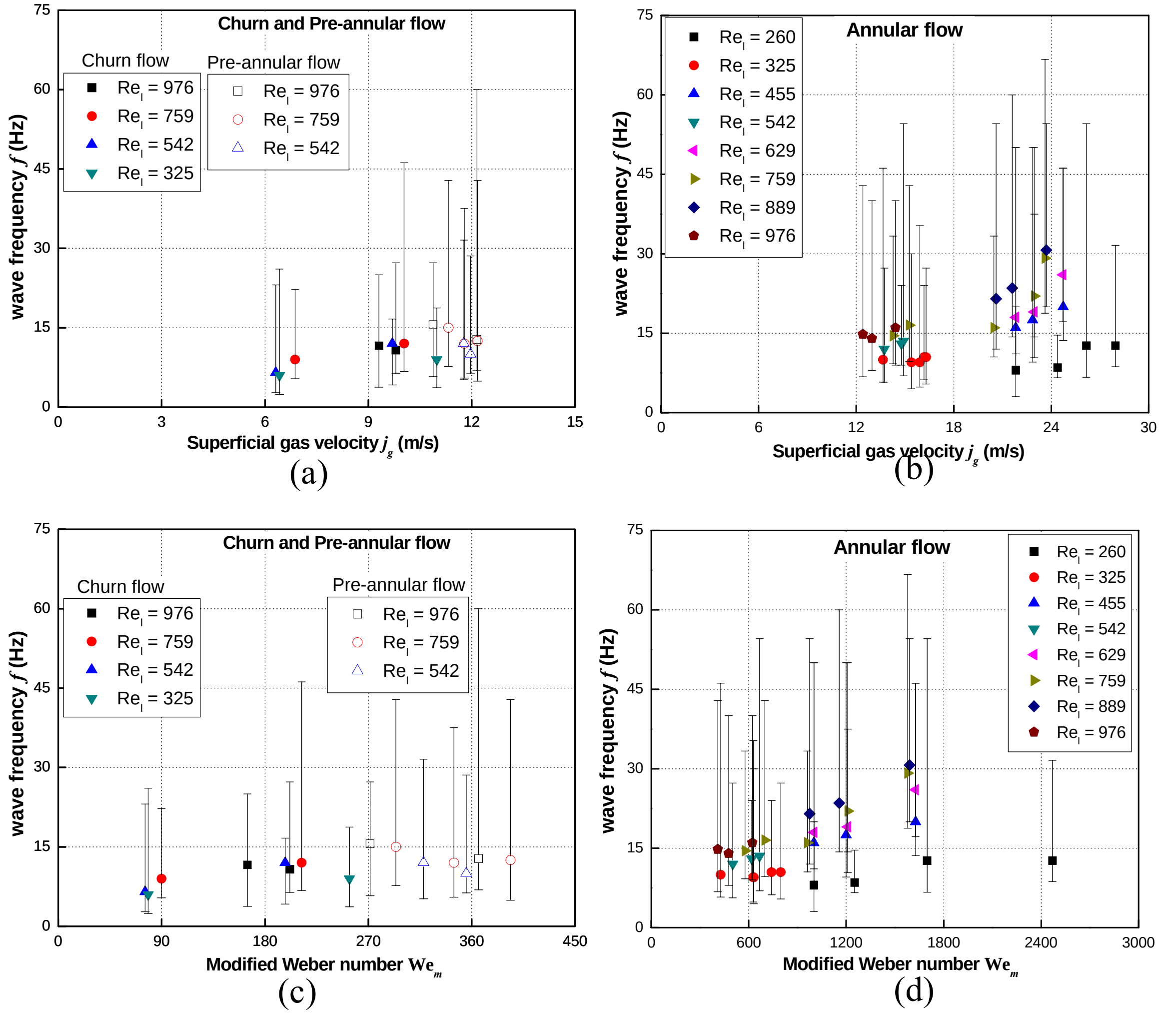

Figure 3-19: Measured wave frequency versus superficial gas velocity for (a) churn, pre-annular and (b) annular flows, and versus Weber number for (c) churn, pre-annular and (d) annular flows

However we have not observed, in annular flow, any limiting j_g below which average frequency is independent of j_g as was observed by Webb [140], Thwaites [117] and Chu [141]. The waves are generally less frequent in the churn and pre-annular flow regimes. In these regimes, the frequency is not seen to be a strong function of either gas flow rate or liquid flow rate. But some increase is seen with gas flow rate.

3.3.2.4 Wavelength

The wavelength in the present context refers to the average distance between two successive large waves. In the present study it is obtained by dividing the wave velocity by the average frequency. It can be observed from Figure 3-20 that average wavelength decreases with the increase in gas flow in churn flow. Thus the flooding waves become more closely spaced as gas flow increases.

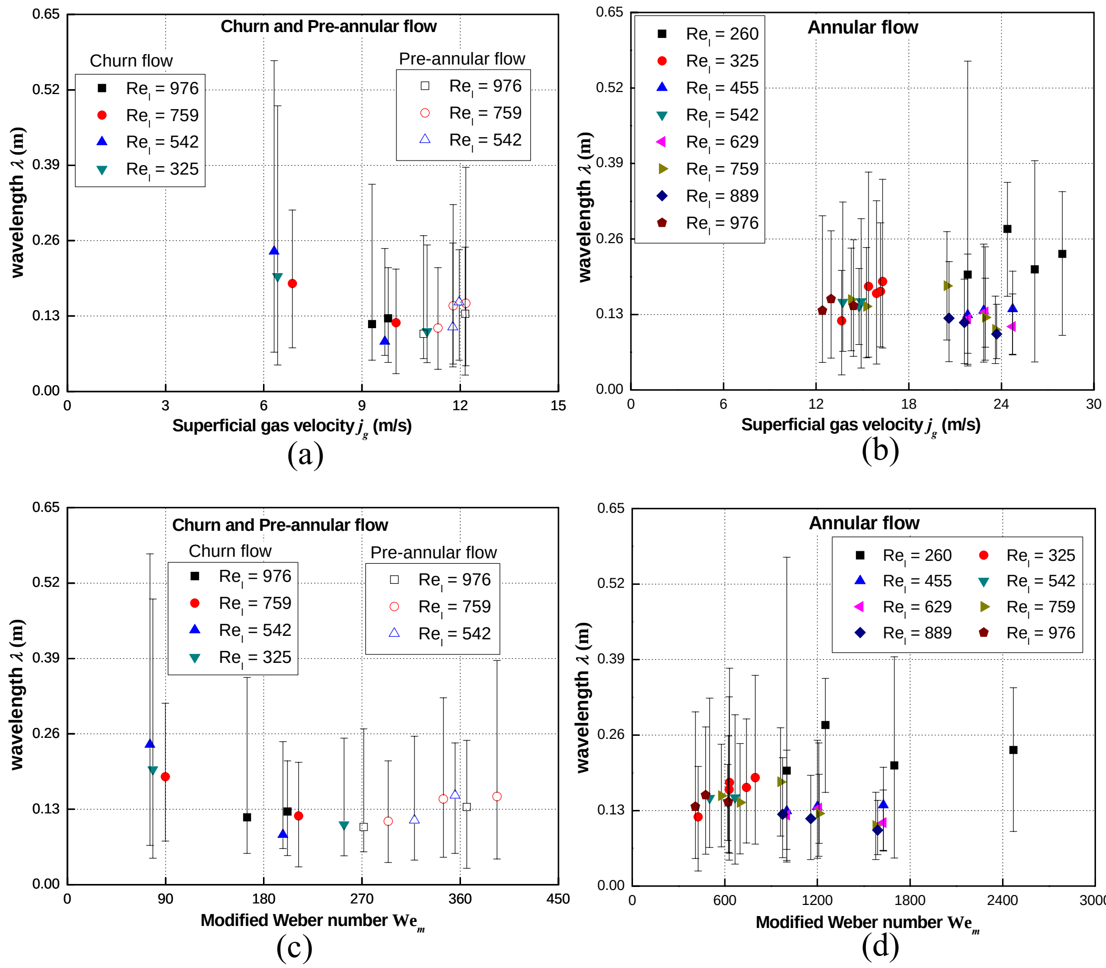

Figure 3-20: Measured wavelength versus superficial gas velocity for (a) churn, pre-annular and (b) annular flows, and versus Weber number for (c) churn, pre-annular and (d) annular flows

In annular flow, the variation of wavelength with gas flow for a given liquid flow is not so marked. However, there is a strong dependence on the liquid Reynolds number, Re_l particularly at lower Re_l. An interesting inference can be drawn from this observation by considering that for low entrainment in annular flow regime, as in present case (see §3.5), we may take the liberty of equating film and liquid Reynolds numbers i.e., $\mathrm{Re}_{lf} \approx \mathrm{Re}_l$. A variation of average wavelength with film Reynolds number is thus plotted in Figure 3-21. It is notable that for film Reynolds number values less than about 400 the distance between disturbance waves rises sharply.

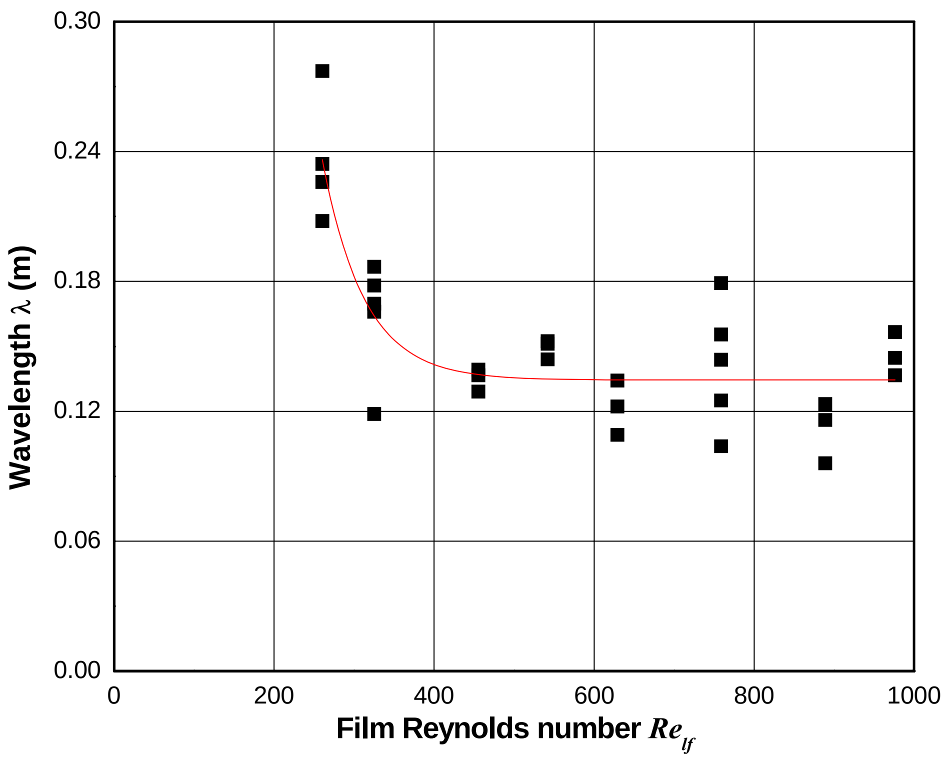

Figure 3-21: Measured wavelength as a function of film Reynolds number for the annular flow regime

A critical film Reynolds number, Re_{lfc} for the onset of entrainment was identified by Hewitt and Govan [4] and correlated as equation (2.25). It is interesting to note that the predicted value of Re_{lfc} (from eqn.(2.25)) for our conditions is about 415 - 450, which is also approximately the value of film Reynolds number below which the wavelength suddenly begins to increase rapidly. This value of critical film Re is also close to what has been observed in the film flow experiments (§3.5)

To investigate further the criterion for onset of entrainment, high-speed films for flows for different liquid flow rate and nearly same gas flow rate were studied, as illustrated in Figure 3-22. Since the present annular flow data were seen to lie in the low entrainment zone (maximum entrainment of ~6%), we cease to make a distinction between liquid and film Re, as for low entrainments, they are essentially equal.

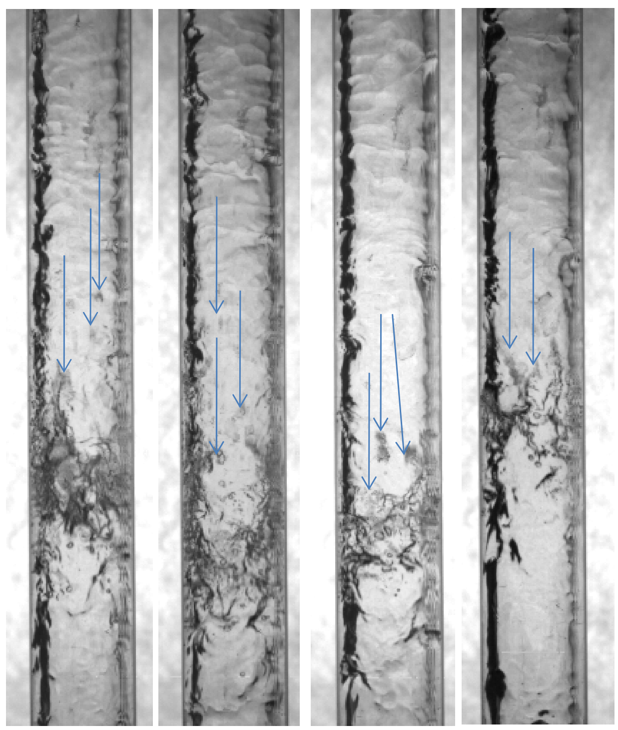

j_g (m/s)	14.4	14.2	14.8	15.4
$\mathrm{Re}_{lf} \approx \mathrm{Re}_l$	976	759	542	325
Re_{lfc}	418.72	422.18	422.18	426.18

Figure 3-22: Measured limiting criteria for the onset of entrainment (a few entrained drops are marked by arrows)

Some of the entrained drops are marked by arrows in Figure 3-22. In this figure, disturbance waves are observed for film Reynolds numbers below Re_{lfc} and entrainment is observed from the wave tips. This is in contrast to the reasoning behind the existence of a critical film Reynolds number given by Ishii and Grolmes [54], who suggest that it is the absence of disturbance waves below Re_{lfc} that would lead to cessation of entrainment (eqn.(2.30)). Their Re_{lfc} is however much lower than that given by equation (2.25). Hewitt and Govan [4], however, do not discuss the physical interpretation of Re_{lfc} as given by equation (2.25).

It is seen from Figure 3-22 that though entrainment is observed from the tip of the waves for $\mathrm{Re}_{lf} < \mathrm{Re}_{lfc}$ the entrainment does not survive downstream of the wave. Beyond Re_{lfc} however, the entrained drops can be seen in videos (and to a lesser extent in the stills in Figure 3-22) to survive a long distance downstream of the wave.

It is thus postulated that for sustained entrainment to exist, the entrainment from one wave must be at least carried in the gas stream up to the next downstream wave. This physical significance of Re_{lfc} is reinforced in Figure 3-21, which relates the critical film Reynolds number to wavelength.

3.4 Comparison of measured wave characteristics with available correlations/data

The present experiments explore wave behavior in a part of the parameter space little covered in earlier works, but which is important in practical applications. Correlations available to the analyst are predominantly derived from results elsewhere (or for which the parameter space of their derivation is uncertain) and we investigate here their effectiveness in predicting behavior of the low-flow space under investigation. It must be noted that the correlations considered are applicable only in annular flow regime and thus compared only with the present annular flow data.

Though an analytical model is available [124] for velocity of flooding waves in churn flow regime and a correlation is available [125] for their frequency, considering the complexity of churn flow it is considered more appropriate to compare present velocity and frequency data against previously reported data.

3.4.1 Wave velocities

3.4.1.1 Pearce correlation for annular flow

The wave velocities (in the annular flow regime) obtained in this experiment are compared with that of the Pearce [142] correlation, equation(3.3):

$$v_w = \frac{K_{pr}\bar{u}_{lf} + j_g\sqrt{\dfrac{\rho_g}{\rho_l}}}{K_{pr} + \sqrt{\dfrac{\rho_g}{\rho_l}}} \tag{3.3}$$

Here, $\bar{u}_{lf}$ is the time-averaged liquid film velocity, and K_{pr} is a parameter depending on pipe diameter. The time-averaged liquid film velocity is obtained from equation (3.4).

$$\bar{u}_{lf} = \frac{d_{eq}G_{lf}}{4\rho_l\delta} \tag{3.4}$$

The average film thickness, δ was evaluated experimentally by using conductance probes [134] as mentioned earlier. As noted above, appreciable entrainment does not exist for the present experimental data set. Thus the film mass flux, G_{lf} was assumed to be equal to inlet liquid mass flux for computation of $\bar{u}_{lf}$. For the present case, the value of K_{pr} is taken as 0.63 for our pipe diameter of 11mm, following the prescription by Ombere-Iyari and Azzopardi [143], who conducted experiments with different pipe diameters.

The predictions of the Pearce [142] correlation are plotted in Figure 3-23. It is seen that the correlation over predicts by 30% for the present data set. Sawant et al. [119] also used this correlation for predicting their data and obtained similar accuracy.

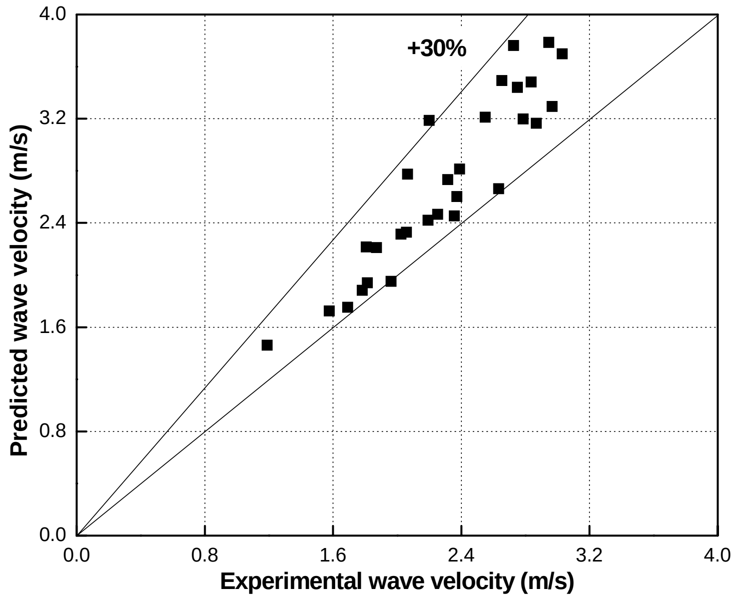

Figure 3-23: Comparison of the present measurements of the wave velocity with the Pearce [142] correlation

3.4.1.2 Kumar et al. correlation for annular flow

The Kumar et al.[144] correlation was derived from experiments in the range

$$\rho_g j_g^2 = 4700 \text{ to } 8300 \text{ kg/ms}^2$$
$$\rho_l j_l^2 = 7.5 \text{ to } 600 \text{ kg/ms}^2$$

which is wholly outside the space of our experiments (and indeed, was from experiments in a rectangular channel 63.5mm x 63.4mm). This correlation is

$$v_w = \frac{K_{kum} j_g + j_l}{1 + K_{kum}} \tag{3.5}$$

where K_{kum} is a constant given by equation (3.6)

$$K_{kum} = a\left(\frac{\rho_g}{\rho_l}\right)^{\frac{1}{2}}\left(\frac{\mathrm{Re}_l}{\mathrm{Re}_g}\right)^{\frac{1}{4}} \tag{3.6}$$

Since as noted this correlation, is for a rectangular channel whereas ours is circular, the constant K_{kum} is obtained with a =7.653, the appropriate value for the present experiment.

Using this, the predictions of the correlation are compared with our measurements in Figure 3-24. As for Pearce, the predictions of the correlation are reasonably consistent with the present measurements; the correlation predicts most of the present data within +20% and -10%, which is better than Pearce [142] correlation. Sawant et al. [119] also obtained better agreement of their data with the Kumar et al. [144] correlation than the Pearce correlation.

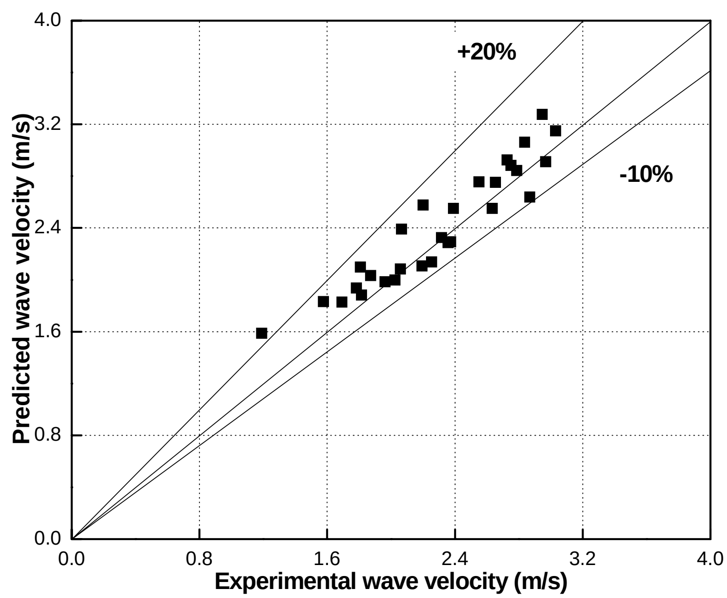

Figure 3-24: Comparison of the present measurements of the wave velocity with the Kumar et al. [144] **correlation**

3.4.1.3 Flooding wave velocities in churn flow

A comparison of the present data with the previous experimental data [123,145] on wave velocity and frequency is shown in Figure 3-25. The wave velocities are plotted with non-dimensional superficial velocity, j_g^*.

$$j_g^* = j_g \sqrt{\frac{\rho_g}{gd\left(\rho_l - \rho_g\right)}} \tag{3.7}$$

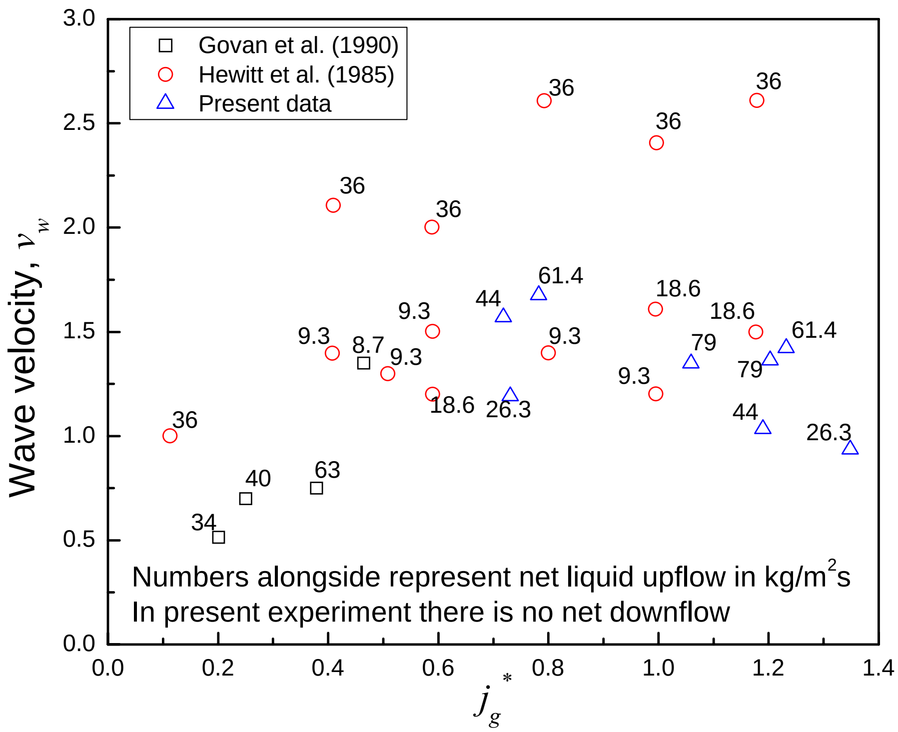

Figure 3-25: Comparison of present flooding wave velocity with previous [123,145] **data**

In the zone of the present data (j_g^*> 0.75), the trend of wave velocity (i.e., reduction upon increasing gas flow) observed is mostly similar. However the wave velocity is seen to be much smaller than previous experiments for same j_g^* and liquid mass flux implying that one would require lower wave velocities to maintain liquid upflow. This may also be due to lower diameter pipe used presently. The effect of liquid mass flux is not found to be as significant as in previous works.

3.4.2 Wave Frequencies

3.4.2.1 Sekoguchi correlation for annular flow

Disturbance wave frequencies have been correlated by Sekoguchi et al. [146]. This correlation is given by eqs.(3.8) - (3.12). This correlation was tested by Hazuku et al. [147] for their experimental data in an 11mm diameter test section. They found the correlation to predict their data within ±25%. The Sekoguchi et al. [146] correlation when compared with the current dataset is seen in Figure 3-26 to predict similarly to within ~30%.

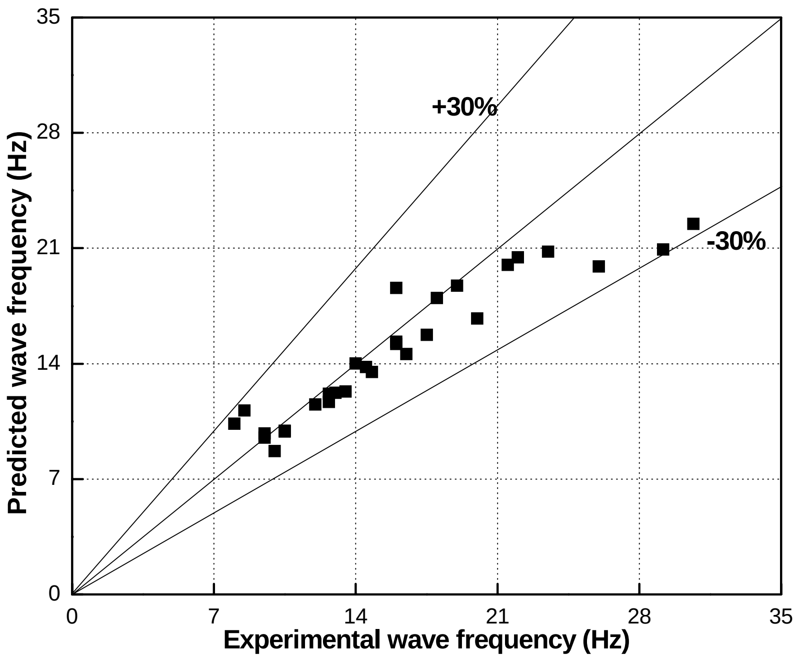

Figure 3-26: Comparison the present measurements of the average disturbance wave frequency with the Sekoguchi et al. [146] **correlation**

$$Sr = \frac{fd_{eq}}{j_g} = f_1\left(Eo\right)g_1\left(\psi\right) \tag{3.8}$$

where

$$f_1(Eo) = Eo^{-0.5}\left(0.5\ln(Eo)\right)g_1(\psi) \quad (3.9)$$

and

$$g_1(\psi) = 0.0076\ln(\psi) - 0.51 \quad (3.10)$$

$$Eo = \frac{gd_{eq}^2\left(\rho_l - \rho_g\right)}{\sigma} \quad (3.11)$$

$$\psi = \frac{\mathrm{Re}_l^{2.5}}{Fr_g} \quad (3.12)$$

$$Fr_g = \frac{j_g}{\sqrt{gd_{eq}}} \quad (3.13)$$

Eo, Fr_g and ψ are the Eötvös number, Froude number and non-dimensional parameter respectively.

3.4.2.2 Flooding wave frequency in churn flow

The frequency is compared against the same dataset [123,145] as for flooding wave velocity. Frequency is seen to increase with gas and liquid flow. This observation concurs with previous data. However, for a given j_g^* and liquid flow rate, presently obtained frequencies are lesser than previous values. This might be due to counting of short lived waves by previous workers. In the present work only sustained flooding waves are considered.

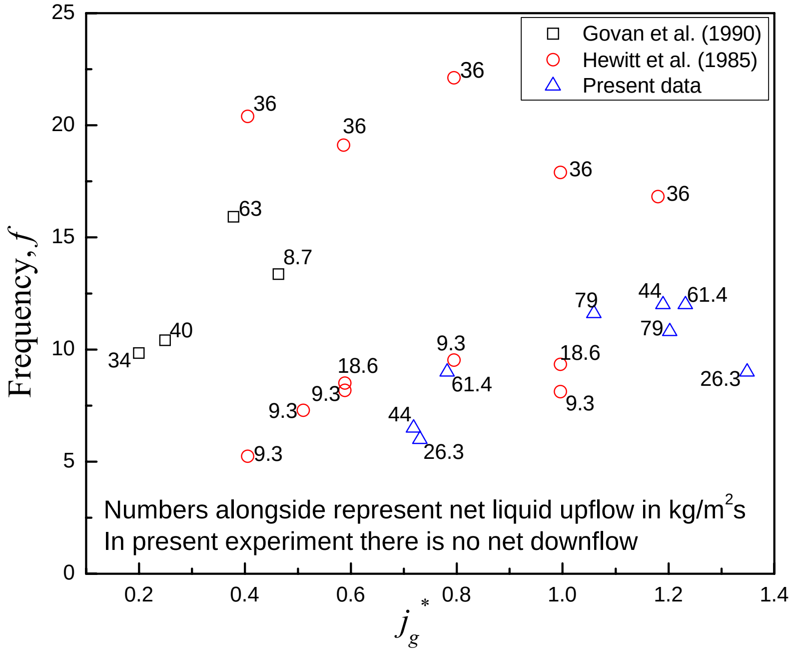

Figure 3-27: Comparison of present flooding wave frequency with previous [123,145] **data**

3.4.3 Closing remarks

Given the good consistency of the earlier correlations with the present measurements, with respect to both disturbance wave frequency and speed, it seems safe to conclude that they can reasonably be applied in the low-flow annular regime explored in the present experiments.

An important inference which may be drawn from the comparison with Pearce [142] correlation is its ability to predict the present and Sawant et al. [119] data with similar accuracy. While the present data are at near atmospheric pressure, Sawant et al. [119] conducted experiments from near atmospheric up to 5.8 bar. This implies density ratio $\left(\rho_l/\rho_g\right)$ variation (in [119]) from 170 to 660. This further subtly indicates that upon the choice of proper parameters (which definitely should include property terms viz., density, surface tension etc.), air-water experimental data can be applied to steam-water conditions too. Examples of such parameters are the modified Weber number and Reynolds number etc. It must be mentioned that for steam water conditions corresponding to BWR operation (i.e., 70 bar) the density ratio is of the order of 20-25, which is beyond the Sawant et al. [119] experiments. However under fault conditions in the reactor, density ratios may be nearer.

The flooding wave velocity and trends obtained in the present experiments are similar to previous works. The frequency however is lesser; possibly due to consideration of only sustained flooding waves in the present work.

3.5 Experimental results on film flow rate

Due to the wavy nature of the film, the instantaneous film flow rate is always changing even if the inlet conditions are steady. This was evidenced by the visualization of periodic increasing and decreasing liquid extraction across the porous device in the extraction chamber. This instantaneous rate could not be quantified in the present experimental arrangement. The collection technique described in §3.2.1.3 by construction, averages the essentially varying film flow rate. Moreover with respect to the steady state mechanistic model which is dealt with in this work, it is the average film flow rate which is important. The experimentally observed film flow rate is plotted (as discrete points) in Figure 3-28. Film extraction was attempted only in the annular flow regime and even here, there were some cases for which the film could not be completely extracted. Specifically, of the 29 annular flow points, complete extraction was possible only for 20 points (which are reported in Figure 3-28).

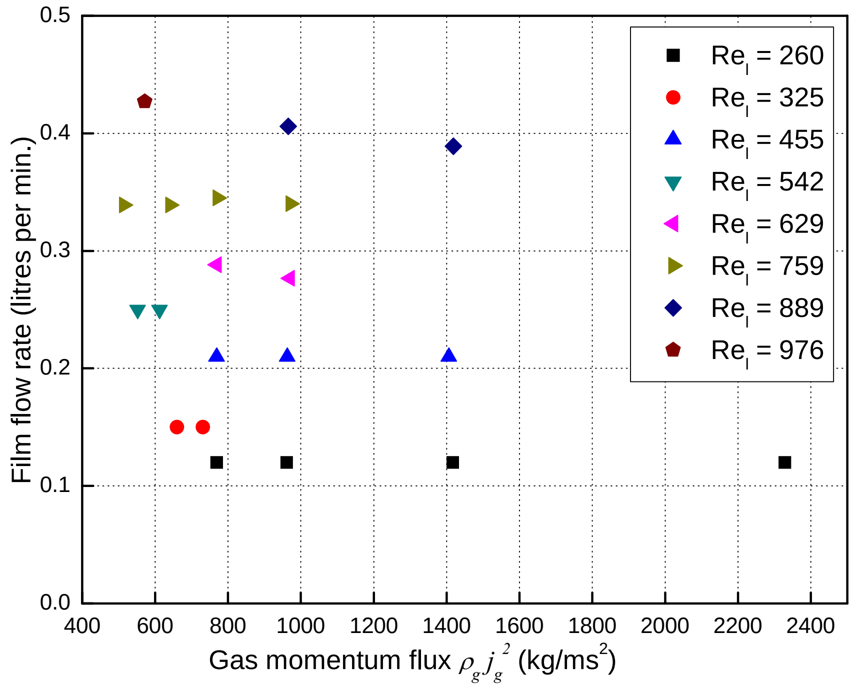

Figure 3-28: Measured film flow rate in air-water annular flow

Expected trends of reduction of film flow rate with air flow and increase with liquid flow rate are observed. For Re_l, 542 and below, no entrainment was observed. In these cases all the liquid was flowing in the film. For the case of Re_l = 542, experiments were performed at low air flow rates and it cannot be conclusively said if entrainment would exist at higher air flows. Thus it may not be conclusively said that this is the limiting liquid film Re (since there is little or no entrainment, film Re and liquid Re are practically the same). However at liquid Reynolds numbers of 455, no entrainment was observed even at high air flow rates. When the critical film Reynolds number is computed using Hewitt and Govan criterion, eqn.(2.25), a value of 415-450 is achieved for the present data set. It may thus be concluded that this particular criterion does indeed describe the onset of entrainment very correctly.

It is perhaps informative to consider (like was done for wave characteristics), where the present data lies in context of already available film flow rate data in air-water flows in small diameter tubes. This is shown in Figure 3-29. The tube diameters for other data [38,131,148,149] presented fall in the range of 5-12 mm. One of these [149] reports Freon-113 experiments apart from air-water. Another [150] reports data on steam-water flow at pressure and temperature conditions similar to that in BWRs. The other experiments referenced in Figure 3-29 use air-water as the working fluid. It may be seen that the present film flow rate measurements cover some portion of parameter space which has not been covered in the literature.

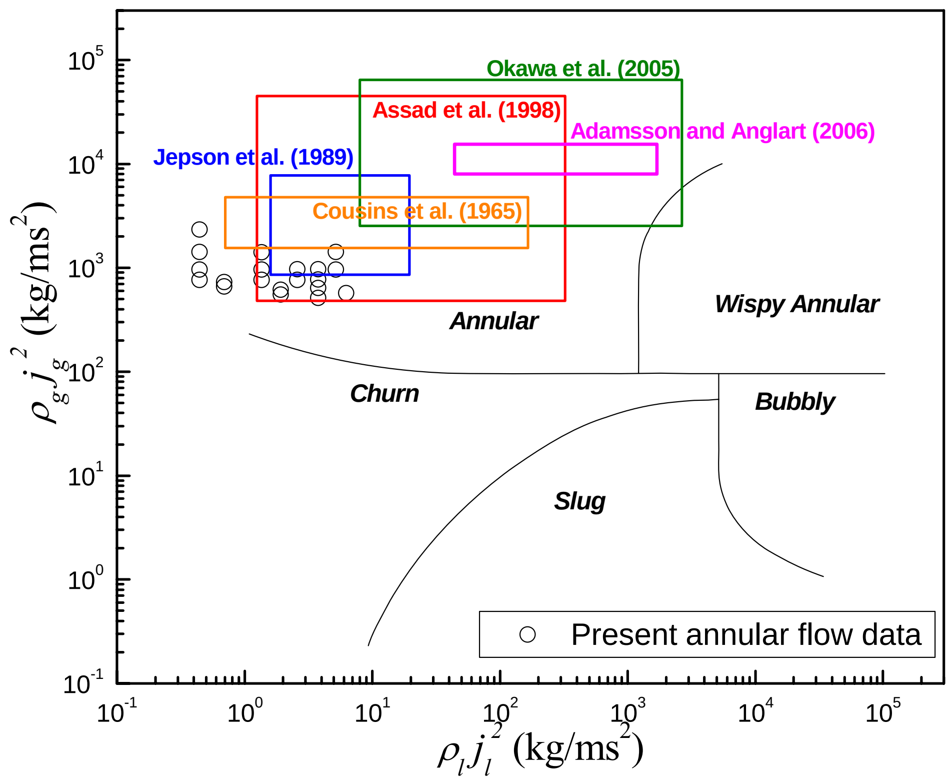

Figure 3-29: The parameter space covered by the present measurements (hollow circles), and the ranges covered by previous small-tube experiments [38,131,148–150] **for film flow rate measurements, plotted on Hewitt and Roberts** [129] **flow pattern map**

3.6 Experimental results on film thickness

As observed from the photographs, the film (in churn, pre-annular and annular flows) is wavy. So is the raw film thickness data (Figure 3-30). The time average film thickness is probably a more useful data representing the gross characteristics. Such average film thickness is what is used in some entrainment rate correlations (eqn. (2.19)). Such average film thickness data from present experiments are tabulated in appendix-1.

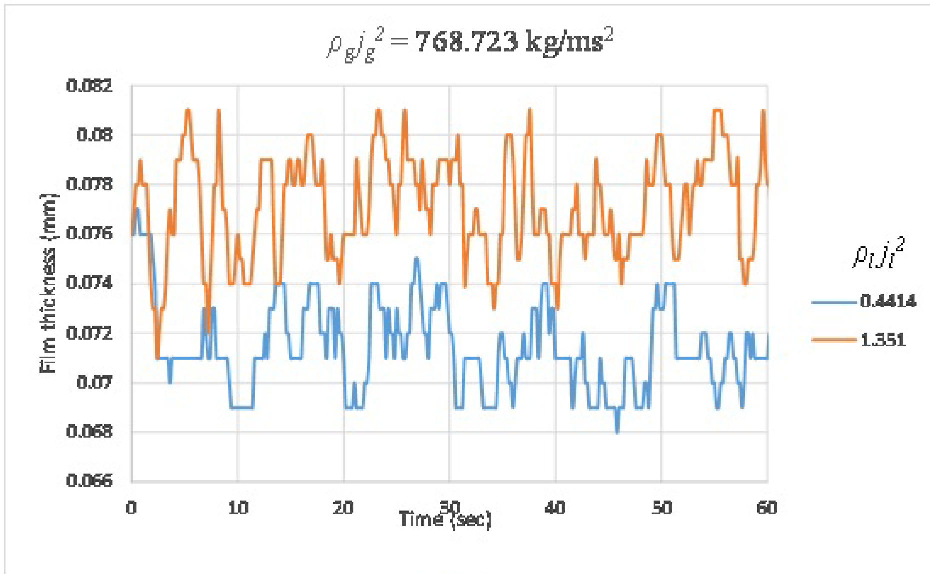

(a)

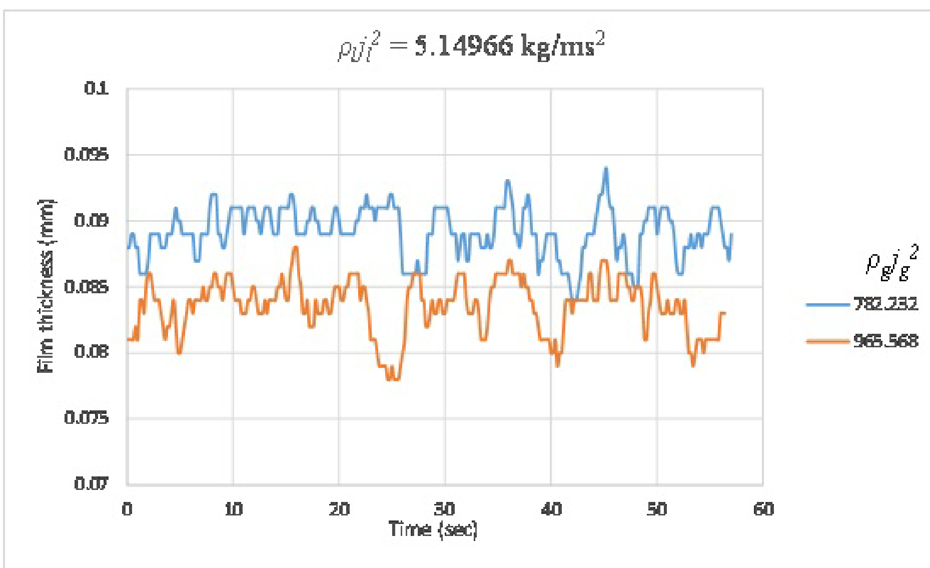

(b)

Figure 3-30: Instantaneous film thickness as a function of (a) liquid mass flux and (b) gas mass flux

The time averaged film thickness is plotted as a function of liquid Reynolds number and gas momentum flux in Figure 3-31 and Figure 3-32 respectively. Essentially both the graphs convey the same information. However, the dependence of film thickness on either liquid or gas flow rate can be more easily observed with the two figures.

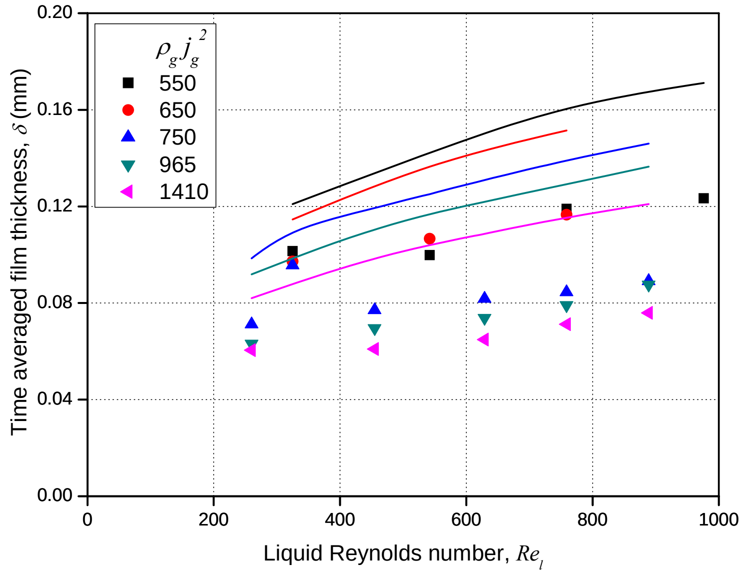

Figure 3-31: Predicted and measured film thickness as a function of liquid Reynolds number for different gas momentum flux. Predictions are shown as lines and experimental data as points

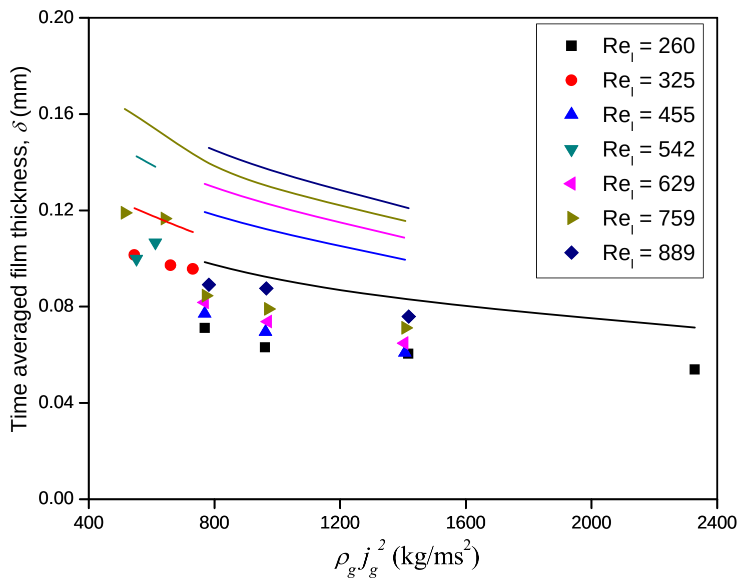

Figure 3-32: Predicted and measured film thickness as a function of gas momentum flux for different liquid Reynolds number. Predictions are shown as lines and experimental data as points

It is seen that the film thickness increases upon reducing air flow rate and increasing water flow rate. These figures also assess the performance of the simplified triangular relationship for evaluation of film thickness (eqs.(2.35) and (2.47)) which has been used in the present work (and described in §2.3.3). The triangular relationship is seen to over-predict the film thickness by a substantial margin.

3.7 Experimental uncertainties

For phenomena such as these, and these kinds of measurements, uncertainties themselves can only be estimated fairly approximately. In this section it is intended to provide best possible indication we can of what they are.

3.7.1 Inlet Flow rates

The inlet water and air flow rate measurements are calibrated by collection technique and calibrating against reference flow meter respectively. The values reported here are accurate to within ±0.02 and ±1.7 litres per minute for water and air flow respectively.

3.7.2 Wave velocities

The wave velocity is estimated as the slope of the streaks on d-t plots. The slopes are measured manually by using a protractor having a least count of 1^{o} (we could thus speak of the measured slopes with an accuracy of $\pm 0.5^{o}$). The error in estimation of $\tan\theta$ increases with increase in θ (or velocity). In our case the maximum θ was approximately 85^{o}. This leads to a maximum error of approximately 11%.

3.7.3 Axial extent of the waves

Our resolution due to digitization of the images is ~ 0.2 mm (which is approximately the length of 1 pixel in our photographs). In annular flows, the expanse of a wave does not vary to a large extent (we have not quantified how large! It's difficult to do so). In churn flows, there is an inherent increase and decrease in the wave expanse as the wave moves along (again, we haven't quantified the variation). We have taken the highest values observed to plot the axial expanse graph (Figure 3-15).

3.7.4 Wave periods and wavelengths

Due to the frame rate of the camera we are limited to a time resolution of 1ms (thus an error of ±0.5ms). The time period measurements between successive waves can also be computed with the same accuracy. The frequency is inverse of time period. Thus, greater the time period (or lesser the frequency), lesser is the error. For high frequency the error would be larger. For our case the maximum frequency (including variation is ~67 Hz.). This implies a time period of 15ms. and a max error of ±3.3%.

$$f = \frac{1}{T}; \left|\frac{df}{f}\right| = \left|\frac{dT}{T}\right| = \frac{0.5}{15} = 0.033 \tag{3.14}$$

Since wavelength is related to wave velocity and frequency, we may write for error estimation;

$$\left|\frac{d\lambda}{\lambda}\right| = \left|\frac{dv_w}{v_w}\right| + \left|\frac{df}{f}\right| \tag{3.15}$$

Thus we may say, conservatively, that the maximum uncertainty in wavelength is ±14.5%.

For the avoidance of doubt, we would just reiterate that the error bars shown on Figure 3-20 and Figure 3-19 do not represent errors in measurement, but the actual variation in observed frequency and wavelength. The ranges indicated by the bars are thus a characteristic of the flow itself. Whilst this type of reporting, of maximum, minimum and average values, is not generally observed in the literature, but we believe it is important.

3.7.5 Film thickness

Chandraker [100] in his doctoral work had used the same sensor and conducted a detailed estimation of the error in this probe. He found that the error varied with film thickness and concluded it to be ±1.96% for thickness ≤ 0.25 mm and ±7% for thickness greater than 0.25 mm. Since all the present data lie below 0.25 mm the error in reported film thickness is 1.96%.

3.7.6 Film flow rate

The error in reported film flow rate of course depends on the least counts of various measuring instruments; inlet flow measurements, Liquid take-off measurements etc. Accuracy in inlet flow rate measurements have been mentioned earlier. The accuracy of liquid take off measurements estimated from the least count of collection vessel graduations and stop watch was found to be better than ±0.27%. However, it is difficult to derive a functional relation between the film flow rate and these quantities. Moreover in spite of best efforts, some manual errors (e.g. during keeping time) might creep in. Thus the repeatability of film flow rate was checked for certain cases; the results were found to be within 3% of each other.

3.8 Conclusions

A new set of data are presented for upward low pressure air-water flow for a 11 mm ID pipe at superficial air and water velocities of j_g =6.0-28.0 m/s and j_l = 0.02-0.08 m/s. This operating parameter space falls in a zone where both air and water flow rates are significantly lower than similar studies in the literature for small diameter tubes, and is a part of the parameter space important for nuclear reactor safety studies.

High speed photographic images were analysed to obtain wave parameters such as wave velocity, frequency and wavelength for different air and water flow rates in the churn and annular flow regimes. Experimental data has been generated for film flow rate and film thickness in annular flow.

The usual flow regimes of churn and annular flow, were clearly observed in the study. An additional intermediate, pre-annular regime was observed, characterised by a distinct region of stationary ripples. Each of these flow regimes could be very accurately located by the motion of ripples in distance-time plots.

The measurements on disturbance waves in annular flow are mostly consistent with previous observations and in reasonable agreement where the measured conditions coincide. Importantly, the predictions in this parameter space made by earlier correlations mostly developed from measurements at higher flow rates were found to be reasonable, and this provides some validation for their employment under these conditions.

Additional quantification of the variation in time period between successive waves has been presented. The results on velocity of flooding waves in churn flow are also reported. It is seen that the velocity of flooding waves reduces with increase in gas flow. This behaviour is opposite to that observed for disturbance waves in annular flow.

The relative velocity $\left(j_g - v_w\right)$ data generated in this work could be particularly useful for simulations of droplet deposition in annular flows. Present day correlations also do not account for the effect of disturbance wave on deposition rates. In light of the present work, the simulations of droplet deposition need to be revisited.

The transition from churn to annular flow has also been studied from the point of view of axial expanse of the disturbed region. An attempt has also been made to quantify the length of the disturbed region in terms of pipe diameters. It is seen that the disturbance length drops sharply from churn to annular flow.

The experimental velocity and frequency data in the annular flow regime has been compared with Pearce [142], Kumar et al. [144] and Sekoguchi et al. [146] correlations. The results were found to be similar to what had been observed by previous investigators [119,147].

A comparison of the present and previous [123,145] velocity and frequency data on churn flow waves indicated a reasonable agreement for velocity. The lower frequency observed in present work could be explained.

In annular flow, the wavelength was found to be a strong function of film Reynolds number up to the critical film Reynolds number for onset of entrainment, Re_{lfc}. This observation coupled with visual observations led us to relate physical significance of Re_{lfc} to the wavelength. This significance of Re_{lfc} is a new and important conclusion of the present study.

4 A NEW METHODOLOGY FOR ESTIMATION OF IEF

The initial entrained fraction which refers to the entrained fraction at the onset of annular flow is one of the important conditions governing the outcome of the mechanistic model (see Figure 2-20). A survey of the available literature on the subject has been presented in §2.3.5. In summary, it can be recapitulated that experimental data on IEF is scarce and earlier methods which exist for estimation of IEF do not have robust foundations. Lately however, Ahmad et al. [73] and Wang et al. [74] have tried to tackle the problem in greater depth by extending simulations to start from onset of churn flow regime. There are however two concerns with this approach.

The first is that rate correlations in churn flow regime are not well known, thus modifications of existing annular flow correlations are used. However as has been observed in previous works [71] and also in the previous chapter, mechanisms governing rate processes in churn and annular flow are different. Thus applicability of annular flow type correlations is questionable.

The second point of concern is that, even if it is shown that the rate correlations of annular flow (or their modifications) are indeed applicable in churn flow, a value of entrained fraction is still required at the onset of churn flow. The problem of IEF is thus solved at the expense of introducing another initial value problem.

A correlation for IEF has been recently developed [75]. But a theoretical justification for the same is required so as to apply it to wider range of conditions.

In view of the above a new methodology for estimation of IEF is proposed in §4.1. This new methodology aims to incorporate the effect of churn flow without requiring an estimate of entrained fraction in churn flow regime. The application of the IEF methodology and formulation of the mechanistic model is described in §4.2. This section also describes some validation performed for the IEF prediction methodology in §4.2.1. This is a particularly difficult task as IEF is difficult to measure and there are no direct measurements available in literature. Nevertheless, there are some indicative data which have been used for the validation. This effect of using the new methodology is evaluated by comparing dryout predictions with and without applying IEF methodology. This is done for various deposition entrainment correlation sets in §4.2.2.

4.1 A new methodology for estimation of IEF

The process of atomization of the liquid slugs during the transition to annular flow (type 5 in Figure 2-16) is a stochastic process and there would generally be a band of values for IEF distributed about a central value. It is generally difficult to simulate and model such complex processes. The basic premise of the present methodology is that – though it is difficult to measure IEF, its effects can be quantified. The effect which has been used for this purpose is the pressure gradient which is a function of the entrained fraction. In this work an estimate of IEF was made by equalizing the pressure gradient obtained from triangular relationship (eqn.(2.47)) with that obtained from a reference two phase correlation (in this case, Lockhart-Martinelli [151] correlation).

4.1.1 Possibility of two solutions for IEF

The triangular relationship (eqn.(2.47) in conjunction with eqn. (2.35)) can be thought of as a flow pattern based pressure drop correlation. Specifically, among these two equations, we can evaluate the liquid film thickness and two-phase pressure gradient for a given film flow rate (or entrained flow rate). The two-phase pressure gradient thus predicted is a function of the fraction of liquid flowing as drops (i.e., IEF at the point of transition to annular flow). The Lockhart and Martinelli [151] correlation on the other hand gives an estimate of the pressure gradient disregarding the droplet distribution between the liquid film and vapour core. Giving credit to the experimental nature of the Lockhart-Martinelli correlation, it is argued that a proper estimate of IEF would imply equality of the pressure gradients predicted from the two correlations at transition to annular flow. Interestingly, the methodology gives two different values of IEF (Figure 4-1) for any given situation. One of these is a particularly high value and the other a low value.

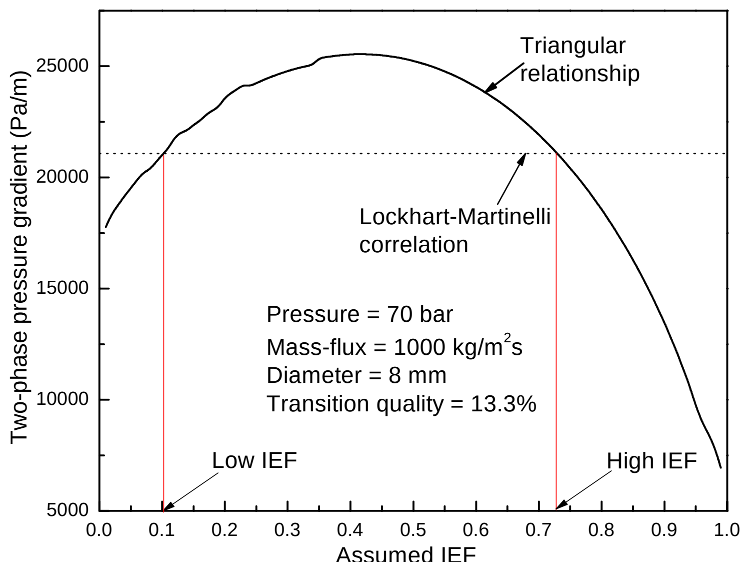

Figure 4-1: The dependence of calculated pressure gradient at onset of annular flow on the assumed IEF, the reference pressure gradient correlation and predicted IEF for a typical case

Physically, two solutions exist due to the competing effects of reducing liquid film thickness and increasing gas core density. While Barbosa et al. [71] experiments in adiabatic equilibrium annular flows pointed towards low IEF, it is generally accepted that IEF in diabatic flows will be high due to the history of churn flow [25,73]. The Bennett et al. [19] cold patch experiments however indicate that low IEF can indeed be possible in heated flows. This seemingly contradicts the assumptions of nearly all of the present day phenomenological dryout models. The new methodology for IEF determination presented here aims to account for this and define conditions when low IEF is possible.

4.1.2 When would the IEF be low (or high)?

In what follows, specific conditions are defined when to choose the lower IEF value over the higher one (for instance in Figure 4-1). The choice takes into consideration churn flow regime which has an important bearing on IEF. Churn flow is distinguished by intermittent counter current flow of liquid and gas and existence of large flooding waves. These waves lead to entrainment of large quantities of liquid into the gas core (and simultaneous gas entrainment in film). Thus churn flow is characterized by large entrained fraction and large entrainment rates. It was seen in adiabatic air-water experiments (Figure 3-15) that the approximate axial expanse of the flooding waves in churn flow is of the order of 10-12 diameters at most. These high entrainment disturbance regions were seen to be spaced apart by a relatively quieter length of falling film with little or no entrainment. The axial expanse of disturbances reduces as the gas velocity increases and there is a sustained co-current movement of liquid and vapor. The entrained fraction and entrainment rate thus reduce as annular flow regime is approached. In annular flow the entrainment is governed by gas core velocity. In fact, it is observed that entrainment is possible only beyond a critical liquid film flow rate and a critical gas core velocity. These criteria for entrainment have been correlated by Ishii and Grolmes [54] and are explained in §2.3.2.

In diabatic flows, high entrained fraction of churn flow will have an (history) effect which progressively diminishes as we move downstream. In other words, the axial expanse of these disturbances reduces as flow quality increases. This can be conceptualized by looking at Figure 3-14 and then imagining a combined picture by putting the pictures one on top of other in sequence of increasing gas flow.

It is argued that if the length in churn flow regime exceeds the 'axial expanse' of flooding waves, then entrained fraction might be low at transition to annular flow depending on the local gas core velocity and liquid film flow rates [54]. If the gas core velocity is less than the critical velocity to entrain droplets then low IEF is postulated (Figure 4-2a). In other cases when the gas velocity is sufficient (Figure 4-2b) or churn flow length is smaller than the axial expanse of the waves (Figure 4-2c), high IEF is postulated.

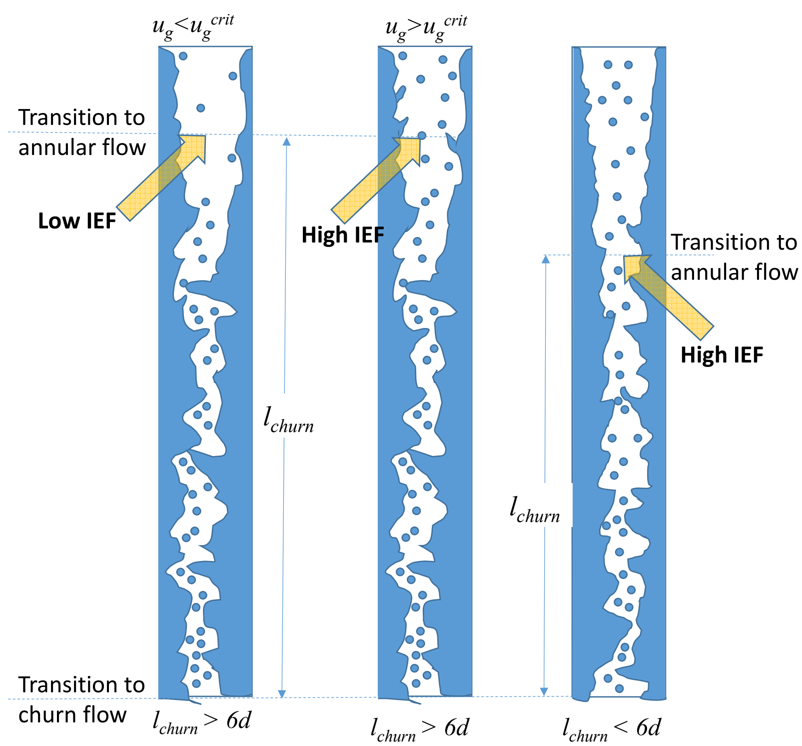

Figure 4-2: Scheme determination of IEF; Churn flow length greater than 6d and (a) gas velocity lower than critical gas velocity leading to low IEF, (b) gas velocity higher than critical gas velocity leading to high IEF, and (c) churn flow length lower than 6d leading to high IEF

The notion of a single value for 'axial expanse' of the flooding waves is a simplification because of the constantly changing quality and resulting disturbance wave structure in diabatic flow. For the purpose of the model an average axial expanse of 6 times the pipe inside diameter ($6d_{eq}$) is chosen. This is the average of an approximate maximum expanse at beginning of churn flow ($12d_{eq}$) to disturbance being confined to a small region (like a disturbance ring) in annular flow (refer Figure 3-15).

The correlation of Jayanti and Hewitt [152] is used to evaluate the transition to churn flow. This along with the correlation for transition to annular flow allows calculating the churn flow length. In the present work, transition is evaluated using Wallis [68] correlation. In its simplified form [27], it is given by equation (4.1). There are indeed other correlations [69,70] describing the transition to annular flow. However, this correlation (eqn. (4.1)) has been widely used by different mechanistic models [27,51,153] and is thus considered for the present work.

$$x^{trns} = \frac{0.6 + 0.4\dfrac{\sqrt{\rho_l(\rho_l - \rho_g)gd}}{G}}{0.6 + \sqrt{\dfrac{\rho_l}{\rho_g}}} \tag{4.1}$$

4.2 Mechanistic modeling and annular flow predictions with the new IEF methodology

The basic equations of mechanistic model are: the mass balance for the film, eqn. (2.2), the entrained drops, eqn.(2.51) and the vapor, eqn. (4.2).

$$\frac{dG_g}{dz} = \frac{4}{d_{eq}} B \tag{4.2}$$

The computations using the model begin from the onset of annular flow determined from eqn. (4.1). Once the transition quality, x^{trns} is determined, the location of transition point can be determined by performing a heat balance. The film flow calculations proceed downstream of this point. The film flow rate is computed by discretization and solution of the mass balance equations, along the axis of the tube. In this process, the flow rates of liquid film, droplet and vapor at a level *i+1* are evaluated from the values at upstream level *i* using the following finite difference equations.

$$G_{lf}^{i+1} = G_{lf}^{i} + \frac{4\Delta z}{d_{eq}}\left(D_i - E_i - B_i\right) \tag{4.3}$$

$$G_{d}^{i+1} = G_{d}^{i} + \frac{4\Delta z}{d_{eq}}\left(E_i - D_i\right) \tag{4.4}$$

$$G_{g}^{i+1} = G_{g}^{i} + \frac{4\Delta z}{d_{eq}} B_i \tag{4.5}$$

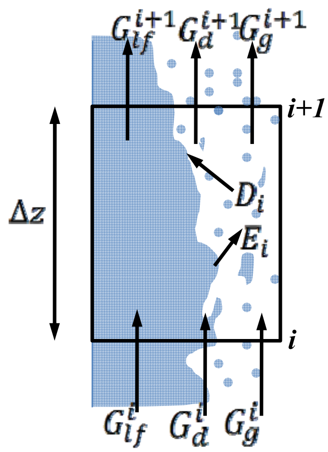

Figure 4-3: Computational cell for mechanistic model

The computational cell is shown in Figure 4-3. It is worth mentioning at this point that deposition and entrainment take place along the whole length Δz. Hence ideally an average of the deposition and entrainment values at *i* and *i+1* would be appropriate. This would entail the use of an implicit solution scheme. If however, Δz is small, the variation from *i* to *i+1* may be neglected and equations (4.3) to (4.5) will hold good. The solution of these equations is obtained using a marching technique where the downstream values are calculated using the immediately upstream quantities. The computation of quantities such as interfacial shear and film thickness which are required for certain entrainment rate correlations (eqn.(2.19) and eqn. (2.21)) are on the lines of description in §2.3.3.

The boundary conditions required at the beginning of annular flow are the flow rates of liquid film, droplets and vapor. The vapor flow rate is calculated from the knowledge of transition quality. The split between film and droplets at the transition to annular flow is computed using the methodology developed in §4.1.

The IEF prediction methodology is validated in §4.2.1. Further, an estimate of the advantage obtained upon using the new methodology for IEF can be gauged by contrasting it against dryout predictions made using ad-hoc high IEF values (as is used by many models) as well as a correlation available in literature [75]. This is done using Becker et al. [72] dryout data in §4.2.2.

4.2.1 Validation of the new model against entrained fraction data in heated tubes

Experimental determination of IEF is difficult due firstly to the inability to correctly identify the location of transition in diabatic flows. Secondly, at or near to the transition, film is thicker, disturbances on the film are large and film extraction for film flow rate (and consequently entrainment rate) evaluation is generally difficult. An idea of the value of IEF can however be obtained from measurements of film flow rate at sufficiently low qualities. One such set of measurements have been performed by Bennett et al. [19], where a (highly) non-uniform heat flux was engineered by leaving a section of the tube unheated. These experiments are more commonly referred to as the Cold-patch experiments. Though many important inferences can be drawn from the cold patch experiments, in the present context of IEF validation, it is important that the entrained flow rate was effectively measured, from a sufficiently low quality to a high value (of the order of 80%) at the end of the tube. An extrapolation of the obtained curves towards lower quality would thus provide a rough estimate of IEF. The mechanistic model can theoretically predict the variation of entrained flow rate with the computed IEF. It has been highlighted earlier that many correlations are available for deposition and entrainment rates. Presently, Hewitt and Govan [4] correlations for entrainment and deposition rate are used to simulate Bennett et al. [19] experiments. At this juncture, there is no specific reason for using this correlation set, but it suffices to say that, prediction of IEF (the object of validation) by the present methodology is not influenced by choice of any deposition-entrainment correlation set.

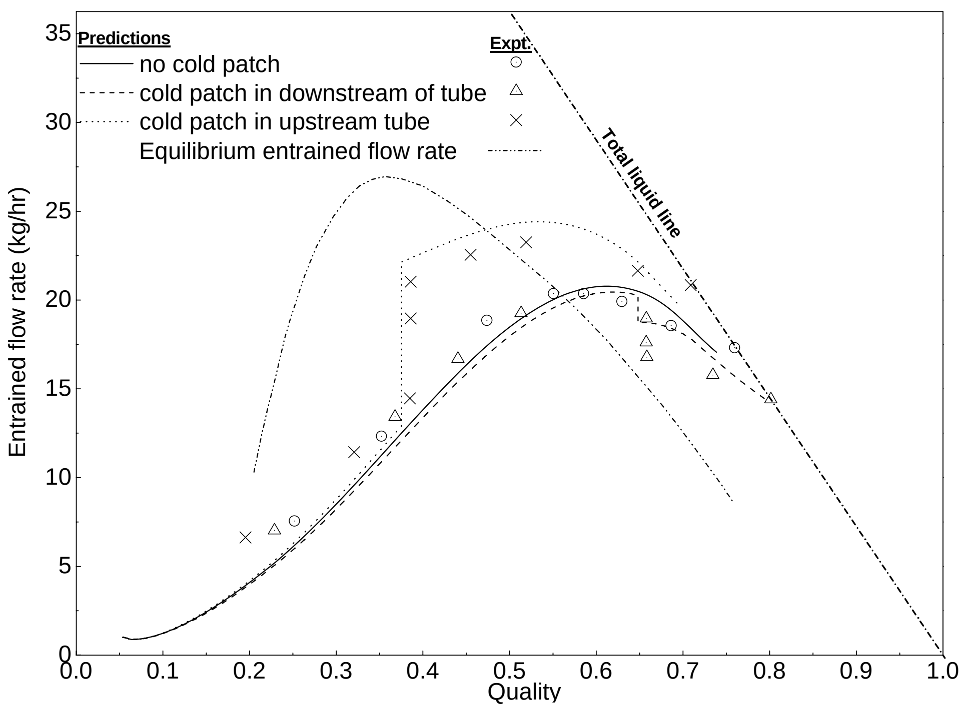

Figure 4-4: Model predictions for cold patch effect. Experimental data of Bennett et al. [19]**. (pressure 3.72 bar; Heat flux ~650 kW/m^2; Mass flux 297 kg/m^{2}s; dia 9.29 mm)**

The predictions for entrained flow rate in the cold patch experiments are plotted alongside the experimental data points in Figure 4-4. The predictions are shown from the transition quality (as computed from eqn.(4.1)) till the end of the tube. The experimental data points (with different symbols) correspond to different locations of the cold patch. It may however be inferred from the plot that an extrapolation of the experimental data for each of these different cases would lead to a value of initial entrainment which is pretty close to that predicted by the methodology developed in this work.

The cold patch experiments indicate that in this particular case, initial entrained fraction is apparently low and not high as argued generally for diabatic flows. The IEF prediction methodology outlined in §4.1 indeed postulates a low IEF for this case.

Though, in this section, the performance of deposition-entrainment correlation set is not being assessed, it is mentioned in passing that in conjunction with the present IEF prediction, the Hewitt and Govan [4] correlations predict the evolution of entrained flow (and consequently the film flow rate) quite accurately. There are some deviations though; lesser reduction in entrained flow is predicted for the downstream cold patch and towards the end of the heated length, predictions show a steeper reduction in entrained flow causing higher predicted dryout power. The Bennett et al. [19] experiments demonstrate the history effect and its mechanism very precisely. On looking at Figure 4-4, it is seen that deposition-entrainment equilibrium is not achieved in diabatic annular flows due to continually changing quality (and thus equilibrium entrainment). Nevertheless, there is a tendency to achieve equilibrium. The cold patch in effect provides an unheated constant quality zone where the equilibrium quality does not change, leading to a redistribution of liquid between film and drops. The greater the cold patch length, more the entrained flow tends towards equilibrium.

When the cold patch is provided in the upstream, where equilibrium lies above the actual entrained flow, there is a net entrainment from the film. The situation is opposite in the net deposition region (downstream cold patch). In this latter case, the dryout power increases as a result of the enhanced deposition. These experiments provide a physical reason for the greater dryout power observed in upstream peaked power profile. Good prediction of the history effect is an indication of the ability of a mechanistic model to properly capture the dynamics of the droplet mass transfer processes. This is discussed in greater detail in the next chapter where the different entrainment-deposition correlations are assessed.

It is interesting to compare the predictions using presently developed IEF method with that using GE IEF correlation [75]. Such is shown in Figure 4-5. The GE correlation is seen to predict a higher IEF. It must be mentioned though that the operating pressure of the cold patch experiments is outside the range of the GE correlation and such a difference may be warranted. But quite interestingly, the deposition-entrainment correlations make up for the initial difference so that beyond a quality of 40%, the differences are not so stark and towards the end of the heated length, they very nearly overlap with the predictions of presently developed model.

The results indicate, that in long length tubes (though the definition of long is subjective, in this case, the tube length is 2.44 m i.e. l/d ~260) and higher exit qualities, the final dryout power will be relatively insensitive to IEF. Taking the discussion a bit further, in presence of spacers (which have to be considered while bundle dryout evaluations), the entrained fraction gets modified at every spacer location. Since, the spacer pitch generally found in fuel clusters is not long enough to fall in the *long tube* range, a correct estimate of entrained fraction after spacer is crucial for reliable dryout prediction. The performance of deposition-entrainment rate correlation set becomes more important in such short length sections.

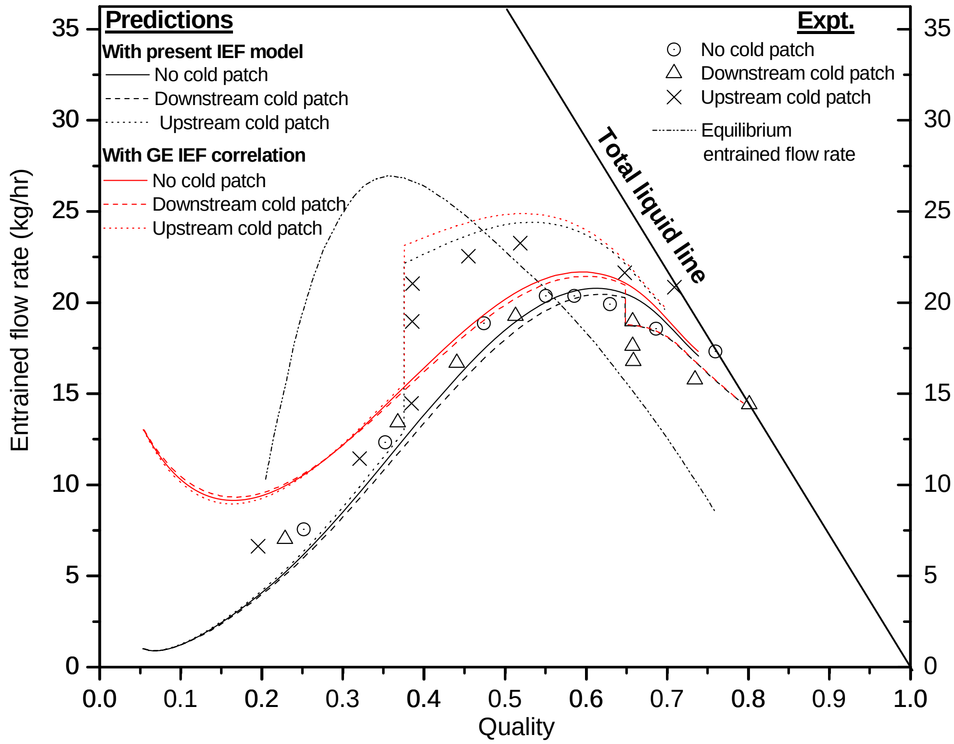

Figure 4-5: Cold patch experiments predicted with present IEF prediction methodology and GE correlation [75]

While cold patch is probably the most severe manifestation of a varying heat flux profile, it is also worthwhile to validate the present methodology against other flux profiles which are more common in nuclear reactors. Experiments with middle, inlet and outlet peaked heat flux profiles have been have been conducted by Adamsson and Anglart [150] under operating conditions similar to BWRs. They have measured the film flow rate along the test section length using extraction technique which is in principle similar to that described in §3.2.1.3.

Figure 4-6 Shows the film flow rate predictions for some of their experimental conditions with the present IEF methodology as well as GE correlation [75]. In both the cases Hewitt and Govan [4] correlations have been used for computation of deposition and entrainment rate computation. The film flow rate is measured in a series of locations which are pretty much in the downstream region. Data are not available at near the transition (to annular flow) location. The usage of GE correlation for IEF prediction is seen to give a very good match with experiments. It must be recalled that these experimental conditions fall inside the validity range of the correlation. The film flow rate predicted with the present methodology is lower than the observed values. But it nevertheless is not very different.

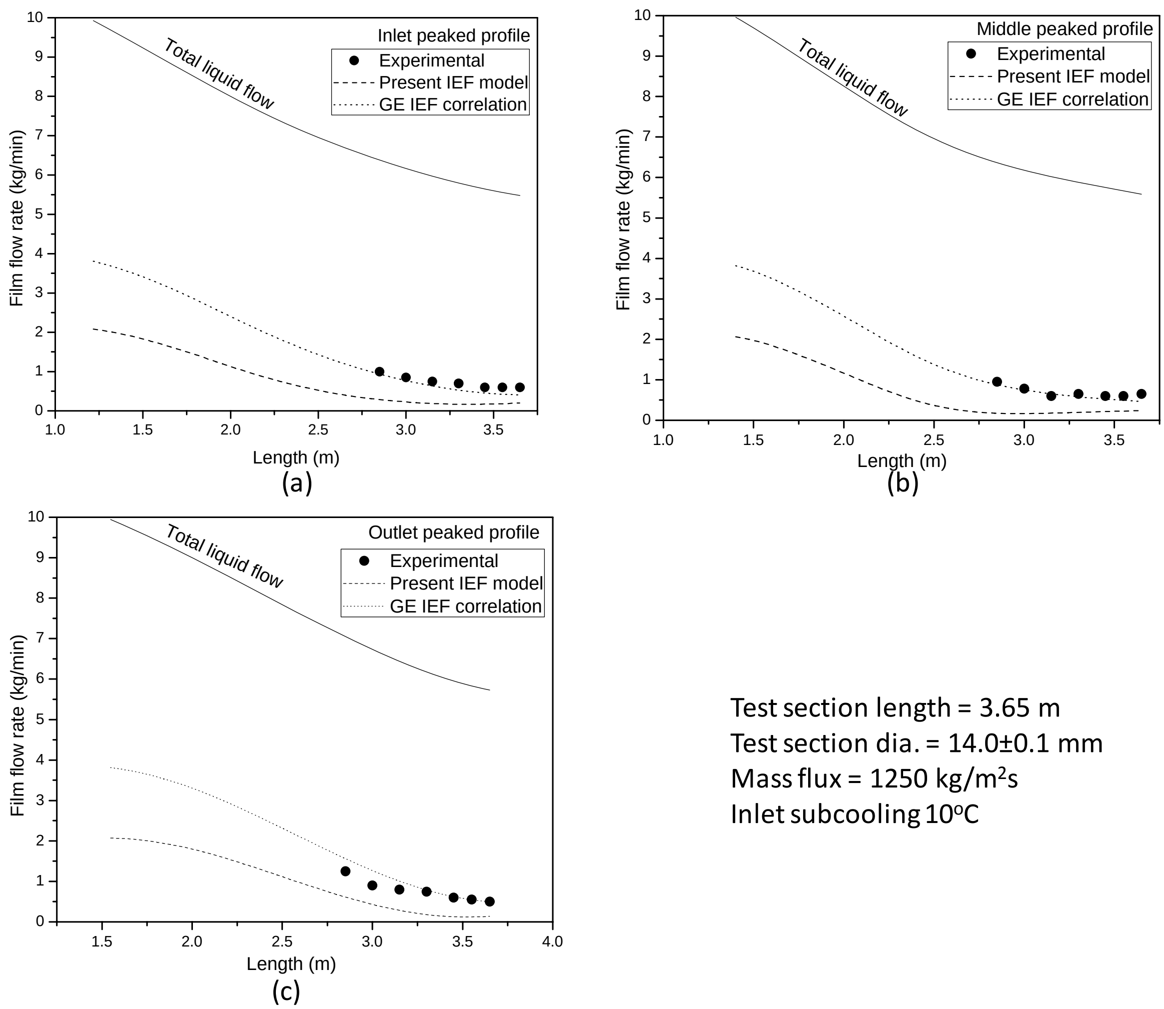

Figure 4-6: Comparison of predicted and measured film flow rates for (a) inlet, (b) middle and (c) outlet peaked heat flux profile. Results are shown for present IEF methodology and GE IEF correlation[75]

It can also be noted from the comparisons that the trend of reduction of film flow rate along the length is captured nicely by the Hewitt and Govan [4] entrainment-deposition correlations.

4.2.2 Improvement in dryout predictions with the new model

To gauge whether and to what extent improvement is obtained upon using the new IEF methodology, predictions are made for experimental dryout data of Becker et al. [72]. This dataset has been chosen primarily due to the wide range of pressures from 2.2 to 101 bar, mass flux of 120 to 5450 kg/m^{2}s and length-to-diameter (l/d) ratios from 40 to 792. The total number of experimental data points is around 3300. These data are for uniformly heated tubes. For the computation of dryout, an iterative approach is employed. The test section geometry is simulated with a certain input power which is adjusted till film flow rate becomes zero at the tube exit.

Table 4-1: Correlation sets studied for comparison

Set no.	Deposition rate	Entrainment rate
1	Katto, eqn. (2.11)	Tomiyama et al., eqn. (2.19)
2	Katto, eqn. (2.11)	Ishii and Mishima, eqn. (2.20)
3	Paleev and Filipovich, eqn.(2.7)	Kataoka et al., eqn. (2.17)
4	Okawa et al., eqn.(2.15)	Adamsson and Anglart, eqn. (2.21)
5	Hewitt and Govan, eqn. (2.12)	Hewitt and Govan, eqn. (2.24)
6	Paleev and Filipovich, eqn.(2.7)	Ishii and Mishima, eqn. (2.20)

Dryout is computed using the different correlation sets (Table 4-1) and effect of using the new IEF prediction scheme contrasted against an ad-hoc high IEF (=0.99). A high value has been used due to the fact that most (rather all) of the present mechanistic models ascribe a high value to IEF. Though it may be argued that the IEF being used is too high, it is also worth mentioning that in absence of any methodology to predict IEF or any strong prescriptions for it, any high value can be considered appropriate. Nevertheless, this concern is addressed, to some extent, later in this section.

Application of an ad-hoc high value of 0.99 as IEF leads to the predictions as shown in plots on the left (i.e., (a)) in Figure 4-7 to Figure 4-12. It is seen that all the correlation sets then under-predict (set 3 and 6 by as much as 60%) the dryout data. The incorporation of the new IEF prediction methodology (plot b in Figure 4-7 to Figure 4-12) reduces this tendency to under predict. The extent of improvement in prediction is however seen to be different for different correlations.

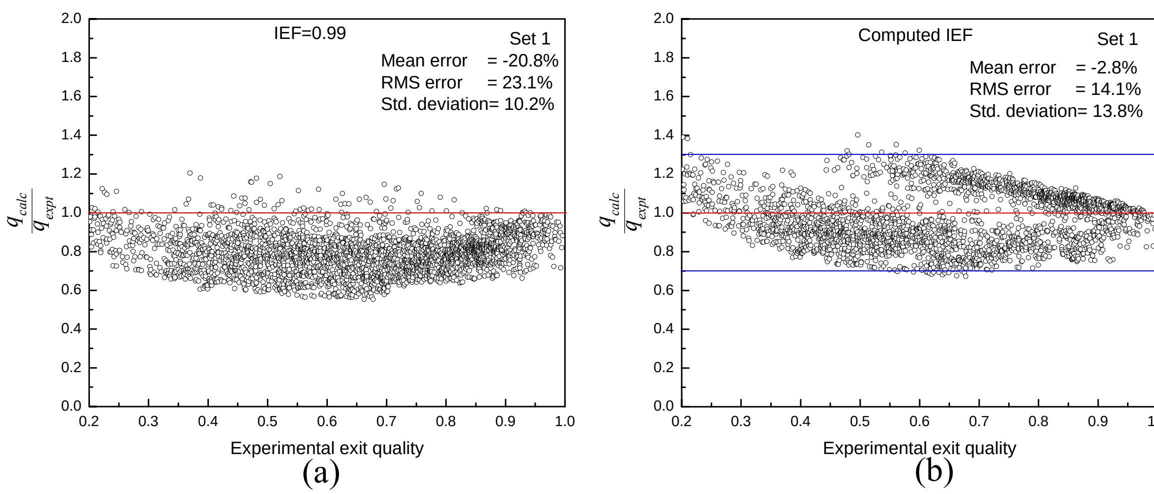

Figure 4-7: Becker et al. [72] **dryout data predicted with set 1 correlations with (a) ad-hoc IEF =0.99 and (b) IEF predicted using new methodology**

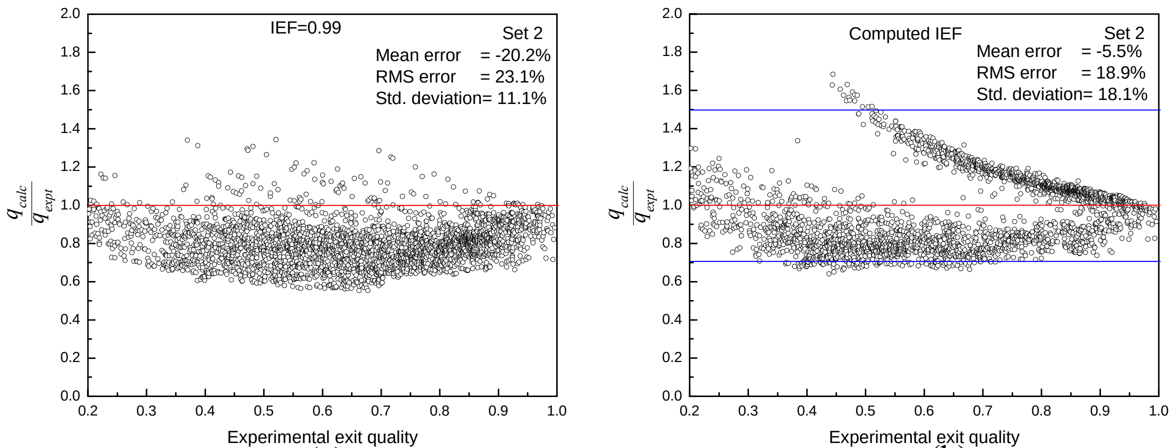

(a) (b)

Figure 4-8: Becker et al. [72] **dryout data predicted with set 2 correlations with (a) ad-hoc IEF =0.99 and (b) IEF predicted using new methodology**

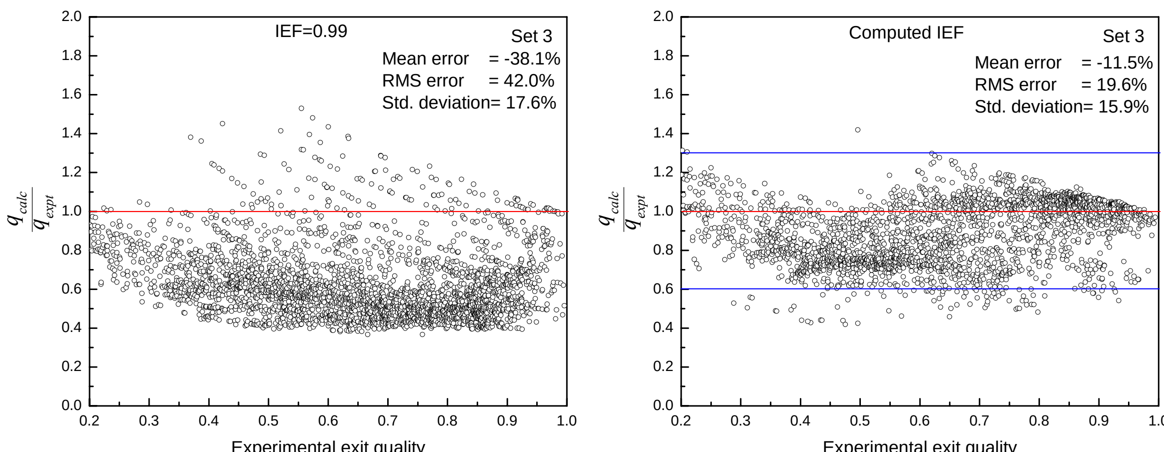

(a) (b)

Figure 4-9: Becker et al. [72] **dryout data predicted with set 3 correlations with (a) ad-hoc IEF =0.99 and (b) IEF predicted using new methodology**

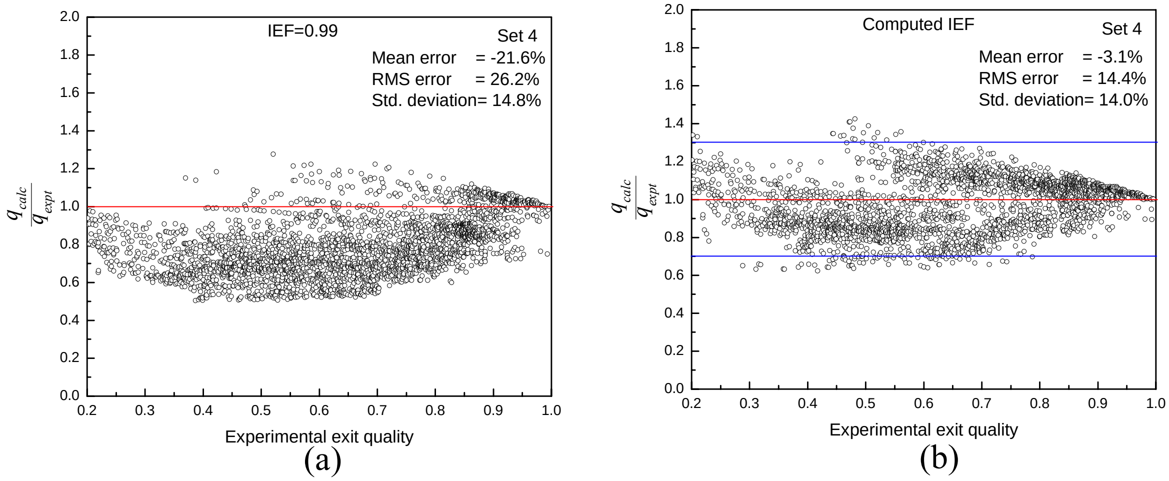

Figure 4-10: Becker et al. [72] **dryout data predicted with set 4 correlations with (a) ad-hoc IEF =0.99 and (b) IEF predicted using new methodology**

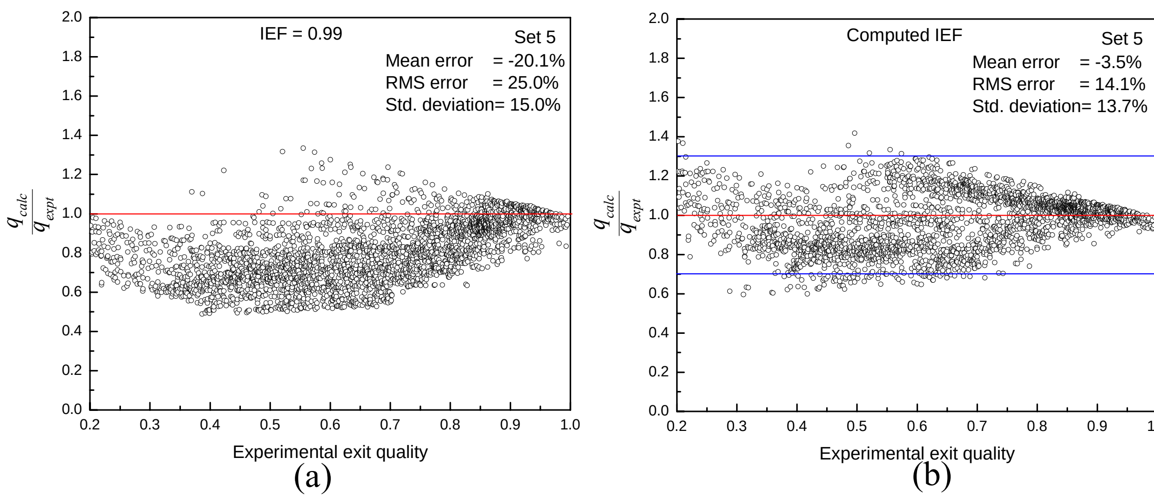

Figure 4-11: Becker et al. [72] **dryout data predicted with set 5 correlations with (a) ad-hoc IEF =0.99 and (b) IEF predicted using new methodology**

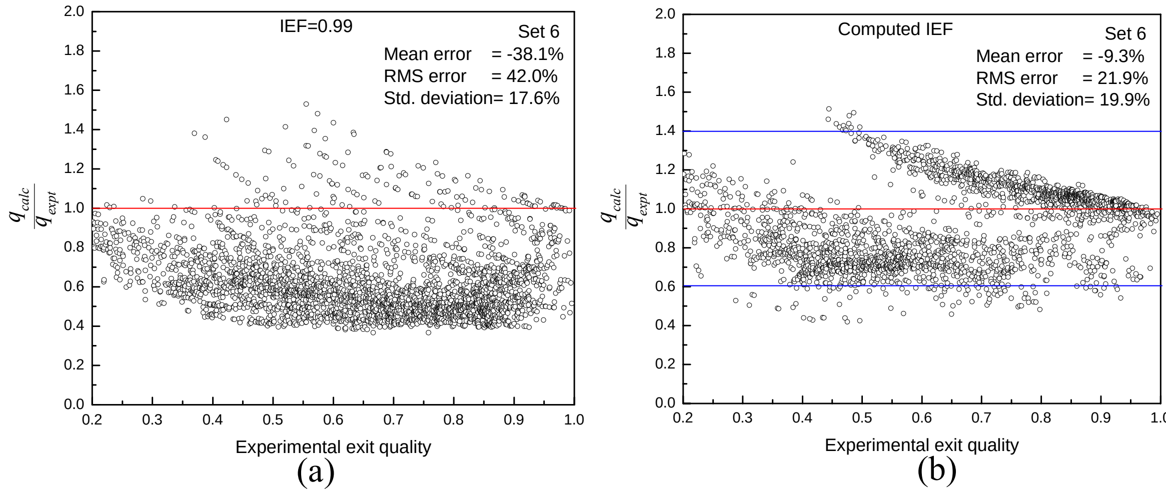

Figure 4-12: Becker et al. [72] **dryout data predicted with set 6 correlations with (a) ad-hoc IEF =0.99 and (b) IEF predicted using new methodology**

The predictions with the new methodology are seen to be divided into two distinct regions for sets 1, 3 and 6. This is a reflection of the low and high IEF predicted by the new methodology.

Sets 3 and 6, due to the similarity of both entrainment and deposition rate correlations predict dryout identically for IEF =0.99. When the new IEF prediction methodology is used, set 3 predictions are seen to improve much more than set 6. In fact, upon a visual glance on the plots, it is evident that set 3 benefits the most from the new methodology and set 2 the least. In fact for set 2, it may be said that the predictions with the predicted IEF are actually poorer in terms of standard deviation implying a greater scatter in predictions. Though, there is an improvement in the mean and RMS errors.

The improvement obtained is quantified in Table 4-2 where the errors are listed for the different correlations.

Table 4-2: Effect of new IEF prediction methodology quantified statistically

	IEF = 0.99			IEF predicted with new methodology		
	Mean Error (%)	Std. dev. (%)	RMS Error (%)	Mean Error (%)	Std. dev. (%)	RMS Error (%)
Set 1	-20.8	10.2	23.1	-2.8	13.8	14.1
Set 2	-20.2	11.1	23.1	-5.5	18.9	18.1
Set 3	-38.1	17.6	42.0	-11.5	15.9	19.6
Set 4	-21.6	14.8	26.2	-3.1	14.0	14.4
Set 5	-20.1	15.0	25.0	-3.5	13.7	14.1
Set 6	-38.1	17.6	42.0	-9.3	19.9	21.9

For all the correlation sets (except set 2), an overall improvement is observed upon using the IEF methodology. However, it is evident that sets 1, 4 and 5 predict better than other correlation sets and the question of the better set of entrainment-deposition correlation arises. A comparison of predicted dryout power alone cannot be used to judge the correlations and a more comprehensive assessment is presented in chapter 5.

An idea of the range of IEF obtained using the new methodology can be obtained by plotting the IEF obtained while simulating Becker et al. [72] dryout data. This is done in Figure 4-13 which shows the variation of predicted IEF with pressure and mass flux corresponding to tubular experiments of Becker et al. [72]. Additionally, the variations with pressure and mass flux alone are plotted as projections on the respective planes. The predicted variation of IEF seems complex and it is not possible to sum it up very conclusively. However it can be said that:

1. The methodology predicts that IEF should be high at high mass fluxes (greater than 1000 kg/m^{2}s). This seems reasonable considering greater interfacial shear and higher entrainment at high mass fluxes.
2. At representative operating conditions of BWRs, i.e., pressure of ~70 bar and mass flux of 1000-1600 kg/m^{2}s, IEF of 0.7 to 0.95 has been predicted by the

methodology. These values are quite close to the (relatively uninformed) values of IEF used by different researchers. For instance Ahmad et al. [154] have used an IEF of 0.7 while Naitoh et al. [27] have used 0.95.

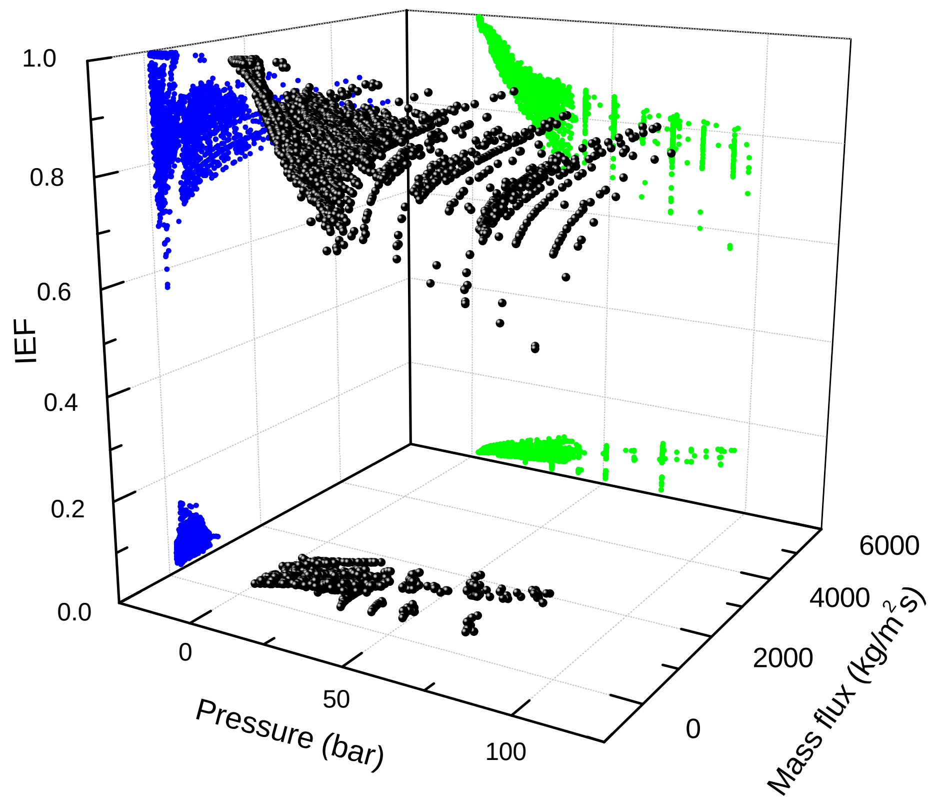

Figure 4-13: IEF predicted using new methodology

It has been noted earlier that IEF = 0.99 has no strong basis. It may in fact be argued that contrasting the newly developed methodology with such a high IEF itself tilts the balance in favor of the new methodology. Hence, dryout power was also computed by using the new correlation developed at GE-Hitachi [75] for IEF prediction and Hewitt and Govan [4] correlations for deposition and entrainment rates. This set was used in light of good performance as observed earlier. The results show that usage of GE correlation leads to gross over prediction of dryout power, though the agreement significantly improves at high qualities. However this agreement may be attributed more to the deposition and entrainment rate correlations rather than IEF predictions as sensitivity to IEF reduces with length in annular flow and dryout at higher qualities generally imply annular flow persisting over longer length.

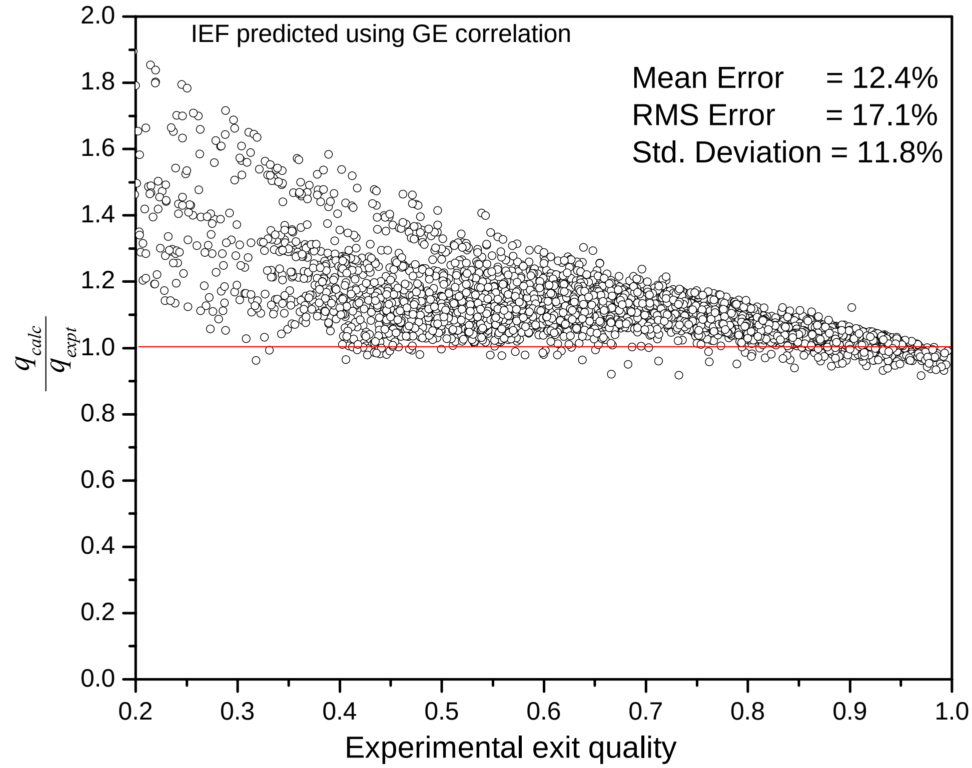

Figure 4-14: Becker et al. [72] **dryout data predicted with set 5 correlations and GE correlation** [75] **for IEF prediction**

In summary, it may be stated that while there are certain cases (as in Figure 4-6) where the GE experimental IEF correlation performs better than the presently developed methodology, it does not fare well in terms of dryout prediction. The lesser credibility for dryout prediction is also due to the fact that usage of GE correlation leads to over prediction of dryout power which is plainly not conservative. And, conservatism is highly stressed in the nuclear industry in case of uncertainty.

Further, it has been seen that in certain cases (as in Figure 4-5), IEF may have low values as against general perception. In those cases, both the GE correlation and present methodology do not predict a high initial entrainment, though there is large difference in their IEF predictions. It is not possible to label one as closer (or farther) to real value as the experiment does not indicate that.

In view of the above, the benefit of the present methodology is to provide a theoretical framework for estimation of IEF. The advantage of this framework over those developed by Ahmad et al. [73] and Wang et al. [74] is that the predicted IEF is independent (which it should be!) of deposition and entrainment rate correlations. Moreover, the differences between the predictions of the present methodology and GE correlation (which is purely experimental) are not starkly different which is reassuring.

4.3 Concluding remarks

A new methodology for estimation of IEF has been presented in this chapter. The new methodology exploits and highlights the importance of distribution of phasic flow fields on pressure drop. The IEF methodology takes the effect of churn flow into account and provides a rationale for high (or low) IEF. The IEF predictions seem to be reasonable when compared against entrained fraction obtained by extrapolating entrained flow data in a tube. The use of IEF prediction methodology is seen to improve dryout predictions for most of the correlation sets. Further, it is seen that for conditions representative of nominal operating conditions of BWRs, the values of entrained fraction predicted in this work are in the range of 0.7-0.95. These values also represent what have been used by different researchers.

In principle IEF is a stochastic quantity due to the phenomena of bursting of liquid slugs leading to initial entrainment of liquid into the vapor core. The values that come out of the methodology are thus possibly only indicative of the values which might exist. It must be also emphasized that the present work endorses the developed methodology for IEF prediction to a greater extent than the correlations used in the methodology (though reasonable results have been obtained upon using them). The simplified triangular relationship may be replaced with some other similar correlation or the reference pressure drop correlation may be different from Lockhart and Martinelli [151] correlation.

That there is scope for improvement in the triangular relationship is evident from Figure 3-31 and Figure 3-32 where the predicted film thickness is substantially higher than measured values. Also, a more appropriate reference correlation might be one where two-phase pressure gradient can be evaluated as a function of heat flux. It seems intuitively that heat flux can have an effect on IEF and heat flux dependent pressure gradient correlations would be able to consider the effect better.

5 ASSESSMENT OF THE RATE CORRELATIONS AND MODEL PRESCRIPTION

As has been discussed in chapter 2, over time, many phenomenological models have been developed for prediction of CHF. In view of the applicability of the basic model over a wide range of geometries and operating conditions lot of interest has been shown in application of the model and further improvements to it. However, considering the development of the mechanistic annular flow model over the last 4 decades, inevitably, there is in practice a significant number (significantly more than the ones listed in chapter 2) of correlations for each of droplet deposition rate, and droplet entrainment rate. There is often no clear guidance as to which correlation is appropriate for which circumstances. The objective of this chapter is not only to present benchmark calculations with the different correlations against variety of different conditions, but also to identify the (differing) extent to which the correlations are in some sense "physically based".

The approach followed in this work is slightly different from few other available works related to assessment of correlations like those of Okawa et al. [38] – who compared few deposition rate correlations against deposition rate data, or Secondi et al. [52] who carried out similar studies for entrainment rate. The philosophy behind the present assessment is that any use of the film flow phenomenological model, entails a need for both an entrainment and a deposition correlation. It is thus of greater interest to compare the performance of correlations in tandem (i.e., set of entrainment and deposition rate) against annular flow data. Physically too the entrainment and deposition processes are intimately linked. The entrainment of drops takes place from the waves which shape the deposition trajectory of these drops (Figure 3-1). Also, most of the parameters affecting entrainment affect deposition as well.

Numerous correlations are available both for entrainment and deposition rates. Testing all correlations is not feasible, thus few common, representative ones are chosen. Further, testing all combinations of these correlations is not practicable. Also as indicated in chapter 2, certain (not all) entrainment correlations are compatible with a certain deposition correlation. For instance, Kataoka et al. entrainment rate correlation is derived by using the Paleev and Filipovich deposition rate correlation. To a limited degree literature correlations form themselves into natural pairings, but this is not comprehensive, however starting from this the pairs listed in Table 4-1 have been adopted. One set (set 2) in the table, however, combines two correlations which have never been used in tandem in literature. However, there is in theory, no restriction on using this combination.

It is reiterated that the correlation sets listed in Table 4-1 is by no means exhaustive. The present study is an attempt to test the sets which are more frequently used in literature. It is, however, expected that the predicted trends might be indicative of the performance of not just these correlations but also of many other correlations which are slight modifications of some of these correlations (e.g., Utsuno and Kaminaga [50] built upon Ishii and Mishima [48] equilibrium entrainment correlation).

Sections 5.2-5.4 are devoted to benchmarking the performance of the correlation sets against experimental adiabatic and diabatic annular flow data and dryout data. For the benchmark, the mechanistic framework used is described in §4.2.

An analysis of the inclusion of important parameters in rate correlations, presented in §5.5, though applied to the present correlation sets, is more generic in nature and can be extended to other correlations available in literature.

The assessment also leads to identification of the better correlation set. This set coupled with the new IEF methodology developed in chapter 4 gives an improved (in terms of being self reliant for IEF estimation) mechanistic model for annular flow. Further validations of this improved model with present adiabatic data and other dryout data are presented in §5.6 and conclusions are drawn in §5.7.

5.1 Experimental dataset used for assessment

As has been highlighted above, the objective of this chapter is to check the performance of correlation sets, thus, the data sets correspond to measured annular flow parameters; entrained fraction and dryout. Experimental data for adiabatic steam-water equilibrium annular flow [23], diabatic steam-water flow [19,64] and dryout [72] have been used. The data sets used are listed in Table 5-1. Among the diabatic sets, one is a uniformly heated pipe [64], the other is a heated pipe with a cold patch [19].

In the first two cases, experimental data are available for the entrained fraction as a function of quality for different mass fluxes and pressures. An advantage of these adiabatic equilibrium flow predictions over diabatic flow predictions is that they are independent of the entrained fraction at the beginning of the test section. For diabatic flows the value of entrained fraction at the onset of annular flow (i.e. IEF) has to be assigned and the results for diabatic flow are sensitive to this value (see for instance Figure 2-20).

Comparison with the third data set checks the ability of the correlation sets to predict the history effect. In the dryout predictions (last data set), experimentally obtained dryout power is compared against the predictions.

Table 5-1: Experimental datasets used for assessment

Set no.	Dataset	Data points	Pressure (bar)	Mass flux (kg/m^{2}s)	Quality	Diameter (mm)	Heat flux (kW/m^2)
E1	Adiabatic (Wurtz [23])	93	30-90	500-3000	0.15-0.7	10, 20	---
E2	Diabatic (Keeys et al. [64])	11	68.9	1360 and 2040	0.2-0.5	12.7	1360, 2040
E3	Diabatic (Bennett et al. [19])	26	3.72	297	0.2-0.8	9.29	652
E4	Dryout (Becker et al. [72])	3300	2.2 - 101	120-5450	0.2-1.0	3.94-24.95	280-5700

5.2 Comparison of the correlations against adiabatic data

In annular two-phase flows without phase change, the only rate processes of significance are deposition and entrainment. In very long tubes, it is expected that beyond a certain length the deposition and entrainment rates balance each other leading to equilibrium entrained fraction in the gas core. Of course, true equilibrium can never really be achieved as pressure changes along the length, but the concept of an equilibrium entrained fraction is found to be a workable hypothesis, particularly for high pressure systems. There is no general prescription for what length is required to achieve equilibrium conditions, however a length equal to ~400 diameters is generally considered suitable.

The correlations for deposition and entrainment rate should be able to predict both the attainment of equilibrium after a sufficient length of annular flow, and the equilibrium entrained fraction itself at various qualities.

For the purpose of comparisons, the adiabatic data of Wurtz [23] has been used. In his experiments adiabatic steam-water annular flow was established in a 9 m long test section. The film flow rate at the end of test section was measured by means of a film extraction technique. The tube diameters used in the experiments were 10 mm and 20 mm. The corresponding length to diameter ratios of 900 and 450 respectively ensure that the data obtained are true equilibrium data. The experiments were conducted at pressures of 30, 50, 70 and 90 bar and mass fluxes between 500 and 3000 kg/m^{2}s. The comparison between the predicted and experimental values of the equilibrium entrained fraction for different pressures is shown in Figure 5-1 to Figure 5-17. The entrained fraction is plotted on the ordinate against quality.

We will first consider the performance of the various correlations as a function of pressure and mass flux and then assess the effect of tube diameter.

5.2.1 Performance of correlations for various pressures and mass flux

The predictions at 30 bar pressure are shown in Figure 5-1 and Figure 5-2. Figure 5-3 to Figure 5-5 show predictions and data for 50 bar pressure at different mass flux. Figure 5-6 to Figure 5-14 show predictions for 70 bar pressure which is typical of BWRs. The predictions at 90 bar pressure are shown in Figure 5-15 to Figure 5-17.

At a pressure of 30 bar, it is seen that Set 1 correlations predict most closely to the experimental data, followed by Set 4. The variation (with quality) of predicted entrained flow fraction (G_d/G) with set 1 and set 4 correlations is also seen to be very similar.

These correlations have a very similar form of the entrainment rate correlation (recall the equivalence between $\tau\delta/\sigma$ and π_e mentioned in §2.3.2). The other correlation sets follow the observed experimental trend, more so at high mass flux and high quality. Barring a few exceptions, similar general behavior is observed at the higher pressures of 50, 70 and 90 bar; i.e., the performance of correlations is not significantly altered due to change in pressure. Part of the reason for this might be that the correlations are constituted of fluid property terms which themselves are pressure dependent. It is further seen that sets 2, 3 and 6 which essentially use the same correlation for equilibrium entrained fraction (eq. (2.20)) lead to high entrained fraction (~1) at higher mass flux and quality. In fact, for the particular case of 70 bar with 2000 and 3000 kg/m^{2}s in 10 mm diameter tube, sets 2 and 6 predict the entrained flow rate to be higher than total liquid flow rate. This clearly unphysical situation occurs due to the asymptotic nature of hyperbolic tan function (in eq.(2.20)) at high We_m and Re_l. The issue has been highlighted and rectification has been attempted [49,155] by multiplying right hand side of equation (2.20) by a limiting entrained fraction which was found to be a function of liquid film Reynolds number. The correlation proposed however only gives the value of equilibrium entrained fraction (in other words C_{eq}). The entrainment rate is not obtainable in a straightforward manner.

Another interesting observation from figures Figure 5-1 to Figure 5-17 is the inequality of predicted entrained fraction by sets 2, 3 and 6 for many of the cases. Ideally Sets 2, 3 and 6 should predict the same values because in the limit of equilibrium annular flow, they should all reduce to the value given by Ishii and Mishima [48] correlation (eqn. (2.20)). However, it is seen that the predictions of Sets 3 and 6 differ from Set 2 particularly at high quality and high mass flux (see for instance Figure 5-1, Figure 5-2, Figure 5-5, Figure 5-9,

Figure 5-10, Figure 5-17 etc.). For certain other cases (Figure 5-4, Figure 5-8, Figure 5-12, Figure 5-13 etc.) all the three sets gave different answers. Such behavior indicates possible non achievement of deposition entrainment equilibrium by either (or all) of the sets 2, 3 and 6.

Overall, it may be concluded that:

Predictions made by Set 1 and Set 4 correlations are closest to experiments. Other sets are able to predict the trends at higher mass flux and quality. Among those sets, set 5 predicts nearest to experimental data.

The inequality of the equilibrium entrained fraction predicted by sets 2, 3 and 6 is suggestive of non achievement of deposition – entrainment equilibrium by either (or all) of the sets 2, 3 and 6.

It is interesting to compare for any one particular case the prediction of equilibrium entrainment and deposition rates and compare its behavior with the equilibrium entrained fraction. Such a comparison is shown in Figure 5-18 for the 10mm ID tube for a particular case of 70 bar pressure with mass-flux of 1000 kg/m^2s and quality of 0.5. The appropriate equilibrium entrained fraction and its predictions can be seen in Figure 5-8. From Figure 5-18, it is seen even though sets 2 and 6 attain practically same equilibrium entrained fraction, the predicted equilibrium entrainment and deposition rates are different as the correlation for deposition coefficient is different. For sets 3 and 6, where the deposition rate correlation is same and entrainment correlations are also related, both equilibrium entrained fraction and entrainment rate have similar values. It is also seen that while set 1 and 5 (and also sets 2 and 3) predict nearly the same equilibrium entrained fraction, the predicted equilibrium rates are quite different for the correlation sets.

Further, different correlation sets predict different lengths to achieve equilibrium. For this case, set 2 and set 6 take a length which is seemingly too high than what is commonly perceived for achievement of equilibrium.

In summary, it may be said with respect to comparison of the correlations that predicted equality of entrained fraction does not imply parity in the entrainment and deposition rates. This coupled with insufficient information in the non-equilibrium region justifies the comparison of correlation sets to be extended to heated tubes (§5.3) where the effects of non-equilibrium of entrainment and deposition rates are marked. Such studies are also warranted considering the local effects spacers might have on droplet distribution (see discussion in §4.2.1 with relation to Figure 4-5).

5.2.2 Effect of tube diameter on entrained fraction

The data and predictions at 70 bar for 10 mm and 20 mm ID tubes can be contrasted by comparing Figure 5-6 through Figure 5-9 with Figure 5-11 through Figure 5-14. From the figures it is seen that the experimental entrained fraction increases with diameter.

This can be explained as follows: For the same mass flux, an increase in diameter increases the mass flow rate with the square of the diameter. With the same mass flux and quality, and hence similar axial velocities, the equilibrium film thickness and velocity will tend to be similar, so the liquid film flow rate is likely to vary with diameter (proportional to perimeter). The fraction of liquid flowing in the film thus is to be expected to decrease with diameter.

This effect is indeed captured by all the correlation sets, though exact correspondence with experimental data is not seen for many of the cases.

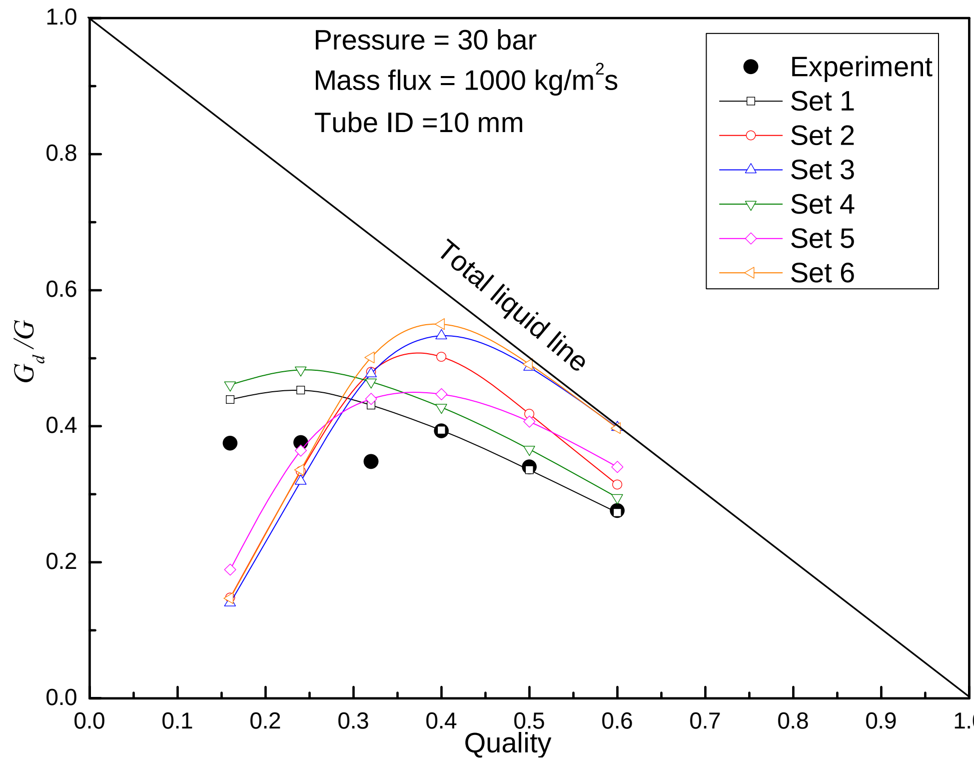

Figure 5-1: Predicted equilibrium entrained fraction compared against experimental data [23]

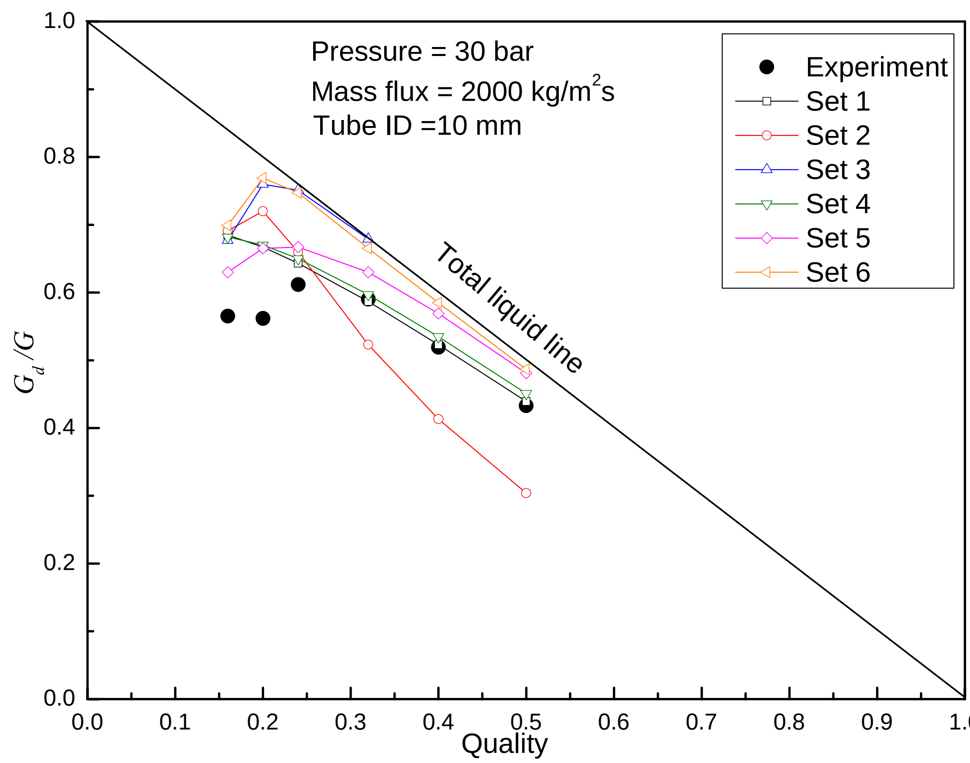

Figure 5-2: Predicted equilibrium entrained fraction compared against experimental data [23]

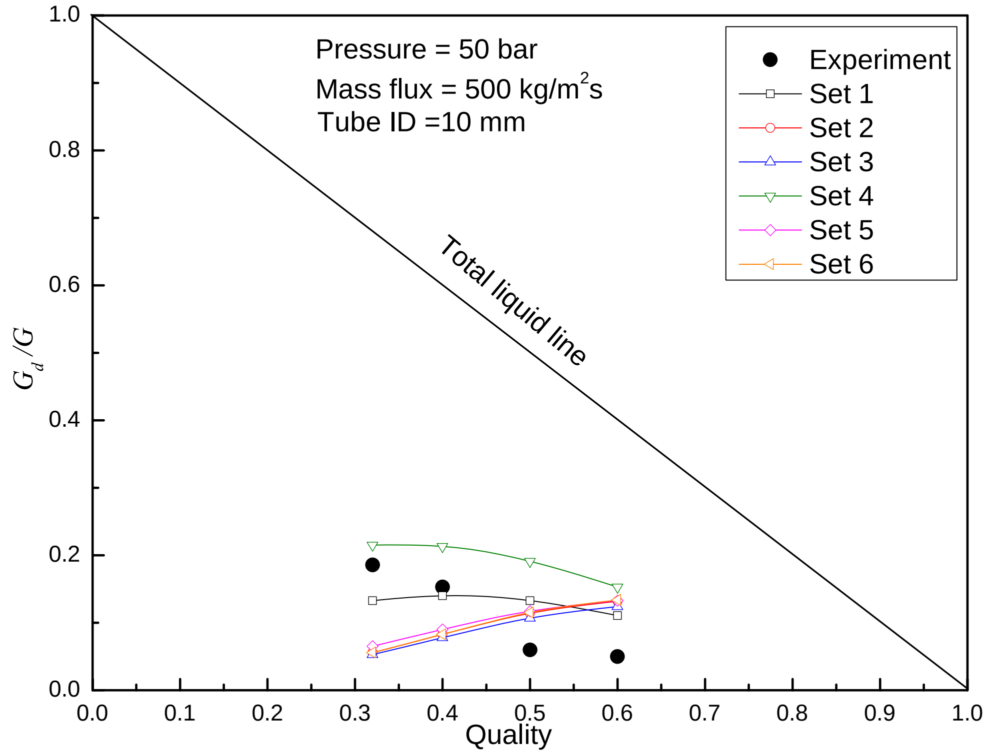

Figure 5-3: Predicted equilibrium entrained fraction compared against experimental data [23]

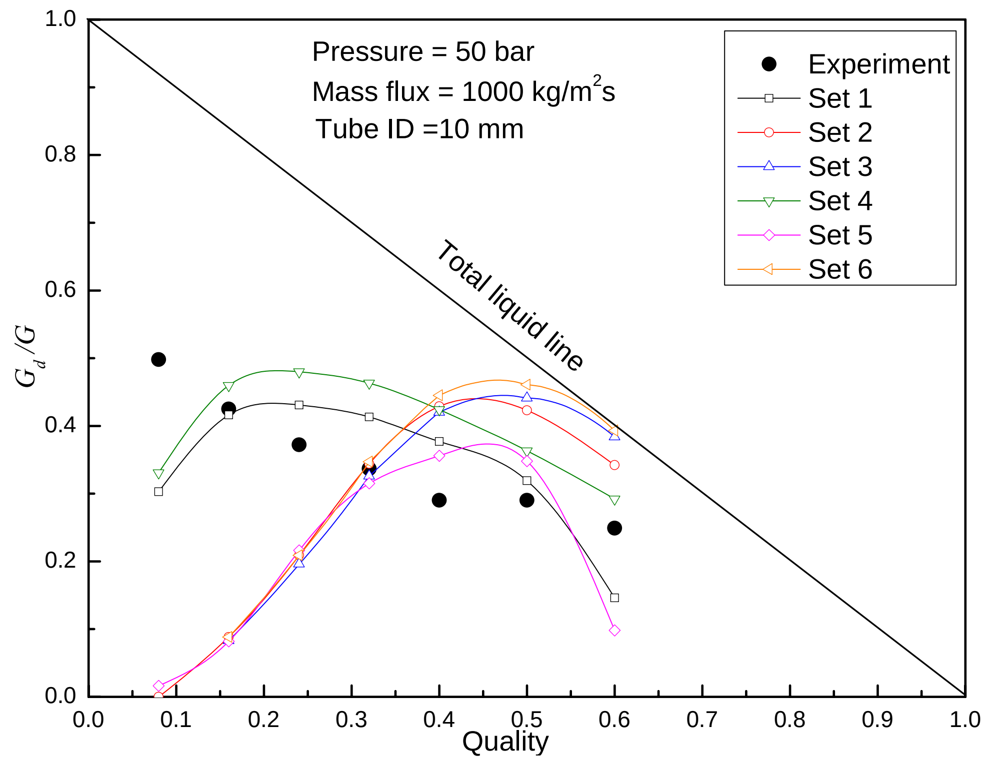

Figure 5-4: Predicted equilibrium entrained fraction compared against experimental data [23]

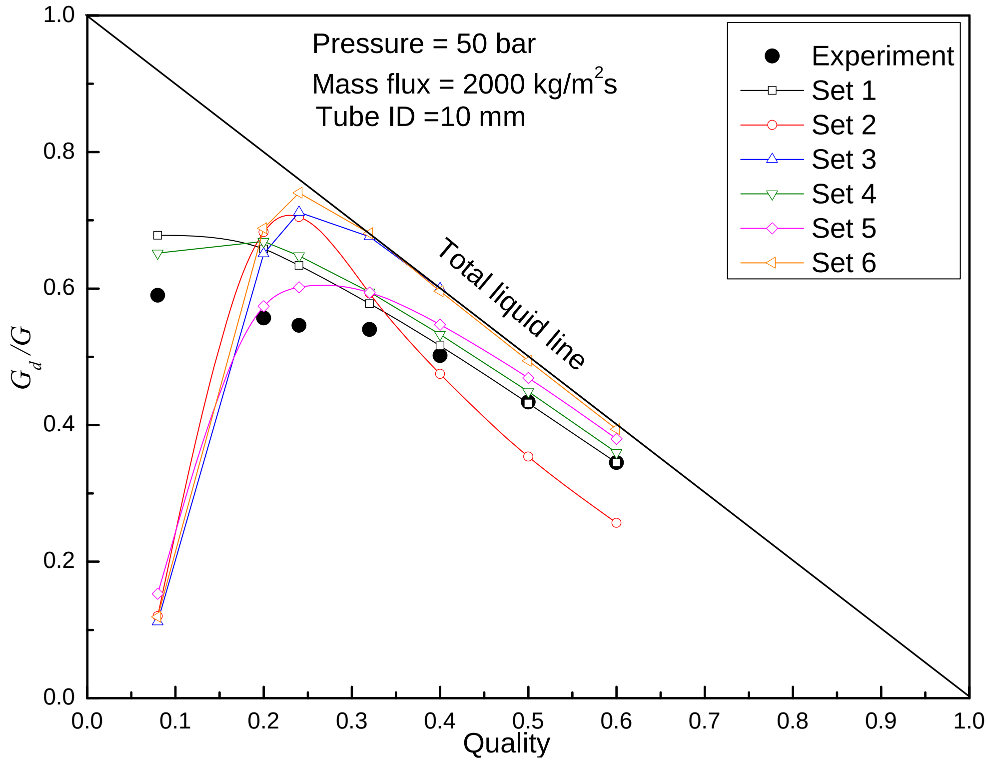

Figure 5-5: Predicted equilibrium entrained fraction compared against experimental data [23]

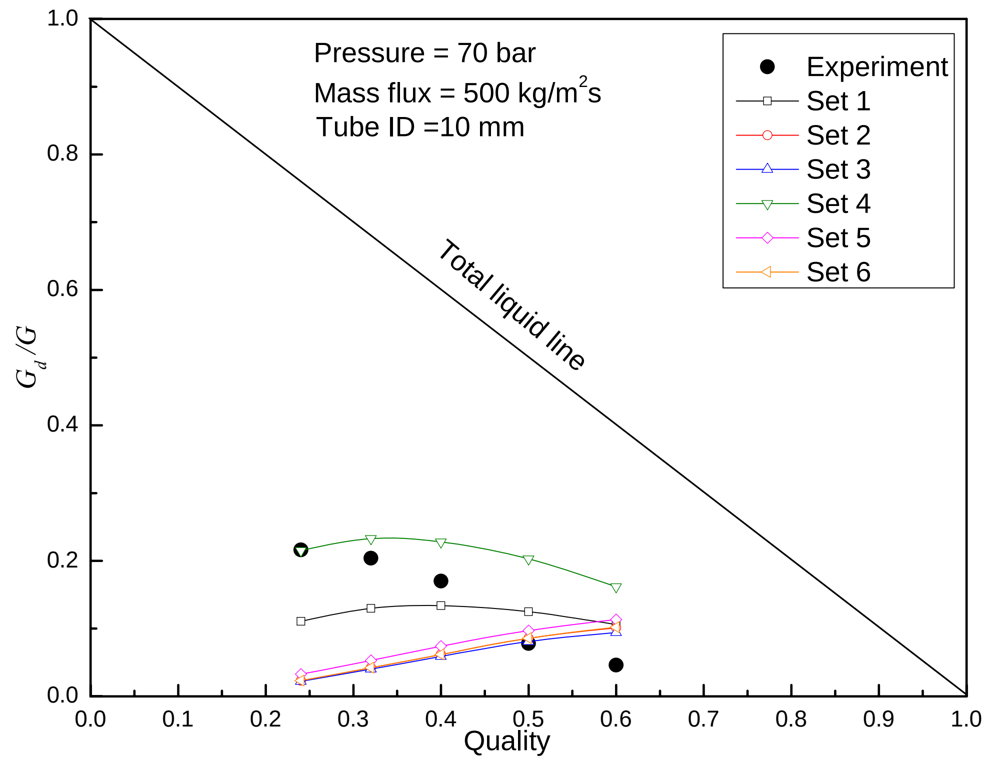

Figure 5-6: Predicted equilibrium entrained fraction compared against experimental data [23]

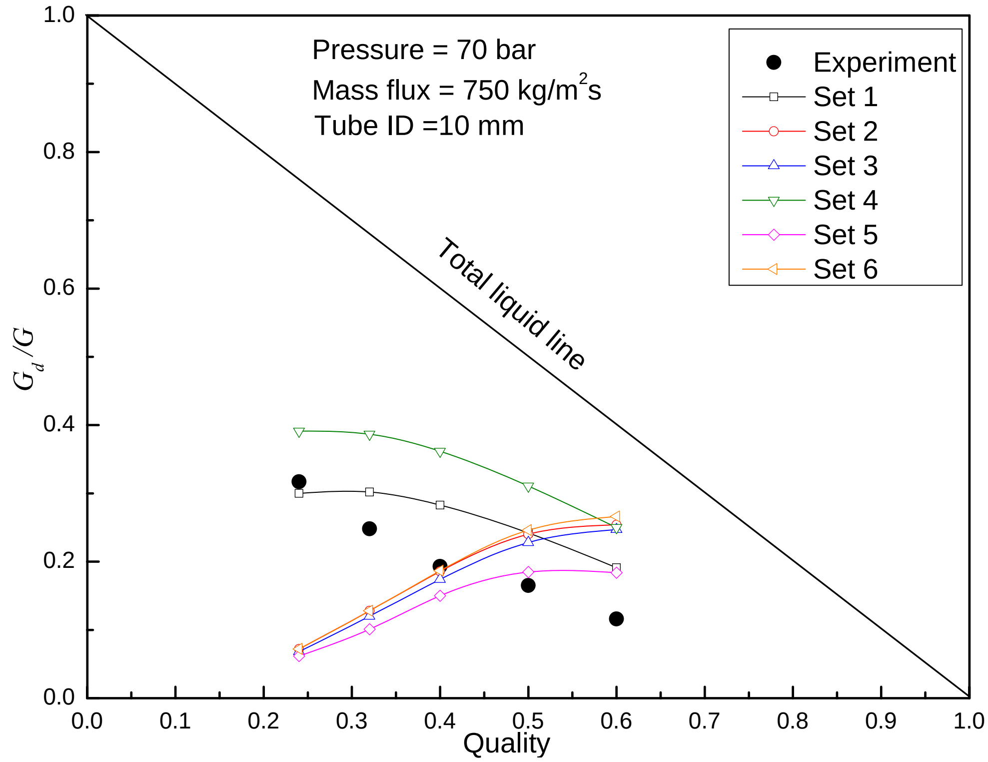

Figure 5-7: Predicted equilibrium entrained fraction compared against experimental data [23]

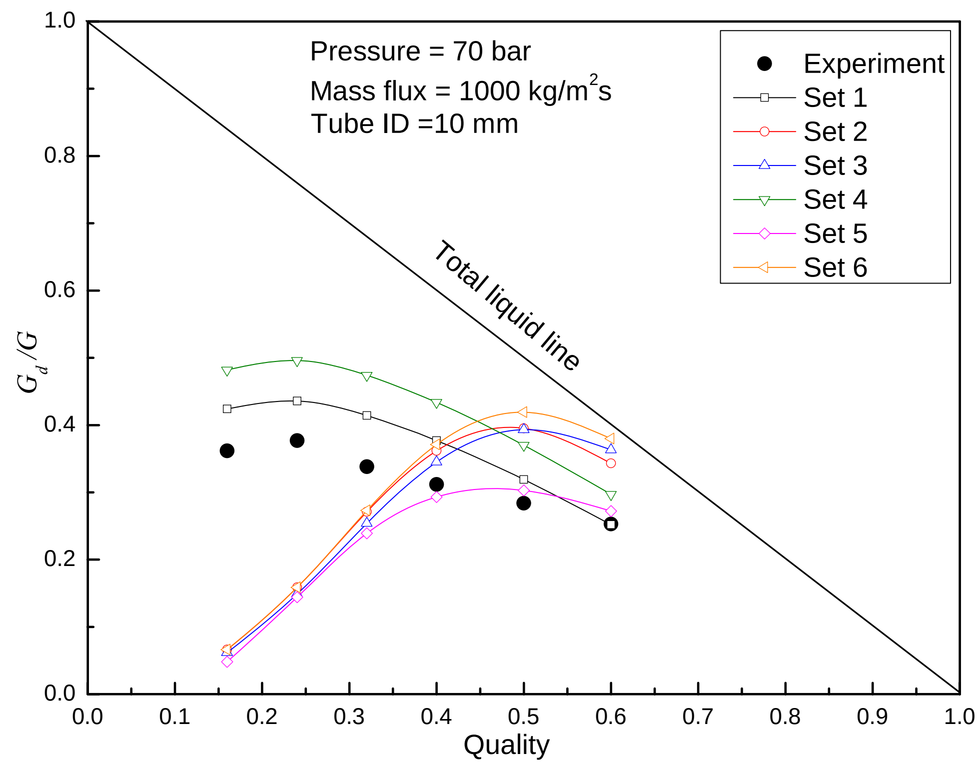

Figure 5-8: Predicted equilibrium entrained fraction compared against experimental data [23]

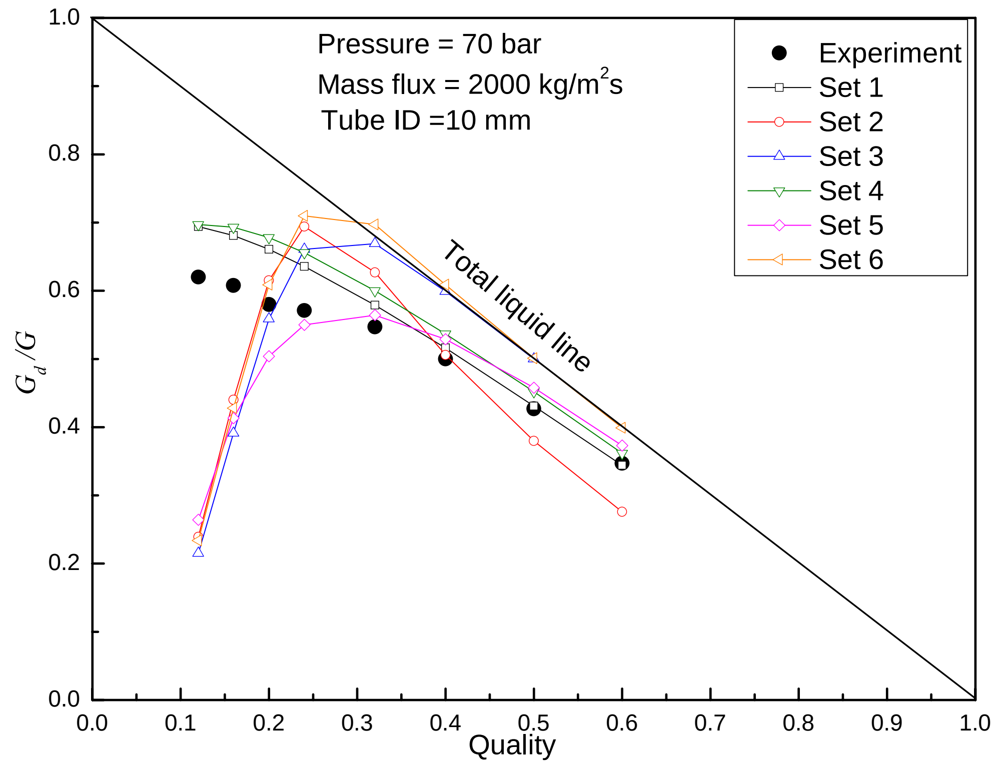

Figure 5-9: Predicted equilibrium entrained fraction compared against experimental data [23]

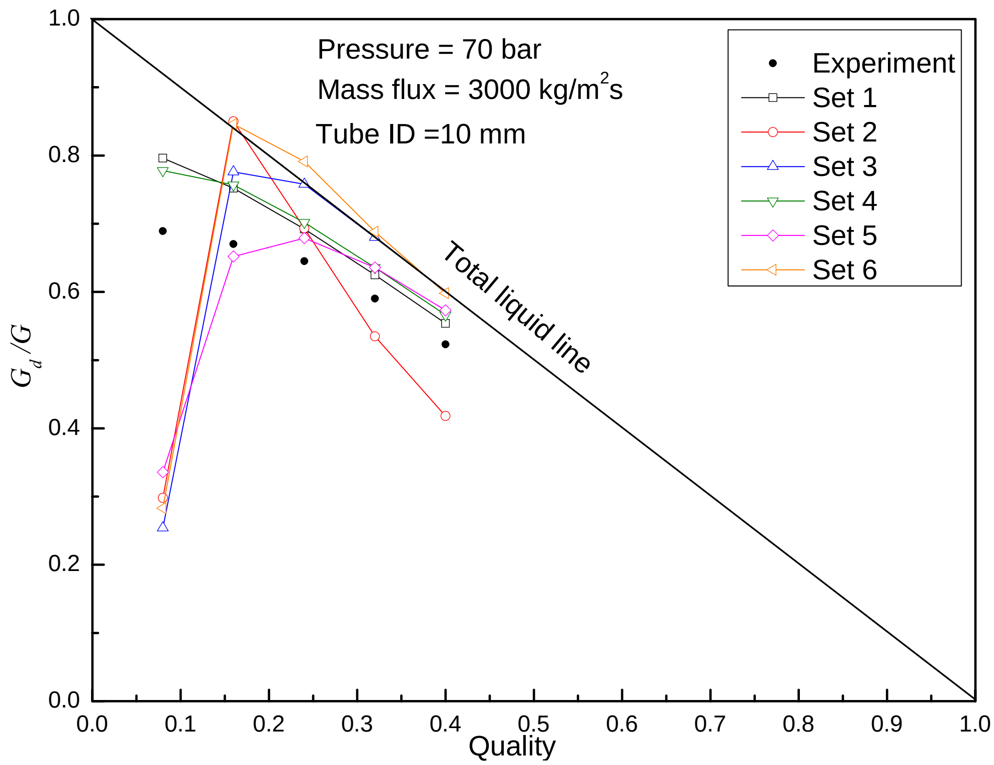

Figure 5-10: Predicted equilibrium entrained fraction compared against experimental data [23]

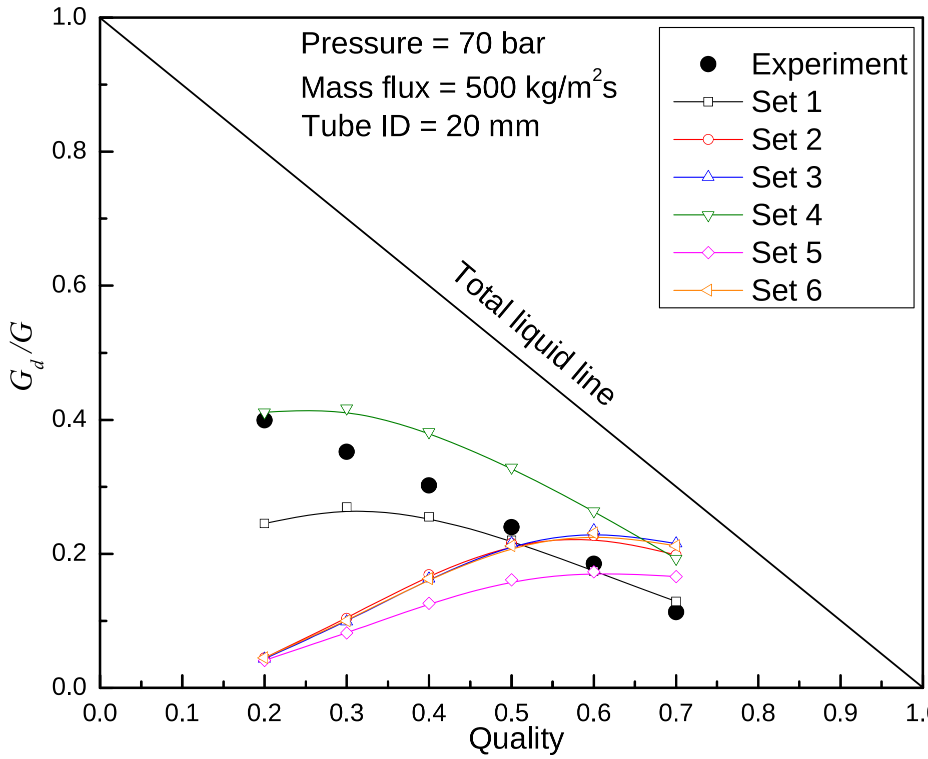

Figure 5-11: Predicted equilibrium entrained fraction compared against experimental data[23]

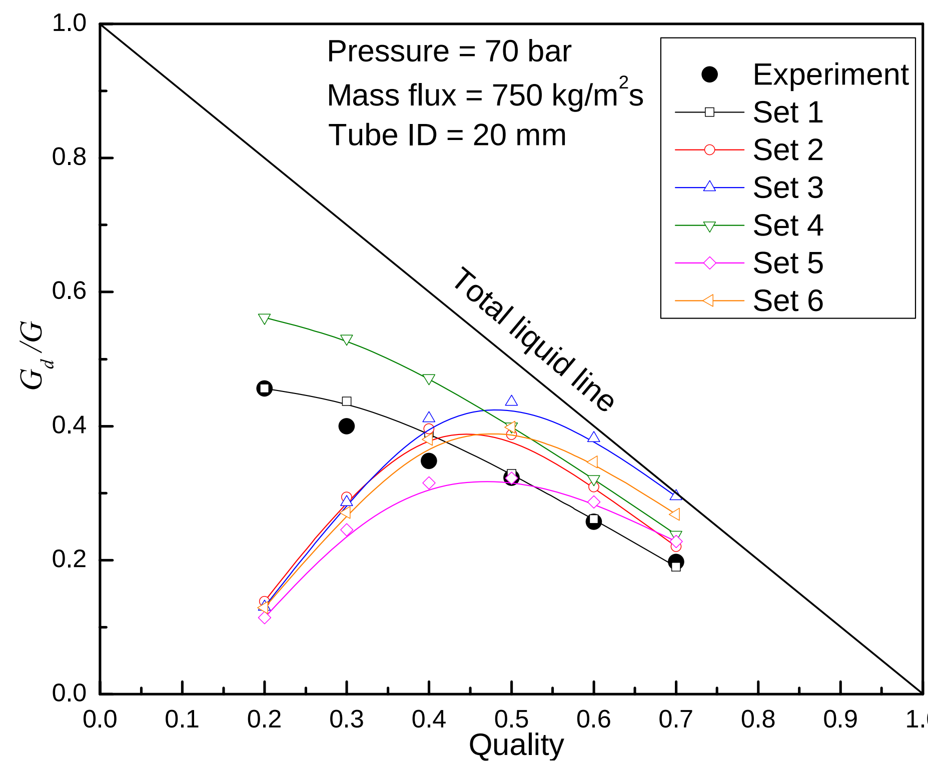

Figure 5-12: Predicted equilibrium entrained fraction compared against experimental data [23]

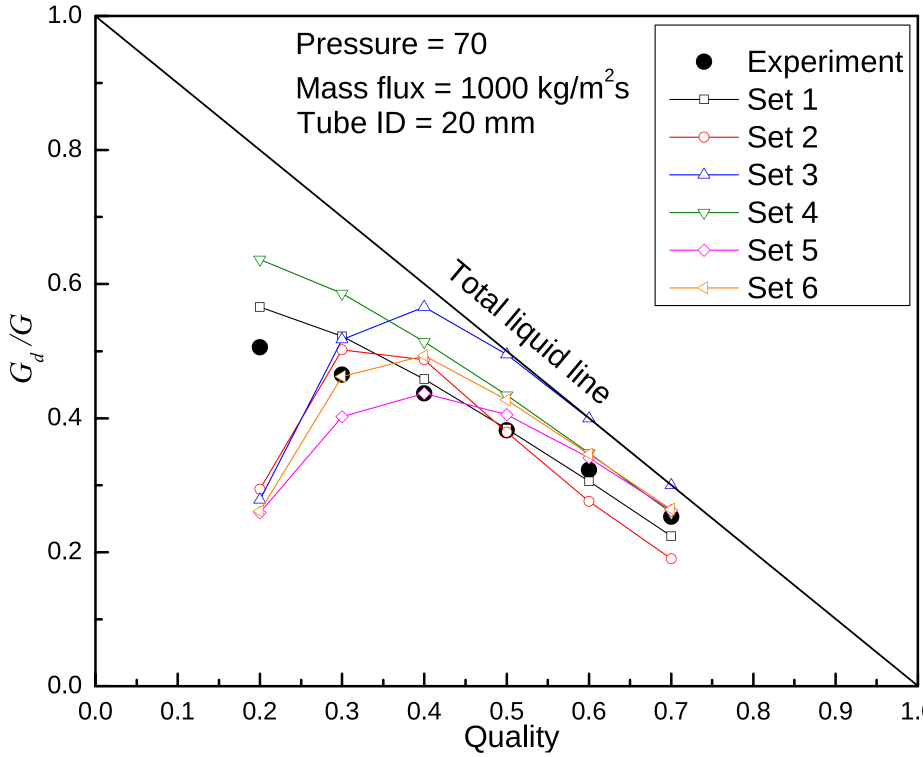

Figure 5-13: Predicted equilibrium entrained fraction compared against experimental data [23]

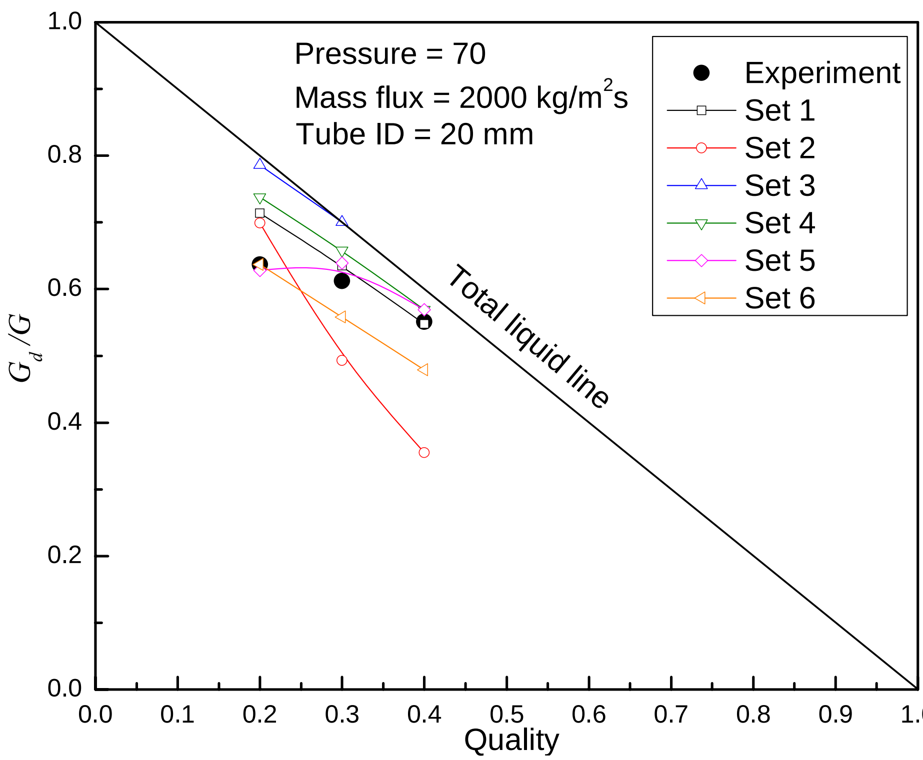

Figure 5-14: Predicted equilibrium entrained fraction compared against experimental data [23]

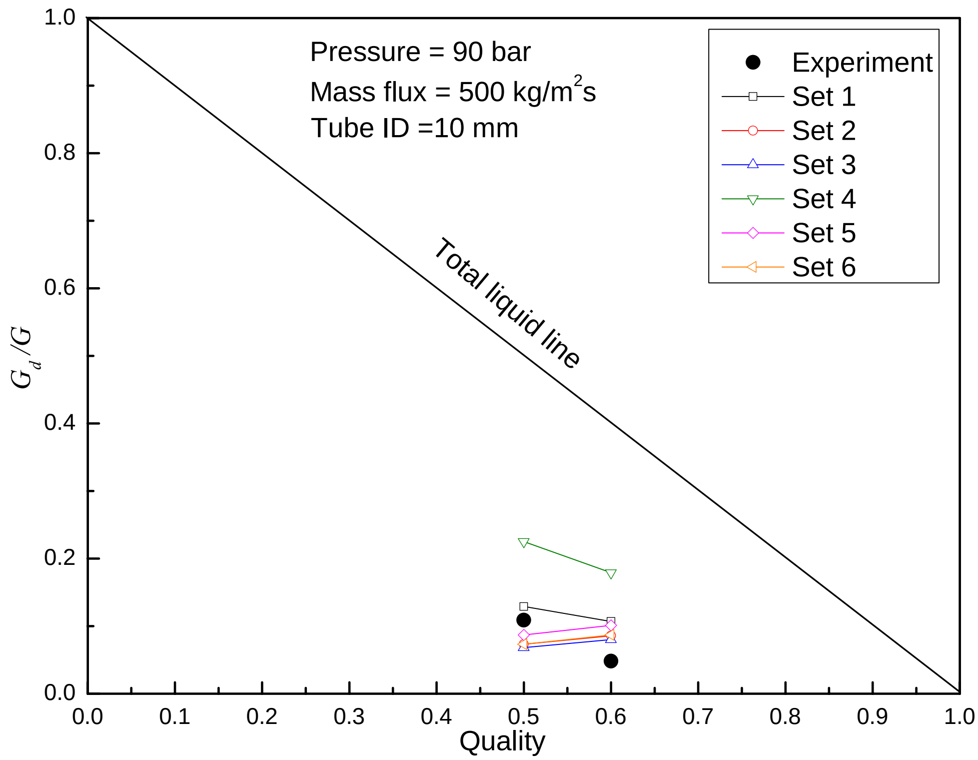

Figure 5-15: Predicted equilibrium entrained fraction compared against experimental data [23]

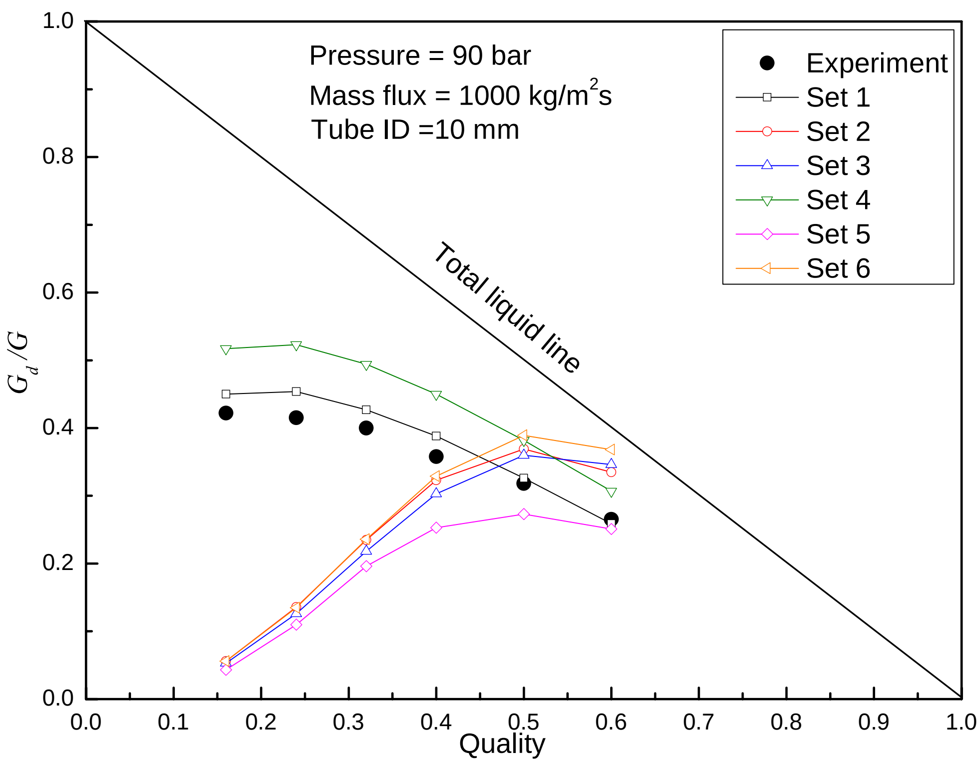

Figure 5-16: Predicted equilibrium entrained fraction at compared against experimental data [23]

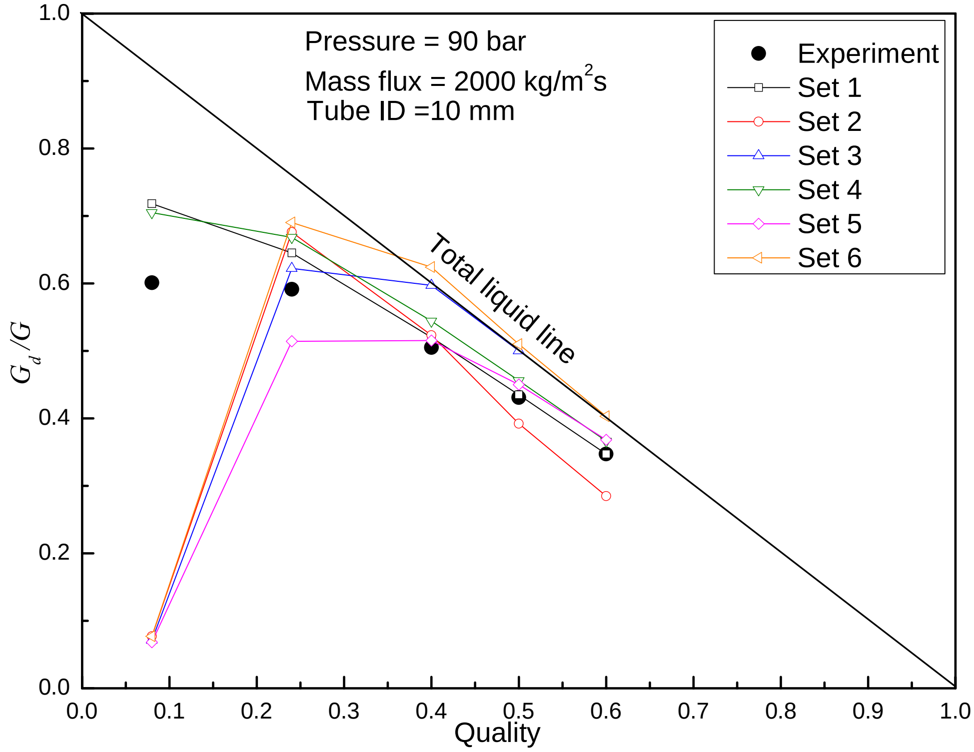

Figure 5-17: Predicted equilibrium entrained fraction compared against experimental data [23]

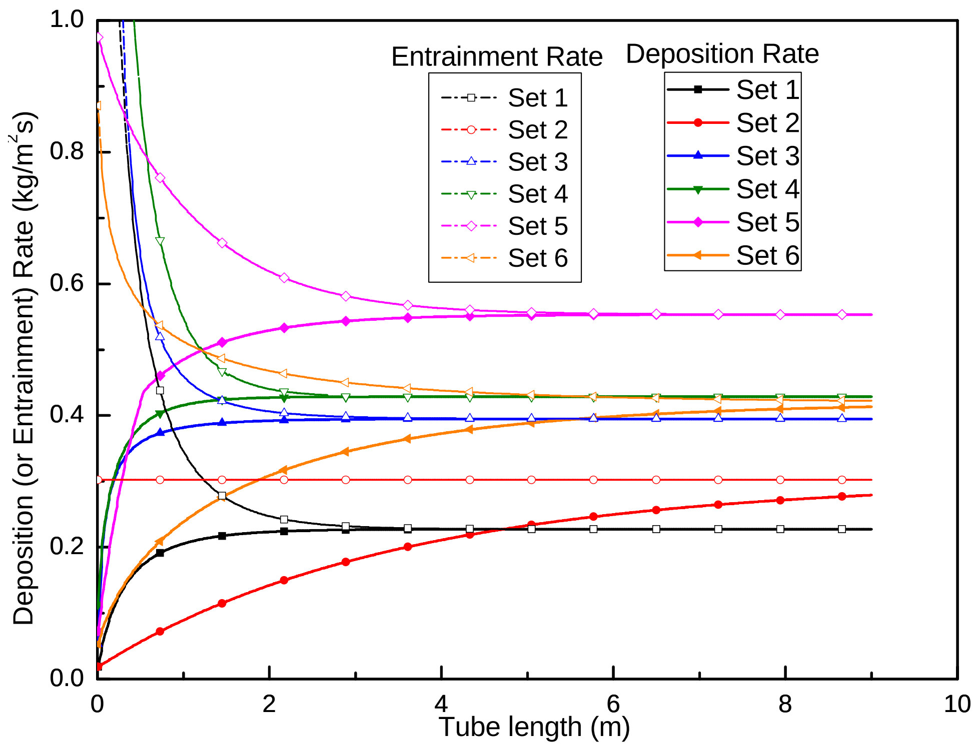

Figure 5-18:Predicted entrainment and deposition rate along a 9 m long tube (mass flux 1000 kg/ m^{2}s, 70 bar, 10 mm tube bore)

5.3 Comparison of the correlations against diabatic data

The need for simulating non-equilibrium data as highlighted in §5.2.1 can be met by simulation of diabatic data. In boiling flows equilibrium is never achieved and the entrained fraction continually evolves along the length. In the present section, the performance of correlations is compared against two sets of heated tube data. In these cases, the results would depend on Initial Entrained fraction (IEF). IEF is predicted using the new methodology developed in this work (§4.1).

5.3.1 Uniformly heated tube experiments (Keeys et al. [64])

The Keeys et al. [64] experiments in effect measured entrained flow rate as a function of axial position. This was done by extracting the film and measuring its flow rate at the end of the heated section for a series of cases with different heated lengths, but with the linear heat flux (and other quantities) held constant. The entrained liquid mass flow rate is then evaluated from the film flow rate and heat input.

The test section diameter was 12.7 mm and operating pressure was 68.9 bar. Measurements were made for mass fluxes of 1398 and 2040 kg/m^{2}s, with respective heat fluxes of 990 and 1140 kW/m^2.

In Figure 5-19 and Figure 5-20 are plotted the Keeys et al. [64] entrainment data, along with predictions of these using the correlation sets of Table 4-1. Dryout is obtained when all the liquid gets entrained. This is signified by the intersection of the entrained flow fraction curve and the total liquid line. It can be seen that experimental data are available till very near to dryout.

For the experimental data considered, the closest predictions are made by correlation Set 1 and Set 5. In both the cases, a rise in entrainment is seen prior to dryout. This is not captured by any of the models. The entrained fraction near dryout (which is a possible indicator of how good the model would be able to predict dryout) is predicted well by sets 1, 4 and 5. Sets 2, 3 and 6 predict dryout to occur much earlier than what is experimentally observed. This under prediction of dryout qualities is possibly due to the effective assumption of maximum possible entrained fraction (entrained flow/total liquid flow) of 1 which leads to a greater tendency to achieve it.

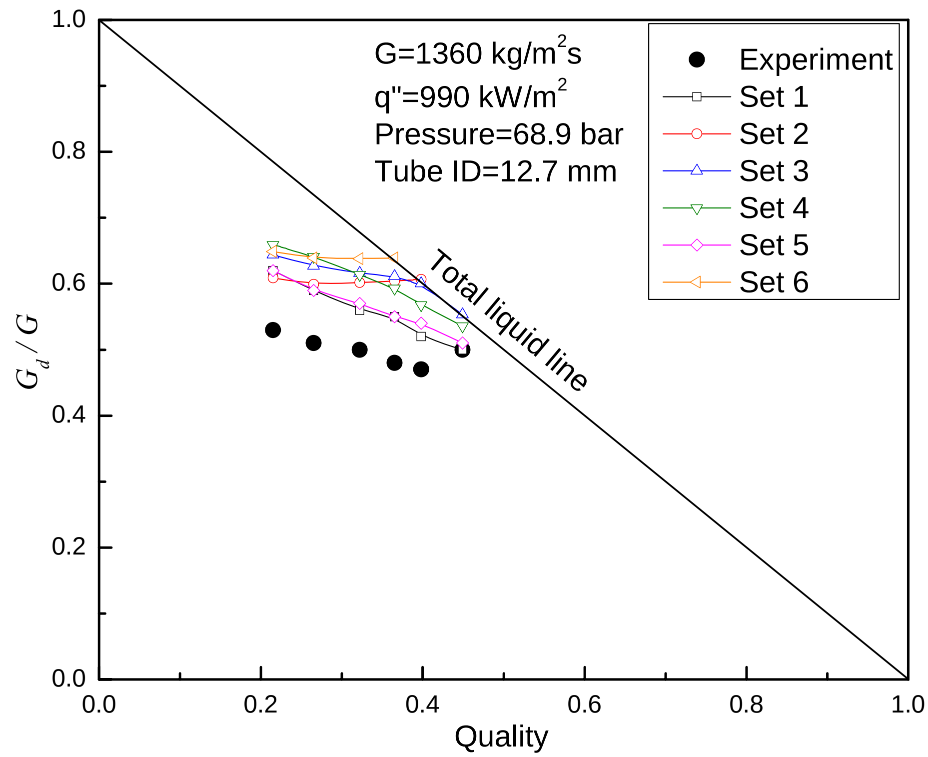

Figure 5-19: Predicted diabatic entrainment compared against Keeys et al. [64] **experimental data**

Another important observation from these graphs is that the initial entrainment fraction would be high in this case. The predictions also show a high value (as evidenced by the entrained flow rate values). These figures serve as another indirect validation of the IEF prediction methodology.

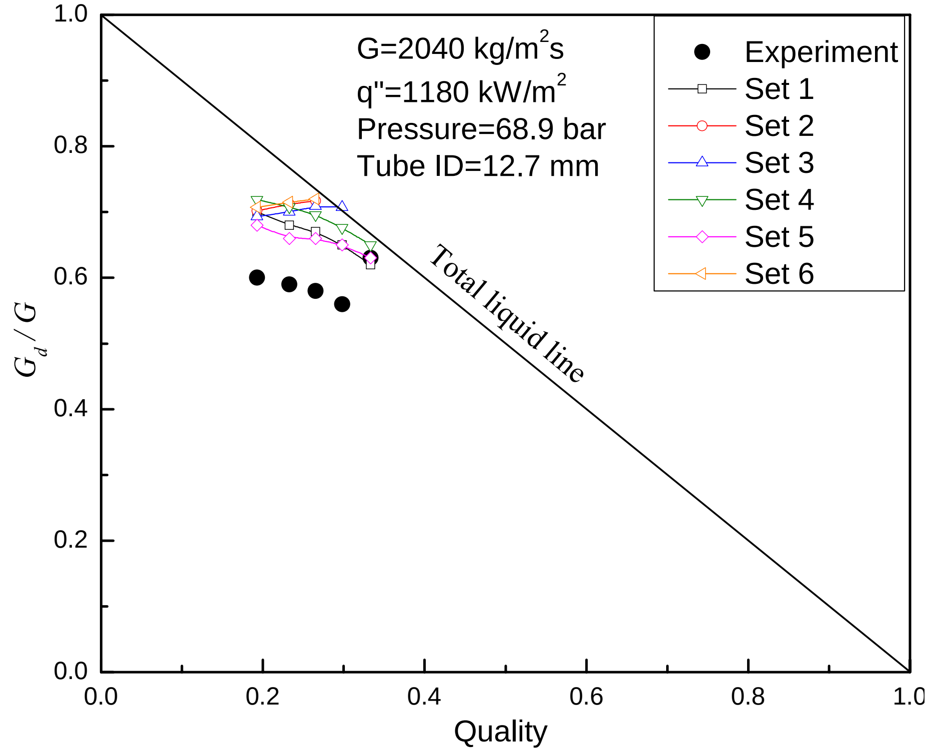

Figure 5-20: Predicted diabatic entrainment compared against Keeys et al. [64] **experimental data (heat flux 1180 kW/m^2, mass flux 2040 kg/ m^{2}s, 68.9 bar, 12.7 mm ID)**

5.3.2 Non-uniformly heated tube experiments (Bennett et al. [19])

One of the major advantages claimed for the phenomenological modeling approach to critical heat flux is its flexibility, and its reduced reliance on the experimental data on which it depends having been obtained under just the conditions for which critical heat flux is sought to be predicted. This is particularly true, perhaps, with regards to the axial variation of the heat flux in the channel. In this section the cold patch experiments of Bennet et al. [19] are presented again for the purpose of validation of the correlation sets.

A set of measurements of dryout under particular conditions of non-uniform heat flux was performed by Bennett et al. [19], where a (highly) non-uniform heat flux was engineered by leaving a section of the tube unheated. These experiments are thus more commonly referred to as the Cold-patch experiments. Due to the abrupt change in heat flux over a short length, the effects of non-equilibrium on rate processes are pronounced. In these experiments, the variation of entrained flow along the length of this non-uniformly heated tube was measured using a technique same as that of Keeys et al. [64]. Some results from their experiments are shown in Figure 5-21, Figure 5-22 and Figure 5-23 giving the entrained flow rate as a function of local quality. Also shown are predictions of these entrained flow rates, using the various correlation sets. Figure 5-21 shows the case of no cold patch and thus is similar to the Keeys et al. [64] data. In the next two figures however, the presence of cold patch leads to a short adiabatic region (thus quality is maintained) in which the entrainment tends towards equilibrium value.

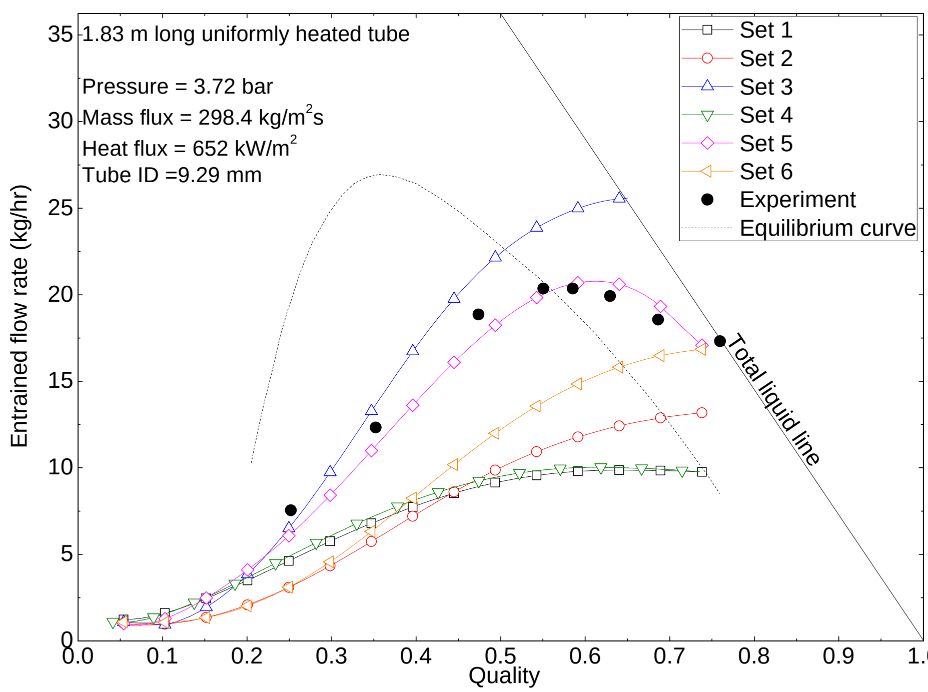

Figure 5-21: Predicted diabatic entrainment compared against experimental data (t/s dia. = 9.29 mm, pressure = 3.72 bar) for no cold patch

It is seen that set 3 predicts dryout to occur much earlier than experiments (as well as other correlations). Set 5 gives best match to experimental data. Though there is some mismatch in the high quality region, the trend seems to have been captured well by set 5.

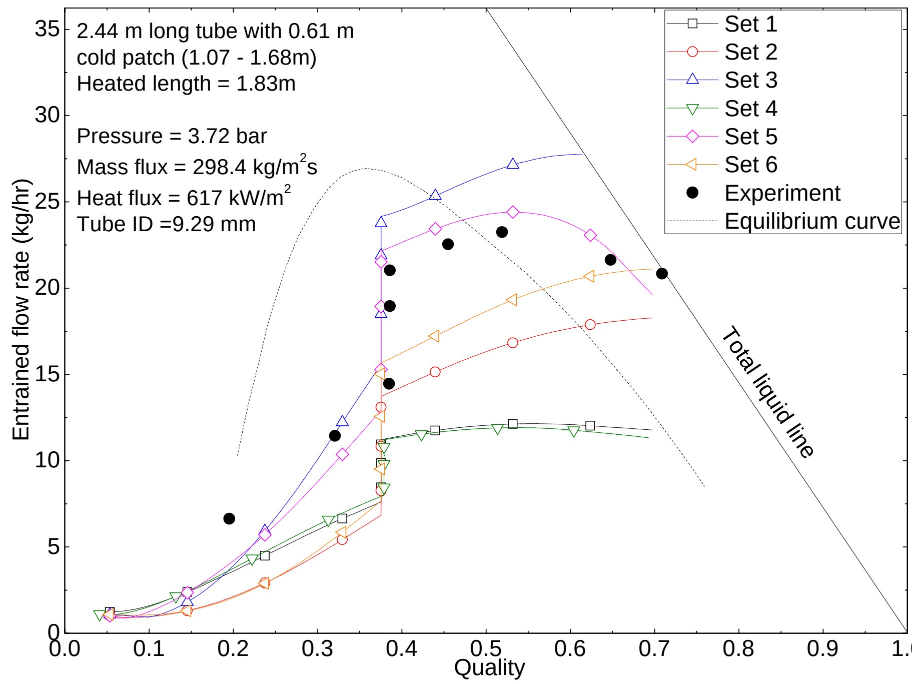

Figure 5-22: Predicted diabatic entrainment compared against experimental data (t/s dia. = 9.29 mm, pressure = 3.72 bar) for upstream cold patch

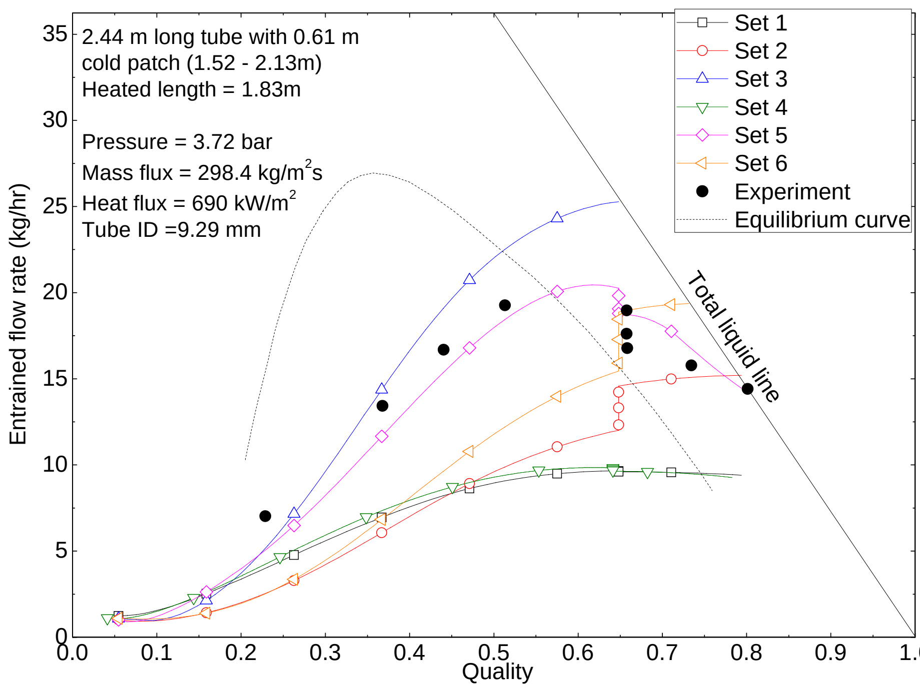

Figure 5-23: Predicted diabatic entrainment compared against experimental data (t/s dia. = 9.29 mm, pressure = 3.72 bar) for downstream cold patch

As observed for the earlier comparisons, the predictions of Set 1 and 4 are very close to each other. To recapitulate, set 1 and 4 have similar entrainment rate correlation (based on $\left(\tau_i\delta/\sigma\right)$), but different deposition rate correlations.

An interesting effect of non-equilibrium on the predictions can be made by considering sets 3 and 6 which use the same deposition rate correlation. The entrainment rate correlations used in these sets also reduce to the same equilibrium entrained fraction. This is because the Kataoka et al. [46] non-equilibrium entrainment rate correlation (used in set 3) is based upon Ishii and Mishima [48] equilibrium entrainment correlation (used in set 6). The results of these two sets are however significantly different for the cold patch cases. The difference can be attributed to the fact that boiling flows are non-equilibrium flows. Thus correlations which agree with each other in terms of equilibrium entrained fraction (see for example Figure 5-8) may give widely different values for entrained fraction in boiling flows.

The ability to predict the rate processes is truly tested under diabatic scenarios. This is truer for non-uniformly heated cases and the cold patch represents an extremity of non-uniformity. The set 5 correlations are seen to perform best in the cold patch test.

5.4 Comparison of the models against experimental dryout data

The prediction of dryout data of Becker et al. [72] with the different correlation sets and the new IEF methodology has already been presented in chapter 4. This particular data set has been chosen for assessment as it covers a wide range of pressures from 2.2 to 101 bar, mass flux of 120 to 5450 kg/m^{2}s and length-to-diameter (l/d) ratios from 40 to 792. The total number of experimental data points is around 3300.Here dryout predictionswith the new IEF methodology, i.e., the (b) plots in Figure 4-7 to Figure 4-12 are plotted again

Figure 5-24 for ease of readability. These predictions are here compared against one another.

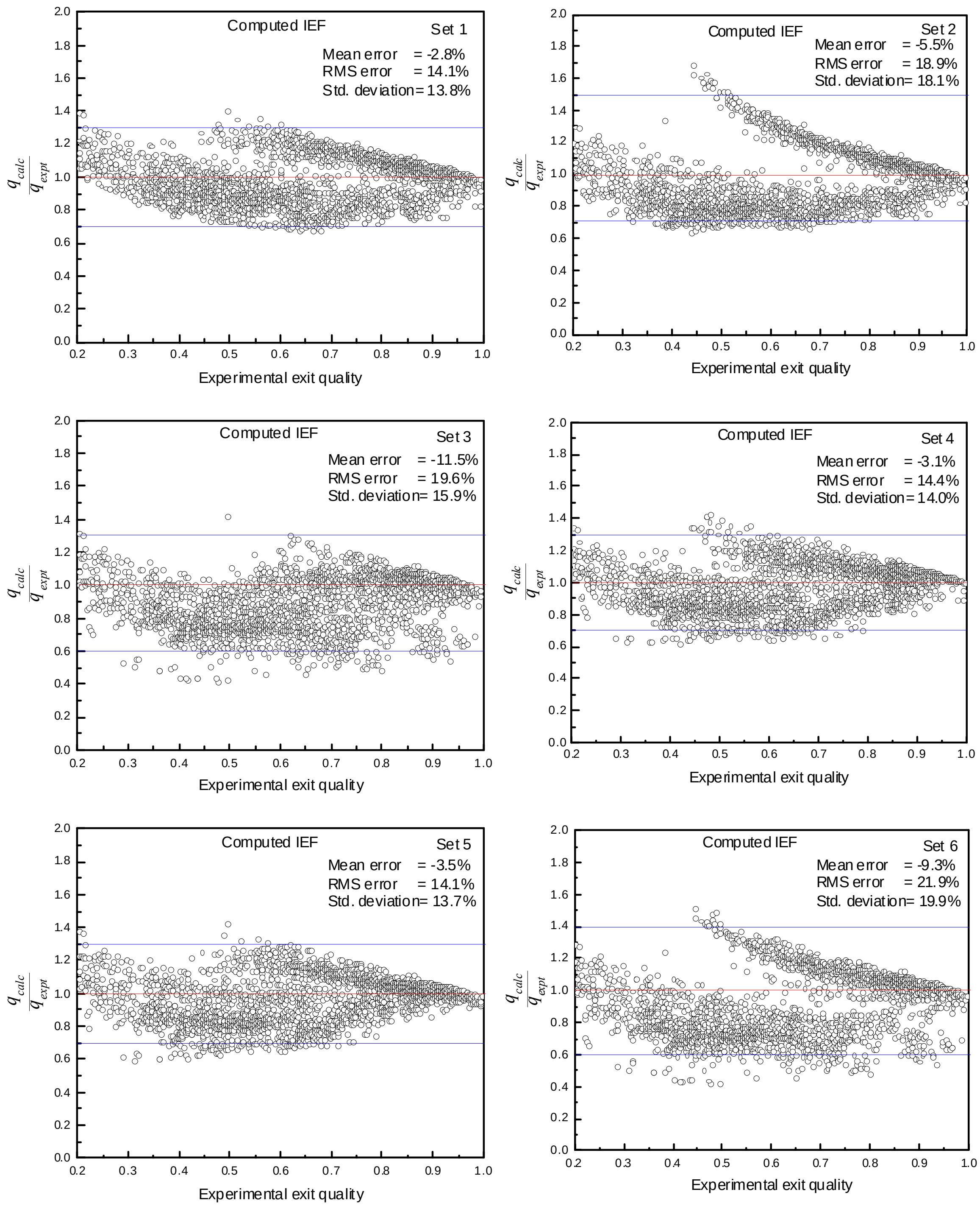

Figure 5-24: Ratio of predicted to experimental dryout power using different correlation sets

Set 1 is seen to predict dryout within ±30%. Though the mean error is only slightly negative (-2.8%), there is an apparent tendency to under predict (q_{calc}/q_{expt}) specifically in the exit quality range of 0.4 to 0.8.

Dryout predictions using set 2 do not look very encouraging. The over prediction is quite high for certain cases. However, if only those data which fall within ±30% are considered, then the prediction trends look very similar to set 1.

The tendency to under predict is also seen in all other sets as well. Set 3 (Figure 4-9b) has the highest mean error. Most of the data predicted by set 3 lies within +30% and -40%. Set 6, which bears the closest resemblance to set 3 in terms of the deposition and entrainment correlations used, however predicts rather differently with most of the data lying in an even greater error band of ±40%. The mean error for set 6 is also high. The fact that both set 3 and 6 under predict dryout data is consistent with the observed tendency to achieve high entrained fraction in previous adiabatic and diabatic comparisons. Looking at the plots it seems that set 3 predicts slightly better than set 6 thereby leading to the conclusion that usage of the non-equilibrium correlation gives better results. While this may be true, for the present case, IEF also plays an important role as seen in §4.2.2.

Among the correlation sets compared, lowest RMS errors (in the range of 14%) are seen for set 1, set 5 and set 4. The prediction accuracy of these correlation sets improves substantially with increase in exit quality. This is perhaps not unexpected. As we move farther from the transition to annular flow point, the effect of the highly chaotic history, which governs the initial entrainment fraction, and the influence of an estimate of this, should diminish. Also, as we move towards higher qualities, the film gets thinner leading to suppression of nucleation within it. This cancels out or reduces the influence of other mechanisms like bubble bursting or film disruption due to bubbles.

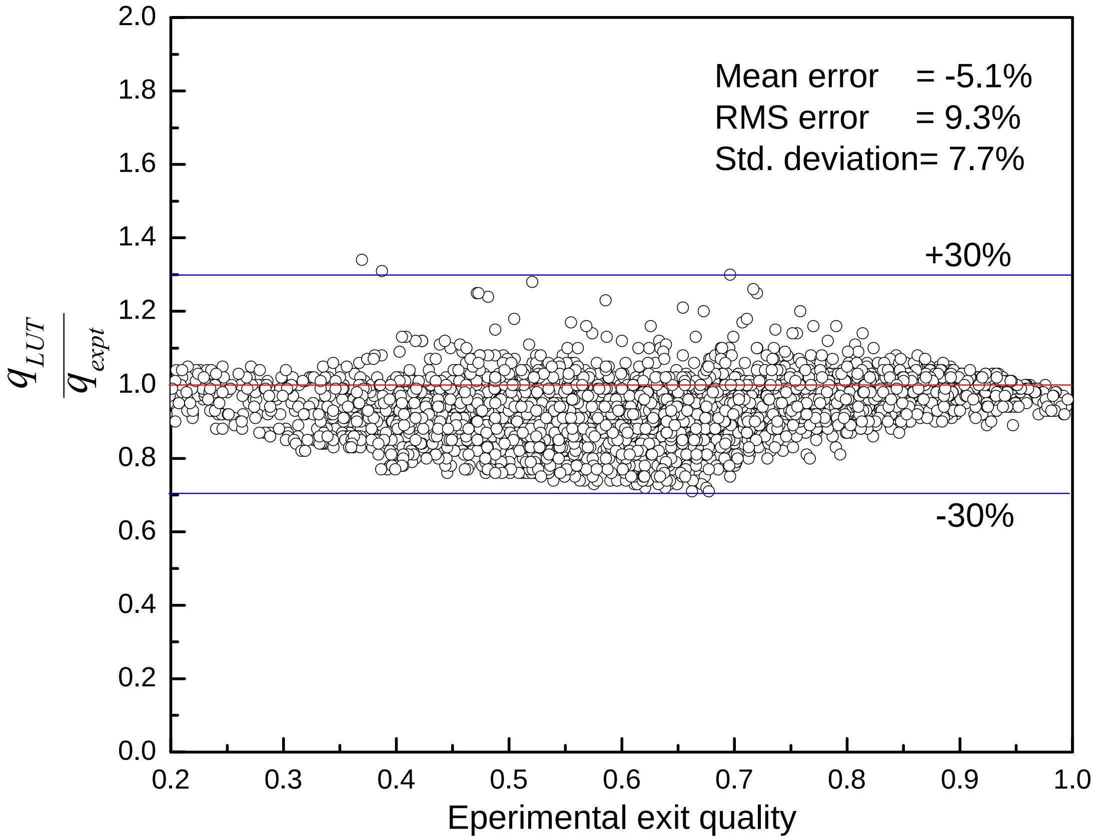

Figure 5-25: Becker et al. [72] **dryout data predicted with CHF LUT**

It is always a question whether the error bounds within which the predictions are made are good enough or whether the mechanistic model is a worthy replacement for the empirical correlation based approach for dryout prediction. In this regard, it is thus worthwhile to check the ability of mechanistic model vis-à-vis the CHF Look-up table (LUT) [156] in predicting Becker et al. [72] dryout data. Since these data are for a uniformly heated tube, the look-up table (which itself is derived from a broad range of experimental data on uniformly heated tubes) is expected to provide a kind of benchmark for prediction accuracy which could be reasonably expected from a first principles model. The predictions of Becker et al. [72] experiments using the CHF Look-up table are shown in Figure 5-25.

It is seen that for this data set:

- dryout power is under predicted by LUT
- The predictions are within ±30%.
- The error band is larger for exit qualities in the range ~0.4 – 0.75 and predictions improve substantially beyond exit quality of 0.8.

Though the RMS error and standard deviations of CHF-LUT are smaller than all the mechanistic models, it may be said that when the IEF prediction methodology is used, the overall trends and error bands observed with better predicting sets 1, 4 and 5 are in line with the CHF-LUT predictions. Also the predictions of the mechanistic model (sets 1,4 and 5) are seen to be more equitably disposed around the parity line. This is evidenced from the lower mean errors. Since both the LUT and Becker et al. [72] data represent a large data set with a fairly wide range of operating parameters, it can be inferred with a greater confidence that the prediction bands of the mechanistic model (i.e., new methodology for IEF prediction with correlation sets 1, 4 and 5) could be termed reasonable.

5.5 Discussion on the validity of correlations in terms of correlating parameters

Judging the applicability of the correlations on the basis of experimental validation alone is questionable. Good consistency with experimental evidence is perhaps necessary but not sufficient; the choice should factor in physical and theoretical considerations too. In what follows, a description of the parameters affecting deposition and entrainment rates is given and their inclusion in the correlations assessed.

The major parameters which affect both deposition and entrainment are surface tension, liquid and gas velocity (or mass flux), droplet diameter, pipe diameter and droplet concentration (which affects only deposition). The effect of these parameters is discussed in this section. Although other parameters like density and viscosity ratios play a role, their effect is not found to be significant (Caraghiaur and Anglart [34]).

Surface tension – Both deposition and entrainment rates are affected by surface tension, σ. It is in fact one of the parameters which interlinks entrainment and deposition rates. Reduction in surface tension causes greater entrainment and ejection of larger volumes from the tip of disturbance waves. Whalley et al. [22] postulated (no quantification of drop size was performed) the ejection of larger drops for reduction in deposition coefficient, k. Recall (Figure 2-11) that increase in particle size leads to reduction in deposition coefficient. Such reduction in k with reduction in σ is also the basis for the Katto [43] correlation. Jepson et al. [157] also report a reduction in k with reduction in σ. They have however observed smaller droplet sizes with reduced surface tension, which would be in accord with the associated change in Weber number. There is thus an apparent contradiction in the behavior of droplets in annular flow and particles in pipe flow. Whereas reduction in particle size clearly leads to increase in k, reduction in droplet sizes does not. This is discussed below in the section on gas/vapor velocity.

All the entrainment rate correlations considered in the present work incorporate the effect of surface tension in a way that is consistent with this physical description. Among the deposition rate correlations, Paleev and Filipovich [41] do not account for surface tension effects.

Gas/vapor velocity – This also has important effects on both entrainment and deposition rates. The gas flow field governs the turbulence in the core and determines the deposition rate. The gas flow also exerts a shear on the liquid film, which is the basis for disturbance wave generation and entrainment. The effect of gas velocity is incorporated in a way consistent with this interpretation in all the entrainment rate correlations studied. In the deposition rate correlations, it is accounted for only in the Paleev and Filipovich [41] correlation. However, the results obtained upon using other deposition rate correlations are not much in error. Caraghiaur and Anglart [34] have predicted, through numerical simulation of particle deposition in smooth pipes, increases in k with gas velocity. It is the author's view that while particle deposition in smooth pipes may well be governed primarily by turbophoresis (Young and Leeming [33]), droplet deposition in annular flows is more dependent on the disturbance wave structure in the liquid film.

The core flow streamlines converge and then diverge when moving over large amplitude disturbance waves (see the sketch in Figure 3-1 which attempts to illustrate this) in the process entraining some liquid from the tip of these waves. In fact most of the entrainment in annular flow is believed to take place at the tips of these waves. Due to the diverging streamlines downstream of the wave, the entrained drops are also given radial velocity just after their creation. The impulse imparted to the droplets due to this directed radial velocity is likely to be of much higher magnitude than that due to turbophoretic force which is based on radial gradient of turbulent fluctuations. The trajectory of these entrained droplets towards the wall is thus determined from the very point of entrainment. The wave shape and wave amplitude may thus be expected to play a role in subsequent deposition.

The observed reduction in k with reduction in σ, in spite of smaller drops being present in the core flow, can also be explained by consideration of Figure 3-1. In annular flow, there is a range of sizes of entrained droplets. The deposition of larger ones is governed by their inertia and the smaller ones by turbulent diffusion. As opposed to particle flows in smooth pipes, where the particles have a dominant axial velocity (the radial component is just due to turbulent fluctuations!), the presence of disturbance waves in annular flow ensure droplet inertia to be directed towards wall. This inertial component is postulated to be a major contributor in deposition process. Reduction in σ causes the average drop size to reduce, tipping the scales in favor of diffusional deposition. This leads to reduction in k with reduction in σ.

Taking this argument further, it is to be expected that at low film flow rates (near dryout), when the disturbance waves are suppressed (or are not large enough), deposition rates will be lower. This phenomenon is not accounted for by any correlation. The correlations, though, predict a reduction in entrainment rate but do not do the same for deposition rate. In fact a direct dependence on gas velocity in some correlations (Paleev and Filipovich [41]) would predict an increase in deposition. The neglect of this possible reduction in deposition rate might explain the predicted (using set 5 correlation) sharper (than experimental) fall in entrainment rate near dryout (Figure 5-21 to Figure 5-23). The Hewitt and Govan [4] correlation reduces only the entrainment rate due to suppression of disturbance waves but leaves the deposition rate as it is.

Droplet concentration – This generally has an effect on only the deposition rate. The effect on deposition coefficient is primarily due to coalescence of drops at high concentration leading to larger drops and lower k. The concentration effect is not included in the Katto [43] correlation but appears in all other correlations considered. Droplet concentration in the gas core can affect the entrainment by increasing the shear on the film. This effect is generally accounted for by introducing an averaged vapor core density in interfacial friction calculations (Tomiyama et al. [25]).

Liquid velocity/flow rate – Physically liquid velocity (or flow rate) can have only a weak influence on the deposition coefficient, *k*, except in cases where the liquid flow rates are so low that the film is thin enough for suppression of the disturbance waves. Since most experimental evaluations of deposition rate are done by making the surface free from the liquid film, there are no data/correlations to support or otherwise this conjecture.

Liquid flow rate, in particular film flow rate, has a lot of bearing on the entrainment. This effect is accounted for in the Hewitt and Govan [4] correlation. Tomiyama et al. [25] and Adamsson and Anglart [32] also account for this effect through the non-dimensional parameters in their respective works. In the Ishii and Mishima [48] and Kataoka et al. [46] correlations the effect is introduced by way of liquid Reynolds number.

Pipe diameter – At low pipe diameters, the curvature of the streamlines (due to the wavy interface) in the gas core falls off more rapidly as we move from the interface to the centre of the pipe. This provides stability against entrainment. Thus a lower entrainment rate is expected for low diameter pipes. Such a reduction is also observed by Pan and Hanratty [158] This effect is incorporated in Ishii and Mishima [48], Hewitt and Govan [4] and Kataoka et al. [46] correlations.

From the point of view of deposition process, the propensity for deposition will increase if the diameter reduces. This is because the “distance” of the drops from the wall reduces. This effect is incorporated in Paleev and Filipovich [41], Okawa [24] and Hewitt and Govan [4] correlations but absent in Katto [43] correlation.

The correlation sets can be assessed in the light of the above arguments. Table 5-2 gives a brief representation of the dependencies mentioned above. Among the entrainment rate correlations, Set 3 (Kataoka et al. [46]), Set 5 (Hewitt and Govan [4]) and Set 6 (Ishii and

Mishima [48]) are found to incorporate all the parameters suggested in our discussion to be relevant. The deposition rate equations in Set 4 (Okawa et al. [51]) and Set 5 (Hewitt and Govan [4]) are seen to include all the discussed dependencies.

Table 5-2: Inclusion of important parameters in Deposition and Entrainment rate correlations

	Set 1		Set 2		Set 3		Set 4		Set 5		Set 6	
	D	E	D	E	D	E	D	E	D	E	D	E
σ	✓	✓	✓	✓	✗	✓	✓	✓	✓	✓	✗	✓
j_g	N.E	✓	N.E	✓	N.E(✓)	✓	N.E	✓	N.E	✓	N.E(✓)	✓
C	✗	N.E	✗	N.E	✓	N.E	✓	N.E	✓	N.E	✓	N.E
j_l	N.E	✓	N.E	✓	N.E	✓	N.E	✓	N.E	✓	N.E	✓
d	✗	✗	✗	✓	✓	✓	✓	✗	✓	✓	✓	✓

✗: Not considered; ✓: Considered; N.E.: No effect expected

Considering the comparison with experimental data and theoretical considerations, among the correlation sets studied, we conclude the correlation of Hewitt and Govan [4] is the most suited for predictions of annular flow.

None of the correlations for deposition rate however consider the effect of disturbance waves, which, as discussed above, may well have an important bearing on the rate processes in annular flow. It is hoped that the data on disturbance waves which has been generated in this work (chapter 3) can contribute towards improved simulations and models of deposition and entrainment rates.

5.6 Validation against additional data

As a result of the assessment and the development of a new IEF prediction methodology, a better model is proposed. This model would use the new IEF prediction methodology along with Hewitt and Govan [4] correlations for entrainment and deposition rate. This model is now used to predict some additional tubular dryout data available from other sources in literature. In particular two data sets as mentioned in Table 5-3 have been used.

Table 5-3: Tubular dryout data set used for comparison

Source	**Mass flux (kg/m^2s)**	**Pressure (bar)**	**Length-to diameter ratio**	**No. of data points**
Bennett, et al. [159]	700-5450	67-71	114.9-440.6	93
Chandraker et al. [160]	850-1650	29-71	400	125

The model is able to predict AERE data (Bennett et al. [159]) within ±10% (Figure 5-26) particularly when the exit quality exceeds 30%. At lower qualities, the dryout heat flux is over predicted for shorter length tubes. This may be explained by considering that the phenomenological model assumes that bubble nucleation is suppressed in the thin liquid film and vaporization takes place by evaporation from surface of the film. While this assumption is justified at low heat flux and when the film is thin, it may not hold true if heat flux is high. For a particular exit quality, short length tubes would have a higher dryout heat flux than long length tubes. Bubble nucleation in the liquid film may, thus, be possible, in short length tubes, at low qualities. This nucleation of bubbles may have two effects viz., increasing the entrainment and/or causing the continuity of the film being disrupted earlier than would be predicted using the surface evaporation model. In presence of any of these effects, dryout power will be lower than what is computed from the present model.

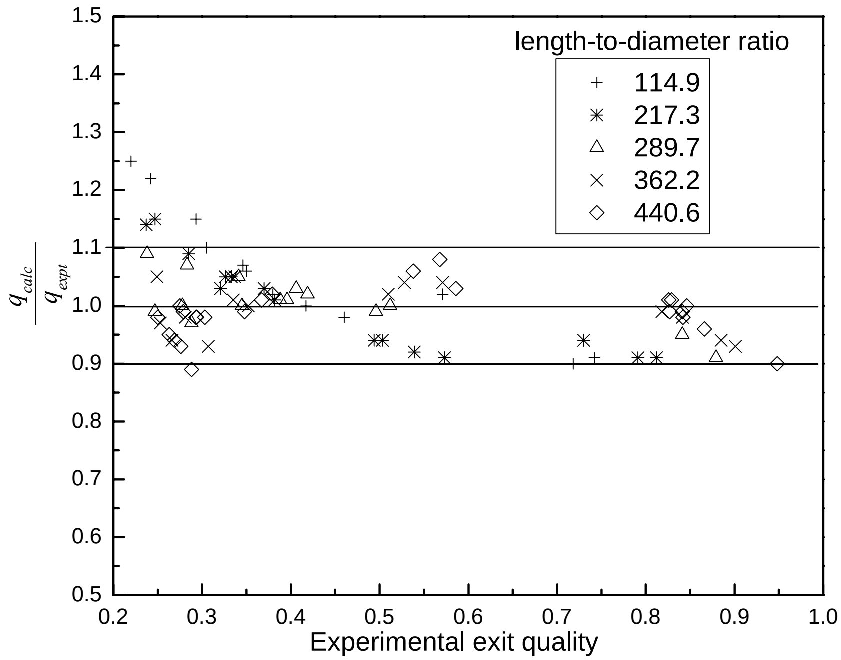

Figure 5-26: Comparison of model with AERE [159] **experimental data**

There is some disagreement in literature with regards to the enhancement of entrainment due to nucleation and inclusion of the effect of heat flux on entrainment. Milashenko et al. [65] found an effect but Keeys et al. [64] did not. There are some models [24,161] in literature which recommend the usage of boiling enhanced entrainment. Others [4,29,67] have not considered any such effect. In the present work, boiling induced entrainment is not considered. The second postulated effect of local disruption of the film due to nucleation is not addressed by any phenomenological model. However it is the author's view that such phenomena, especially for low qualities and high heat flux, need to be investigated in greater detail both experimentally and theoretically for better dryout modeling.

The range of exit quality (60% to 90%) in BARC experiments (Chandraker et al. [160]) is small. Thus the data have been plotted as a function of pressure (Figure 5-27). In this case, the predictions are seen to be within ±15%.

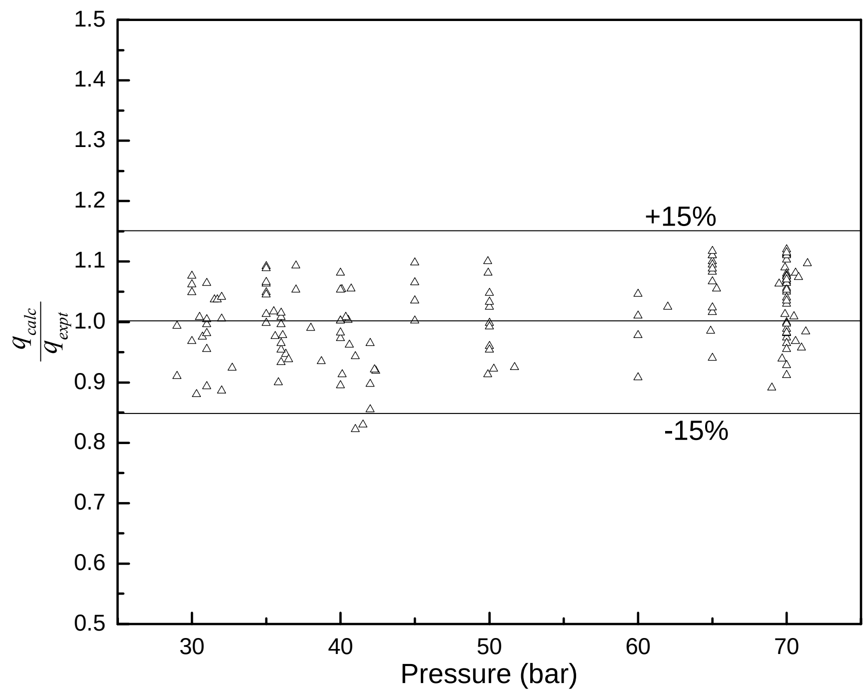

Figure 5-27: Comparison of present model with BARC [160] **experimental data**

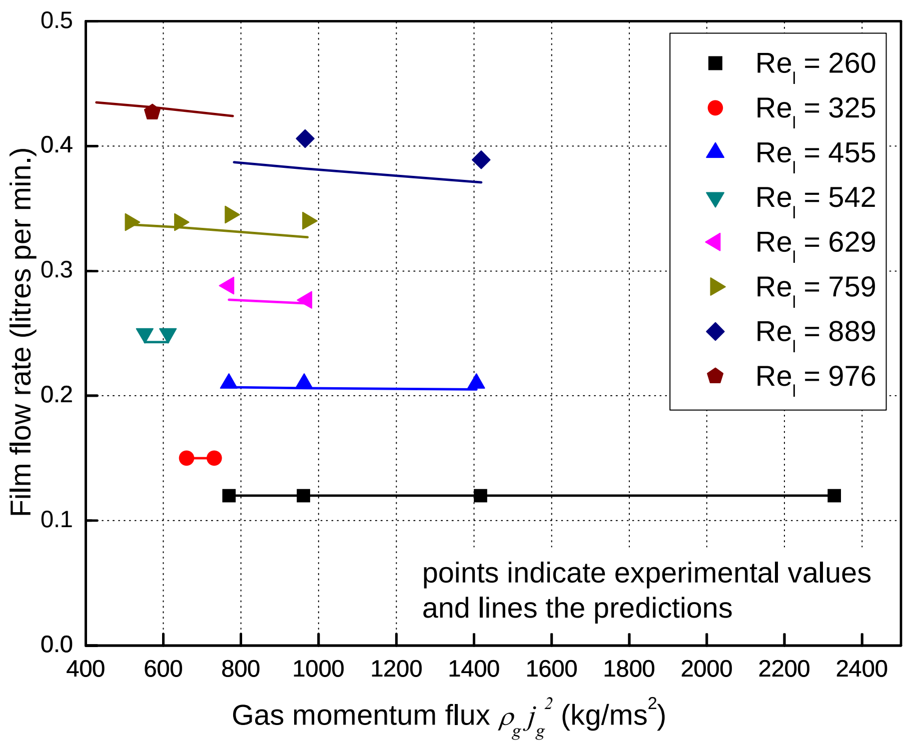

Figure 5-28: Film flow rate in air-water annular flow; present experimental data and predictions using improved model

Apart from dryout data, the improved model is used to simulate the conditions of air-water annular flow experiments reported in chapter 3. The film flow rate thus predicted is plotted along with the experimental data in Figure 5-28. Since the data are for adiabatic conditions, whether or not the IEF methodology is used becomes irrelevant. Therefore, in practice it is an additional validation for the Hewitt and Govan [4] correlation set.

It has already been mentioned in §3.5 that the onset of entrainment criterion is predicted well by Hewitt and Govan [4] correlation. Apart from that, the predictions, as seen in Figure 5-28, are close to the experiments. Further, it was mentioned (§3.5) that some of the data generated is outside the range available in literature and also, this is air-water (not-steam-water) data. This reposes additional confidence in the Hewitt and Govan [4] correlations.

5.7 Concluding remarks

Among the many available correlations for deposition and entrainment rates selected few have been assessed against experimental data for adiabatic and diabatic annular flows. Further, experimental dryout data were simulated using the different entrainment and deposition rate correlations, and the effectiveness of the correlations sets in predicting these were investigated.

A discussion of the physical processes likely to be important in the entrainment and deposition processes has been presented. The correlations have then been assessed by a discussion of how completely the parameters they incorporate map onto those so identified as important.

The major findings are summarized:

1. Adiabatic predictions: Set 1 gives the best match to adiabatic annular flow data. The fact that this correlation includes only the effect of surface tension and yet is able to perform so well indicates the importance of surface tension in deposition rate predictions. Set 4 predicts very near to Set 1 correlations. Set 5 correlations also perform well particularly at high qualities and high mass flux. The use of Ishii and Mishima [48] or Kataoka et al. [46] correlations (as in sets 3 and 6) lead to high equilibrium entrained fraction predictions.
2. Predictions in uniformly heated tube: Among the correlation sets studied, sets 1 and 5 predict nearest to experimental observations. The prediction accuracy of sets 1, 4 and 5 improve substantially near to dryout. It may thus be expected that these sets would predict dryout with similar accuracy. Sets 2, 3 and 6 predict dryout to occur earlier (i.e., at lower quality) than expected.
3. Predictions in non-uniformly heated tube: The history effect in Bennett et al.[19] data is best predicted by Hewitt and Govan [4] (set 5) correlation set, suggesting it is well suited to cases with non-uniform heat fluxes.
4. Dryout predictions: The dryout predictions indicate that among the correlations studied, sets 1, 4 and 5 predict with the lowest RMS errors. The standard deviation for all these sets is comparable indicating similar statistical scatter in prediction. The predictions with sets 4 and 5 improve substantially at higher qualities.
5. Physical considerations: Based on both comparison with experimental data and theoretical considerations, surface tension, droplet concentration and channel diameter have a strong influence on deposition coefficient. The effect of gas

velocity is however weaker, possibly due to presence of disturbance waves that have an over-riding influence on droplet deposition.

Entrainment rate correlations studied in this work take into account, most of the parameters we have identified as physically important into consideration.

From theoretical considerations, as well as via comparison with experimental data, the Hewitt and Govan [4] correlation set is seen to be the best among the sets studied for annular two-phase flow predictions. Though it seems that Set 4 is also able to predict dryout with similar accuracy, it fails to capture the cold patch experiments effectively. Hewitt and Govan [4] correlations also are able to predict the present air-water experiments with good agreement. Finally, an improved model is proposed which uses the new IEF methodology along with Hewitt and Govan [4] correlations for entrainment and deposition rate.

A prediction of Becker et al. [72] dryout data with the CHF-LUT [156] gives some confidence in the error bands of the predictions with the mechanistic model. The scatter in dryout predictions in intermediate quality region (which is also observed with LUT) however indicate that the models for deposition and entrainment must be enhanced so as to be applicable to a wider range of conditions and achieve even greater consistency between the predicted dryout power to experimental values. Entrainment rate correlations, as they are based (through some form) on force balance over the wave, are sounder. There is more scope for improvement in deposition rate analysis. The possible importance of the radial gas velocities associated with large disturbance waves has been postulated. It is suggested that this might be a fruitful area for further study. In that direction, it is hoped that the data on disturbance waves which has been generated in this work (chapter 3) can contribute towards improved simulations and models of deposition and entrainment rates.

6 APPLICATION OF MECHANISTIC MODEL TO ROD BUNDLES

Once a dryout model has been verified in tubes, its application to rod bundles is a natural step forward. Rod bundles are different from tubes in that they have internal boundaries. Subchannel analysis is the most common method for analyzing flows within rod bundles. In this technique, the flow area within a rod bundle is divided into a number of parallel interacting flow subchannels which communicate with each other all along the axial length. Continuity, momentum and energy balances are solved for each subchannel with approximate equations and empirical models to account for transverse exchange.

The phenomenological dryout model developed for tubes cannot be directly applied to rod bundles as, in a subchannel, the flow keeps changing axially. Also the different rods in a bundle generally have different power generation. Thus, the model has to obtain input from a subchannel calculation. The dryout model described in the previous chapter has been coupled with a subchannel analysis model (§6.1) resulting in the development of SCADOP (SubChannel Analysis and DryOut Prediction) – a mechanistic tool for prediction of dryout in rod bundles.

A good number of subchannel models are described in literature and the interested reader is advised to look into such detailed works to get an in-depth understanding of the method. Here (§6.1) only a brief introduction is given along with the relevant conservation equations for subchannel analysis. The application of phenomenological model to rod bundles is described in §6.2. The model is then used to predict rod bundle dryout which is detailed in §6.3 and §6.4.

6.1 Subchannel conservation equations

Subchannel analysis is basically a contraption to represent and model three-dimensional phenomena with a computational scheme which is essentially one dimensional. It works on the principle that the cross-flow occurring from one subchannel to another is much lesser than axial flow and thus it may be assumed that the cross-flow loses its sense of direction after crossing the gap. Two kinds of subchannels have been used in literature – rod centered and coolant centered. The former approach was pioneered by CISE labs in 1970s [162]. In this approach, the rod is at the centre of a subchannel and the imaginary lines demarcating the subchannels are the 'lines of zero shear'. It is interesting to note that the rod centered model was developed precisely for the ease of modeling annular flow dryout in rod bundles. In the coolant centered approach on the other hand, subchannels are demarcated by imaginary lines drawn through rod centers. Each subchannel thus consists of part rods and coolant in the middle. Most of the available subchannel analysis codes (COBRA-TF [81], VIPRE [163] etc.) use coolant centered subchannels.

With respect to mechanistic modeling of dryout in rod bundles, some of the works use a rod centered [29] approach while others [28] use coolant centered approach. Though there are no very strong points for or against any one particular subchannel formulation, in this work coolant centered subchannels (as shown in Figure 6-1) are considered. This consideration stems from the fact that the coolant centered approach seems more logical considering that the subchannels are then more representative of wall bounded channel flows. Thus firstly, it may be expected that adjacent subchannels (sharing a particular fuel rod) having different axial gas core mass flux would lead to circumferentially varying interfacial shear in the film on a rod. Since the entrainment rate is a function of gas core mass flux, there would be circumferentially varying film flow rate in a single rod. This effect cannot be captured by the rod-centered approach. Secondly and more importantly, the models for deposition and entrainment rates have been developed using mostly tubular experimental data. Thus the coolant centered approach, bearing greater resemblance to the tubular geometry is preferred over rod centered approach.

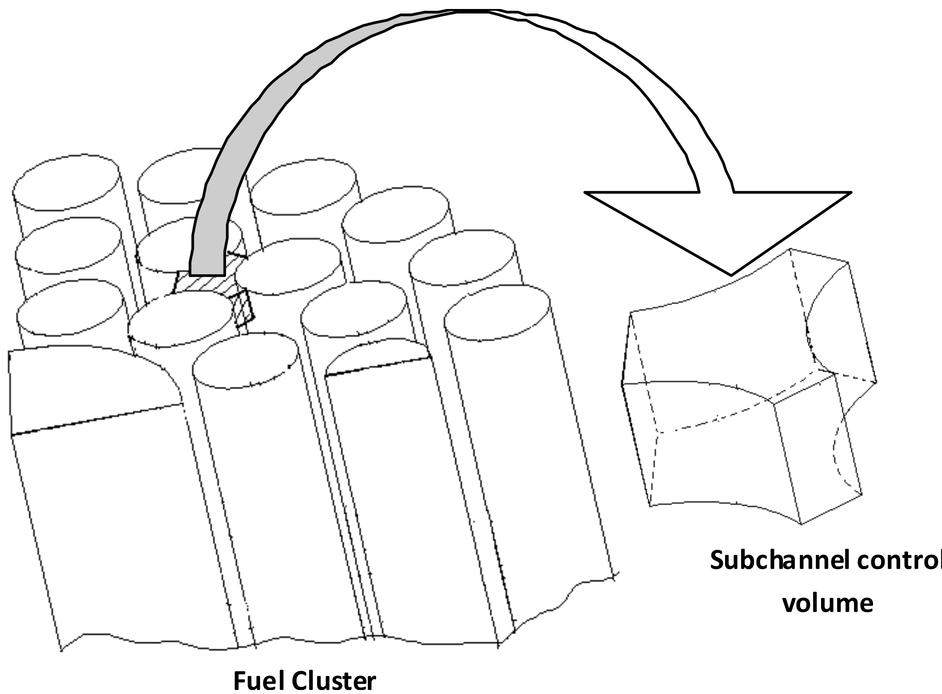

Figure 6-1: Typical coolant centered subchannel control volume and its relation to the fuel cluster

The conservation equations for a subchannel '*i*', surrounded by subchannel(s) '*j*' are listed in eqns. (6.1) to (6.4) and are basically the same as that used in COBRA-IIIC [164]. Since no discretization is done within a subchannel, the subchannel is treated as an equivalent circular flow channel with wetted, heated perimeters and flow area determined from actual subchannel geometry. Equation (6.1) is the continuity equation, where, m_i is the mass flow rate in subchannel i. w_{ij} accounts for the diversion cross flow between the adjacent subchannels. The subscript j indicates adjacent subchannels.

$$\frac{dm_i}{dz} = -\sum_{j=1}^{N} w_{ij}; \qquad w_{ij} = 0 \text{ if } i = j \tag{6.1}$$

The energy equation is given by eqn.(6.2). It basically performs the balance of enthalpy, h_i which is modified due to linear heat input $q_i^{'}$ to the subchannel, conduction heat transfer between subchannels due to difference in temperature, $\left(T_i - T_j\right)$, convective heat transfer due to diversion cross flow and that due to turbulent interchange, $w_{ij}^{'}$.

$$\frac{dh_i}{dz} = \frac{q_i^{'}}{m_i} - \sum_{j=1}^{N}(T_i - T_j)\frac{c_{ij}}{m_i} - \sum_{j=1}^{N}(h_i - h_j)\frac{w_{ij}^{'}}{m_i} + \sum_{j=1}^{N}(h_i - h^*)\frac{w_{ij}}{m_i} \tag{6.2}$$

The axial momentum balance equation (6.3) equates the total pressure drop to the frictional, local and acceleration pressure drop terms (first term on RHS), gravitation pressure drop term (second term on RHS) and the momentum flux contributions made by diversion and turbulent crossflow terms due to different velocities, u existing in the adjacent subchannels.

$$A_i\frac{dp_i}{dz} = -A_i\left(\frac{m_i}{A_i}\right)^2\left[\frac{v_i f_i \phi_i}{2D_i} + \frac{K_{sp}v_i^{'}}{2\Delta z} + \frac{dv_i^{'}}{dz}\right] - gA_i\rho_i\cos\psi - (u_i - u_j)w_{ij}^{'} + (2u_i - u^*)w_{ij} \tag{6.3}$$

K_{sp} is the spacer loss coefficient f_i is the friction factor and v is the specific volume.

The transverse momentum equation (6.4) is based on the premise that the transverse flow is negligible compared to the axial flow thus the velocity as well as the gradients in the transverse direction are neglected. This allows the subchannels to be connected in an arbitrary manner without the need for a fixed coordinate system. Here *s* denotes the gap width, *l* the notional length up to which the effect of the gap are significant and *p* the pressure. The frictional term, due to flow through the gap region is incorporated using a loss coefficient, *K*. The starred terms represent the values in the gap region.

$$\frac{d(u^{*}w_{ij})}{dz}=\left(\frac{s}{l}\right)(p_i-p_j)-\frac{K\left|w_{ij}\right|w_{ij}}{2s^2\rho^{*}}\left(\frac{s}{l}\right) \tag{6.4}$$

6.2 Modifications to the mechanistic dryout model for application to rod bundles

A subchannel in which annular flow has initiated will in general be surrounded by subchannels which may or may not have annular flow. From subchannel analysis, the cross-flow and quality are known for each axial location. Thus the amount of liquid and vapor exchange between the subchannels is known. It is however not known how much of the liquid being exchanged is in the form of droplets (or film). In the present work, liquid portion of the cross-flow is fully ascribed to droplets. Though there is no experimental basis for justifying such an approximation, it is expected that since the liquid film adheres to the wall which is a low velocity region and the droplets are present in the high velocity core, the contribution of droplets to crossflow will be substantially higher than the film. Adamsson and Le Corre [153] have observed that the predictions of dryout power are not very sensitive to the split between the drops and film.

The film mass balance is modified (eqn.(6.5)) to account for the number of distinct rod surfaces (indicated as the subscript *r*) in a subchannel. While the entrainment and vaporization rates depend on the rod on which the film is solved, the deposition rate does not.

$$\frac{dG_{lf,r}}{dz}=\frac{\zeta_{w,r}}{A_i}\left(D-E_r\right)-\frac{\zeta_{h,r}}{A_i}B_r \tag{6.5}$$

The vapor and drop flow balances are also modified (eqs.(6.6) and (6.7)) while applying to rod bundle to account for the cross flow. In these equations, w_l^{xf} and w_g^{xf} denote the mass flux per unit length for cross-flow of liquid and vapor respectively. These values are obtained from the subchannel calculations. The subscript *nb* denotes all the neighbouring rods of a subchannel

$$\frac{dG_d}{dz} = \frac{1}{A_i}\left(\sum_{nb}\zeta_{w,r}\left(E_r - D\right)\right) + w_l^{xf} \tag{6.6}$$

$$\frac{dG_g}{dz} = \frac{1}{A_i}\sum_{nb}\zeta_{h,r}B_r + w_g^{xf} \tag{6.7}$$

The partitioning of the liquid film between the rods and unheated wall ensures that the film flow rate, apart from being calculated for the subchannel as a whole, is also calculated over each rod in the subchannel and in the unheated regions as well. This is necessary because in the case of unheated regions like the channel wall, the vaporization term vanishes and the film present on those walls does not contribute to heat transfer. The vaporization term is also modified for different rods in a subchannel due to local peaking effects.

This formulation leads to different film flow rates on the different rods in a subchannel. Thus, the approach to dryout can be predicted differently on different rods in a subchannel. Also, in principle, the circumferential location of dryout on a rod can be predicted. Of course, the location can be identified only to the extent of the subchannel discretization.

6.2.1 Discussion of applicability of rate correlations to subchannel geometry

The Hewitt and Govan rate correlations have been derived from tube data and are presented in a form which is applicable to tubes. For application to rod bundles, modification is required in the entrainment rate correlation. This is due to the fact that there is now no single film mass flux and critical film mass flux in a subchannel. Each rod has to be given consideration and entrainment is different from each rod. This has been discussed in detail by Adamsson [53] in his thesis. In this work, following his prescription, the entrainment equation is modified to:

$$E_r = 5.75 \text{ x } 10^{-5} G_g \left[\left(\frac{G_{lf,r} - G_{lfc,r}}{\left(\zeta_{w,r} / \zeta_w \right)} \right)^2 \frac{\rho_l d}{\rho_g^2 \sigma} \right]^{0.316} \quad ; G_{lf}^i > G_{lfc}^i$$
$$= 0 \quad ; G_{lf}^i \le G_{lfc}^i \tag{6.8}$$

The subscript r indicates the r$^{\text{th}}$ rod in a subchannel. The mass flux G is still referenced to the total subchannel area. ζ_w is the wetted perimeter of the subchannel. The critical film mass flux for a particular rod is modified in the ratio of wetted perimeters, $\left(\zeta_{w,r} / \zeta_w \right)$. This technique is in essence same as that of Adamsson [53], only the presentation is in terms of mass flux rather than mass flow rate.

A greater uncertainty in the applicability of tube correlations to rod bundles stems from the experimental observations by Wurtz [23] in concentric and Butterworth [165] in eccentric annuli. They had observed that the inner rods tend to have lower film flow rates than outer shroud. This implies that either entrainment is more easily facilitated from convex surfaces or deposition to them takes place at a reduced rate. Not much modeling work has been done in this field except for some very recent papers by Zhang and Hewitt [166–168]. Perhaps the saving grace for rod bundles is the fact that in an assembly of many rods only the outer ones see a condition as extreme as that of the annulus. For the inner rods, possibly the effect cancels out.

It is important at this juncture to recall the discussion pertaining to governing parameters (Table 5-2) for the rate correlations. Diameter was the only geometrical parameter which was encountered. Its significance for rod bundles also needs to be relooked upon. This is done here briefly. Generally film flow analysis in rod bundles is carried out using the subchannel analysis results as the basis. Subchannels are non-circular ventilated channels which are generally characterized by hydraulic diameter. To some extent, it represents the flow area available in a subchannel i.e., higher hydraulic diameter implies higher available flow area. Consequently the logical deductions made in §5.5 with respect to diameter should hold. In conventional fluid mechanics, the hydraulic diameter is considered a workable representation for the wall shear. However, the friction factor values in tubes are quite different from bundles even in single phase flows. This indicates a strong geometry effect.

Considering the highly non-circular and quite arbitrary shape of subchannels, hydraulic diameter might not be able to uniquely quantify droplet dynamics. That is to say, two channels of different shape having the same hydraulic diameter will in general have different droplet dynamics. In the author's knowledge, there are no available studies which attempt to quantify the extent of difference.

6.3 Solution scheme

6.3.1 Solution of the subchannel conservation equations

The complete details pertaining to derivation of discretization equations, evaluation of closure terms and solution scheme are similar to that outlined in Masterson and Wolf [169]. This is however described in this section for completeness.

The conservation equations are first order equations and thus can be easily recast in a finite difference formulation. Due to the possibility of existence of a large number of subchannels, it is conventional to represent the equations in a matrix form. Here, however, for the purpose of description the matrix notation is not used and rather simple forms of the subchannel equations are presented and discretized. We may rewrite the conservation equations ((6.1)-(6.4)) for mass, energy, axial momentum and transverse momentum in the following form (eqns. (6.9)-(6.12)).

$$\frac{dm}{dz} = \mathrm{A}^m\left(w\right) \tag{6.9}$$

$$\frac{dh}{dz} = \mathrm{A}^h\left(m, w\right) \tag{6.10}$$

$$\frac{dp}{dz} = \mathrm{A}^p\left(m, w\right) \tag{6.11}$$

$$\frac{d\left(u^* w\right)}{dz} = \mathrm{A}^w\left(p, w\right) \tag{6.12}$$

The subscripts denoting the subchannel indices have been intentionally removed for greater clarity. Further, terms on the right hand side of these equations have been represented as a variable A^x. Each of these variables in general depends on a number of other variables. However only those which are essential to the description which follows are bracketed along with. These being first order equations implies the requirement of a single boundary value each for axial flow (or axial velocity), pressure, enthalpy and crossflow. In SCADOP, the solution scheme requires axial flow, enthalpy and crossflow be specified at the inlet and pressure be specified at the exit of the fuel cluster.

The energy equation is discretized in a space explicit fashion such that the right hand side is evaluated from the values at the previous axial node. The nodes are denoted by the subscript.

$$\frac{h_j - h_{j-1}}{\Delta z} = \mathrm{A}_{j-1}^h \tag{6.13}$$

The transverse momentum equation is discretized in a semi-implicit fashion, with weightage being given to upstream values too.

$$\frac{u_j^* w_j - u_{j-1}^* w_{j-1}}{\Delta z} = \gamma \mathrm{A}_j^w + \left(1-\gamma\right) \mathrm{A}_{j-1}^w \tag{6.14}$$

The continuity and axial momentum are discretized space implicit.

$$\frac{m_j - m_{j-1}}{\Delta z} = \mathrm{A}_j^m \tag{6.15}$$

$$\frac{p_j - p_{j-1}}{\Delta z} = \mathrm{A}_j^p \tag{6.16}$$

An equation for cross flow (as a function of pressure) at the j^{th} node is then obtained from equation (6.14). This when combined with equation (6.16) gives an equation from which the pressure at node $\left(j-1\right)$ can be evaluated from the knowledge of pressure at the next downstream node j.

The solution scheme is described in the following:

1. Starting with the first node (inlet), the energy equation (6.13) is solved to evaluate the enthalpy field at the second axial node for all the subchannels. This evaluated enthalpy enables evaluation of the density and temperature.
2. The pressure is then evaluated at the inlet node by making an assumption for the pressure at second node. Such a computation scheme allows effect of downstream disturbances (like flow restrictions) to be felt upstream.
3. With the knowledge of pressure field at the second node, the cross flow is evaluated from equation (6.14).
4. Finally the mass flow rate at the second node is updated from equation (6.15).

5. The preceding steps are repeated and the marching solution scheme proceeds till the last node where the pressure value gets updated to the imposed boundary value. During successive iterations through the core, the pressure is communicated to the inlet. Convergence is said to be achieved when the values at a particular node are within 0.1% of previous iteration.

Since the governing subchannel equations of SCADOP are same as that of COBRA-IIIC; only the solution scheme is different, a hypothetical case was run with both SCADOP and COBRA-IIIC to verify the correctness of numerical scheme programmed.

The details of the geometry used are given in Figure 6-2 and operating conditions are as follows:

Table 6-1: Details of hypothetical bundle for code comparison

Bundle length	3.15 m
Inlet enthalpy	1134 kJ/kg
Exit pressure	7.197 MPa
Inlet crossflow	0.0 kg/s
Heat flux	400 kW/m^2

Assuming that the power distribution is uniform in each of the circular rods, we can expect that the outer zone will have same average subchannel parameters. Thus we can have a large subchannel 2 (as in Figure 6-2a) or divide this larger subchannel into identical smaller subchannels 2, 3 and 4 (as in Figure 6-2b). These are for ease of reference called the two subchannel layout and four subchannel layout.

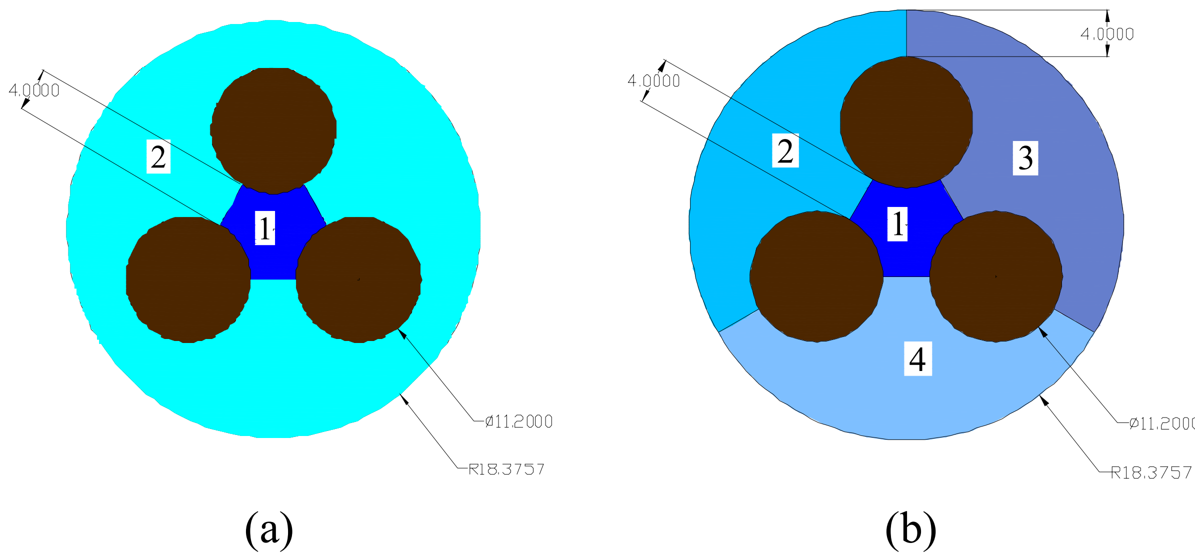

Figure 6-2: Hypothetical bundle geometry used for SCADOP and COBRA-IIIC verification discretized in (a) two subchannel and (b) four subchannel layout

In both the cases, it is expected that SCADOP results match those of COBRA-IIIC and it is also checked if the predictions of subchannel 2 (in Figure 6-2a) are equal to those of 2, 3 and 4 (in Figure 6-2b).

The results are shown first for the two subchannel layout in Figure 6-3. Excellent correspondence between COBRA-IIIC and SCADOP is observed in predicting the subchannel flow parameters. At ~2.0 m, crossflow and mass flow rates show a sudden change. This corresponds to beginning of saturated boiling in subchannel 1. Subcooled boiling is not accounted for by SCADOP.

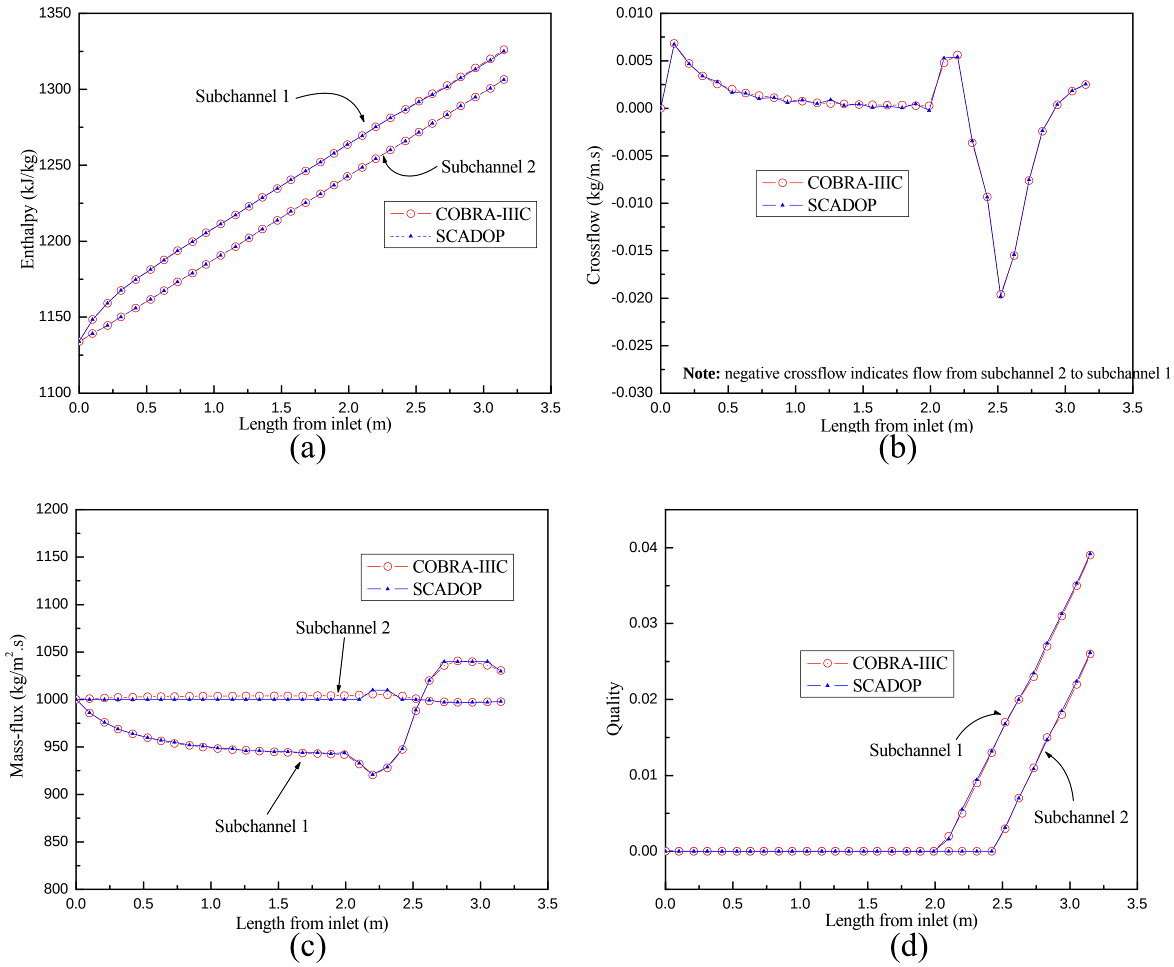

Figure 6-3: Results for two subchannel layout; variation along length of (a) enthalpy, (b) crossflow, (c) Mass flux and (d) quality

The results for the four subchannel case are presented in Figure 6-4. Again a good correspondence with COBRA-IIIC is seen. Moreover, the equivalence in predictions are seen for the outer subchannels. It can also be seen that the crossflow per unit length in the four subchannel case is actually 1/3rd of what was observed in the two subchannel case.

It may thus be said from the results of the hypothetical case that the subchannel solution scheme of SCADOP has been successfully verified against COBRA-IIIC which is an established subchannel analysis tool.

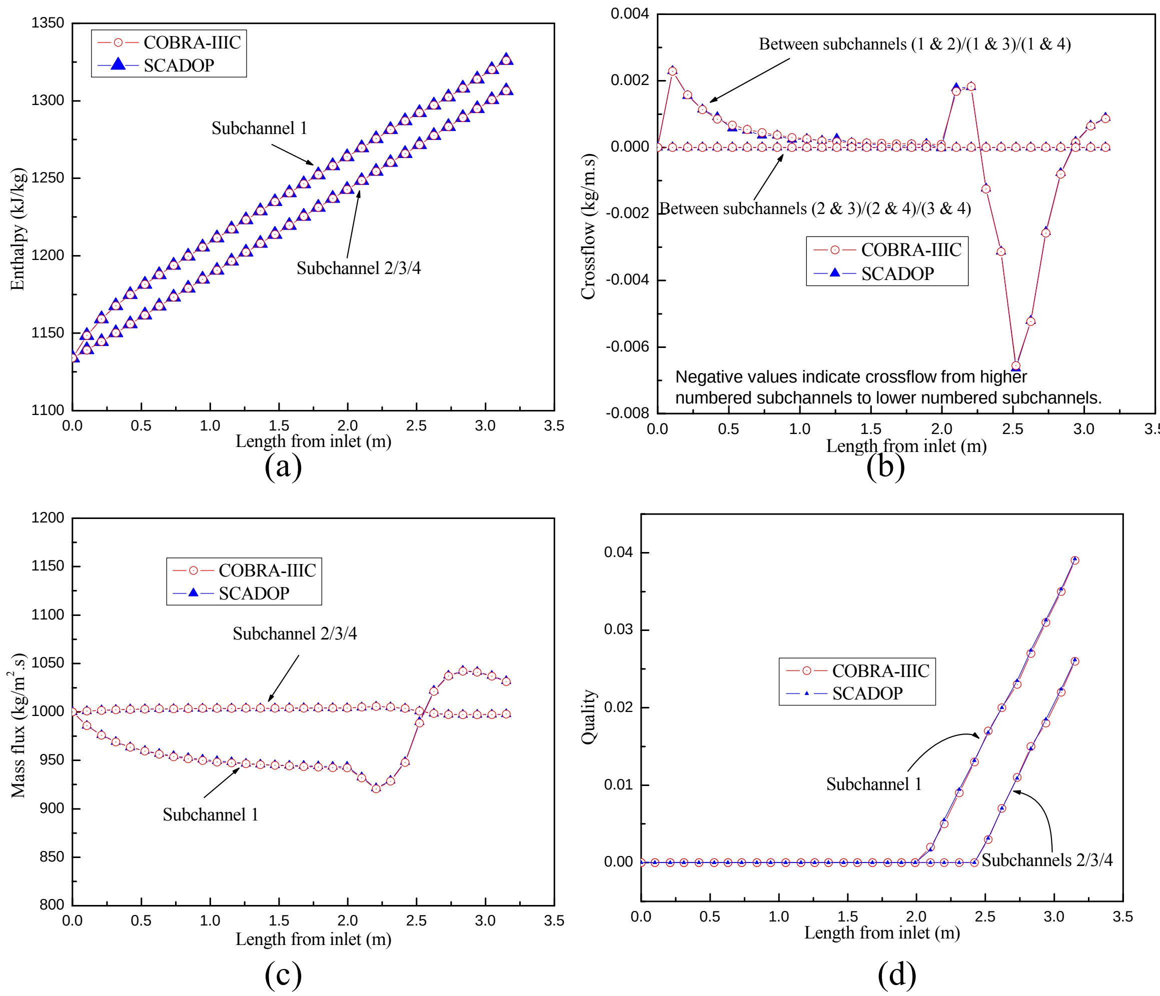

Figure 6-4: Results for four subchannel layout; variation along length of (a) enthalpy, (b) crossflow, (c) Mass flux and (d) quality

6.3.2 Coupling the film dryout model with subchannel analysis

The subchannel code calculates the pressure, mass flux and quality in each subchannel at each axial location. Subchannels are different from tubes in the sense that they are continually communicating with adjacent subchannels, exchanging mass and energy between them. These values of cross-flow mass and energy serve as the guide posts while performing the liquid film flow analysis. This is shown in equations (6.6) and (6.7).

In each of the subchannels at the onset of annular flow, the film mass flux is divided among the different walls (heated as well as unheated) according to the portion of their perimeters, $\left(\zeta_{w,r}/\zeta_w\right)$. The evolution of film on each of the rods in a subchannel is then computed through eqn.(6.5).

6.4 Prediction of rod bundle dryout

In this section SCADOP predictions are compared with experimental data of Becker et al.[72] and PELCO experiments (Evangelisti et al.[170]). The former data is for a 7-rod cluster (Figure 6-5) arranged in circular pitch. The axial heat flux distribution is uniform. The latter case is for a 16 pin bundle arranged in square pitch (Figure 6-6) and the heat flux distribution is non-uniform. These experiments also mention the location of dryout. The subchannel configuration considered for the subchannel analysis is also shown in the respective rod bundle cross-sections. For the 7-rod cluster, a 1/6th symmetry sector is adopted and for the 16-rod cluster, 1/4th symmetry sector is chosen for analysis. The conditions for the two experiments are reported in Table 6-2.

Table 6-2: Rod bundle dryout data used for validation

Source	**Mass-flux (kg/m^2s)**	**Pressure (bar)**	**Axial flux profile**	**Length (m)**	**Data points**
Becker et al. (1965)	181-880	11-41	Uniform	1.67	40
PELCO (Evangelisti et al., 1972)	700-1620	69-71	Stepped (initial 1.04m has twice the flux of the remaining length)	2.7	43

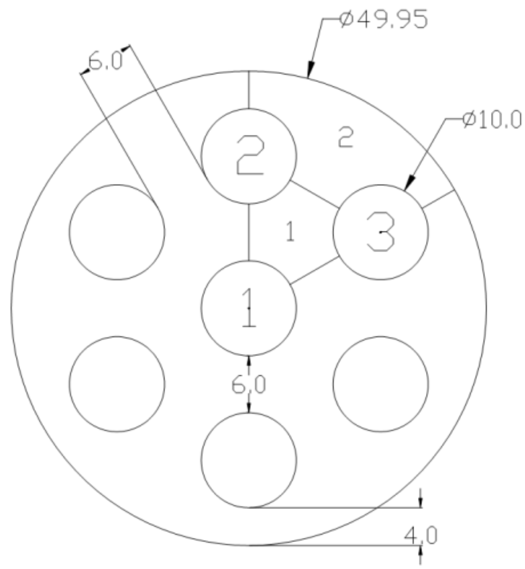

Figure 6-5: Geometry of 7 rod cluster (Becker et al. [72]**). Subchannels and rods are numbered using smaller and larger font respectively**

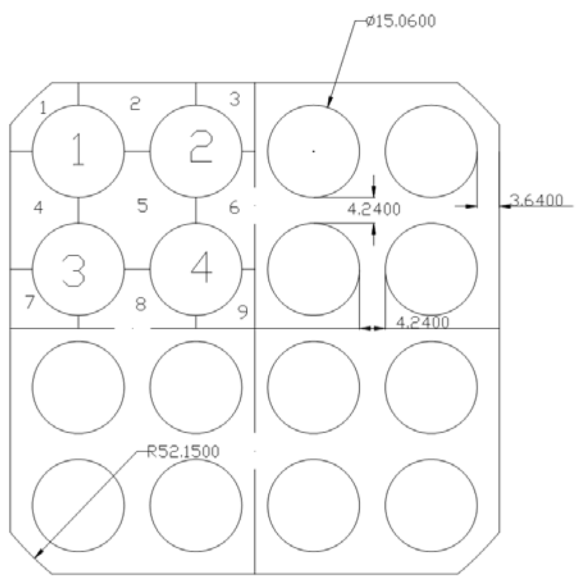

Figure 6-6: Geometry of 16 rod cluster (Evangelisti, et al. [170]**). Subchannels and rods are numbered using smaller and larger font respectively**

The predictions for Becker et al.[72] experiments are plotted as the ratio of predicted to experimental Critical Heat Flux (CHF) versus experimental exit quality (Figure 6-7). For most of the cases, dryout was predicted to occur in the outer pins, towards the outer subchannel (Figure 6-5). The experiments also indicate that the dryout occurred on the outer side of outer pins. All the predictions are within +15% of experimental dryout data. The model is thus seen to over-predict the experimental CHF. It can be reasoned from Figure 4-4 that towards the end of the channel length, the entrainment and deposition model [4] predicts a greater reduction in entrained flow rate (or greater increase in film flow rate) with quality than is experimentally observed. This predicts a greater than actual film flow rate leading to dryout at higher quality. Another factor which might lead to over prediction is the fact that the film generally tends to be thicker on the concave surfaces (channel walls) than on the convex surfaces (rods) even for adiabatic cases [23]. This has not been modeled in the present case.

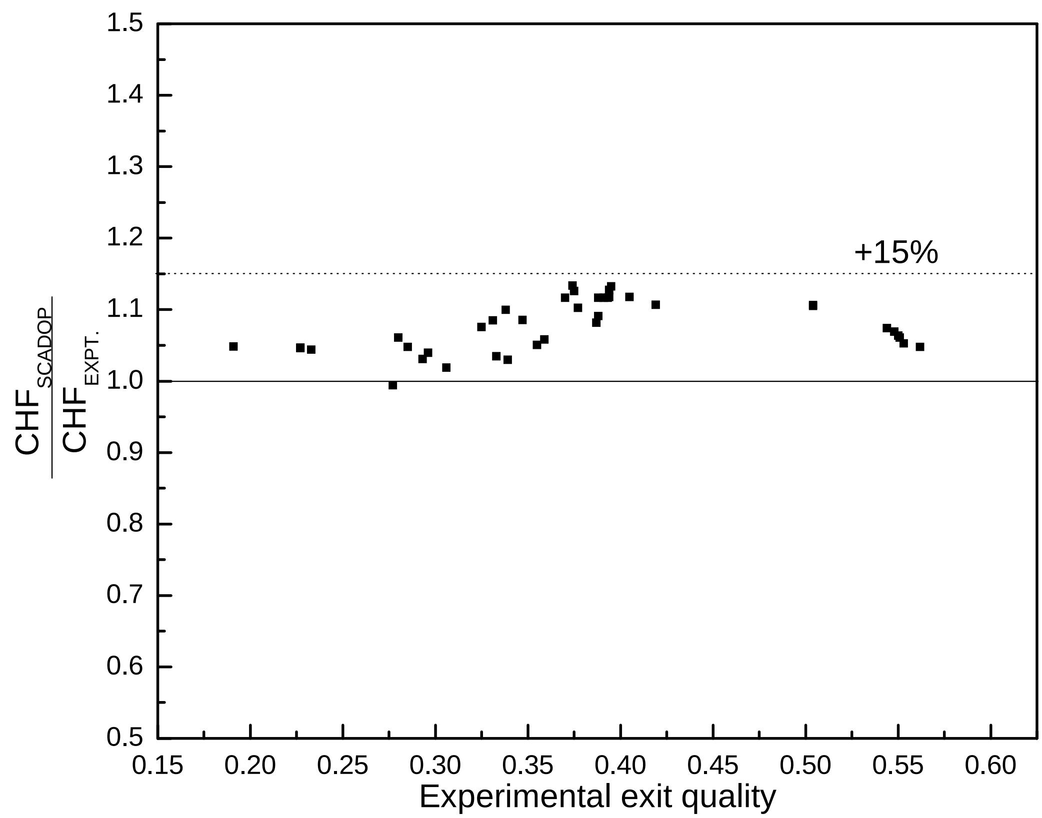

Figure 6-7: SCADOP predictions compared against Becker et al.[72] **rod bundle dryout data**

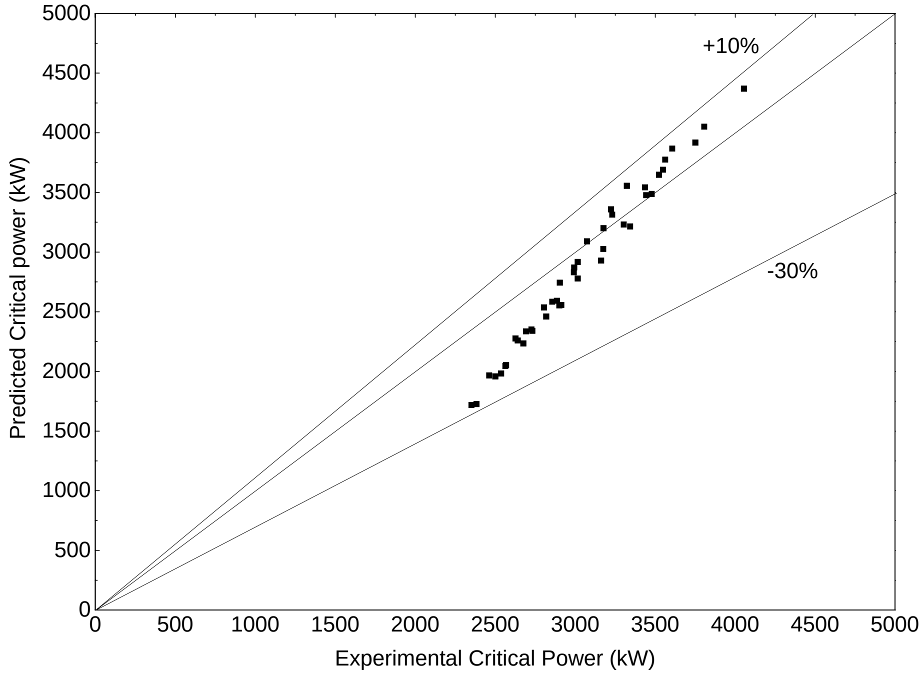

Figure 6-8: SCADOP predictions compared against Evangelisti et al. [170] **rod bundle dryout data**

The predictions of PELCO [170] experiments are on an average under predicted and lie in the band of -30% to +10% of experimental critical power (Figure 6-8). In this case Critical Power (CP) is compared since in a non-uniform heat flux profile, the terminology Critical Heat Flux (CHF) loses its meaning and CP is a better representation of dryout conditions. Here, as opposed to Figure 6-7, the dryout power is mostly under predicted. Moreover, the errors are not randomly distributed and a clear trend is visible. The reason for this is not clear at present and needs investigation. One possible reason might be non-inclusion of spacers in the modeling work. In the experiments, dryout was observed in the corner rods (i.e., rod no. 1, Figure 6-6). The predicted dryout however was not always seen at that location. This discrepancy might also be due to not modeling the greater entrainment (or lower deposition) rate at rods. The incorporation of such models which account for curvature of the surface [166–168] is important for dryout modeling in rod bundle geometries. With such improvements, the locations prone to dryout can be correctly identified. This advantage which can be realized from phenomenological dryout modeling is not possible with empirical correlations.

6.5 Concluding remarks

A model has been presented for mechanistic estimation of dryout power in nuclear fuel rod bundles. The highlight of the model is that it uses a new methodology for prediction of IEF. Apart from this, the model uses coolant centered subchannel approach accounting for different films on different rods in a subchannel. The model which has been programmed into a computational tool – SCADOP has been applied to two experimental rod bundle geometries. The model is able (for most cases) to predict the location of dryout correctly. This is a distinct advantage of mechanistic models over the correlation based approach for dryout prediction. Such predictions can be further improved by considering the effect of surface curvature.

Presently the model does not include the effect of spacers and predictions are expected to improve upon incorporating them.

7 HEAT TRANSFER TO DROPLETS IN POST DRYOUT REGIME

Droplets play an important role in post dryout heat transfer both during blow down as well as reflood. Their contribution towards heat transfer depends upon whether they are able to wet the wall or not. Kendall and Rohsenow [92] present a study in which they have experimentally determined the effectiveness of heat transfer as a function of wall superheat. There have been gross studies [5,7] which experimentally ascribe up to 10% of total wall heat transfer to that due to non-wetting drops. There have been models which have attempted to model both the heat transfer to droplets [9] as well as their deformation upon impaction [92]. These models have been incorporated as the wall – droplet heat transfer component in the complete Dispersed Flow Film Boiling (DFFB) model [8,9,171] and have been validated against experimental data of wall temperature transient during blowdown as well as reflood phases.

While this holistic approach towards validation is necessary, it seems desirable to also check if the heat transfer contributions predicted by each of the components of a three-part model (§2.4.2) indeed match experimental values. To a large extent the wall–vapor and vapor–droplet models are validated (may be for other reasons as these phenomena have applications widely different from rewetting). The wall-drop heat transfer has however been studied more from a mathematical point of view. The approach has been to derive some mechanistic model or equation and then simply incorporate them to the model. Exclusive validation particular to this heat transfer mechanism was missing. Part of the reason might be the absence of detailed experimental data on drops, their shape and motion. But the other argument would be since two out of three components are validated, a check of the whole is sufficient to guarantee the correctness of the third mechanism.

Nevertheless, it is always good to check the validity of a particular model by comparing against experimental data.

In the present work a model is first proposed for a sessile droplet on a surface above Leidenfrost point. The intent in considering a sessile droplet is validation of the model as relatively recent experimental data [10] is now available in the form of thickness of the vapor layer under the drop. It is shown in what follows that the vapor layer thickness and heat transfer are intimately linked. Another reason for considering sessile drops is the feeling that the transverse velocities in post dryout regime are not very high. Typically they would be of an order of magnitude similar to or lesser than the deposition coefficient existing in BWRs. This is seen [172] to be in the range of 0.003 – 0.017 m/s. At such small radial velocities, the deformation due to impaction would not be very high [173] and the value of heat transfer obtained from a sessile drop model will not be very ill placed.

A model based on the dominant forces acting on the droplet is described in §7.1. The results obtained from the model are discussed in §7.2. More recent experiments have been conducted which shed new light on the phenomena. Other new experimental data are now available describing drop shape under stationary as well as on impact.

7.1 A mechanistic model for droplet heat transfer

In this work, a stagnant Leidenfrost drop at saturation temperature is considered. The droplet is being constantly fed so that the amount of liquid in the drop doesn't vary with time. This of course is a huge simplification which should be considered as a first step in analyzing the complex problem of impinging vaporizing droplets.

A surface heated beyond the Leidenfrost temperature, will not get wetted by water. The heat transfer to a Leidenfrost drop causes vigorous vapor generation at its bottom surface preventing direct contact between the droplet and heater surface. The drop thus levitates over the heated surface (Figure 7-1). The model is formulated to be applicable only to the thin vapor film (also referred to as vapor layer) region bounded by the droplet and heated surface.

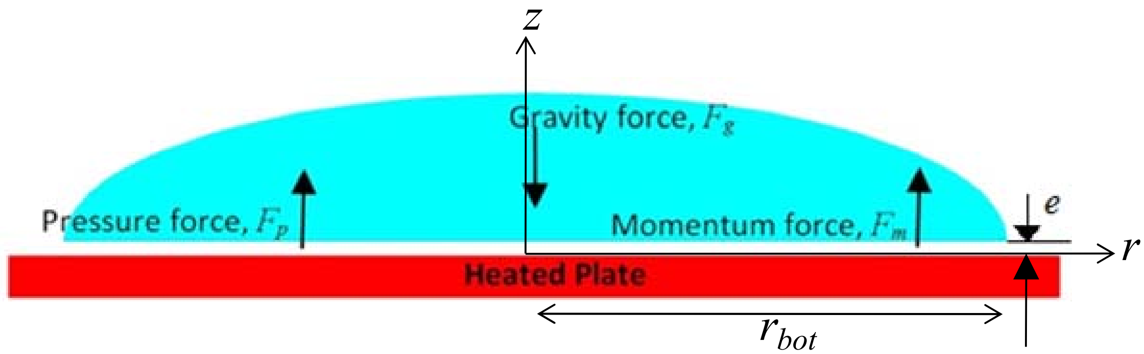

Figure 7-1: Forces acting on a Leidenfrost drop

The assumptions used in this analysis are:

1. Roughness of the substrate is not accounted for.
2. No undulations are considered at the bottom surface of Levitating drop and it is considered to be parallel to the heated surface. This is a simplification which has been used by previous workers and discussed later.
3. The water in droplet is assumed to be homogenously mixed. No temperature variation is assumed in the drop. This holds well for drops near saturation.
4. Internal circulation of water within the drop is not considered. This is justified considering uniform temperature within the drop.
5. Since the vapor film is thin, lubrication assumption is valid in the vapor film region.

The drop is acted upon by the forces of gravity due to self weight, pressure in the vapor film and reaction force of the vapor velocity. These forces are discussed in what follows.

7.1.1 Gravity Force

The gravity force is simply evaluated by taking into account the mass inside the drop. The force, F_g is given as:

$$F_g = \rho_l V g \tag{7.1}$$

The geometry of the levitating drop is not spherical and depends on the size of the drop. If the droplet radius is smaller than the capillary length, it is nearly spherical except at the bottom where it is flattened. For droplet radius larger than capillary length, the droplet becomes flat and puddle shaped. The drop height in such cases is equal to twice the capillary length. The drop volume can then be evaluated by considering the drop to be cylindrical [10].

7.1.2 Pressure Force

Underneath the drop the pressure builds up to a level where there is a balance between vapor generation rate and vapor escape rate. Considering that the vapor layer is thin, the lubrication assumption (i.e., viscous forces are dominant over inertia forces) holds. The radial momentum equation for the vapor can thus be written as[174]:

$$\mu_v \frac{\partial^2 u}{\partial z^2} = \frac{\partial p}{\partial r} \tag{7.2}$$

The variation of the radial vapor velocity, u, can be obtained upon integrating eqn.(7.2) from heater surface to bottom of drop. The boundary condition at the heater surface is taken to be no slip i.e., ($z = 0, u = 0$). At the drop-vapor interface, no-slip between water and steam would hold but some radial velocity may exist as the interface is between two fluids. However, since water is much denser and viscous than steam, velocity at interface is expected to be small and often assumed zero in most of the earlier works [10,174].

Moreover, the steam emanating from the bottom of the drop would tend to cushion the drop against the shear due to radial steam movement. Thus the assumption of zero velocity at the interface ($z = e, u = 0$) may be justified. But, in the absence of information on velocity at interface, it is instructive to consider the other extreme condition of zero shear at interface ($z = e,\ \partial u/\partial z = 0$). The two extreme boundary conditions discussed above are referred to as zero velocity and zero shear in the rest of the paper. For the zero velocity case, integration of eqn.(7.2) gives,

$$u = \frac{1}{2\mu_v}\left(\frac{\partial p}{\partial r}\right)z\left(z-e\right) \tag{7.3}$$

The similar expression for zero shear case is given by eqn.(7.4).

$$u = \frac{1}{2\mu_v}\left(\frac{\partial p}{\partial r}\right)z\left(z-2e\right) \tag{7.4}$$

At the drop-vapor interface, the vapor velocity normal to the interface would be in the downward direction for water drops smaller than ~10 mm radius. For larger sized drops, the vapor generated, being the lighter phase, tends to move upwards through the drop destroying its integrity. This phenomena has been modeled as the Rayleigh-Taylor instability at the drop-vapor interface [10]. The vapor velocity, w in the downward direction is obtained by using the continuity equation (7.5):

$$\frac{1}{r}\frac{\partial\left(ru\right)}{\partial r} + \frac{\partial w}{\partial z} = 0 \tag{7.5}$$

Which on integrating again from $z = 0$ to $z = e$, with the condition that $w = 0$ at $z = 0$ gives, for the zero velocity case,

$$w = -\frac{1}{r}\frac{\partial}{\partial r}\left(r\frac{\partial p}{\partial r}\right)\frac{z^2}{12\mu_v}\left(2z-3e\right) \tag{7.6}$$

And for the zero shear case,

$$w = -\frac{1}{r}\frac{\partial}{\partial r}\left(r\frac{\partial p}{\partial r}\right)\frac{z^2}{6\mu_v}\left(z-3e\right) \tag{7.7}$$

The vapor ejection velocity at the bottom of the drop, W is governed by the rate of heat input to the drop. Thus we may write

$$w\big|_{z=e} = W = -k_v \frac{\left(dT/dz\right)_{z=e}}{\rho_v h_{fg}} \tag{7.8}$$

An expression for the variation of pressure along radius is obtained by equating at $z = e$, eqns. (7.6) and (7.8) for zero velocity case and eqns. (7.7) and (7.8) for zero shear case. Thus for the zero velocity case, we obtain

$$p = -\frac{3k_v\mu_v}{e^3\rho_v h_{fg}}\left(\frac{dT}{dz}\right)_{z=e}\left(r^2 - r_{bot}^2\right) \tag{7.9}$$

And for the zero shear case,

$$p = -\frac{3k_v\mu_v}{4e^3\rho_v h_{fg}}\left(\frac{dT}{dz}\right)_{z=e}\left(r^2 - r_{bot}^2\right) \tag{7.10}$$

The total pressure force at the bottom of the drop is obtained by integrating the pressure over the total area at bottom of drop. Equation (7.11) is for the zero velocity and (7.12) for zero shear assumption.

$$F_p = \int_0^{r_{bot}} 2\pi rp\,dr = \frac{3\pi k_v\mu_v r_{bot}^4}{2e^3\rho_v h_{fg}}\left(\frac{dT}{dz}\right)_{z=e} \tag{7.11}$$

$$F_p = \int_0^{r_{bot}} 2\pi rp\,dr = \frac{3\pi k_v\mu_v r_{bot}^4}{8e^3\rho_v h_{fg}}\left(\frac{dT}{dz}\right)_{z=e} \tag{7.12}$$

7.1.3 Momentum Force

The momentum force is basically the reaction force exerted by the vapor emanating from the bottom of the drop. This force, neglected by other workers [10,174] can be written as:

$$F_m = -W\frac{dm}{dt} = \left(\frac{dT}{dz}\right)^2_{z=e}\left\{\frac{k_v}{h_{fg}}\right\}^2\frac{\pi r_{bot}^2}{\rho_v} \tag{7.13}$$

where (dm/dt) represents the rate at which vapor is ejected from bottom of the drop.

The final force balance on the drop yields:

$$F_g = F_p + F_m \tag{7.14}$$

Thus for zero velocity,

$$\rho_l Vg = \frac{3\pi k_v \mu_v r_{bot}^4}{2e^3\rho_v h_{fg}}\left(\frac{dT}{dz}\right)_{z=e} + \left(\frac{dT}{dz}\right)^2_{z=e}\left\{\frac{k_v}{h_{fg}}\right\}^2\frac{\pi r_{bot}^2}{\rho_v} \tag{7.15}$$

And for zero shear,

$$\rho_l Vg = \frac{3\pi k_v \mu_v r_{bot}^4}{8e^3\rho_v h_{fg}}\left(\frac{dT}{dz}\right)_{z=e} + \left(\frac{dT}{dz}\right)^2_{z=e}\left\{\frac{k_v}{h_{fg}}\right\}^2\frac{\pi r_{bot}^2}{\rho_v} \tag{7.16}$$

The available models [10,174] assume linear temperature distribution in the vapor layer leading to eqns. ((7.17), (7.18)), which are bi-quadratic equations for vapor layer thickness, e.

$$\rho_l Vge^4 - \left\{\frac{k_v\left(T_{surf} - T_{sat}\right)}{h_{fg}}\right\}^2\frac{\pi r_{bot}^2}{\rho_v}e^2 - \frac{3\pi\mu_v r_{bot}^4 k_v\left(T_{surf} - T_{sat}\right)}{2h_{fg}\rho_v} = 0 \tag{7.17}$$

$$\rho_l Vge^4 - \left\{\frac{k_v\left(T_{surf} - T_{sat}\right)}{h_{fg}}\right\}^2\frac{\pi r_{bot}^2}{\rho_v}e^2 - \frac{3\pi\mu_v r_{bot}^4 k_v\left(T_{surf} - T_{sat}\right)}{8h_{fg}\rho_v} = 0 \tag{7.18}$$

In both of these equations, only one of the four roots is positive and physical. The implication of assuming a linear temperature can be gauged by including the effect of convection on the temperature distribution in the vapor layer. An earlier work [174] assuming zero velocity at interface had used an ad-hoc substrate-to-vapor heat transfer coefficient with the zero velocity assumption to match their predictions to experimental data of Biance et al. [10]. Such ad-hoc assumptions, though helpful in validations, give room for questioning the credibility of the model. In the present work, it is intended to reduce ad-hoc coefficients and justify the phenomena through models and postulated mechanisms. Physically, the convection of the vapor from the interface would cause the effect of saturation temperature existing at the drop-vapor interface to percolate further downwards, reducing the temperature gradient at the interface and consequently the thickness of the vapor film.

7.1.4 Energy Equation

The need for introduction of an ad-hoc heat transfer coefficient [174] can be obviated by solving the energy equation in the vapor layer. This would give the temperature distribution in the layer and temperature gradient at drop vapor interface. A scheme is thus devised to iteratively obtain vapor layer thickness as well as heat transfer to the drop. The energy equation in cylindrical coordinates assuming axi-symmetry can be written as:

$$u\frac{\partial T}{\partial r}+w\frac{\partial T}{\partial z}=-\alpha\left\{\frac{1}{r}\frac{\partial}{\partial r}\left(rk_v\frac{\partial T}{\partial r}\right)+\frac{\partial^2 T}{\partial z^2}\right\};\alpha=\frac{k_v}{\rho c_p} \tag{7.19}$$

Since the thickness of the vapor layer, e is much smaller than its radial extent, r_{bot}, the relative importance of the terms is obtained from an order of magnitude analysis. Using the reference quantities as given in Table 7-1, we obtain the non-dimensional equation comprising of the dominant terms as eqn. (7.20).

Table 7-1: Non-dimensional parameters for vapor energy equation

Parameter	**Reference value**	**Non-dimensional parameter**
z	e	$z^* = z/e$
r	r_{bot}	$r^* = r/r_{bot}$
u	$U_r = \frac{r_{bot}}{e}W$	$u^* = u/U_r$
w	W	$w^* = w/W$
T	$(T_{sur} - T_{sat})$	$T^* = \frac{T - T_{sat}}{T_{sur} - T_{sat}}$

$$u^* \frac{\partial T^*}{\partial r^*} + w^* \frac{\partial T^*}{\partial z^*} = \frac{\alpha}{eW} \frac{\partial^2 T^*}{\partial z^{*2}} \tag{7.20}$$

Thus, the radial diffusion can thus be neglected and the equation which needs to be solved to determine the temperature field in the vapor layer is eqn.(7.21).

$$u \frac{\partial T}{\partial r} + w \frac{\partial T}{\partial z} = \alpha \frac{\partial^2 T}{\partial z^2} \tag{7.21}$$

Physically this implies that in the radial direction, the properties are influenced only by the upstream side. The solution of eqn. (7.21) requires two boundary conditions in the z-direction and one boundary condition in radial direction. These are given by:

$$\mathrm{T} = \mathrm{T_{sat}} \quad \text{at} \quad \mathrm{z} = \mathrm{e}$$

$$\mathrm{T} = \mathrm{T_{sur}} \quad \text{at} \quad \mathrm{z} = 0$$

$$\frac{\partial \mathrm{T}}{\partial \mathrm{r}} = 0 \quad \text{at} \quad \mathrm{r} = 0$$

It must be mentioned here that in spite of some pressure build up in the vapor layer, the saturation temperature, T_{sat} is assumed to be equal to the value at 1 atm. pressure. Further, the radial velocity field is obtained from equations (7.3) and (7.9). Axial velocity field is similarly obtained from equations (7.6) and (7.9). Fields appropriate for the zero shear case can be obtained from analogous equations (7.4), (7.7) and (7.10)

7.1.5 Solution methodology for energy equation

The solution of eqn. (7.21) is obtained by finite volume method. Upwind differencing scheme is used for the first order terms and central differencing for second order term. A representative computational cell is shown in Figure 7-2. The temperature field and gradient at the bottom of the drop is iteratively obtained.

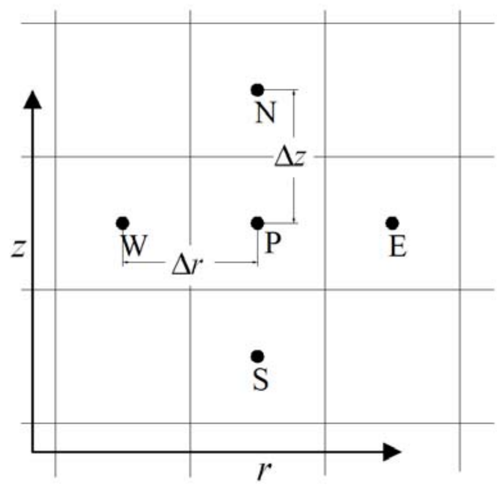

Figure 7-2: A computational cell in the vapor layer

The discretized energy equation for evaluation of temperature T_P at point P is given as

$$a_P T_P = a_W T_W + a_N T_N + a_S T_S \tag{7.22}$$

The coefficients a_P, a_W, a_N, a_S are given as

$$\begin{aligned} a_W &= u/\Delta r \\ a_N &= \alpha/(\Delta z)^2 - w/\Delta z \\ a_S &= \alpha/(\Delta z)^2 \end{aligned} \tag{7.23}$$

It must be noted that the east side coefficients do not play any role in the discretized form of the equation. Physically this implies that in the radial direction, the properties are influenced only by the upstream side.

The iteration scheme to arrive at the final temperature field and vapor film thickness is given below for zero velocity assumption.

1. The vapor layer thickness obtained by solving eqn. (7.17) is used as the first approximation to solve eqn.(7.21) and obtain the temperature field.
2. $(dT/dz)_{z=e}$ thus obtained is used to evaluate the vapor layer thickness,e using eqn. (7.15).
3. The new value of e is fed as the new boundary condition for eqn.(7.21) and steps 2 and 3 are repeated till converged temperature field and vapor layer thickness is arrived upon.

The above scheme is for the zero velocity case. For zero shear case, the treatment is similar, only the relevant equations need to be used.

7.2 Comparison of the model predictions with experimental data

7.2.1 Comparison with sessile drop experiments

The experimental data of Biance et al. [10] has been used to validate this model. In their experiments, they have considered a stationary droplet. The droplet was constantly fed to ensure that the drop volume remains same in spite of evaporation from the drop. The drop was maintained at a temperature of 99±1^{o}C. The surface was maintained at 300^{o}C. The thickness of the vapor film was estimated from the diffraction patterns obtained when a laser beam was passed through the thin vapor layer.

The values of vapor layer thickness obtained from equations (7.17) and (7.18) (i.e., the zero velocity and zero shear assumptions) are plotted as the solid lines in Figure 7-3. Neglecting the momentum force term in eqn. (7.17) gives the same expression for e as that of Biance et al. [10]. The difference in film thickness calculated from eqn. (7.17) and Biance et al. [10] is however negligible. It is the author's view that though the effect of momentum force is negligible for stationary drops, it will be important in the study of impinging droplets. Thus this term is retained in the present model.

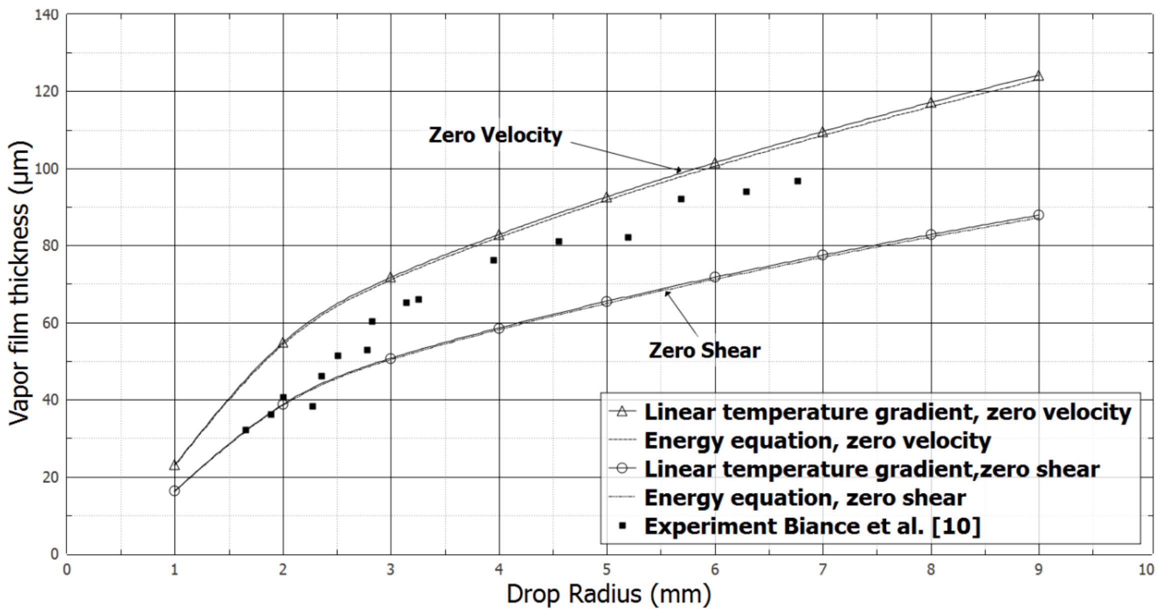

Figure 7-3: Experimental and calculated vapor layer thickness. Experiments were performed at atmospheric pressure with surface superheat of 200^{o}C

It is seen that the experimental values are bounded by the zero velocity and zero shear assumptions (Figure 7-3). This is suggestive that vapor would have a radial velocity at the interface and that it lies between the two extremes considered in the present work. For lower drop radii (< 2.5 mm, interestingly this is the capillary length!) the zero shear assumption seems to give a good match. But, for higher drop radii, the zero velocity predictions are nearer to the experimental observations. Further, the overall trend is better predicted by the zero velocity assumption. This indicates that the interfacial condition possibly changes with drop radius. A more detailed analysis simulating the flow within the drop would give a better picture.

The film thickness evaluated using the computed temperature gradient (§7.1.4) are plotted as the dashed lines in Figure 7-3. In this case, it is seen that the predicted vapor film thickness is reduced only marginally (this is the reason why the dashed lines are not very much distinguishable from the solid ones) from that obtained upon assuming linear temperature gradient. It may thus be said that neglect of convection does not contribute to the mismatch between the predictions and experimental values. The use of an ad-hoc heat transfer coefficient by Myers and Charpin [174] to justify the lesser thickness observed is unable to capture the physics of the phenomena.

The computed temperature field for a particular case (of 6 mm drop radius) with zero velocity assumption is shown in Figure 7-4. No appreciable temperature gradient is observed in the radial direction. This is possibly the reason for insignificant difference between linear temperature gradient assumption and solving the energy equation.

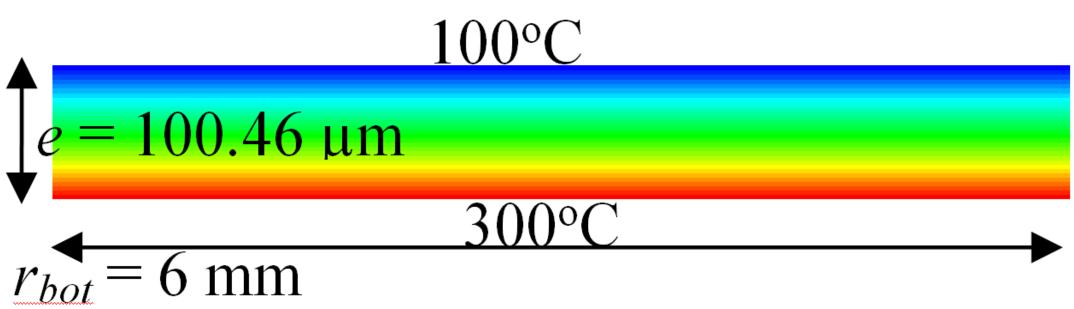

Figure 7-4: Temperature field in vapor layer for a drop of radius 6 mm

Figure 7-5 shows the temperature gradient at the drop-vapor interface evaluated using a linear temperature gradient and that using the energy equation for the zero velocity assumption. It is seen that the temperature gradient and consequently the heat transfer from the substrate to the drop is actually lesser than what is predicted by a linear temperature gradient model. Also the heat flux is very large for smaller drops and falls as drop size increases. This can be attributed to increasing vapor layer thickness with drop size. A Nusselt number, Nu can be defined by evaluating an effective heat transfer coefficient, h and considering the vapor layer thickness, e as the characteristic length for heat transfer (eqn.(7.24)). Here the computed gradient at surface $\left(\left(dT/dz\right)_{z=0}\right)$ is considered, as knowledge of heat transfer from the heated surface is often more relevant in practical scenario.

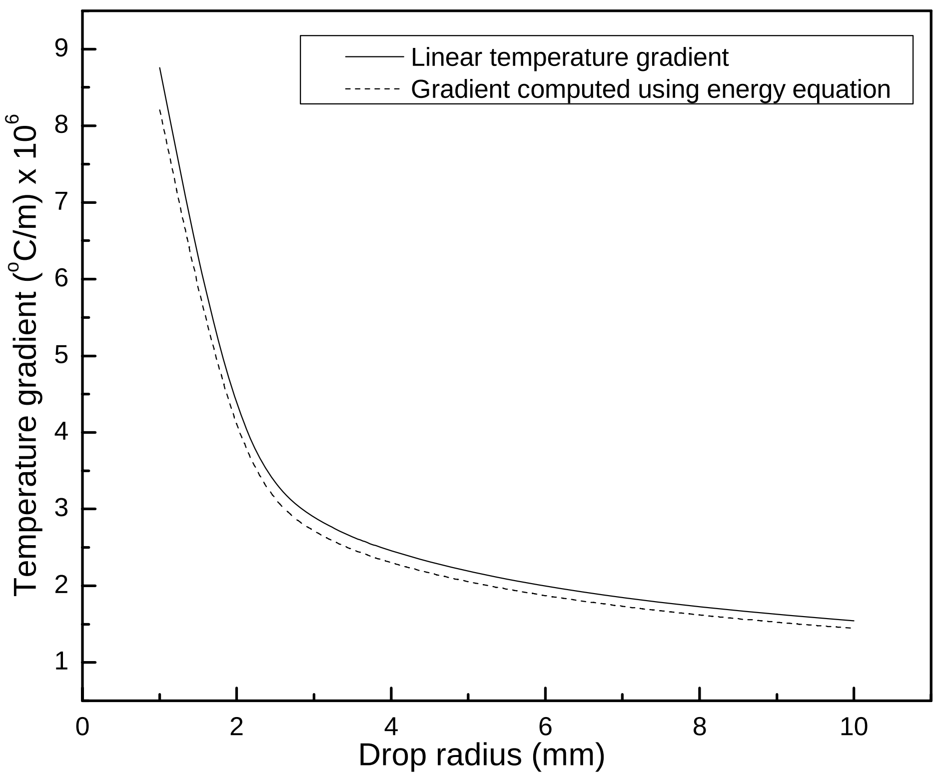

Figure 7-5: Predicted temperature gradient at drop-vapor interface with zero velocity assumption

$$h = \frac{k_v \left(dT/dz\right)_{z=0}}{\left(T_{sur} - T_{sat}\right)}; Nu = \frac{he}{k_v} = \frac{\left(dT/dz\right)_{z=0}}{\left(T_{sur} - T_{sat}\right)/e} \tag{7.24}$$

It is evident from the definition that Nu represents the enhancement of heat transfer rate from the surface due to convection. The computed Nusselt number is plotted as a function of Reynolds number, Re (eqn.(7.25)) in Figure 7-6 for the zero velocity assumption. Re changes with drop diameter, thus the abscissa is an indirect indication of the different drop diameters. Nu remains constant in the range of relevant Re (drop diameters) and is just over 1. This is due to the fact that the flow is laminar and effect of convection is small.

$$\mathrm{Re} = \frac{\rho_v \left(\pi r_{bot}^2 W \middle/ \pi r_{bot} e \right) e}{\mu_v} = \frac{\rho_v W r_{bot}}{\mu_v} \tag{7.25}$$

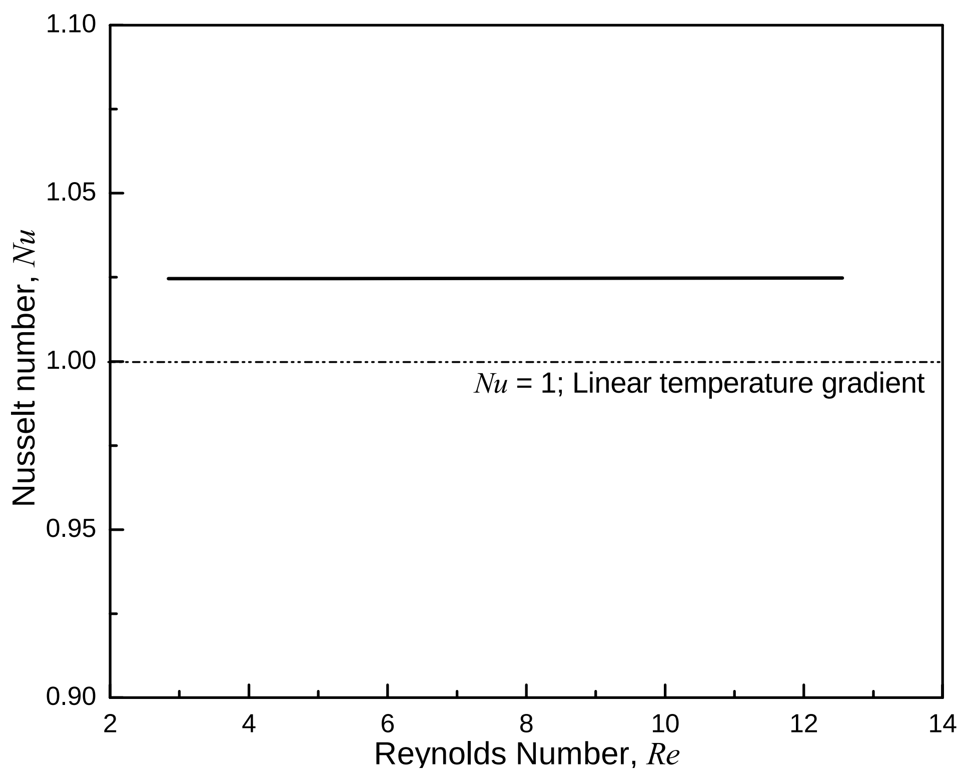

Figure 7-6: Nusselt number variation with Reynolds number

7.2.1.1 Another aspect of the drop vapor interface

Recent experiments of Burton et al. [175] and Caswell [176] with evaporating drops have revealed that the bottom surface of the drop is not flat. The edges (neck region) of the drop are closer to the heated surface while the centre arches higher. The shapes of such Leidenfrost drops have been calculated using Axi-symmetric Drop Shape Analysis (ADSA) [177] coupled with simple relations for the measured curvatures [175] at the neck and bottom-center. The shape of the Leidenfrost drop for two different drop sizes is shown in Figure 7-7.

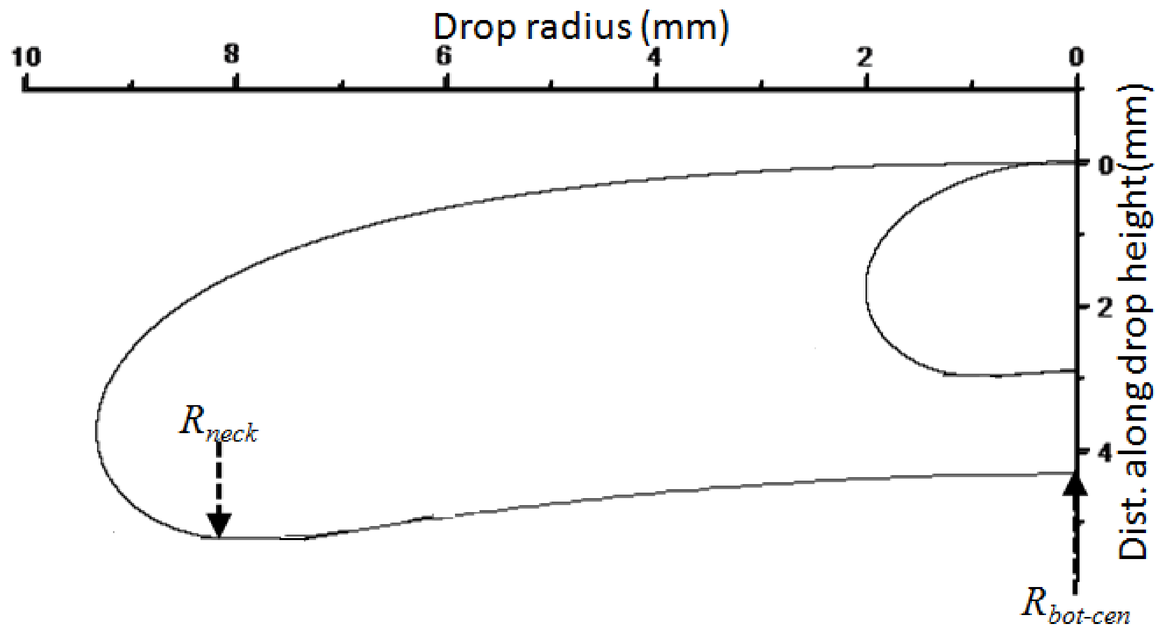

Figure 7-7: Computed drop shapes for two different drop radii

It is also worth mentioning that the drop radius is not equal to but slightly greater than bottom radius. The elevation difference between neck and bottom-centre of the drop is in fact higher than the difference between predicted (zero velocity) and experimental values in Figure 7-3. Such quantification of the curvature at the bottom of droplet is not allowed in the measurement system adopted by Biance et al. [10] and their experimental values of vapor film thickness may actually correspond to that at the neck of the drop. The predictions, assuming drop-vapor interface to be parallel to the substrate, thus indicate an average film thickness (which would always be greater than the thickness at the edge) derived basically from heat transfer considerations. This furthers the argument against the usage of ad-hoc coefficients as they [174] have tried to match an average thickness with thickness in neck region. The present model can be further improved by considering the actual geometry at the drop interface.

7.2.2 Semi-quantitative comparison with results of other workers – mobile droplets

The results in §7.2.1 compared the model against an experiment which is an appropriate representation of the model assumptions. In this section the model is applied to scenarios different from the previous. Specifically mobile rather than sessile drops are considered. The motivation behind this is the fact that we expect wall normal velocities of drops to be small in post dryout flow in channels. Predicting such low impingement velocity phenomena with present sessile drop model is thus an interesting prospect to ascertain how good (or bad) the present model compares against data on impinging drops.

Recently Chatzikyriakou [5] has performed CFD simulations of heat transfer to sessile as well as impinging droplets using TrasnAT [178]. This study is an interesting one as actual drop shapes are evaluated. Results on velocity at the drop-vapor interface are however not reported by them. This as seen from Figure 7-3 might play an important role. They have further validated their computations against their experiments with controlled size (1.5 mm) droplets impinging on a heated surface kept at ~400^{o}C. The heat transfer was estimated using thermal imaging. The droplets were made to impact the surface at a constant initial velocity of 0.53 m/s. The angle at which they were directed at the wall ranged from 15^{o} (grazing) to 90^{o} (direct impingement). The component of velocity towards wall thus varied from 0.13 m/s to 0.53 m/s. This is apparently higher than the deposition coefficient (which is indicative of radial droplet velocity) in annular and post dryout flow. However, these data do give a good insight into the phenomena occurring. Chatzikyriakou

[5] reported most of the results for a 45^{o} impingement angle and found that a single droplet can cumulatively extract about 0.07J over a time of ~10 ms. Further they also report from a study of literature and application of the Wachters and Westerling correlation [179] that in the post dryout regime, a near saturated drop of 1.15 mm radius with a low approach velocity is able to extract ~0.05J.

It is interesting to see how the present computations with sessile drop fare against these values. For the sake of parity, computations were repeated for a heated surface temperature of 400^{o}C. The heat flux at the bottom of the drop was estimated from the temperature gradient at the drop-vapor interface. Vapor conductivity was taken as 0.032 W/mK. For droplets having radius smaller than the capillary length, its complete surface (not just the bottom of the drop) takes place in heat transfer [10]. A good representation of the heat transfer area is the bottom surface area of the drop, $2\pi R^2$ and not just the bottom area. The contact time for millimetric drops at low velocities is experimentally seen[173] to be ~10 ms. The results are tabulated in Table 7-2.

Table 7-2: Present computations for data reported by Chatzikyriakou[5]

	Drop radius = 1.15 mm	**Drop radius, R = 1.5 mm**
Computed heat flux to drop	0.422 MW/m^2	0.303 MW/m^2
Heat transfer area, $2\pi R^2$	8.305 mm^2	14.14 mm^2
Computed gradient at drop bottom (K/m)	1.318 x 10^7	0.946 x 10^7
Cumulative heat transferred to drop over 10 ms	0.035 J	0.04 J
Corresponding heat transfer values reported by Chatzikyriakou[5]	0.05 J	0.07 J

The computations of the present model (equations (7.17) and (7.21)) are closer to the value computed (by Chatzikyriakou [5]) using Wachters and Westerling correlation [179]. A comparison with the experimental data of Chatzikyriakou [5] however indicates greater gap. The probable reason for this difference might be the substantially higher wall normal velocities (corresponding to 45^{o} impact angle) in their experiments.

It may however be said that the sessile drop model is able to predict to a good degree the heat transfer to drops with low impact velocities and thus it would be possible to apply to post dryout scenarios in nuclear reactors.

7.3 Modification for application to nuclear reactors

The final goal of this model is to be applied to conditions relevant to nuclear reactors. To the authors' knowledge, there are no experimental studies which quantify heat transfer (only) to drops in the Post Dryout (PDO) regime. Further, the model developed in this work is for droplet interaction over a horizontal surface. In most of the nuclear reactors (except CANDU and Indian PHWRs), the fuel cluster is vertical and the formulation developed needs modification to be applicable.

In vertical systems, the drop moves towards the wall with a wall normal velocity which is of the same order of magnitude as the deposition coefficient, k in annular flows. As the drop approaches the heated wall, vapor starts to generate and accumulate in the region between drop and wall. To apply the presently developed model to vertical walls, it is important to recognize that the vapor present in the vapor layer pushes against the radial motion of drop towards the wall. The formulation of the pressure force term thus remains the same. Thus, we have

$$F_p = \int_0^{r_{bot}} 2\pi r p dr = C_{vel} \frac{\pi k_v \mu_v r_{bot}^4}{e^3 \rho_v h_{fg}} \left(\frac{dT}{dz} \right)_{z=e} \tag{7.26}$$

The constant C_{vel} is 3/2 for zero velocity assumption and 3/8 for zero shear assumption.

The momentum force term, F_m due to ejection of vapor from the drop is also retained. This force acts in the same direction as the pressure force, i.e., to force the drop away from the wall.

$$F_m = \left(\frac{dT}{dz} \right)_{z=e}^2 \left\{ \frac{k_v}{h_{fg}} \right\}^2 \frac{\pi r_{bot}^2}{\rho_v} \tag{7.27}$$

The equivalent of the gravitational force term i.e., the one pushing the drop towards the wall is the initial wall directed momentum of the droplet. Here a parallel may be drawn between grazing droplets in horizontal flow and it may be assumed that:

1. The droplet interaction time, Δ_i is 10 ms.
2. The droplet rebound velocity is of the same magnitude as the incoming velocity.

The latter assumption is the same as that used by Guo and Mishima [9] for the model developed by them. With these assumptions the force pushing the drop towards the wall is:

$$F_{wall} = \frac{2\rho_l V k}{\Delta_i} \tag{7.28}$$

It is seen that this force is analogous to the gravity force term and the term $2k/\Delta_i$ replaces acceleration due to gravity. Thus, the same formulation as discussed in §7.1 can be used. As a passing remark it may be mentioned that k is seen to be of the order of 0.01 m/s for reactor conditions. This translates into an equivalent acceleration ($2k/\Delta_i$) of the same order (though somewhat lesser) as that due to gravity. Thus the predictions made by the 'sessile drop on a horizontal surface' model won't be grossly in error, though use of eqn. (7.28) should improve the modeling.

It can be gauged from Figure 7-5 that droplet size will have an important influence on the heat transfer. In annular flow the droplets sizes are seen to follow an Upper Limit Log Normal (ULLN) distribution. It is expected that such distributions will persist after dryout as well. This conjecture is also supported by considering observations of Jepson et al. [148] who had measured drop size distributions before and after film extraction in air-water and helium-water annular flow studies. The distribution after complete film extraction can be likened to the case of film dryout. They had observed the general character of the size distributions to be similar. Most of the workers have evaluated drop sizes for air-water flows [35,37,180–182]. Only a few report studies with steam-water [183]. Though the drop sizes vary depending on liquid and gas flow rates and pressures, these studies report drop sizes to vary from 0.05 mm to about 2 mm. Most of these studies are however at low pressures and in author's knowledge, there are none which simulate pressures and mass flux same as that of BWRs. Thus, while evaluating drop diameters in the present context, reliance has to be made upon available correlations for mean droplet diameter which would be representative of heat transfer processes for the agglomerate of drops of different sizes. A good summary of such correlations can be found in Azzopardi [55] and Fore et al. [182].

7.4 Concluding remarks

A computational scheme has been presented for evaluation of the temperature gradient and vapor film thickness below a Leidenfrost drop based on force balance. In the model, the drop-vapor interface is assumed to be planar. Two extreme assumptions of the radial vapor velocity at the drop-vapor interface (zero velocity and zero shear) have been considered.

The predictions using these assumptions flank the experimental data of Biance et al.[10]. However, in light of more recent measurements [175,176] which indicate concave shaped drop interface, it is concluded that the measurements of Biance et al. [10] may actually correspond to the vapor film thickness at the neck region of the drop. Thus it should be expected that the model predictions, representing an average thickness, should be higher than Biance et al. [10] values. The zero velocity assumption, mostly used in literature, predicts higher than Biance et al. [10] experiments and also predicts the trend. But its validity needs to be checked using an improved model incorporating both shape of the drop vapor interface and motion of liquid in drop. A similar model has been developed by Chatzikyriakou [5]. Comparison of the present model with her results indicates a good degree of agreement.

In view of the foregoing, the usage of ad-hoc heat transfer coefficient by Myers and Charpin [174] to fit their model to Biance et al. [10] experimental data needs to be revisited.

Finally, the aim of this model is to simulate transient post dryout scenarios like reflooding. A reasonable comparison with the data reported in Chatzikyriakou [5] shows promise for using this simple model.

8 CONCLUSIONS AND FUTURE WORK

The importance of dryout and post dryout heat transfer in the context of nuclear reactor safety studies cannot be under-estimated. This has led to a large number of experimental, semi-empirical and theoretical treatments of the subject.

In the present work, the stress has been towards development of a validated mechanistic model for annular flow dryout phenomena. The reason for this is the failure of empirical; correlation based models in predicting dryout under wide range of scenarios. This fact has been known since a long time now but due to the ease of applicability of correlations and greater reliance of regulators on experiments, the correlation based approach has lingered.

Nevertheless, the scientific community has always been interested in finding better answers for complex phenomena such as dryout. This has led to development of the mechanistic dryout model very much in parallel with the correlation based approach since the last 4 decades. Inevitably there are a large number of such mechanistic models available in literature. Each model distinguishes oneself from the other in terms of the constitutive relations for deposition and entrainment rates. There are thus a large number of such constitutive relations as well and for a researcher new to this field, the choice of an appropriate relation presents a challenge. Further the models require boundary values like entrained fraction at onset of annular flow. This boundary condition, also known as Initial Entrained Fraction (IEF), has received attention only very lately and not much work has been done in this regard. Part of the reason for this is the non-availability of data under diabatic conditions. In fact mechanistic predictions can always be questioned due to their sensitivity to IEF.

After the occurrence of dryout, heat transfer takes place due to the flow of vapor in which droplets are dispersed. It is expected that the deposition phenomena and its dynamics existing in the annular flow, prior to dryout, remain the same after dryout. This presents an interesting possibility of application of the mechanistic model to post dryout scenarios as well. The heat transfer from the wall to droplets in this regime is a component which though not very large requires attention for best estimate predictions. Models for this heat transfer mechanism, though present have not been validated extensively. These issues of modeling in pre and post dryout regimes are highlighted in chapter 2.

8.1 Conclusions

Due to the importance of waves in churn and annular flow, characteristics of waves in churn and annular flow were studied in chapter 3. In the experiments, some portion of the operating parameter range was exclusive to data available in literature. This provides an opportunity to test the presently available correlations for wave characteristics outside the range of their applicability.

- The present data fall in the nil to very low entrainment region
- From this study, large wave characteristics such as velocity, wavelength and frequency were obtained. Such basic quantities are important for possible mechanistic models of deposition and entrainment phenomena. Truly the essence of mechanistic models is to go from basic (for instance deposition rate) to even more basic (in the present context wave characteristics) while not losing sight of the overall problem (i.e., dryout).
- For any given air and water flow rate, there was a large variation in wave frequencies and consequently wavelengths. These variations, which are not

reported by previous workers, have been quantified in this work. The wave velocity, however, did not show much variation.

- The distance-time plots presented in this chapter present a method to quantify the flow regime in terms of the slope of the ripples. An intermediate pre-annular regime could be identified from these plots.
- Apart from wave characteristics, gross annular flow parameters like film flow rate and average film thickness have been measured. These were used to validate the mechanistic model proposed and the triangular relationship. It was found that the triangular relationship as used in this work over predicts the film thickness.
- The film flow rate evaluations led to the conclusion that the onset of entrainment is predicted correctly by Hewitt and Govan [4] criterion. This, in conjunction with measurements of wavelength led to a new interpretation of the criterion for onset of entrainment that *the entrained liquid from one wave must carry to the next downstream wave for measurable entrainment to exist*.

A new methodology for IEF prediction is presented in chapter 4.

- This methodology underlines the importance of distribution of liquid among film and droplet fields on pressure gradient. The effect of churn flow is incorporated in the new methodology from observations of churn flow in chapter 3.
- The methodology is seen to predict high as well as low IEF whenever such is apparent experimentally.
- The incorporation of the IEF model was seen to lead to an improvement in dryout prediction with most of the different deposition-entrainment correlation sets studied.

The dilemma of choice among many constitutive relations for deposition and entrainment rates is attempted to be resolved in chapter 5 through a comparison against experimental entrained flow data in unheated and heated tubes as well as dryout data.

- The strategy of assessment of models is different from other assessment efforts in literature where entrainment and deposition rates have been assessed in isolation. In the present work, their performance has been assessed in tandem.
- The deposition and entrainment correlations are also assessed from the point of view of theoretical considerations and inclusion of important parameters.
- The Hewitt and Govan [4] correlation set was found to be better among those studied. This led to proposal of an improved mechanistic model using the new IEF methodology and Hewitt and Govan [4] correlation set.
- It was further seen that the prediction trends of the mechanistic model are similar to the CHF Look-up table when the uniformly heated tubular dryout data of Becker et al. [72] were simulated. Though, the RMS error and standard deviation were higher than CHF-LUT, the mechanistic predictions were more evenly distributed about the parity line. This is an important conclusion considering that the CHF-LUT is derived from experiments and can be considered as a benchmark for accuracy in uniformly heated tubes.
- The film flow rate data in air water flow are compared with predictions using Hewitt and Govan [4] correlations and good agreement is observed.

The improved mechanistic dryout model was applied to rod bundle situations and validated against experimental dryout data in chapter 6. The model was seen to fare reasonably for cases with both uniform and non-uniform axial heat flux profile.

A mechanistic model for the post-dryout heat transfer to non-wetting drops through the wall-to-drop mechanism has been presented and validated against vapor layer thickness data in chapter 8. The new model incorporates a momentum force term absent in previous models. The model is also seen to fare well against the values reported for impinging drops. This confirms the ability of the model to be applied for post dryout scenario.

8.2 Recommendations for future work

The work presented in this thesis highlights avenues which might lead to fruitful research and better understanding of phenomena leading to dryout. These are enumerated below:

1. Quantification of disturbance wave shapes and numerical evaluation of their effect on deposition and entrainment rates. Essentially, entrainment and deposition rates though treated separately in modeling are actually intimately linked through the disturbance waves. In depth study and detailed modeling of these waves would lead to better mechanistic models.
2. Experiments to evaluate initial entrained fraction and the effect (if any) heat flux has on it. This is difficult primarily because of the uncertainty in pin-pointing the exact location of transition to annular flow. Also the chaotic churn flow upstream doesn't help in measurements.
3. Modeling the effect of surface curvature on deposition and entrainment rates. This is particularly important for annulus geometries and rod bundles, where film flow is seen to be lesser on the rod (convex surface) walls.
4. With view to predicting rod bundle dryout, the establishment of equivalence or some kind of relation between rate correlations in tubes and ventilated subchannels needs to be established. This along with quantification of spacer effect are, in

author's view very important and challenging aspects which if addressed will go a long way in putting the mechanistic model on a strong footing for rod bundle dryout prediction.

5. The point of transition to annular flow in subchannels of rod bundles is another area where not many studies are available. The subchannel calculations in the present work predict transition to annular flow in one channel while adjacent channels may not have had that transition. While this scenario might be easier to visualize with some channel having purely co-current liquid and vapor flow and few adjacent ones having some counter current flow, it is difficult to grasp such predictions as the existence of low IEF (as predicted in the present work) in subchannels being surrounded by subchannels having churn flow. Studies giving information on the annular flow data like subchannel level film flow rate and entrained flow rate and mass interchange among subchannels in terms of drop flow rate and film flow rate are thus important but unfortunately not available.
6. With regards to post-dryout heat transfer to drops, it is important to study the effect of interface curvature and velocity of liquid at drop-vapor interface. Such studies will give greater confidence in the mechanistic modeling of heat transfer to non-wetting drops.

9 References

[1] A.W. Kramer, Boiling Water Reactors, Addison-Wesley Publishing Co., 1958.

[2] D.C. Groeneveld, J.Q. Shan, A.Z. Vasić, L.K.H. Leung, A. Durmayaz, J. Yang, et al., The 2006 CHF look-up table, Nuclear Engineering and Design. 237 (2007) 1909–1922. doi:10.1016/j.nucengdes.2007.02.014.

[3] IAEA, General film boiling heat transfer prediction methods for advanced water cooled reactors, in: Thermohydraulic Relationships for Advanced Water Cooled Reactors, IAEA, 2001: p. 54.

[4] G.F. Hewitt, A.H. Govan, Phenomenological modelling of non-equilibrium flows with phase change, International Journal of Heat and Mass Transfer. 33 (1990) 229–242. doi:10.1016/0017-9310(90)90094-B.

[5] D. Chatzikyriakou, Transient surface cooling by non-contacting droplet impingement, Ph.D. Thesis, Imperial College, London, 2011.

[6] R.P. Forslund, W.. Rohsenow, Dispersed flow film boiling, Journal of Heat Transfer. 90 (1968) 399–407.

[7] R.A. Moose, E.N. Ganic, On the calculation of wall temperatures in the post dryout heat transfer region, International Journal of Multiphase Flow. 8 (1982) 525–542.

[8] M. Andreani, G. Yadigaroglu, A 3-D Eulerian-Lagrangian model of dispersed flow film boiling including a mechanistic description of the droplet spectrum evolution—

I. The thermal-hydraulic model, International Journal of Heat and Mass Transfer. 40 (1997) 1753–1772.

[9] Y. Guo, K. Mishima, A non-equilibrium mechanistic heat transfer model for post-dryout dispersed flow regime, Experimental Thermal and Fluid Science. 26 (2002) 861–869.

[10] A.L. Biance, C. Clanet, D. Quéré, Leidenfrost drops, Physics of Fluids. 15 (2003) 1632–1637. doi:10.1063/1.1572161.

[11] S. Nukiyama, Maximum and minimum values of heat q transmitted from metal to boiling water under atmospheric pressure, International Journal of Heat and Mass Transfer. 9 (1965) 1419–1433.

[12] J.G. Collier, J.R. Thome, Convective boiling and condensation, Third Edit, Clarendon Press, Oxford, 1994.

[13] T.L. Bergmann, A.S. Lavine, F.P. Incropera, D.P. DeWitt, Fundamentals of Heat and Mass Transfer, Seventh ed, John Wiley and Sons, 2011.

[14] G.F. Hewitt, Burnout, in: J.G. Jinoux (Ed.), Two-Phase Flows and Heat Transfer with Application to Nuclear Reactor Design Problems, Hemisphere Publishing Corporation, 1978: pp. 133–155.

[15] J.-M. Le Corre, S.-C. Yao, C.H. Amon, Two-phase flow regimes and mechanisms of critical heat flux under subcooled flow boiling conditions, Nuclear Engineering and Design. 240 (2010) 245–251. doi:10.1016/j.nucengdes.2008.12.008.

[16] G.F. Hewitt, H.A. Kearsey, P.M. Lacey, D.J. Pulling, Burnout and nucleation in climbing film flow, International Journal of Heat and Mass Transfer. 8 (1965) 793–814. doi:10.1016/0017-9310(65)90025-6.

[17] R.A. De Bortoli, S.J. Green, B.W. Le Tourneau, M. Troy, A. Weiss, Forced-convection heat transfer burnout studies for water in rectangular channels and round tubes at pressure above 500 psia, WAPD-188, 1958.

[18] R.T. Lahey Jr., F.J. Moody, The thermal-hydraulics of a boiling water nuclear reactor, second edi, American Nuclear Society, 1993.

[19] A.W. Bennett, G.F. Hewitt, H.A. Kearsey, R.K.F. Keeys, D.J. Pulling, Studies of burnout in boiling heat transfer to water in round tubes with non-uniform heating. AERE-R-5076, Harwell, UK, 1966.

[20] B.S. Shiralkar, Analysis of non-uniform flux CHF data in simple geometries, NEDM-13279, 1972.

[21] General Electric BWR Thermal analysis Basis (GETAB): Data, correlation and design application, NEDO-10958, 1973.

[22] P.B. Whalley, P. Hutchinson, G.F. Hewitt, The calculation of critical heat flux in forced convective boiling, AERE-R 7520, 1973.

[23] J. Wurtz, An experimental and theoretical investigation of annular steam-water flow in tubes and annuli at 30-90 bar, RISO report no. 372, 1978.

[24] T. Okawa, A. Kotani, I. Kataoka, M. Naito, M. Naitoh, Prediction of critical heat flux in annular flow using a film flow model, Journal of Nuclear Science and Technology. 40 (2003) 388–396. doi:10.1080/18811248.2003.9715370.

[25] A. Tomiyama, O. Yokomizo, Y. Yoshimoto, S. Sugawara, Method of critical power prediction based on film flow model coupled with subchannel analysis, Journal of Nuclear Science and Technology. 25 (1988) 914–928. doi:10.1080/18811248.1988.9735949.

[26] S. Sugawara, Y. Miyamoto, FIDAS: Detailed subchannel analysis code based on three-fluid and three-field model, Nuclear Engineering and Design. 120 (1990) 147–161.

[27] M. Naitoh, T. Ikeda, K. Nishida, T. Okawa, I. Kataoka, Critical power analysis with mechanistic models for nuclear fuel bundles, (I) models and verifications for boiling water reactor application, Journal of Nuclear Science and Technology. 39 (2002) 40–52. doi:10.1080/18811248.2002.9715155.

[28] C. Adamsson, J.-M. Le Corre, Modeling and validation of a mechanistic tool (MEFISTO) for the prediction of critical power in BWR fuel assemblies, Nuclear Engineering and Design. 241 (2011) 2843–2858.

[29] S. Talebi, H. Kazeminejad, A mathematical approach to predict dryout in a rod bundle, Nuclear Engineering and Design. 249 (2012) 348–356.

[30] G.F. Hewitt, N.S. Hall Taylor, Annular two-phase flow, Pergamon Press, 1970.

[31] A.W. Bennett, G.F. Hewitt, H.A. Kearsey, R.K.F. Keeys, R.A. Stinchcombe, Measurement of liquid film flow rates at 1000 psia in upward steam water flow in a vertical heated tube, AERE-R-5809, Harwell, UK, 1969.

[32] C. Adamsson, H. Anglart, Influence of axial power distribution on dryout: Film-flow models and experiments, Nuclear Engineering and Design. 240 (2010) 1495–1505. doi:10.1016/j.nucengdes.2010.02.013.

[33] J. Young, A. Leeming, A theory of particle deposition in turbulent pipe flow, Journal of Fluid Mechanics. 340 (1997) 129–159. doi:10.1017/S0022112097005284.

[34] D. Caraghiaur, H. Anglart, Drop deposition in annular two-phase flow calculated with Lagrangian Particle Tracking, Nuclear Engineering and Design. 265 (2013) 856–866. doi:10.1016/j.nucengdes.2013.06.026.

[35] D.F. Tatterson, J.C. Dallman, T.J. Hanratty, Drop sizes in annular gas-liquid flows., AIChE Journal. 23 (1977) 68–76. doi:10.1002/aic.690230112.

[36] L.E. Gill, G.F. Hewitt, Sampling probe studies of the gas core in annular two-phase flow: III, distribution of velocity and droplet flow rate after injection through an axial jet, AERE-M-1202, Harwell, UK, 1966.

[37] L.B. Cousins, G.F. Hewitt, Liquid mass transfer in annular two-phase flow: droplet deposition and liquid entrainment, AERE-R5657, Harwell, UK, 1968.

[38] T. Okawa, A. Kotani, I. Kataoka, Experiments for liquid phase mass transfer rate in annular regime for a small vertical tube, International Journal of Heat and Mass Transfer. 48 (2005) 585–598. doi:10.1016/j.ijheatmasstransfer.2004.08.030.

[39] E.R. Quandt, Measurement of some basic parameters in two-phase annular flow, AIChE Journal. 11 (1965) 311–318.

[40] S.A. Schadel, G.W. Leman, J.L. Binder, T.J. Hanratty, Rates of atomization and deposition in vertical annular flow, International Journal of Multiphase Flow. 16 (1990) 363–374. doi:10.1016/0301-9322(90)90069-U.

[41] I.I. Paleev, B.S. Filippovich, Phenomena of liquid transfer in two-phase dispersed annular flow, International Journal of Heat and Mass Transfer. 9 (1966) 1089–1093. doi:10.1016/0017-9310(66)90031-7.

[42] S. Sugawara, Droplet deposition and entrainment modeling based on the three-fluid model, Nuclear Engineering and Design. 122 (1990) 67–84. doi:10.1016/0029-5493(90)90197-6.

[43] Y. Katto, Prediction of critical heat flux for annular flow in tubes taking into account the critical liquid film thickness concept, International Journal of Heat and Mass Transfer. 27 (1984) 883–891. doi:10.1016/0017-9310(84)90009-7.

[44] T. Okawa, I. Kataoka, Correlations for the mass transfer rate of droplets in vertical upward annular flow, International Journal of Heat and Mass Transfer. 48 (2005) 4766–4778. doi:10.1016/j.ijheatmasstransfer.2005.06.014.

[45] J.L. Binder, T.J. Hanratty, Use of Lagrangian methods to describe drop deposition and distribution in horizontal gas—liquid annular flows, International Journal of Multiphase Flow. 18 (1992) 803–820. doi:10.1016/0301-9322(92)90060-T.

[46] I. Kataoka, M. Ishii, A. Nakayama, Entrainment and deposition rates of droplets in annular two-phase flow, International Journal of Heat and Mass Transfer. 43 (2000) 1573–1589. doi:10.1016/S0017-9310(99)00236-7.

[47] P. Hutchinson, P.B. Whalley, A possible characterisation of entrainment in annular flow, Chemical Engineering Science. 28 (1973) 974–975.

[48] M. Ishii, K. Mishima, Correlation for liquid entrainment in annular two-phase flow of low viscous fluid, ANL/RAS/LWR81-2, 1981.

[49] P. Sawant, M. Ishii, M. Mori, Prediction of amount of entrained droplets in vertical annular two-phase flow, International Journal of Heat and Fluid Flow. 30 (2009) 715–728. doi:10.1016/j.ijheatfluidflow.2009.03.003.

[50] H. Utsuno, F. Kaminaga, Prediction of liquid film dryout in two-phase annular-mist flow in a uniformly heated narrow tube. Development of analytical method under BWR conditions, Journal of Nuclear Science and Technology. 35 (1998) 643–653. doi:10.1080/18811248.1998.9733920.

[51] T. Okawa, A. Kotani, I. Kataoka, M. Naitoh, Prediction of the critical heat flux in annular regime in various vertical channels, Nuclear Engineering and Design. 229 (2004) 223–236. doi:10.1016/j.nucengdes.2004.01.005.

[52] F. Secondi, C. Adamsson, J.-M. Le Corre, An assessment of entrainment correlations for the dryout prediction in BWR fuel bundles, in: NURETH-13, Kanazawa City, Japan, 2009.

[53] C. Adamsson, Dryout and power distribution effects in boiling water reactors, Ph. D. thesis, Royal institute of Technology, 2009.

[54] M. Ishii, M.A. Grolmes, Inception criteria for droplet entrainment in two-phase concurrent film flow, AIChE Journal. 21 (1975) 308–318. doi:10.1002/aic.690210212.

[55] B.J. Azzopardi, Drops in Annular Two-Phase Flow, International Journal of Multiphase Flow. 23 (1997) 1–53.

[56] M.J. Holowach, L.E. Hochreiter, F.B. Cheung, A model for droplet entrainment in heated annular flow, International Journal of Heat and Fluid Flow. 23 (2002) 807–822. doi:10.1016/S0142-727X(02)00194-7.

[57] G.B. Wallis, Annular Two-Phase Flow Part 1 : A Simple Theory, Journal of Fluids Engineering. 92 (1970) 59–72. doi:10.1115/1.3424950.

[58] J.M. Turner, G.B. Wallis, An analysis of liquid film in annular flow, NYO-3114-13, 1965.

[59] S.W. Peng, Heat flux effect on the droplet entrainment and deposition in annular flow dryout, Communications in Nonlinear Science and Numerical Simulation. 13 (2008) 2223–2235. doi:10.1016/j.cnsns.2007.06.008.

[60] G.P. Celata, K. Mishima, G. Zummo, Critical heat flux prediction for saturated flow boiling of water in vertical tubes, International Journal of Heat and Mass Transfer. 44 (2001) 4323–4331.

[61] T. Ueda, M. Inoue, S. Nagatome, Critical heat flux and droplet entrainment rate in boiling of falling liquid films, International Journal of Heat and Mass Transfer. 24 (1981) 1257–1266.

[62] J.R. Barbosa Jr., G.F. Hewitt, S.M. Richardson, J.R. Barbosa, G.F. Hewitt, S.M. Richardson, High-speed visualisation of nucleate boiling in vertical annular flow, International Journal of Heat and Mass Transfer. 46 (2003) 5153–5160. doi:10.1016/S0017-9310(03)00255-2.

[63] G.F. Hewitt, D.J. Pulling, The influence of heat flux, subcooling, wall thickness and type of heating on film flow in the evaporation of water in a vertical tube, AERE-R6117, Harwell, UK, 1969.

[64] R.K.F. Keeys, J.C. Ralph, D.N. Roberts, The effect of heat flux on liquid entrainment in steam water flow in a vertical tube at 1000 psia, AERE-R6294, Harwell, UK, 1970.

[65] V.I. Milashenko, B.I. Nigmatulin, V.V. Petukhov, N.I. Trubkin, Burnout and distribution of liquid in evaporative channels of various lengths, International Journal of Multiphase Flow. 15 (1989) 393–401. doi:10.1016/0301-9322(89)90009-8.

[66] V.E. Doroschuk, L.L. Levitan, Investigation of droplet deposition from annular dispersed steam-water flow core on wall liquid film, Therm. Phys. High Temp. 9 (1971) 591–596.

[67] C. Adamsson, H. Anglart, Annular Flow in a Tube With Various Axial Power, in: NURETH-11, Avignon, France, 2005.

[68] G.B. Wallis, The transition from flooding to upwards cocurrent annular flow in a vertical pipe, AEEW-R-142, Winfirth, UK, 1962.

[69] Y. Taitel, D. Bornea, A.E. Dukler, Modeling flow pattern transitions for steady upward gas-liquid flow in vertical tubes, AIChE Journal. 26 (1980) 345–354. doi:10.1002/aic.690260304.

[70] K. Mishima, M. Ishii, Flow regime transition criteria for upward two-phase flow in vertical tubes, International Journal of Heat and Mass Transfer. 27 (1984) 723–737. doi:10.1016/0017-9310(84)90142-X.

[71] J.R. Barbosa, G.F. Hewitt, G. König, S.M. Richardson, Liquid entrainment, droplet concentration and pressure gradient at the onset of annular flow in a vertical pipe, International Journal of Multiphase Flow. 28 (2002) 943–961. doi:10.1016/S0301-9322(02)00003-4.

[72] K.M. Becker, G. Hernborg, M. Bode, O. Eriksson, Burnout data for flow of boiling water in vertical round ducts, Annuli and Rod Clusters, AE-177, Atomenergi, Stockholm, Sweden, 1965.

[73] M. Ahmad, D.J. Peng, C.P. Hale, S.P. Walker, G.F. Hewitt, Droplet entrainment in Churn flow, in: 7th International Conference on Multiphase Flow, Tampa, Florida, USA, 2010.

[74] K. Wang, B. Bai, W. Ma, An improved liquid film model to predict the CHF based on the influence of churn flow, Applied Thermal Engineering. 64 (2014) 422–429. doi:10.1016/j.applthermaleng.2013.12.064.

[75] S. Oh, B. Hizoum, P. Saha, B. Dooies, D. Miranda, Film-droplet split correlation at the onset of annular-mist flow, in: NURETH-16, American Nuclear Society, Chicago, IL, USA, 2015.

[76] M. Andreani, G. Yadigaroglu, Prediction methods for dispersed flow film boiling, International Journal of Multiphase Flow. 20 (1994) 1–51.

[77] E.K. Kalinin, I.I. Berlin, V.V. Kostiouk, Film boiling heat transfer, Advances in Heat Transfer. 11 (1975) 51–197.

[78] A. Yamanouchi, Effect of core spray cooling in transient state after loss of coolant accident, Journal of Nuclear Science and Technology. 5 (1968) 547–558.

[79] S.K. Sahu, P.K. Das, S. Bhattacharyya, An experimental investigation on the quenching of a hot vertical heater by water injection at high flow rate, Nuclear Engineering and Design. 240 (2010) 1558–1568.

[80] M. Andreani, G. Yadigaroglu, A 3-D Eulerian-Lagrangian model of dispersed flow film boiling—II. Assessment using quasi-steady-state data and comparison with the

results of 1-D analyses, International Journal of Heat and Mass Transfer. 40 (1997) 1773–1793.

[81] M.J. Thurgood, J.M. Kelly, T.E. Guidotti, R.J. Kohrt, K.R. Crowell, COBRA/TRAC-A thermal hydraulics code for transient analysis of nuclear reactor vessels and primary coolant systems. NUREG/CR-3046, Richland, 1983.

[82] W.F. Laverty, W.M. Rohsenow, Film boiling of saturated nitrogen flowing in a vertical tube , 65-WA/HT-26, in: ASME Heat Transfer Division, 1965: p. 12.

[83] O.C. Iloeje, W.M. Rohsenow, P. Griffith, Three-Step Model of Dispersed Flow Heat Transfer (Post CHF Vertical Flow), 75- WA/HT-1, in: ASME Heat Transfer Division, 1975: p. 10.

[84] E.N. Ganic, W.M. Rohsenow, Dispersed flow heat transfer, International Journal of Heat Mass Transfer. 20 (1977) 855–866.

[85] E.N. Ganic, W.M. Rohsenow, On the mechanism of liquid drop deposition in two-phase flow, Journal of Heat Transfer. 101 (1979) 288–294.

[86] G.L. Yoder, Jr., W.M. Rohsenow, A solution for dispersed flow heat transfer using equilibrium fluid conditions, Journal of Heat Transfer. 105 (1983) 10–17.

[87] A.F. Varone, Jr., W.M. Rohsenow, Post Dryout Heat Transfer Prediction, Nuclear Engineering and Design. 95 (1986) 315–327.

[88] A.F. Varone, Jr., W.M. Rohsenow, The influence of the dispersed phase on the convective heat transfer in dispersed flow film boiling, Report Number 71999-106, Massachusetts Institute of Technology, 1990.

[89] D.C. Groeneveld, G.G.J. Delorme, Prediction of thermal non-equilibrium in the post-dryout regime, Nuclear Engineering and Design. 36 (1976) 17–26.

[90] G. Hadaller, S. Banerjee, Heat transfer to superheated steam in round tubes, WDI-147, Atomic Energy of Canada Limited, 1969.

[91] W.E. Ranz, W.R. Marshall, Evaporation from drops, Chemical Engineering Progress. 48 (1952) 141–146.

[92] G.E. Kendall, W.M. Rohsenow, Heat transfer to impacting drops and post critical heat flux dispersed flow, Report no. 85694-100, Massachusets Institute of Technology, 1978.

[93] E. Janssen, Two-phase flow and heat transfer in multirod geometries-final report, GEAP-10347, 1971.

[94] B.S. Shiralkar, R.T. Lahey Jr., The effect of obstacles on a liquid film, ASME Journal of Heat Transfer. 95 (1973) 528–533.

[95] A. Tomiyama, O. Yokomizo, Spacer Effects on Film Flow in BWR Fuel Bundle, Journal of Nuclear Science and Technology. 25 (1988) 204–206. doi:10.1080/18811248.1988.9733577.

[96] K. Nishida, T. Kanazawa, O. Yokomizo, Y. Masuhara, Spacer Effect on Liquid Film Flow and Critical Power in BWR Fuel Bundles, Journal of Nuclear Science and Technology. 31 (1994) 213–221. doi:10.1080/18811248.1994.9735140.

[97] A. Kawahara, M. Sadatomi, S. Imamura, Y. Shimoharai, Y. Hirakata, M. Endo, Effects of grid spacer with mixing vane on entrainments and depositions in two-phase annular flows, Nuclear Engineering and Technology. 47 (2015) 389–397. doi:10.1016/j.net.2015.04.002.

[98] S. Mori, T. Fukano, Influence of a flow obstacle on the occurrence of burnout in boiling two-phase upward flow within a vertical annular channel, Nuclear Engineering and Design. 225 (2003) 49–63.

[99] C. Adamsson, H. Anglart, Dryout predictions in BWR fuel assemblies with spacers, in: NUTHOS-6, Nara, Japan, 2004: p. 3690.

[100] D.K. Chandraker, Study on critical power for Advanced Heavy Water Reactor, Ph.D. Thesis, Tokyo Institute of Technology, Tokyo, 2012.

[101] T. Yano, E.I. Kodama, M. Aritomi, H. Kikura, H. Obata, Mechanistic modeling for ring-type BWR fuel spacer design. 1. Drift flow model, Nuclear Engineering and Design. 201 (2000) 177–188. doi:10.1016/S0029-5493(00)00279-X.

[102] T. Yano, M. Aritomi, H. Kikura, H. Obata, Mechanistic modeling for ring-type BWR fuel spacer design 2. Local pressure drop and narrow channel effect, Nuclear

Engineering and Design. 205 (2001) 295–303. doi:10.1016/S0029-5493(00)00392-7.

[103] T. Yano, M. Aritomi, H. Kikura, H. Obata, Mechanistic modeling for ring-type boiling water reactor fuel spacer design (3) run-off effect and model formulation, Nuclear Engineering and Design. 210 (2001) 21–36.

[104] S.H. Pham, T. Kunugi, Annular flow in rod-bundle□: Effect of spacer on disturbance waves, Flow Measurement and Instrumentation. 50 (2016) 280–288. doi:10.1016/j.flowmeasinst.2016.07.001.

[105] T. Kanazawa, K. Nishida, T. Nagayoshi, T. Kawasaki, O. Yokomizo, Critical power evaluation with consideration of differences in droplet behavior due to spacer shape influence, Journal of Nuclear Science and Technology. 32 (1995) 301–312.

[106] Y. Yamamoto, A. Hoshide, T. Mitsutake, S. Morooka, Analytical study on effects of BWR fuel spacer on droplet deposition, 175 (1997) 119–129.

[107] S. Jayanti, K.R. Reddy, Effect of spacer grids on CHF in nuclear rod bundles, Nuclear Engineering and Design. 261 (2013) 66–75.

[108] I.G. Anghel, H. Anglart, Post-dryout heat transfer to high-pressure water flowing upward in vertical channels with various flow obstacles, International Journal of Heat and Mass Transfer. 55 (2012) 8020–8031. doi:10.1016/j.ijheatmasstransfer.2012.08.036.

[109] G.L. Yoder, Heat transfer near spacer grids in rod bundles, in: National Heat Transfer Conference, Denver, CO, USA, 1985.

[110] S.L. Lee, S.K. Cho, H.J. Sheen, A Study of Droplet Hydrodynamics Across a Grid Spacer, NUREG/CR-4034, 1984.

[111] H. Xie, S. Koshizuka, Y. Oka, Simulation of drop deposition process in annular mist flow using three-dimensional particle method, Nuclear Engineering and Design. 235 (2005) 1687–1697. doi:10.1016/j.nucengdes.2005.01.011.

[112] H. Han, Z. Zhu, K. Gabriel, A study on the effect of gas flow rate on the wave characteristics in two-phase gas-liquid annular flow, Nuclear Engineering and Design. 236 (2006) 2580–2588. doi:10.1016/j.nucengdes.2006.03.015.

[113] A. V. Cherdantsev, D.B. Hann, B.N. Hewakandamby, B.J. Azzopardi, Study of the impacts of droplets deposited from the gas core onto a gas-sheared liquid film, International Journal of Multiphase Flow. 88 (2017) 69–86.

[114] R.M. Nedderman, C.J. Shearer, The motion and frequency of large disturbance waves in annular two-phase flow of air-water mixtures, Chemical Engineering Science. 18 (1963) 661–670. doi:10.1016/0009-2509(63)85036-8.

[115] N. Hall-Taylor, G.F. Hewitt, P.M.C. Lacey, The motion and frequency of large disturbance waves in annular two-phase flow of air-water mixtures, Chemical Engineering Science. 18 (1963) 537–552. doi:10.1016/0009-2509(63)85014-9.

[116] B.J. Azzopardi, Disturbance wave frequencies, velocities and spacing in vertical annular two-phase flow, Nuclear Engineering and Design. 92 (1986) 121–133. doi:10.1016/0029-5493(86)90240-2.

[117] G.R. Thwaites, N.N. Kulov, R.M. Nedderman, Liquid film properties in two-phase annular flow, Chemical Engineering Science. 31 (1976) 481–486. doi:10.1016/0009-2509(76)80033-4.

[118] T. Tomida, T. Okazaki, Statistical character of large disturbance waves in upward two-phase flow of air-water mixtures, Journal of Chemical Engineering of Japan. 7 (1974) 329–333. doi:10.1252/jcej.7.329.

[119] P. Sawant, M. Ishii, T. Hazuku, T. Takamasa, M. Mori, Properties of disturbance waves in vertical annular two-phase flow, Nuclear Engineering and Design. 238 (2008) 3528–3541. doi:10.1016/j.nucengdes.2008.06.013.

[120] S.H. Pham, Z. Kawara, T. Yokomine, T. Kunugi, Detailed observations of wavy interface behaviors of annular two-phase flow on rod bundle geometry, International Journal of Multiphase Flow. 59 (2014) 135–144.

[121] S.H. Pham, Z. Kawara, T. Yokomine, T. Kunugi, Measurements of liquid film and droplets of annular two-phase flow on a rod-bundle geometry with spacer, International Journal of Multiphase Flow. 70 (2015) 35–57.

[122] M. Vijayan, S. Jayanti, A.R. Balakrishnan, Effect of tube diameter on flooding, International Journal of Multiphase Flow. 27 (2001) 797–816.

[123] A.H. Govan, G.F. Hewitt, S.B. Lim, Visualization studies of churn flow in a vertical pipe., in: Second Irish Research Colloquia, 9th March, Institution of Chemical Engineers, Belfast, 1990.

[124] J.R. Barbosa, A.H. Govan, G.F. Hewitt, Visualisation and modelling studies of churn flow in a vertical pipe, International Journal of Multiphase Flow. 27 (2001) 2105–2127. doi:10.1016/S0301-9322(01)00048-9.

[125] K. Wang, B. Bai, W. Ma, Huge wave and drop entrainment mechanism in gas-liquid churn flow, Chemical Engineering Science. 104 (2013) 638–646. doi:10.1016/j.ces.2013.09.022.

[126] M. Vijayan, S. Jayanti, A.R. Balakrishnan, Experimental study of air-water counter current annular flow under post-flooding conditions, International Journal of Multiphase Flow. 28 (2002) 51–67.

[127] A.H. Govan, G.F. Hewitt, H.J. Richter, A. Scott, Flooding and churn flow in vertical pipes, International Journal of Multiphase Flow. 17 (1991) 27–44.

[128] A. Wolf, S. Jayanti, G.F. Hewitt, Flow development in vertical annular flow, Chemical Engineering Science. 56 (2001) 3221–3235. doi:10.1016/S0009-2509(00)00546-7.

[129] G.F. Hewitt, D.N. Roberts, Studies of two-phase flow patterns by simultaneous X-ray and flash photography, AERE-M 2159, Harwell, UK, 1969.

[130] S. V Alekseenko, A. V Cherdantsev, O.M. Heinz, S.M. Kharlamov, D.M. Markovich, Analysis of spatial and temporal evolution of disturbance waves and ripples in annular gas – liquid flow, International Journal of Multiphase Flow. 67 (2014) 122–134. doi:10.1016/j.ijmultiphaseflow.2014.07.009.

[131] L.B. Cousins, W.H. Denton, G.F. Hewitt, Liquid mass transfer in annular two-phase flow, AERE-R-4926, Harwell, UK, 1965.

[132] K. Singh, C.C. St. Pierre, W.A. Crago, E.O. Moeck, Liquid Film Flow-Rates in Two-Phase Flow of steam and water at 1000 psia., AIChE Journal. 15 (1969) 51–56.

[133] Y. Zhao, C.N. Markides, O.K. Matar, G.F. Hewitt, Disturbance wave development in two-phase gas–liquid upwards vertical annular flow, International Journal of Multiphase Flow. 55 (2013) 111–129. doi:10.1016/j.ijmultiphaseflow.2013.04.001.

[134] R. Rajalakshmi, G.J. Gorade, D.. Chandraker, B.S.V.. Sharma, P.K. Vijayan, Development of conductance based sensor for film thickness measurements in annular flow regime of the two-phase flow system, in: Global Conference and Exhibition towards Smarter and Greener Flow Measurement and Control, FCRI, Palakkad, Kerala, India, 2012.

[135] S. Alekseenko, V. Antipin, A. Cherdantsev, S. Kharlamov, D. Markovich, S. Alekseenko, et al., Two-wave structure of liquid film and wave interrelation in annular gas-liquid flow with and without entrainment Two-wave structure of liquid film and wave interrelation in annular gas-liquid flow with and without entrainment, 061701 (2009). doi:10.1063/1.3151999.

[136] S. V Alekseenko, A. V Cherdantsev, M. V Cherdantsev, S. V Isaenkov, D.M. Markovich, Study of formation and development of disturbance waves in annular gas – liquid flow, International Journal of Multiphase Flow. 77 (2015) 65–75. doi:10.1016/j.ijmultiphaseflow.2015.08.007.

[137] K. Sekoguchi, M. Takeishi, Interfacial structures in upward huge wave flow and annular flow regimes, International Journal of Multiphase Flow. 15 (1989) 295–305. doi:10.1016/0301-9322(89)90002-5.

[138] A. Wolf, S. Jayanti, G.F. Hewitt, On the nature of ephemeral waves in vertical annular flow, International Journal of Multiphase Flow. 22 (1996) 325–333.

[139] H. Han, K.S. Gabriel, Z. Wang, A new method of entrainment fraction measurement in annular gas-liquid flow in a small diameter vertical tube, Flow Measurement and Instrumentation. 18 (2007) 79–86. doi:10.1016/j.flowmeasinst.2007.01.001.

[140] D. Webb, Studies of characteristics of downward annular two-phase flow, Ph.D. Thesis,University of Cambridge, 1970.

[141] K.J. Chu, Statistical characterization and modeling of wavy liquid films in vertical two-phase flow, Ph.D. Thesis, University of Houston, 1973.

[142] D.L. Pearce, Film waves in horizontal annular flow: space time correlator experiments, RD/L/N/111/79, Central Electricity Research Laboratories, 1979.

[143] N.K. Omebere-Iyari, B.J. Azzopardi, A study of flow patterns for gas/liquid flow in small diameter tubes, Chemical Engineering Research and Design. 85 (2007) 180–192. doi:http://dx.doi.org/10.1205/cherd05059.

[144] R. Kumar, M. Gottmann, K.R. Sridhar, Film thickness and wave velocity measurements in a vertical duct, Journal of Fluids Engineering. 124 (2002) 634–642. doi:10.1115/1.1493808.

[145] G.F. Hewitt, C.J. Martin, N.S. Wilkes, Experimental and modelling studies of annular flow in the region between flow reversal and the pressure drop minimum, Physico Chemical Hydrodynamics. 6 (1985) 69–86.

[146] K. Sekoguchi, U. Takashi, T. Osamu, An investigation of the flow characteristics in the disturbance wave region of annular flow□: 2nd report, on correlation of principal flow parameters, Transactions of Japanese Society of Mehanical Engineers. 51 (1985) 1798–1806.

[147] T.T. Hazuku, N. Fukamachi, Experimental study of interfacial wave on a liquid film in vertical annular flow, in: 10th International Topical Meeting on Nuclear Reactor Thermal Hydraulics (NURETH-10), Seoul, Korea, 2003: pp. 1–18.

[148] D.M. Jepson, B.J. Azzopardi, P.B. Whalley, The effect of gas properties on drops in annular flow, International Journal of Multiphase Flow. 15 (1989) 327–339. doi:10.1016/0301-9322(89)90004-9.

[149] A. Assad, C. Jan, M. Lopez de Bertodano, S. Beus, Scaled entrainment measurements in ripple-annular flow in a small tube, Nuclear Engineering and Design. 184 (1998) 437–447. doi:10.1016/S0029-5493(98)00214-3.

[150] C. Adamsson, H. Anglart, Film flow measurements for high-pressure diabatic annular flow in tubes with various axial power distributions, Nuclear Engineering and Design. 236 (2006) 2485–2493. doi:10.1016/j.nucengdes.2006.03.002.

[151] R.W. Lockhart, R.C. Martinelli, Proposed correlation of data for isothermal two-phase, two-component flow in pipes, Chemical Engineering Progress. 45 (1949) 39–48.

[152] S. Jayanti, G.F. Hewitt, Prediction of the slug-to-churn flow transition in vertical two-phase flow, International Journal of Multiphase Flow. 18 (1992) 847–860. doi:10.1016/0301-9322(92)90063-M.

[153] C. Adamsson, J.M. Le Corre, Transient dryout prediction using a computationally efficient method for sub-channel film-flow analysis, Nuclear Engineering and Design. 280 (2014) 316–325.

[154] M. Ahmad, D.K. Chandraker, G.F. Hewitt, P.K. Vijayan, S.P. Walker, Phenomenological modeling of critical heat flux: The GRAMP code and its validation, Nuclear Engineering and Design. 254 (2013) 280–290.

[155] P. Sawant, M. Ishii, M. Mori, Droplet entrainment correlation in vertical upward co-current annular two-phase flow, Nuclear Engineering and Design. 238 (2008) 1342–1352.

[156] D.C. Groeneveld, L.K.H. Leung, P.L. Kirillov, V.P. Bobkov, I.P. Smogalev, V.N. Vinogradov, et al., The 1995 look-up table for critical heat flux in tubes, Nuclear Engineering and Design. 163 (1996) 1–23. doi:http://dx.doi.org/10.1016/0029-5493(95)01154-4.

[157] D.M. Jepson, B.J. Azzopardi, P. B. Whalley, The effect of physical properties on drop size in annular flow, in: 9th International Heat Transfer Conference, 1990: pp. 6:95–100.

[158] L. Pan, T.J. Hanratty, Correlation of entrainment for annular flow in vertical pipes, International Journal of Multiphase Flow. 28 (2002) 363–384. doi:10.1016/S0301-9322(01)00073-8.

[159] A.W. Bennett, G.F. Hewitt, H.A. Kearsey, R.K.F. Keeys, Measurements of burnout heat flux in uniformly heated round tubes at 1000 psia. AERE-R-5055, Harwell, UK, 1965.

[160] D.K. Chandraker, A.K. Vishnoi, P.K. Vijayan, D. Saha, Experimental investigation on critical heat flux and assesment of look-up table approach, in: 19th National and 8th ISHMT-ASME HMTC, Hyderabad, india, 2008.

[161] N. Hoyer, Calculation of dryout and post-dryout heat transfer for tube geometry, International Journal of Multiphase Flow. 24 (1998) 319–334. doi:10.1016/S0301-9322(97)00057-8.

[162] G.P. Gaspari, A. Hassid, F. Lucchini, A rod-centered subchannel analysis with turbulent (enthalpy) mixing for critical heat flux prediction in rod clusters cooled by boiling water, paper no. B6.12, in: 5th International Heat Transfer Conference, Tokyo, 1974.

[163] C.W. Stewart, J.M. Cuta, A.S. Koontz, J.M. Kelly, K.L. Basehore, T.L. George, et al., VIPRE-01: A thermal-hydraulic analysis code for reactor cores, EPRI-NP-2511-CCM-A-Vol.1-Rev.3, 1989.

[164] D.S. Rowe, COBRA-IIIC: A digital computer program for steady state and transient thermal-hydraulic analysis of rod bundle nuclear fuel elements, BNWL-1695, 1973.

[165] D. Butterworth, Air water climbing film flow in an eccentric annulus, AERE-R5787, Harwell, UK, 1968.

[166] H. Zhang, G.F. Hewitt, New models of droplet deposition and entrainment for prediction of CHF in cylindrical rod bundles, Nuclear Engineering and Design. 305 (2016) 73–80. doi:10.1016/j.nucengdes.2016.04.044.

[167] H. Zhang, G.F. Hewitt, Phenomenological modelling of CHF in annular flow in annuli using new models of droplet deposition and entrainment, Nuclear Engineering and Design. 305 (2016) 284–292.

[168] H. Zhang, G.F. Hewitt, New models of droplet deposition and entrainment for prediction of liquid film flow in vertical annuli, Applied Thermal Engineering. 113 (2017) 362–372.

[169] R.E. Masterson, L. Wolf, COBRA-IIIP: An improved version of COBRA for full-core light water reactor analysis, Nuclear Engineering and Design. 48 (1978) 293–310.

[170] R. Evangelisti, G.. Gaspari, L. Rubiera, G. Vanoli, Heat transfer crisis data with steam-water mixture in a sixteen rod bundle, International Journal of Heat and Mass Transfer. 15 (1972) 387–402. doi:10.1016/0017-9310(72)90205-0.

[171] M.J. Meholic, D.L. Aumiller, F.B. Cheung, A mechanistic model for droplet deposition heat transfer in dispersed flow film boiling, The 14th International Topical Meeting on Nuclear Reactor Thermal Hydraulics. (2011) 1–12.

[172] T. Saito, Multi-fluid modeling of two-phase flow and heat transfer: Application to critical heat flux prediction for BWR conditions, Ph.D. Thesis, University of Wisconsin-Madison, 1977.

[173] A.L. Biance, F. Chevy, C. Clanet, G. Lagubeau, D. Quere, On the elasticity of an inertial liquid shock, Journal of Fluid Mechanics. 554 (2006) 47–66. doi:10.1017/S0022112006009189.

[174] T.G. Myers, J.P.F. Charpin, A mathematical model of the Leidenfrost effect on an axisymmetric droplet, Physics of Fluids. 21 (2009) 063101. doi:10.1063/1.3155185.

[175] J.C. Burton, A.L. Sharpe, R.C.A. van der Veen, A. Franco, S.R. Nagel, Geometry of the vapor layer under a Leidenfrost drop, Physical Review Letters. 109 (2012) 074301–1–4. doi:10.1103/PhysRevLett.109.074301.

[176] T.A. Caswell, Dynamics of the vapor layer below a Leidenfrost drop, Physical Review E. 90 (2014) 013014–1–10. doi:10.1103/PhysRevE.90.013014.

[177] O.I. Del Rio, A.W. Neumann, Axisymmetric drop shape analysis: computational methods for the measurement of interfacial properties from shape and dimensions of pendant and sessile drops, Journal of Colloid and Interface Science. 196 (1997) 136–147. doi:10.1006/jcis.1997.5214.

[178] C. Narayanan, Multi-fluid Navier-Stokes Solver TransAT, User Manual, Zurich, Switzerland, 2008.

[179] L.H.J. Wachters, N.A.J. Westerling, The heat transfer from a hot wall to impinging water drops in the spheroidal state, Chemical Engineering Science. 21 (1966) 1047–1056.

[180] S. Namie, T. Ueda, Droplet transfer in two-phase annular mist flow. Part 1, experiment of droplet transfer rate and distributions of droplet concentration and velocity, Bulletin of JSME. 15 (1972) 1568–1580.

[181] S. Namie, T. Ueda, Droplet transfer in two phase annular mist flow. Part 2, prediction of droplet transfer rate, Bulletin of JSME. 16 (1973) 752–764.

[182] L.B. Fore, B.B. Ibrahim, S.G. Beus, Visual measurements of droplet size in gas-liquid annular flow, International Journal of Multiphase Flow. 28 (2002) 1895–1910. doi:10.1016/S0301-9322(02)00121-0.

[183] J.T. Pogson, J.H. Roberts, P.J. Waibler, An investigation of the liquid distribution in annular-mist flow, Journal of Heat Transfer. 92 (1970) 651–658.

APPENDIX-1: EXPERIMENTAL DATA FOR AIR-WATER ANNULAR AND CHURN FLOW

The results of air water experiments (chapter 3) are given below. The flow regime identification is done through d-t plots. Film flow rates were measured only for some annular flow conditions.

Q_g	Q_l	$\rho_g j_g^2$	$\rho_l j_l^2$	Re_l	δ	W_{lf}	v_w	f	λ	Regime	Video set no.
LPM	*LPM*	*kg/ms²*	*kg/ms²*	*--*	*mm*	*LPM*	*m/s*	*Hz.*	*m*		
53.1	0.45	120.293924	6.23465566	975.8171	0.217591398	-----	1.347929849	11.6	0.116200849	Churn	1
55.8	0.45	155.031207	6.23465566	975.8171	0.181202128	-----	1.363810928	10.8	0.12627879	Churn	2
62.0	0.45	218.072943	6.23465566	975.8171	0.167128527	-----	1.550849315	15.6	0.099413418	Pre-annular	3
69.2	0.45	305.559433	6.23465566	975.8171	0.147699647	-----	1.715648327	12.8	0.134035026	Pre-annular	4
70.7	0.45	353.80566	6.23465566	975.8171	0.14041958	-----	2.023347679	14.8	0.136712681	Annular	5
73.9	0.45	424.566792	6.23465566	975.8171	0.137551237	-----	2.192670036	14	0.156619288	Annular	6
82.1	0.45	571.878603	6.23465566	975.8171	0.123329897	0.427	2.315579605	16	0.144723725	Annular	7
39.2	0.35	65.6148678	3.77158182	758.9688	0.198891986	-----	1.676028108	9	0.186225345	Churn	14
57.2	0.35	162.750603	3.77158182	758.9688	0.16377972	-----	1.42245981	12	0.118538317	Churn	13
64.5	0.35	236.084867	3.77158182	758.9688	0.148976109	-----	1.642412471	15	0.109494165	Pre-annular	12
67.2	0.35	287.547509	3.77158182	758.9688	0.14	-----	1.775266916	12	0.14793891	Pre-annular	11
69.4	0.35	340.296716	3.77158182	758.9688	0.134039474	-----	1.901569019	12.5	0.152125522	Pre-annular	10
81.4	0.35	514.626414	3.77158182	758.9688	0.110859589	0.339	2.253640071	14.5	0.155423453	Annular	9
87.0	0.35	641.353169	3.77158182	758.9688	0.109214789	0.339	2.372868124	16.5	0.143810189	Annular	8
36.0	0.25	55.3223395	1.92427644	542.1206	0.153855124	-----	1.569723171	6.5	0.241495872	Churn	15
55.3	0.25	151.814792	1.92427644	542.1206	0.190692029	-----	1.034530663	12	0.086210889	Churn	16
67.1	0.25	255.383358	1.92427644	542.1206	0.132553191	-----	1.334150276	12	0.11117919	Pre-annular	17
68.2	0.25	296.553471	1.92427644	542.1206	0.131147368	-----	1.543424129	10	0.154342413	Pre-annular	18
78.2	0.25	432.929471	1.92427644	542.1206	0.115631746	-----	1.815073235	12	0.151256103	Annular	19
84.3	0.25	551.936829	1.92427644	542.1206	0.099834802	0.25	1.871873571	13	0.143990275	Annular	20
85.0	0.25	612.405433	1.92427644	542.1206	0.094231788	0.25	2.057268495	13.5	0.152390259	Annular	21
36.6	0.15	57.2521886	0.69273952	325.2724	0.186056291	-----	1.191915068	6	0.198652511	Churn	28

62.6	0.15	194.914754	0.69273952	325.2724	0.132797872	-----	0.935227169	9	0.10391413	Churn	27
77.7	0.15	342.869848	0.69273952	325.2724	0.114738971	-----	1.188026029	10	0.118802603	Annular	26
90.7	0.15	524.275659	0.69273952	325.2724	0.10355036	-----	1.576791045	9.5	0.165978005	Annular	25
87.8	0.15	544.860716	0.69273952	325.2724	0.101492837	-----	1.692488296	9.5	0.178156663	Annular	24
92.1	0.15	660.008376	0.69273952	325.2724	0.097226537	0.15	1.781781158	10.5	0.169693444	Annular	23
92.9	0.15	731.412791	0.69273952	325.2724	0.095668142	0.15	1.961505904	10.5	0.186810086	Annular	22
124.3	0.12	768.723206	0.44335329	260.2179	0.06	0.12	1.80789631	8	0.225987039	Annular	29
124.3	0.21	768.723206	1.35776946	455.3813	0.065	0.21	2.064685307	16	0.129042832	Annular	30
124.3	0.29	768.723206	2.58930638	628.8599	0.07	0.288	2.199880994	18	0.122215611	Annular	31
116.7	0.35	771.939621	3.77158182	758.9688	0.085	0.345	2.86838391	16	0.179273994	Annular	32
117.4	0.41	782.232149	5.17553391	889.0778	0.085	-----	2.653310937	21.5	0.123409811	Annular	33
123.1	0.41	965.567809	5.17553391	889.0778	0.08	0.406	2.725195614	23.5	0.115965771	Annular	34
130.9	0.35	971.357357	3.77158182	758.9688	0.08	0.34	2.751026054	22	0.125046639	Annular	35
130.8	0.29	970.07079	2.58930638	628.8599	0.075	0.2766	2.549305134	19	0.134173954	Annular	36
130.3	0.21	962.994677	1.35776946	455.3813	0.07	0.21	2.390394592	17.5	0.136593977	Annular	37
139.0	0.12	961.064828	0.44335329	260.2179	0.055	0.12	2.357005569	8.5	0.277294773	Annular	38
135.1	0.41	1418.43905	5.17553391	889.0778	0.09	0.389	2.946203701	30.67	0.09607186	Annular	39
134.6	0.35	1408.14653	3.77158182	758.9688	0.08	-----	3.03014422	29.17	0.103890659	Annular	40
140.9	0.29	1404.93011	2.58930638	628.8599	0.075	-----	2.836497702	26	0.109096065	Annular	41
141.0	0.21	1406.21668	1.35776946	455.3813	0.065	0.21	2.786921273	20	0.139346064	Annular	42
149.1	0.12	1417.15249	0.44335329	260.2179	0.06	0.12	2.632750996	12.67	0.207848763	Annular	43
159.3	0.12	2328.68452	0.44335329	260.2179	0.05	0.12	2.968088212	12.67	0.234322754	Annular	44